

Ultra-wideband Channel Modeling using Singularity Expansion Method

Gaurav Joshi

Dissertation submitted to the Faculty of the
Virginia Polytechnic Institute and State University
in partial fulfillment of the requirements for the degree of

Doctor of Philosophy

in

Electrical and Computer Engineering

Dr. Warren L. Stutzman, Chair

Dr. William A. Davis

Dr. Jeffrey H. Reed

Dr. Annamalai Annamalai

Dr. Christopher Beattie

April 21, 2006

Blacksburg, Virginia

Keywords: Dispersion, Channel Model, Ultra-wideband, Distortion, Correlation
Receiver, Matched Filter

Copyright 2006, Gaurav G. Joshi

Ultra-wideband Channel Modeling using Singularity Expansion Method

Gaurav Joshi

Abstract

Ultra-wideband (UWB) communications is expected to revolutionize high data-rate, short-distance wireless communications, providing data-rates in excess of 100 Mbps. However, the wireless channel distorts the transmitted signal by dispersing the signal energy over time. This degrades the output signal-to-noise ratio (SNR) of a correlation based matched-filter receiver, limiting the achievable data-rate and user capacity. Most wideband channel models do not account for all the identified dispersion mechanisms namely the frequency dispersion, the resonant dispersion and the multipath dispersion. The objective of this research is to model resonant dispersion based on the Singularity Expansion Method (SEM) and provide guidelines for UWB receiver design to meet the data capacity.

The original contribution of this research is a novel pole dispersion channel model that includes resonant dispersion characterization. An empirical investigation supports our claim that a correlation type matched-filter receiver using a template signal based on the pole dispersion channel model overcomes distortion related losses. Various physical mechanisms responsible for dispersion in UWB communication systems are described in detail. The applicability of the proposed dispersive channel model is evaluated using the optimal matched filter (OMF) receiver.

The SEM approach, which was originally proposed for target identification using short pulse radars, offers limited benefits of due to its susceptibility to noise. A combined fuzzy-statistical approach is proposed to improve the robustness of resonant dispersion channel modeling in presence of noise. A natural extension of this doctoral research is to improve buried landmine detection as well as breast tumor detection by applying statistical and fuzzy analysis to the backscatter response. Moreover, radar target identification using UWB short pulses stands to gain tremendously from this research.

Acknowledgement

I would like to thank my advisor, Dr. Warren L. Stutzman, for his invaluable support, encouragement and guidance over my entire stay with the Virginia Tech Antenna Group. I sincerely thank Dr. William A. Davis for his guidance, motivation and technical assistance with my research. My sincere appreciation goes to my other committee members Dr. Jeffrey H. Reed, Dr. Annamalai Annamalai, and Dr. Christopher Beattie for their support in reviewing this dissertation.

I would like to express my gratitude to Dr. Gary S. Brown, Dr. Ravi Saraf, Dr. Karen DePauw, Dr. Carl Dietrich, and Randall Nealy for their persistent help and inspiration. I would like to thank all my fellow students in the Virginia Tech Antenna Group, for their encouragement and help including, Kai Dietze, Stanislav Licul, Ko Takamizawa, Mike Barts, Minh-Chau Huynh, Seong-Youp Suh, Nathan Cummings, Taeyoung Yang, Chris Hearn, Laure Mousselon, Derek Wells, John Kim, Terry Vogler and Scott Bates. I would also like to thank the assistance of Melanie and the ECE Dept. staff.

I would like to express my deepest gratitude to Laura and Darrell Cook and their wonderful children. I also thank Tracy and Trey McCoy, and their families for their emotional support. Most of all, I am grateful to my parents, my parents-in-law, my family, my friends, and my sister. And of course, no words can express the support and love I received from my wife Vidhi for making this doctoral journey enjoyable and deeply rewarding.

Ultra-wideband Channel Modeling using Singularity Expansion Method

Gaurav Joshi

Table of Content

List of Tables	ix
List of Figures	x
Chapter 1 – Introduction	1
1.1 Challenges to Wideband Communications and Motivation	2
1.2 Brief Summary of Channel Dispersion Research	3
1.3 Research Objective and Original Contributions	5
1.4 Overview of Dissertation	7
Chapter 2 – Overview of Ultra–Wideband Channel Dispersion	11
2.1 Overview of Propagation Mechanisms	12
2.1.1 Reflection	14
2.1.2 Diffraction	15
2.1.3 Scattering	15
2.2 Ultra-Wideband Signal Dispersion and Characterization	16
2.2.1 Frequency Dispersion	16
2.2.2 Resonant Dispersion	19
2.2.3 Multipath Channel Dispersion	22
2.3 Comparison of Frequency, Resonant and Multipath Dispersions	24
2.4 Dispersive Characteristics of UWB Propagation Channels	25
2.4.1 UWB Outdoor Channel	26
2.4.2 UWB Indoor Channel	27
2.5 Chapter Summary	28
Chapter 3 – Overview of Ultra–Wideband Channel Dispersion Modeling	35
3.1 Large-Scale UWB Channel Models	37
3.1.1 Analytical UWB Path Loss Channel Modeling	38
3.1.2 Statistical UWB Path Loss Channel Modeling	39
3.1.3 Deterministic UWB Path Loss Channel Modeling	40

3.2 Small-Scale UWB Channel Modeling.....	41
3.2.1 Deterministic UWB Small-Scale Channel Modeling	42
3.2.1.1 Ray-tracing Modeling Method.....	42
3.2.1.2 Geometric Theory of Diffraction (GTD) Modeling Method	42
3.2.1.3 Uniform Theory of Diffraction (UTD)	43
3.2.2 Statistical UWB Small-Scale Channel Modeling	46
3.2.2.1 Stochastic Tapped-Delay-Line Channel Model.....	47
3.2.2.2 Saleh-Valenzuela (SV) UWB Impulse Response Channel Model	47
3.3 Frequency-dependent UWB Channel Modeling.....	49
3.3.1 Frequency domain Autoregressive (AR) Channel Model.....	50
3.3.2 Frequency-dependent Scatter Center Channel Modeling	51
3.4 Chapter Summary	52
Chapter 4 – Scatterer Response Modeling and Pole-Dispersion UWB Channel Model	61
4.1 Scatter Response Modeling using the Singularity Expansion Method (SEM).....	62
4.1.1 Frequency Domain Search Method.....	64
4.1.2 Time Domain Prony’s Method	65
4.1.3 Matrix Pencil Method	67
4.2 Time-domain Scatter Response Measurement and Analysis.....	69
4.2.1 Measurement Setup.....	70
4.2.2 Measured Scatterer Response Data Analysis.....	71
4.2.3 Pole-Residue Extraction using the Matrix Pencil Method (MPM).....	75
4.3 Pole-Residue Scattering Signatures of Canonical Structures	78
4.3.1 Spherical Scatterer	79
4.3.2 Cylindrical Scatterer	80
4.4 Pole-Dispersion UWB Channel Model.....	83
4.5 Chapter Summary	85
Chapter 5 – Validation of Scatterer Response	91
5.1 Analytical Response of Canonical Objects.....	92
5.1.1 Pole-Residue Dispersion Signature of a Conducting Sphere.....	94
5.1.2 Pole-Residue Dispersion Signature of a Thin Wire Scatterer.....	97
5.2 Validation Experiment Setup.....	100
5.2.1 Canonical Objects over a Ground Plane	101
5.2.2 Canonical Objects inside an Anechoic Chamber.....	102

5.2.3 Canonical Objects inside an Indoor Hallway Environment.....	103
5.3 Dominant Complex Poles from Measured Scatter Responses.....	104
5.3.1 Dominant Complex Poles based on Residue Magnitude.....	107
5.3.2 Dominant Complex Poles based on Pole Energy content.....	108
5.4 Scatter Response Validation using Canonical Sphere.....	110
5.4.1 Conducting Hemisphere over a Ground-Plane.....	110
5.4.2 Conducting Spheres inside an Anechoic Chamber.....	112
5.4.3 Conducting Sphere inside an Indoor Hallway Environment.....	114
5.5 Scatter Response Validation using Thin Wire Scatterers.....	116
5.5.1 Thin Wire Scatterer Inside an Anechoic Chamber.....	116
5.5.2 Thin Wire Scatterer inside an Indoor Hallway Environment.....	118
5.6 Chapter Summary.....	119
Chapter 6 – Fuzzy Pole Characterization of Scatterer Response.....	123
6.1 Effect of Noise on Complex Pole Estimation.....	124
6.2 The Unsupervised Optimal Fuzzy Clustering (UOFC) Algorithm.....	130
6.2.1 Fuzzy K–Means (FKM) Algorithm.....	132
6.2.2 Fuzzy modification of the Maximum Likelihood Estimation (FMLE).....	134
6.2.3 Performance Parameters for Fuzzy Clustering.....	135
6.2.3.1 Fuzzy Hyper Volume (FHV).....	136
6.2.3.2 Partition Density (PD).....	137
6.3 Modified UOFC Algorithm.....	138
6.4 Simulation and Measurement Results.....	140
6.4.1 Fuzzy Analysis of the Simulated Response of a Thin Wire Scatterer.....	141
6.4.2 Fuzzy Analysis of the Measured Response of a Thin Wire.....	143
6.4.3 Fuzzy Analysis of the Measured Response of a Conducting Sphere.....	147
6.5 Chapter Summary.....	149
Chapter 7 – Statistical Characterization of Scatterer Response.....	153
7.1 Framework for Statistical Analysis of Estimated Poles.....	155
7.1.1 Dominant Poles of a Thin Wire Scatterer.....	157
7.1.2 Pole Energy to Noise Ratio (E_p/N_o).....	160
7.1.3 Cluster identification prior to statistical analysis.....	162
7.2 Statistical Analysis of the Estimated Poles within a cluster.....	163
7.2.1 Student’s t-distribution.....	163

7.2.2 Curve Fitting to the histogram of the estimated poles	164
7.2.3 Validity check of the E_p/N_o parameter	166
7.3 Noise Effect on Statistical Distribution of the Estimated Poles	168
7.3.1 Effect of noise on the estimation of the real and the imaginary components	169
7.3.2 Effect of noise on the estimation of the statistical parameters.....	171
7.4 Joint distribution over the complex s-plane.....	175
7.4.1 Correlation between the real and the imaginary components.....	175
7.4.2 Joint distribution of the real and the imaginary components.....	176
7.4.3 Enhanced Pole estimation with Fuzzy Clustering	177
7.5 Chapter Summary	179
Chapter 8 – System level Performance Improvement using Pole–Dispersion Scatter Channel Model.....	183
8.1 Matched Filtering Overview.....	185
8.1.1 Matched Filtering in a Non-Dispersive Distortionless Channel	186
8.1.2 Matched Filtering in a Dispersive Channel with Pulse Distortion	187
8.1.3 Matched-Filter Implementation using Correlation Detection.....	190
8.2 Matched Filtering in a Non-Dispersive LOS UWB Channel	191
8.2.1 Experiments in an Indoor LOS Hallway Environment.....	192
8.2.2 Correlation based Matched Filter Receiver	194
8.2.3 Bit-Error-Rate Performance in a Distortionless UWB Channel	195
8.3 Matched Filtering in a Dispersive NLOS UWB Channel.....	198
8.3.1 Indoor NLOS Hallway Environment.....	198
8.3.2 Conventional and Optimal Matched Filtering	202
8.3.3 Bit-Error-Rate Performance in a Resonant Dispersive UWB Channel	204
8.4 Optimal Matched Filtering with Noisy Channel Estimate.....	206
8.4.1 Experimental Investigation of Resonant Dispersion Channel Modeling Error	207
8.4.2 Investigation of BER Performance for Resonant Dispersion Channel Estimation Error due to Noisy Received Signal	208
8.4.3 Investigation of BER Performance for Fuzzy-Statistical Estimation of Resonant Dispersion Channel.....	210
8.5 Chapter Summary	212
Chapter 9 – Conclusions	217
9.1 Resonant Dispersion Modeling and Advantages	217

9.2 Summary of Contributions.....	219
9.3 Opportunities and Future Work	221
Author Vitae.....	223

List of Tables

Table 3-1 Comparison of Channel Modeling Approaches.....	37
Table 3-2 Overview of Statistical UWB Path Loss Channel Models reported in literature	39
Table 3-3 Ultra-wideband (UWB) Large-Scale Channel Characterization using Deterministic Ray-Tracing Methods reported in literature	41
Table 3-4 Ultra-wideband (UWB) Small-Scale Channel Characterization using Deterministic Ray-Tracing Methods reported in literature	45
Table 3-5 Statistical Small-Scale Channel Characterization reported in literature for Ultra-wideband (UWB) Communications	48
Table 5-1 Comparison of the Approximate Complex Poles of a Conducting Sphere [4] to the Exact Complex Poles [14] obtained by Solving the Mie Series.....	96
Table 5-2 Three types of Validation Experiment Setups	100
Table 6-1 Thin Wire Scatterer Response Example	125
Table 7-1 Energy Content of the Dominant Pairs of Complex Conjugate Poles of a Thin Wire Scatterer described in Table 6-1 and Section 7.1 for $SNR = 25$ dB.....	161

List of Figures

Figure 1.1 Time duration comparison of measured UWB transmit-pulse, measured resonant dispersion from a 15.2 cm (6-inch) diameter sphere, and measured frequency (phase) dispersion from a log-periodic antenna. (Amplitude not to scale).	6
Figure 2.1 Illustration of basic propagation mechanisms as observed in a typical indoor channel.	13
Figure 2.2 Time-domain response of a link of two log-periodic antennas in a line-of-sight path from a 50 pico-second Gaussian pulse excitation.	17
Figure 2.3 Frequency amplitude response of a link of two log-periodic antennas in a line-of-sight path from a 50 pico-second Gaussian pulse excitation.	18
Figure 2.4 Phase delay response of a link of two log-periodic antennas in a line-of-sight path from a 50 pico-second Gaussian pulse excitation.	19
Figure 2.5 A measurement setup in a hallway environment with an empty Coke [®] can as a scatterer illuminated using two planar TEM horn antennas. The measured data were collected using a VNA HP8510 over a frequency range of 400 MHz to 12 GHz.	20
Figure 2.6 Time-domain response of a scatterer (Coke [®] can) due to a 50 pico-second Gaussian pulse excitation. The scatter response is corrected for unwanted reflections from the hallway structures and deconvolved of the antenna response.	21
Figure 2.7 Frequency amplitude response of a scatterer (Coke [®] can) due to a 50 pico-second Gaussian pulse excitation.	22
Figure 2.8 Measured Power Delay Profile of an indoor hallway environment using a VNA HP 8510B and two planar TEM horn antennas placed at a distance of 3.1 m (10.2 ft.), using 0.83 m antenna height within a frequency of 100 MHz to 12 GHz.	23
Figure 2.9 Comparison of the time-dispersion in nano-second of the three dominant dispersive phenomena in a typical indoor environment. The time duration of a typical UWB pulse (150 ps to 2 ns, corresponding to the application frequency range of 7 GHz and 500 MHz, respectively) is also shown for reference.	25
Figure 4.1 Time-domain scatterer response measurement setup using planar TEM horn antennas on a 1.2 m x 1.2 m square ground surrounded by absorber using a VNA-HP8510.	71
Figure 4.2 Frequency amplitude and time-domain response of the line-of-sight (LOS) link between two planar horn antennas ($s_{21,LOS}$).	73

Figure 4.3 Time domain response when the two horn antennas are oriented toward a 15.2 cm (6 inch) diameter conducting hemispherical scatterer on a ground plane, deconvolved by the LOS impulse response using (4.23).....	74
Figure 4.4 Measured time-domain response of a 15.2 cm (6 inch) diameter hemisphere mounted on a ground plane deconvolved with antenna response using (4.22), (4.23), and (4.24)....	75
Figure 4.5 Estimated 25 pairs of complex conjugate poles of a conducting hemisphere of diameter 15.2 cm (6 inch) mounted on a 1.2 m x 1.2 m ground plane as shown in Fig. 4.1. The complex poles are estimated using the matrix pencil algorithm and the least squares Prony's method. The real and imaginary axes are scaled by (a/c) , where a is the radius of the hemisphere and c is the speed of light.....	77
Figure 4.6 Singular value decomposition of the matrix $[\mathbf{Y}_1]$ given by (4.13) for the case of a conducting hemisphere of diameter 15.2 cm (6 inch) mounted on a 1.2 m x 1.2 m ground plane as shown in Fig. 4.1. The complex poles are estimated using the matrix pencil algorithm and the least squares Prony's method.	78
Figure 4.7 Estimated dominant poles and residues of a 15.2 cm (6 inch) diameter hemisphere over a 1.2 m x 1.2 m ground plane based on the energy content of the poles using the Matrix Pencil method.	79
Figure 4.8 Comparison of the estimated transient response using only the 6 pairs of dominant poles shown in Fig. 4.7 and the measured late time response of a 15.2 cm (6 inch) diameter hemisphere over a 1.2 m x 1.2 m ground plane.....	80
Figure 4.9 Scatter signature of a conducting cylinder of base diameter 10.2 cm (4 inch) and height 25.4 cm (10 inch). Axes scaled by (a/c) where a is the base radius of the cylinder and c is the speed of light.	82
Figure 4.10 Comparison of the estimated transient response using only the 10 pairs of dominant poles shown in Fig. 4.9 to the measured late time response of a conducting cylinder of base diameter 10.2 cm (4 inch) and height 25.4 cm (10 inch).....	83
Figure 5.1 Complex frequency domain representation of complex frequency $s_l = \sigma_l + j\omega_l$	93
Figure 5.2 Approximate complex poles $s_n^f = \sigma_n^f + j\omega_n^f$ and $s_n^g = \sigma_n^g + j\omega_n^g$ of a conducting sphere computed using the Singularity Expansion Method (SEM) of (5.6) and (5.7). The axes are normalized by the factor a/c , where a is the sphere radius and c is the speed of light.....	96
Figure 5.3 Analytically determined complex poles of a thin wire scatterer using the eigenvalue approach (5.18) [5].	99
Figure 5.4 Validation experiment setup for Scenario # 1 using two flat planar horn antennas mounted on diagonal corners of a 1.2 m x 1.2 m square ground plane.....	101

Figure 5.5 Validation experiment setup for Scenario # 2 using two curved planar TEM horn antennas mounted on pedestals inside an anechoic chamber of dimensions 3.35 m x 3.35 m x 3.35 m with 5.79 m taper (11' x 11' x 11' with 19' taper)..... 103

Figure 5.6 Scatterer response validation experiment setup for Scenario # 3 using two curved planar TEM horn antennas mounted on pedestals inside a hallway..... 104

Figure 5.7 All 23 estimated complex poles and their corresponding residues used to characterize a 15.2 cm diameter hemisphere mounted over a ground plane. The s_{21} scatter parameter measured with VNA–HP8510 was used to compute the complex poles using the Matrix Pencil Method (MPM) of Section 4.1.3. The real and imaginary axes are normalized by the factor $g = a/c \log_e 10$, where a is the sphere radius and c is the speed of light..... 106

Figure 5.8 All 23 estimated complex poles of a 15.2 cm diameter hemisphere mounted over a ground plane for Scenario # 1 compared to the poles of a conducting sphere analytically determined from (5.18) [4]. 107

Figure 5.9 The dominant complex poles of a 15.2 cm diameter hemisphere over a ground plane selected from poles in Fig. 5.8 for residue magnitudes greater than a threshold of $A_{thresh} = 8e^{-4}$. The real and imaginary axes are normalized by the factor $g = a/c \log_e 10$, where a is the sphere radius and c is the speed of light. 108

Figure 5.10 The dominant complex poles of a 15.2 cm diameter hemisphere over a ground plane selected from the poles in Fig. 5.8 for energy greater than a threshold of $E_{Threshold} = 1e^{-4}$. The real and imaginary axes are normalized by the factor $g = a/c \log_e 10$, where a is the sphere radius and c is the speed of light. 109

Figure 5.11 Comparison of scatter signature in terms of complex-pole position in the s-plane between the dominant measured poles of a 15.2 cm (6-inch) hemisphere over a ground plane in Scenario # 1 normalized by the factor $g = a/c \log_e 10$ and the analytical poles obtained by solving (5.6) and (5.7). The dominant poles are based on the magnitude of the residue (square) and the energy content (star)..... 111

Figure 5.12 Measured (solid) and estimated late-time impulse response of a 15.2 diameter hemisphere over a ground plane using all poles (dash-dot), dominant poles based on the magnitude of the residues (dash), and dominant poles based on the energy content (dotted) 112

Figure 5.13 Comparison of scatter signature in terms of complex-pole position in the s-plane between the measured dominant poles of 10.2 cm, 12.7 cm and 15.2 cm diameter conducting spheres inside an anechoic chamber in Scenario # 2 normalized by the factor $g = a/c \log_e 10$ and the analytical poles obtained by solving (5.6) and (5.7). The dominant poles are selected based on the magnitude of the residue (5.20) and the energy content (5.21). 114

Figure 5.14 Comparison of scatter signature in terms of complex-pole position in the s-plane between the measured dominant poles of 15.2 cm diameter conducting sphere inside an indoor hallway (Scenario # 3) normalized by the factor $g = a/c \log_e 10$ and the analytical

poles obtained by solving (5.6) and (5.7). The dominant poles are selected based on the magnitude of the residue (5.20) and the energy content (5.21).....	115
Figure 5.15 Comparison of scatter signature in terms of complex-pole position in the s-plane between the measured dominant poles of 29 cm, 46 cm and 64 cm length thin wire scatterers inside an anechoic chamber in Scenario # 2 normalized by the factor $h = L / (\pi \bullet c)$ and the analytical poles obtained by solving (5.18). The dominant poles are selected based on the magnitude of the residue (5.20) and the energy content (5.21).....	117
Figure 5.16 Measured dominant complex poles of a 27 cm length thin wire scatterer of thickness 0.125 inch inside an anechoic chamber	118
Figure 6.1 Analytically determined complex poles and the corresponding noiseless time-domain response of the thin wire scatterer described in Table 6.1.....	126
Figure 6.2 Time-domain response of the thin wire scatterer of Table 6.1 corrupted with a noise level corresponding to 5 dB SNR.....	127
Figure 6.3 The estimated complex poles for a single snapshot of the noisy data with 5 dB SNR using the MPM for the thin wire scatterer of Table 6.1.	128
Figure 6.4 The estimated complex poles for all the 91 snapshots or realizations of the noisy data with 5 dB SNR using the MPM for the thin wire scatterer of Table 6.1.....	129
Figure 6.5 A flow diagram of the proposed solution to the problem of representing a noisy scatterer response with cluster centroids ('fuzzy poles') using the Unsupervised Optimal Fuzzy Clustering (UOFC) algorithm.....	132
Figure 6.6 Fuzzy Hyper Volume (F_{HV}) for increasing number of clusters from 2 to 15, computed for the 2-D estimated complex poles shown in Fig. 6.4 for the example of Table 6.1.	136
Figure 6.7 Partition Density (P_D) for the number of clusters from 2 to 15 computed for the data points shown in Fig. 6.4 using (6.13) for the example of the thin wire scatterer of Table 6.1.	137
Figure 6.8 Computed fuzzy cluster centers and cluster centroids (using modified UOFC algorithm for the estimated poles shown in Fig. 6.4 and the optimal cluster size shown in Fig. 6.7 for the example of a thin wire scatterer described in Table 6.1.	139
Figure 6.9 Estimated time-domain responses using fuzzy cluster centers and cluster centroids (using modified UOFC algorithm with pole-energy weighting) for the estimated poles shown in Fig. 6.4 and optimal cluster size of 10 as shown in Fig. 6.7 for the example of a thin wire scatterer described in Table 6.1.....	140
Figure 6.10 Partition Density (P_D) for increasing number of clusters from 2 to 15 computed for simulated response of a thin wire for two levels of noise corresponding to 50 dB and 10 dB SNR for the example of a thin wire scatterer described in Table 6.1.	141

Figure 6.11 Estimated fuzzy poles of a thin wire scatterer of Table 6.1 for two levels of noise corresponding to 50 dB and 10 dB <i>SNR</i>	142
Figure 6.12 Estimated response of a thin wire scatterer of Table 6.1 using the fuzzy poles shown in Fig. 6.11 for two levels of noise corresponding to 50 dB and 10 dB <i>SNR</i>	143
Figure 6.13 Analytically determined and estimated poles from a measured response of a thin wire scatterer of length $L = 27$ cm and diameter $d = 0.1$ cm using the VNA and MPM for an averaging factor (<i>AF</i>) of 4096.	144
Figure 6.14 A comparison of analytically determined poles, estimated poles from 11 snapshots of a noisy measured response of a thin wire scatterer of length $L = 27$ cm and diameter $d = 0.1$ cm with $AF = 256$ and the computed fuzzy poles using the modified UOFC algorithm.	145
Figure 6.15 Partition Density (P_D) for increasing number of clusters from 2 to 10 computed for the measured response of a thin wire of length $L = 27$ cm and diameter $d = 0.1$ cm for 12 dB of noise corresponding to $AF = 256$	146
Figure 6.16 Comparison of estimated poles for $AF = 4096$ and fuzzy poles for $AF = 256$ & 16 determined from the measured response of the thin wire scatterer of length 27 cm and diameter $d = 0.1$ cm to the analytically determined poles [16].	147
Figure 6.17 Comparison of estimated poles for $AF = 4096$ and fuzzy poles for $AF = 256$ & 16 determined from the measured response of a conducting sphere of diameter $d = 15.25$ cm to the analytically determined poles [21].	148
Figure 7.1 Outline of an approach to improve pole estimation from noisy data using both the fuzzy and the statistical analysis.....	154
Figure 7.2 The flow diagram of the proposed framework to statistically analyze the real and imaginary components of the estimated complex poles of noisy transient response.	156
Figure 7.3 Estimated complex poles using MPM compared to the analytically determined complex poles for a noiseless time-domain response of a thin wire scatterer [14] (described in Table 6-1).	157
Figure 7.4 Comparison of the estimated TD response using only the three dominant pairs of complex conjugate poles shown in Fig. 7.3 to the analytically determined noiseless response of a thin wire scatterer [14] (described in Table 6-1). Inset picture: zoomed view of the comparison demonstrating a small deviation of the estimated response from the analytical response.....	158
Figure 7.5 Residues of the three dominant pairs of complex conjugate poles identified and shown in Fig. 7.2.	159

Figure 7.6 The estimated complex poles for 91 realizations of the noisy TD response with $SNR = 25$ dB using the MPM for the example of a thin wire scatterer [14] (described in Table 6-1).....	160
Figure 7.7 Estimated poles in the complex s -plane for the thin wire scatterer of Table 6-1 for 25 dB SNR . The cluster of estimated poles about the 3 rd order pair of dominant poles is due to using MPM from 91 realizations of noisy transient response and applying the modified fuzzy clustering algorithm described in Section 6.3.....	162
Figure 7.8 Student's t-distribution for various values of the degrees of freedom ν , compared to the normal distribution. (Curves are normalized to unity peak value with zero mean and unit variance).....	164
Figure 7.9 Best curve fit (95% confidence level) using Normal and Student's t-distribution to the histogram of the real component of the estimated poles in the cluster of the 3 rd dominant pole identified in Fig. 7.7.	165
Figure 7.10 Best curve fit (95% confidence level) using Normal and Student's t-distribution to the histogram of the imaginary component of the estimated poles in the cluster of the 3 rd dominant pole identified in Fig. 7.7.	166
Figure 7.11 Comparison of the Student's t-distribution using the statistical parameters estimated from best curve fit to the corresponding histograms of the real and the imaginary components of the estimated poles in the clusters of the 1 st , 3 rd , and 5 th dominant poles identified in Fig. 7.6.	168
Figure 7.12 Comparison of the Student's t-distribution using the statistical parameters estimated from best curve fit to the corresponding histograms of the real and the imaginary components of the estimated poles in the cluster of the 3 rd dominant pole identified in Fig. 7.7 for various E_p/N_o values.....	170
Figure 7.13 The estimated mean (μ), standard deviation (σ), and degrees of freedom (ν) recorded for the best fit Student's t-distribution to the corresponding histograms of the real and the imaginary components of the estimated poles in the cluster of the 3 rd dominant pole identified in Fig. 7.7 for various E_p/N_o values.....	172
Figure 7.14 The estimated standard deviation (σ) values recorded for the best fit Student's t-distribution to the corresponding histograms of the real and the imaginary components of the estimated poles in the cluster of the 1 st , 3 rd and 5 th dominant poles identified in Fig. 7.7 for different SNR values.	173
Figure 7.15 The estimated degrees of freedom (ν) values recorded for the best fit Student's t-distribution to the corresponding histograms of the real and the imaginary components of the estimated poles in the cluster of the 1 st , 3 rd and 5 th dominant poles identified in Fig. 7.7 for different SNR values.	174

Figure 7.16 Cross-correlation coefficient ($C_{\sigma\omega}$) between the real and imaginary components of the estimated poles recorded for the cluster of the 3 rd dominant pole identified in Fig. 7.7 for different E_p/N_o values.....	176
Figure 7.17 Joint distribution of the real and the imaginary components of the three dominant poles of the thin wire scatterer (described in Table 6-1) for $SNR = 0$ dB.	177
Figure 7.18 The estimated statistical mean values with fuzzy clustering and the fuzzy poles for $SNR = 0$ dB and 10 dB compared to the analytically determined complex poles of the thin wire scatterer described in Table 6-1.....	178
Figure 8.1 Correlation-based implementation of matched-filter (MF) receiver.	191
Figure 8.2 Measurement setup using two planar TEM horn antennas mounted on pedestals in a hallway environment oriented for direct line-of-sight (LOS).	192
Figure 8.3 The Gaussian pulse of duration 50-psec at the input to the transmitting antenna obtained after IFFT of the measured frequency-domain response using an HP-8510 vector network analyzer (VNA).	193
Figure 8.4 Received pulse in an indoor hallway environment at a distance of 0.95 m from the transmit antenna for the experiment setup shown in Fig. 8.2 and transmit pulse-shape shown in Fig. 8.3.	194
Figure 8.5 Correlation-based matched-filter output given by (8.4) for ideal distortionless channel conditions using the reference template waveform as the transmitted signal pulse-shape as given by (8.14). The received signal shown in Fig. 8.4 and the reference signal shown in Fig. 8.3 are energy normalized before matched-filtering.	195
Figure 8.6 Block diagram of a UWB communication link simulated to determine bit-error-rate (BER) based on the <i>measured</i> transmit and received signals respectively shown in Fig. 8.3 and Fig. 8.4 in an indoor LOS hallway environment.	196
Figure 8.7 Bit-error-rate (BER) performance of a communication system simulated with binary phase modulation shown in Fig. 8.6 using <i>measured</i> transmit pulse (Fig. 8.3) and receive pulse (Fig. 8.4) waveforms in a distortionless UWB channel. The simulated BER performance from measured signals is shown by dashed line and the analytically determined BER given by (8.17) is shown by solid line.	197
Figure 8.8 Measurement setup using two planar TEM horn antennas mounted on pedestals in a non-line-of-sight (NLOS) around a corner hallway environment.	199
Figure 8.9 Received distorted pulse from a fire extinguisher of diameter 13 cm, and height 43.25 cm around a corner in an indoor hallway environment for the transmitted pulse shown in Fig. 8.3, with obstructed condition between antennas as shown in Fig. 8.4.	200
Figure 8.10 Dominant pairs of complex conjugate poles of a fire extinguisher of diameter 13 cm, and height 43.25 cm, and the corresponding residue amplitudes found by processing the	

received signal shown in Fig.8.9 using the Matrix Pencil Method (MPM) described in Section 4.2.	201
Figure 8.11 Received pulse from a fire extinguisher of diameter 13 cm, and height 43.25 cm after post-processing to remove unwanted scatterer and antenna responses. The modeled response uses 4 dominant pairs of complex-conjugate poles extracted using Matrix Pencil Method outlined in Section 4.2.	202
Figure 8.12 Correlation output of the matched filter given in Section 8.1.3 using (a) CMF receiver with the transmit pulse-shape (shown in Fig. 8.3) chosen as the reference signal, and (b) OMF receiver with the reference signal (shown in Fig. 8.11) and given by (8.15).	203
Figure 8.13 Block diagram of a UWB communication link simulated to determine bit-error-rate (BER) based on the <i>measured</i> transmit and distorted received signals respectively shown in Fig. 8.3 and Fig. 8.9 in an indoor NLOS hallway environment around a corner using a fire extinguisher as a scatterer.	204
Figure 8.14 Bit-error-rate (BER) performance of a UWB communication system simulated with binary phase modulation in a NLOS dispersive channel shown in Fig. 8.13. The simulated BER performance curves for CMF and OMF receivers are respectively given by circular and square marks. The simulation uses the <i>measured</i> transmit pulse (Fig. 8.3) and receive pulse (Fig. 8.9) waveforms. The analytical performance of the conventional matched filter (CMF) receiver given by dotted line is from (8.19) using the measured value of $\xi^2 = 0.73$. The optimal performance is given by solid line and calculated from (8.17).	205
Figure 8.15 BER performance of a phase modulated dispersive UWB communication link shown in Fig. 8.13 using optimal matched filter (OMF) for various estimates of the channel impulse response (CIR) with the increasing number of dominant pole-pairs P . The mismatch factor γ is obtained by the measured correlation peak of the received signal $r(t)$ (shown in Fig. 8.9) and the reference signal obtained from (8.15) using the estimated CIR given by (8.21). The optimum performance is given by solid line and calculated from (8.17).	208
Figure 8.16 BER performance of a phase modulated UWB communication link calculated using (8.20) for decreasing SNR of the received signal. Noise causes error in resonant dispersive channel model estimation based on the received signal as described in Section 4.2. The resulting reference signal of the OMF receiver $v_{ref,OMF}(t)$ given by (8.15) and cross-correlated with the distorted received signal $r(t)$, gives the OMF receiver output γ^2 given by (8.12). The optimum performance is given by solid line and calculated from (8.17).	210
Figure 8.17 BER performance of a phase modulated UWB communication link calculated using (8.20) for improved dispersion channel estimation $h_c'(t)$ from the combined fuzzy-statistical approach for SNR = 0 dB and 10 dB. A thin wire described in Table 6-1 is used as a scatterer. The reference signal of the OMF receiver $v_{ref,OMF}(t)$ given by (8.15) is cross-correlated with the distorted received signal $r(t)$ to give the OMF receiver output (8.12). The optimal performance is given by solid line and calculated from (8.17).	212

Chapter 1 – Introduction

Wireless communication services have experienced a tremendous increase in the bandwidth, from transmitting voice (AMPS with 30 kHz) to transmitting integrated multimedia services (WCDMA with 5 MHz or more). The next generation wideband wireless applications like multi-carrier modulation techniques, and ultra-wideband (UWB) systems will require RF bandwidths in excess of 500 MHz and as much as 7 GHz [1]. As wideband wireless communication systems evolve, reliable signal reception and achievable channel capacity are of paramount importance. The antennas, as well as the wireless channel, distort wideband-transmitted signals by dispersing (spreading) the signal energy over time [2].

Dispersion in wideband wireless applications introduces pulse distortion and limits achievable channel capacity, resulting in the performance degradation of correlation-based matched filter receivers [3]. The trend towards nanosecond pulses further increases the challenges of overcoming distortion due to dispersion. Moreover, given the emergence of ultra-wideband wireless communication systems for short distance high data rate applications with a minimum bandwidth of 500 MHz, the need to accurately predict the time and frequency dispersive wireless channel is greater than ever before. In order to meet this challenge, novel channel modeling techniques are required that incorporate dispersion.

The main objective of this dissertation is to investigate the characterization of dispersion in wideband wireless communication systems and the mitigation of distortion related losses for maximum achievable SNR. Most channel models are narrowband and the few wideband channel

models have not accounted for the dispersive nature of the channel [4]. Limited simulations or measurements have been reported that investigate dispersive channel impairments in the open literature. At present, there does not exist a comprehensive treatment of the dispersive effects on the wireless channel. Tools are needed that enable communication systems to compensate for dispersion effects. The aim of this research is to accurately characterize channel dispersion using electromagnetic principles and statistical modeling techniques to meet the needs of wideband wireless system applications. Contributions from this work in scatter response characterization and modeling could benefit applications such as radar target identification, breast tumor detection, and buried landmine detection [5, 6].

This dissertation presents models, simulations and measurements that characterize scattering mechanisms and dispersion. Results from a measurement campaign performed in the 50 MHz – 20 GHz frequency band reveal the dispersive nature of scatterer response. Based on the observed dispersion, a novel pole-dispersion channel model is presented. Measured responses of canonically shaped scatterers not only validate the new pole-dispersion channel model but also pave the way for future research on wideband wireless channels.

1.1 Challenges to Wideband Communications and Motivation

Wireless communication channel modeling methods have changed little since their inception. The primary reason is that most of the channel models are for narrowband wireless applications that dominate the applications. However, with the advent of ultra-wideband (UWB) wireless communication systems, conventional channel models may no longer be applicable.

UWB communication systems have been proposed for high data rate, short-range (less than 10 meters) applications with a fractional bandwidth of 20% or a minimum bandwidth of 500 MHz at -10 dB points [1]. UWB systems will operate with a bandwidth that significantly exceeds the applicability of conventional channel models and this will require novel channel modeling supported by measurements. Receiver designs will be required to combat the distortions introduced by the dispersive wireless channel. Channel models that accurately simulate the dispersive channel characteristics would provide significant advancement towards UWB receiver design.

In an ideal wireless communication system with a distortionless channel and non-dispersive antennas, matched filtering provides the maximum achievable signal-to-noise ratio (SNR_{MF}) at the filter output [7, 8]. However, dispersion spreads the transmit signal energy over time and matched filtering is no longer optimal because of distorted received signal waveform. This mismatch in signal waveform reduces the SNR_{MF} at the output of the matched filter. The achievable data rate and user capacity, determined by the output SNR_{MF} of the matched filter are thus limited by the dispersive nature of the multipath channel. Antennas also distort the pulse shape, which adversely affects the performance of correlation-based matched filtering at the receiver [2, 9]. Dispersion introduced by the antennas and the channel can limit the data rate of a UWB system by spreading the signal energy over space and time. In a spread spectrum implementation of wireless communication systems, any uncaptured signal energy is perceived as interference and, has a deleterious effect on the useful capacity [10]. The receiver must account for the dispersive effects of the channel as well as the transmit-receive antennas.

Scattering is a frequency dependent phenomenon that causes signal distortion due to its dispersive nature [11]. Wave propagation mechanisms, especially the effects of scattering from objects in a UWB channel, are not very well understood, affecting reliable design and deployment of UWB receivers. In order to perform ideal correlation and achieve maximum SNR at the output of the matched filter, the receiver must accurately replicate all the distortions introduced by the dispersive channel.

This dissertation addresses some fundamental shortcomings of conventional channel models when they are applied to the new class of wideband wireless communications. Over the past four decades, researchers have well characterized the frequency-selective, time-varying, and spatial-polarization characteristics of the wireless channel for relatively narrowband applications. Unfortunately, little attention has been given to the frequency-dependent, dispersive nature of responses from channel objects. This research characterizes and models the channel dispersive effects motivated by application of ultra-wideband dispersive propagation channel.

1.2 Brief Summary of Channel Dispersion Research

Conventional channel models have emphasized reflection of the transmitted signal from scatterers. Such characterization of scattering is geometric in nature and hence, frequency

independent. Frequency-dependent dispersion has not been extensively investigated because its effects are usually not significant until signal bandwidth exceeds the channel coherence bandwidth. The channel coherence bandwidth is defined as the frequency range over which the channel characteristics are constant, which typically ranges about 2 – 5 MHz for indoor channels [12]. Hurst and Mittra [13] first employed time-domain analysis to decompose electrically large objects into several frequency dependent scattering centers and to distinguish the contributions of different multipath components. This approach has been found to be useful in acoustic communications by time-domain characterization of a dispersive ocean channel [14].

In 1995, Qiu proposed a frequency dependent channel model [15] that incorporates the diffraction mechanism of multipath components. Qiu later performed measurements in the 2 – 2.67 GHz band to validate the frequency dependent channel model by decomposing the received field into scattering centers [16]. In his works, Qiu modifies the traditional Turin's multipath channel model [17] by adding a frequency dependent diffraction term for each multipath component and compares the results with the geometric theory of diffraction (GTD) approximations.

Over the past several decades, researchers have well characterized the multipath dispersive characteristics of the wireless channel in terms of a linear time-varying filter defined completely by its impulse response. A generalized impulse response model of the multipath dispersive nature of the wireless channel was first proposed by Turin [17]. Since then, several investigators have studied the multipath propagation for wideband applications in outdoor environments [18], and indoor environments [19].

However, little attention has been given to other types of dispersive channels. Physics-based wireless channel measurement and modeling is needed to understand dispersion. At present, there is a lack of comprehensive treatment of channel dispersion applied to wireless communication systems. The research on dispersive channel characterization is limited to multipath dispersion with neither simulation nor have measurement results been reported that characterize resonant dispersion and frequency dispersion for ultra-wideband wireless communication systems. Moreover, the cost effectiveness of incorporating dispersion compensation at the receiver and its impact at the system level has not been addressed so far.

1.3 Research Objective and Original Contributions

Propagation mechanisms for UWB applications with bandwidths up to 7.5 GHz exhibit transient characteristics that are best studied in the time-domain. A generalized channel impulse response can be expressed as a sum of various multipath components each with a different propagation mechanism. Reflection has been extensively investigated and modeled deterministically using the ray-tracing methods such as Geometrical and Physical Optics (GO/PO), and stochastically modeled using impulse response models. Diffraction is deterministically modeled by methods such as Geometrical and Uniform Theory of Diffraction (GTD/UTD). Although there is no complete stochastic model for diffraction, a scatter-center channel model [20, 21] incorporates frequency dependent mechanisms using diffraction coefficients.

Scattering can be correctly modeled if the environment geometry and scatterer response are accurately known. However, most of the effort towards scatter characterization has focused on determining the geometry of the environment using site-specific channel sounding and geometrically based single/multiple bounce channel-modeling approaches. Because all the wireless application bandwidths are relatively narrow compared to that of UWB applications, the response of the scatterers have not been investigated extensively. One possible to model the dispersive pulse response of finite dimensional objects to a wideband incident pulse is by using the Singularity Expansion Method (SEM) [22]. The SEM approach models the response of a finite dimensional object to incident wideband pulse as a weighted sum of complex exponentials or damped sinusoids.

Dispersion is commonly defined as any phenomenon in which the signal spreads in time as it propagates through a medium. Dispersion introduces pulse distortion, degrades the output signal-to-noise ratio (SNR) of the matched-filter receiver, and thus, limits achievable channel capacity. Characterization of channel dispersion in wideband wireless communication can mitigate distortion related losses and achieve maximum achievable SNR. Based on the underlying phenomenon, dispersion can be classified into following categories [3]

- i. Resonant dispersion: caused by ringing response from scatterers
- ii. Frequency (phase) dispersion: caused by frequency dependent delay
- iii. Multipath dispersion: caused by multipath propagation and well characterized by RMS delay spread.

Ultra-wideband communication systems employ Gaussian shaped nano-second pulses to achieve high data rates (in excess of 100 Mbps) over a short distance. The maximum pulse width of a Gaussian UWB pulse is 2 nano-seconds corresponding to the minimum allowable bandwidth of 500 MHz [1]. Figure 1.1 compares a 500 nsec Gaussian pulse with the observed resonant dispersion from a conducting sphere of diameter 15.2 cm (6 inch) and frequency dispersion from using a log-periodic antenna. The signal amplitudes have been scaled for comparison. Multipath dispersion, which dominates for large indoor environments, is not shown in Fig. 1.1. However, for office or residential indoor environments, frequency and resonant dispersive mechanisms cannot be ignored.

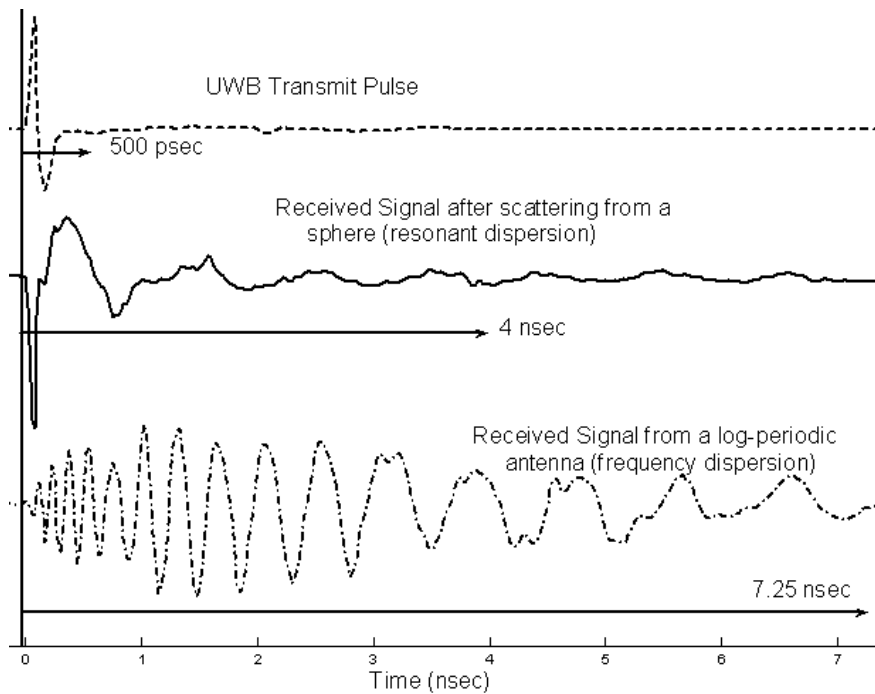


Figure 1.1 Time duration comparison of measured UWB transmit-pulse, measured resonant dispersion from a 15.2 cm (6-inch) diameter sphere, and measured frequency (phase) dispersion from a log-periodic antenna. (Amplitude not to scale).

The goal of this research is to complement the research reported in [9] and [10] on frequency dispersion by investigating resonant channel dispersion from the perspective of Singularity Expansion Method (SEM). More specifically, the research objective is to model UWB resonant channel dispersion based on the Singularity Expansion Method (SEM) and statistical modeling techniques to improve UWB communication performance.

This research investigates improvement in UWB signal reception achieved by compensating for the distortion due to all the identified dispersive mechanisms. Various underlying phenomena that lead to dispersion in UWB communication systems are investigated and classified into frequency (phase), resonant (time) and, multipath dispersion. Frequency dependent scatterer response to incident UWB pulse in a typical multipath channel is modeled by extending frequency-independent conventional channel models to include frequency-dependent scatterer response. The proposed model permits implementation of optimum matched filtering. Original contributions of this research include:

- Resonant dispersion modeling in presence of noise using modified fuzzy clustering approach.
- Statistical pole-residue scatterer-response modeling
- A novel pole-dispersion channel model that includes frequency-dependent scatter response using the Singularity Expansion Method (SEM).
- System level performance evaluation of the proposed pole-dispersion channel model for a communication link using correlation based matched-filter receivers.

1.4 Overview of Dissertation

The early chapters of the dissertation provide an overview of the dispersive channel using scatterer characterization, while the latter chapters validate the proposed new dispersive channel model using measurements and simulations. Chapter 2 presents a framework to understand and characterize dispersion in wideband wireless channels. Dispersion is poorly understood and illustrations are provided to identify and classify dispersive phenomena. Dispersive characteristics of outdoor and indoor ultra-wideband channels are also briefly addressed.

Chapter 3 presents an overview of various conventional wideband wireless channel models. Traditional channel characterization and modeling approaches are briefly discussed followed by a summary of the published work on UWB channel dispersion modeling. Analytical, deterministic, and stochastic channel modeling approaches are also briefly discussed.

Chapter 4 offers insight into the resonant scattering responsible for the signal distortion. The scatterer response from finite dimensional objects is modeled in terms of poles and residues

using the Singularity Expansion Method (SEM). Results from measurements are provided to illustrate waveform classification and unique pole-residue signatures of the scatterers. Pole-residue extraction algorithms such as Prony's method and the Matrix Pencil Method (MPM) are also described. A novel pole-dispersion channel model is presented based on the analysis of scatterer responses collected through measurements.

Chapter 5 provides validation for the wideband wireless measurement campaign performed in the 50 MHz – 20 GHz frequency band. Responses of canonical structures such as conducting spheres and thin wire scatterers of various sizes are used to validate the scatterer response modeling incorporated in the pole-dispersion channel model. The pole-residue dispersion characteristics of scatterer response are validated through comparison of the estimated complex-pole positions from measured data and the complex-pole positions available analytically for canonical objects.

Chapter 6 presents an alternate approach to the pole-residue dispersion characterization of scatterer response in terms of a small number of equivalent poles termed 'fuzzy poles'. Measured and simulated scatterer responses of a straight wire and a conducting sphere are evaluated to extract equivalent 'fuzzy poles' at various noise levels. A modified fuzzy clustering approach is proposed as a solution to overcome the effect of noise. The original contribution is the demonstration that the estimated fuzzy poles offer a close match to the actual poles.

Chapter 7 demonstrates that the pole estimation using fuzzy clustering approach can be further improved by incorporating the statistical behavior of the estimated poles in presence of noise. The combined fuzzy-statistical approach in estimating the true poles offers near-accurate results. The probability distribution, mean and standard deviation of the estimated poles is presented for a thin wire scatterer. The original contribution is a joint distribution of the real and imaginary components of the estimated poles evaluated for various noise levels.

The proposed pole-dispersion channel model is evaluated in Chapter 8. The effect of dispersion on UWB communication systems can be quantified in terms of the cross-correlation peak at the output of the correlation-based matched filter receivers. This chapter presents simulated and measured results demonstrating the advantage of using the proposed pole-dispersion channel model over the conventional frequency-independent channel models in modeling the resonant channel dispersion. The robustness of the proposed dispersive channel model is evaluated using optimal matched-filter (OMF) approach with noisy channel estimates.

Finally, Chapter 9 presents an overall summary and conclusions. The original contributions of this dissertation are summarized followed by a short discussion on the possibilities for future work.

References

- [1] FCC, "Authorization of Ultrawideband Technology, First Report and Order," Federal Communications Commission, Washington D.C. *FCC 02-48*, February 14, 2002.
- [2] H. G. Schantz, "Dispersion and UWB antennas," *Proceedings of International Conference and Workshop on Ultra Wideband Systems, Joint UWBST & IWUWBS '04*, pp. 161-165, May 2004.
- [3] G. G. Joshi, W. A. Davis, and W. L. Stutzman, "Ultra-wideband (UWB) channel dispersion: classification and modeling," *IEEE Antennas and Propagation Society International Symposium*, vol. 1B, pp. 702-705, July 2005.
- [4] H. Hashemi, "Impulse response modeling of indoor radio propagation channels," *IEEE Journal on Selected Areas in Communications*, vol. 11, pp. 967-978, Sept. 1993.
- [5] G. G. Joshi, W. A. Davis, and W. L. Stutzman, "Statistical and fuzzy pole characterization of the complex poles of a conducting sphere and a wire," *presented at the URSI National Radio Science Meeting at Boulder, CO*, Jan. 2006.
- [6] C. E. Baum, E. J. Rothwell, K. M. Chen, and D. P. Nyquist, "The singularity expansion method and its application to target identification," *Proceedings of the IEEE*, vol. 79 (10), pp. 1481-1492, Oct. 1991.
- [7] J. G. Proakis, *Digital Communications*, 4th ed. Boston: McGraw-Hill, 2001.
- [8] J. G. Proakis and M. Salehi, *Communication Systems Engineering*, 2nd ed. Upper Saddle River, N.J.: Prentice Hall, 2002.
- [9] S. Licul, "Ultra-Wideband Antenna Characterization and Modeling," in *Bradley Dept. of Electrical and Computer Engineering, Ph.D Dissertation*. Blacksburg: Virginia Polytechnic Institute and State University, 2004.
- [10] R. C. Qiu, "A study of the ultra-wideband wireless propagation channel and optimum UWB receiver design," *IEEE Journal on Selected Areas in Communications*, vol. 20 (9), pp. 1628-1637, Dec. 2002.
- [11] W. L. Stutzman and G. A. Thiele, *Antenna Theory and Design*, 2nd ed. New York: J. Wiley, 1998.
- [12] J. D. Parsons, *The Mobile Radio Propagation Channel*, 2nd ed. New York, NY: John Wiley & Sons Inc., 2000.

- [13] M. Hurst and R. Mittra, "Scattering center analysis via Prony's method," *IEEE Transactions on Antennas and Propagation*, vol. 35 (8), pp. 986-988, Aug. 1987.
- [14] J. P. Hermand and W. I. Roderick, "Acoustic model-based matched filter processing for fading time-dispersive ocean channels: theory and experiment," *IEEE Journal of Oceanic Engineering*, vol. 18 (4), pp. 447-465, Oct. 1993.
- [15] R. C. Qiu and I. T. Lu, "A novel approach with superresolution and path frequency dependence for channel modeling and application in CDMA cellular system," *Proceedings of the IEEE Wireless Communication System Symposium*, pp. 27-32, Nov. 1995.
- [16] R. C. Qiu and I. T. Lu, "A novel model of time-dispersion multipath channel for wideband CDMA systems," *Proceedings of the 5th IEEE International Conference on Universal Personal Communications*, vol. 1, pp. 350-354, Sept. - Oct. 1996.
- [17] G. Turin, "On the estimation in the presence of noise of the impulse response of a random, linear filter," *IEEE Transactions on Information Theory*, vol. 3, pp. 5-10, Jan. 1957.
- [18] H. Suzuki, "A Statistical Model for Urban Radio Propagation," *IEEE Transactions on Communications*, vol. 25 (7), pp. 673-680, July 1977.
- [19] H. Hashemi, "The indoor radio propagation channel," *Proceedings of the IEEE*, vol. 81 (7), pp. 943-968, July 1993.
- [20] R. C. Qiu, "A generalized time domain multipath channel and its application in ultra-wide-band (UWB) wireless optimal receiver design: system performance analysis," *Proceedings of IEEE Wireless Communications and Networking Conference, WCNC '04*, vol. 2, pp. 901-907, Mar. 2004.
- [21] R. C. Qiu, Z. Chenming, and L. Qingchong, "Physics-based pulse distortion for ultra-wideband signals," *IEEE Transactions on Vehicular Technology*, vol. 54, pp. 1546-1555, Sept. 2005.
- [22] C. E. Baum, "On the Singularity Expansion Method for the Solution of Electromagnetic Interaction Problems," *Interaction Notes #88, AFRL Directed Energy Directorate*, Dec. 1971.

Chapter 2 – Overview of Ultra–Wideband Channel Dispersion

Ultra-wideband (UWB) communication is expected revolutionize high data rate indoor wireless communications, providing data rates in excess of 100 Mbps [1, 2]. However, the indoor wireless channel distorts the transmitted sub-nanosecond pulse signal by dispersing the signal energy over time [3-5]. The channel dispersion degrades the output signal-to-noise ratio (SNR_{out}) of a correlation based matched-filter receiver [6-8]. The motivation is to model the channel dispersion in order to improve the signal-to-noise ratio at the output of the matched filter receiver because SNR_{out} determines the achievable channel data capacity in ultra-wideband communication systems.

This chapter presents an overview of the UWB channel dispersion keeping in line with the objective to model dispersion and provide guidelines for UWB receiver design. The output signal-to-noise ratio (SNR_{out}) of a correlation based matched-filter receiver is limited by the dispersive nature of the channel including the antenna effects. The channel dispersion can be classified as multipath dispersion, frequency dispersion, and resonant dispersion [3]. Prior research on dispersive channel characterization for ultra-wideband communication systems is limited to multipath dispersion with neither simulation nor measurement results reported that completely characterize other dispersive mechanisms such as resonant and frequency dispersion. There is a need to investigate all dispersion mechanisms in the study of means to mitigate distortion related losses.

The understanding of how the channel spreads transmit signal energy in time can lead to a receiver system design that compensates for dispersive distortion. Scattering wave propagation mechanisms, especially the response of scattering objects to ultra-wideband pulse excitation, have not been comprehensively investigated. Simple and accurate characterization of the scatterer response to incident ultra-wideband pulse contributes to the design of UWB receivers.

This chapter examines dispersion and the various phenomena that lead to dispersion. A brief overview of basic wireless propagation mechanisms such as the reflection, diffraction, and scattering is presented in Section 2.1. Section 2.2 defines and classifies various dispersive phenomena observed in a wireless channel such as the multipath, frequency, and resonant dispersion. Section 2.3 compares the dispersion from the three types of the identified dispersive phenomena in terms of the time-duration of dispersed pulse. Section 2.4 briefly summarizes the dispersive characteristics of the outdoor and the indoor ultra-wideband (UWB) channels as reported in literature. Finally, Section 2.5 presents a summary of important issues addressed in this chapter.

2.1 Overview of Propagation Mechanisms

Basic propagation mechanism physics completely describes the dispersive characteristics of the channel. The basic propagation mechanisms, namely reflection, diffraction and scattering have proved to be useful in determining the multipath dispersive nature of wireless channel [9]. A graphical presentation of these mechanisms is shown in Fig. 2.1, which represents a typical indoor wireless channel. In this section, an overview of these three basic propagation mechanisms is presented and used to build a complete dispersive characterization of wireless channel.

In an indoor environment, the ultra-wideband transmit signal interacts with the surrounding objects such as walls, the floor, the ceiling, windows, and furniture to produce multipath components at the receiver. Propagation mechanisms exhibit transient characteristics that are best studied in the time-domain because the ultra-wideband (UWB) applications have a very wide bandwidth (as much as 3.1 GHz – 10.6 GHz for indoor application). In an indoor multipath environment each propagation mechanism needs separate treatment to characterize different dispersion phenomena.

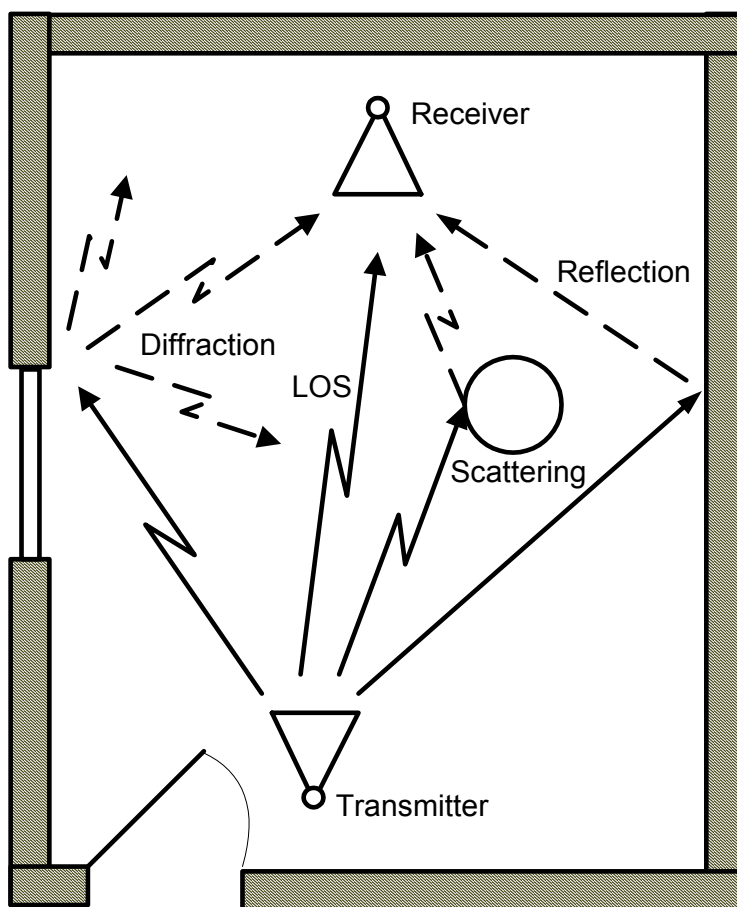


Figure 2.1 Illustration of basic propagation mechanisms as observed in a typical indoor channel.

A generalized channel impulse response can be expressed as the summation multipath components each representing a different propagation mechanism [10]:

$$h_C(t, \tau) = h_{LOS}(t, \tau) + h_r(t, \tau) + h_d(t, \tau) + h_s(t, \tau) \quad (2.1)$$

where $h_C(t, \tau)$ = complete channel impulse response

$h_{LOS}(t, \tau)$ = channel impulse response of the line-of-sight component

$h_r(t, \tau)$ = channel impulse response of single or multi-reflected rays

$h_d(t, \tau)$ = channel impulse response of diffracted multipath components

$h_s(t, \tau)$ = channel impulse response of scattered multipath components

Reflection, which occurs when the object size is much greater than the wavelength of an incident electromagnetic wave, is a well-characterized and modeled mechanism. In a typical indoor environment, the walls, the floor, and the ceiling reflect the incident electromagnetic

wave. In a line-of-sight (LOS) scenario, the LOS component is usually the strongest in terms of energy content followed by the reflected component. Diffraction occurs when an electromagnetic wave strikes the edge of an object such as a windowsill or a piece of furniture. Some of the diffracted waves reach the receiver even if the receiver is shadowed from the transmitter. Scattering occurs when the object size is comparable to or smaller than the incident electromagnetic wave wavelength [10]. Scattering typically occurs from rough surfaces, small furniture objects in an indoor environment and foliage, and lampposts in an outdoor environment.

2.1.1 Reflection

Reflection is usually the dominant indirect propagation mechanism and determines the multipath nature of the wireless channel. Reflection occurs when an electromagnetic wave propagating in a medium encounters another medium in its path with different electromagnetic properties (permittivity ϵ_r , permeability μ_r , and conductance σ). The amplitude of the multipath component due to reflection from the objects in the environment can be determined by the reflection coefficient, which is a function of frequency, polarization, angle of incidence and the type of material.

Realistic channel modeling of an indoor multipath environment requires consideration of multipath components that have significant contribution to the received signal. Three-dimensional deterministic modeling of an indoor environment with reflections is computationally intensive. Ray-tracing methods like Geometrical Optics (GO) and Physical Optics (PO) deterministically model reflection mechanism [11]. Ray-tracing methods in time-domain determine the amplitude of the reflected multipath component using the time-domain dyadic reflection coefficient [12]

$$\overline{\overline{\Gamma}}_r(t) = \Gamma_{hp}(t) \hat{e}_\perp^i \hat{e}_\perp^r + \Gamma_{vp}(t) \hat{e}_\parallel^i \hat{e}_\parallel^r \quad (2.2)$$

where Γ_{hp} and Γ_{vp} are reflection coefficients for horizontal and vertical polarizations. Stochastically, reflection is modeled by the distribution of amplitude in the multipath channel impulse response. Statistical modeling of various dispersion mechanisms is described in detail in the next chapter.

2.1.2 Diffraction

The diffraction component of the received signal is weak compared to the reflection component. Diffraction occurs when an electromagnetic wave propagating in a medium strikes an object edge, resulting in secondary radiation in all directions [13]. The components diffracted from an edge exhibit different amplitude and waveform distortion compared to the multipath components reflected from smooth surfaces. Similar to reflection, the amplitude of the diffracted multipath components can be determined by the diffraction coefficient that depends on the object, incident angle, and exiting angle.

Simplistic channel models almost always neglect diffraction and consider only the reflection mechanism. However, for wideband signal applications, accurate characterization of propagation requires inclusion of principal diffraction mechanisms, especially in an indoor multipath environment. Just as reflection can be modeled deterministically by ray-tracing methods, so can diffraction be deterministically modeled by incorporating diffraction principles into ray tracing methods, such as in the Geometrical Theory of Diffraction (GTD) and the Uniform Theory of Diffraction (UTD) [14-16]. Hybrid statistical-deterministic methods allow inclusion of diffraction through statistical impulse response characterization combined with the deterministic diffraction coefficient determination [17].

2.1.3 Scattering

Scattering is the least understood and modeled of the three basic propagation mechanisms. Scattering occurs when the object size is comparable or smaller than the wavelength of the incident electromagnetic wave [10]. Scattering mechanisms can be completely determined by knowing [18]

- The geometrical relationship between the transmitter, receiver and scatterers in a given environment
- The response of scatterers to incident electromagnetic waves.

Most research efforts in scattering phenomenon characterization have focused on determining the environment geometry. The geometrical relationship of the communication system to the surrounding scatterers helps in understanding the multipath propagation. It can be found deterministically using site-specific numerical channel measurement tools [19-21].

Although such site-specific experimental tools provide complete details of the environment, they require large measured data sets. In comparison, simple geometrically based single scatter bounce channel models can statistically model the geometric nature of the environment with sufficient accuracy [22]. Such models require knowledge of the time-dispersion characteristics of the channel specified in terms of the delay spread.

The response of scatterers to an incident wideband electromagnetic pulse is frequency dependent [23-25]. The responses of the scatterers to wideband pulses have not been included into channel modeling because most wireless application bandwidths are relatively narrow (a few MHz) compared to that of the ultra-wideband applications (500 MHz – 7.5 GHz bandwidths). The later chapters of this dissertation address statistical characterization and modeling of the scattering response mechanism that include the resonant dispersion and frequency dispersion.

2.2 Ultra-Wideband Signal Dispersion and Characterization

Dispersion is commonly defined as any phenomenon in which the signal-energy or information spreads over time; however, there are other definitions for various applications. Classical electromagnetism defines dispersion to be any phenomenon in which the velocity of propagation of an electromagnetic wave is wavelength dependent [13, 26]. Frequency dependent velocity causes some frequency components to experience different time delays. In the field of signal processing, dispersion is defined as the spreading of the signal over time when passed through a band-limited channel or filter [27, 28]. Wireless communications defines dispersion as the time spreading of the signal observed at the receiver due to the multipath phenomena [29, 30].

This section investigates the following basic dispersion phenomena:

- 1) Frequency (phase) dispersion
- 2) Resonant dispersion
- 3) Multipath dispersion

2.2.1 Frequency Dispersion

Frequency dispersion is the spreading in time of signal energy due to frequency dependent time-delay and is observed in the response of most wideband antennas. It can be viewed as the failure

of the antenna structure or scatterer to radiate or re-radiate all frequency components simultaneously [13]. For example, spiral antennas exhibit chirp-like time-domain response to UWB pulse excitation. The frequency dispersive characteristics of spiral antennas have been investigated for sub-nanosecond wide Gaussian impulse excitation [31, 32]. Similarly, log periodic and TEM horn antennas are also dispersive [33, 34].

Wideband antennas introduce frequency selective time-delay due to their physical structures. Figure 2.2 shows the time-domain response of a link consisting of two log-periodic antennas with a direct line-of-sight (LOS) path from a 50 pico-second Gaussian pulse excitation. A vector network analyzer (VNA-8510) was used to measure the LOS link between the two log-periodic antennas.

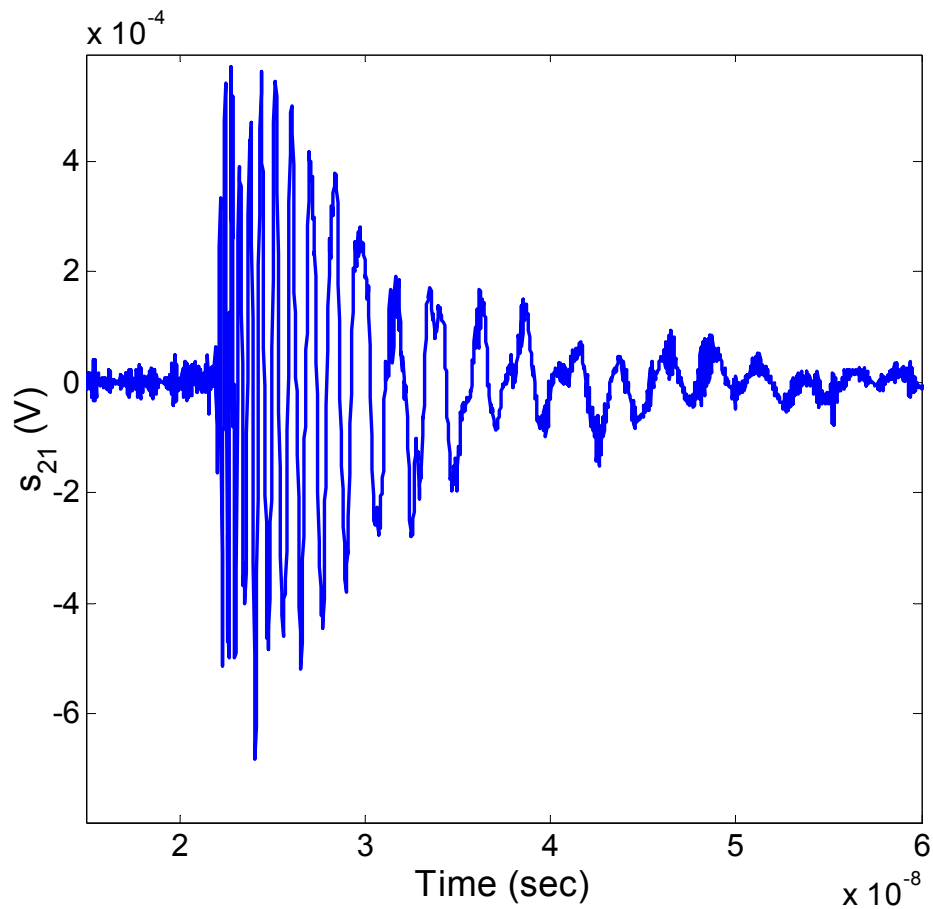


Figure 2.2 Time-domain response of a link of two log-periodic antennas in a line-of-sight path from a 50 pico-second Gaussian pulse excitation.

When these wideband antennas are excited with a sub-nanosecond Gaussian pulse, the pulse travels from the point of excitation in the center to the edge of the antenna, resulting in the radiation of the high frequency components followed in time by lower frequency components. This phenomenon is called frequency dispersion, which is exhibited by a chirp-like signal that extends the pulse duration by 2–10 nsec.

The amplitude of the frequency response of the link between two log-periodic antennas is fairly flat over the UWB range of frequencies as seen in Fig. 2.3. This indicates that all frequency components of the wideband Gaussian pulse are transmitted with nearly equal strength. However, the associated phase response shown in Fig. 2.4 is not linear, indicating that some frequency components of the transmitted signal experience more time delay compared to some other frequency components. High frequency components have less time delay than the low frequency components, resulting in a chirp-like response as seen in Fig. 2.2.

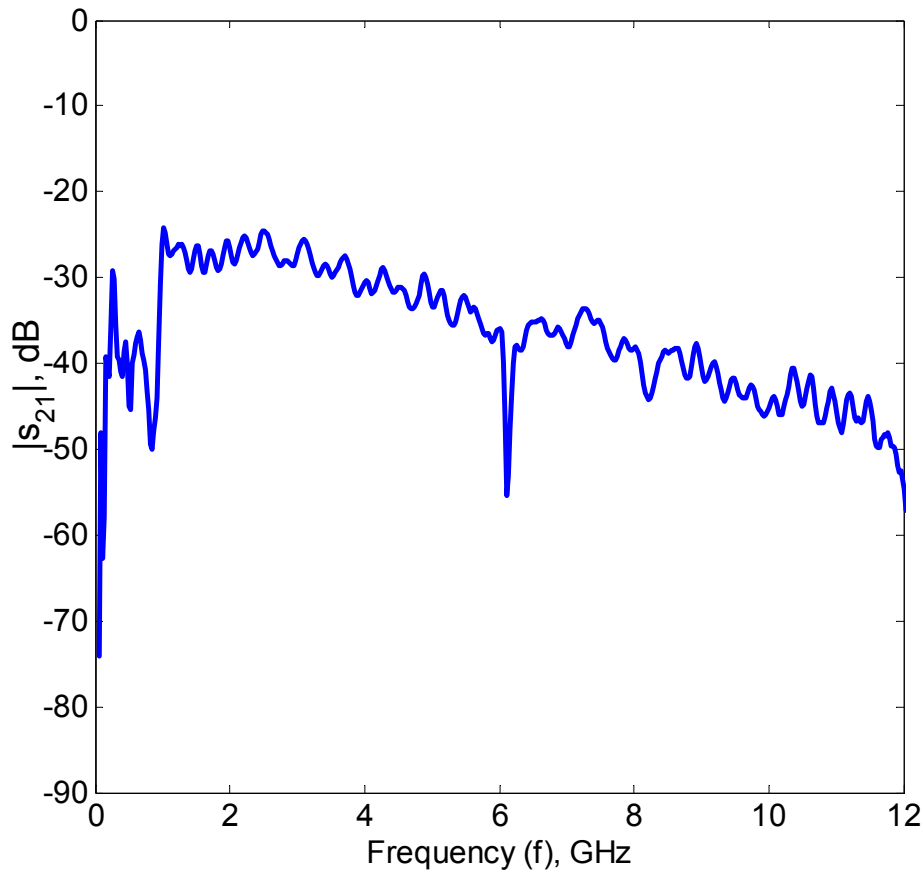


Figure 2.3 Frequency amplitude response of a link of two log-periodic antennas in a line-of-sight path from a 50 pico-second Gaussian pulse excitation.

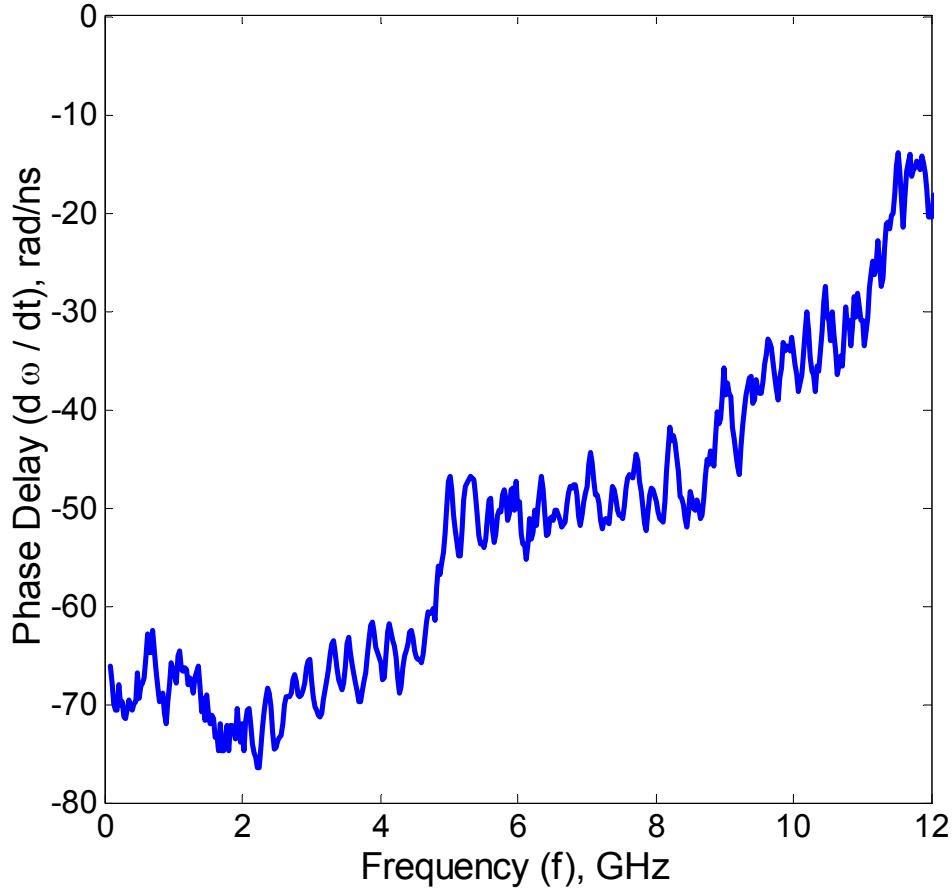


Figure 2.4 Phase delay response of a link of two log-periodic antennas in a line-of-sight path from a 50 pico-second Gaussian pulse excitation.

2.2.2 Resonant Dispersion

Resonant dispersion is the spreading of pulse energy over a time duration longer than that of the excitation pulse due to the presence of surface current resonant modes. It can be viewed as the failure of the antenna structure to radiate all frequency components with equal gain. Some frequency components are emphasized which causes resonance at those frequencies after the excitation pulse has passed giving a lingering excitation and response.

Resonant dispersion is observed in the time-domain response of an arbitrary scatterer in an indoor environment. Figure 2.5 shows a measurement setup in a hallway environment with an empty Coke[®] can as a scatterer illuminated using two TEM horn antennas. The measured data were collected using a VNA HP8510 over a frequency range of 400 MHz to 12 GHz in

accordance with the FCC specifications for indoor UWB communications [35]. The experiment setup is explained in detail in Section 5.2.3. When excited with a Gaussian pulse of duration 50 pico-seconds, the time-domain response exhibits a specular component that corresponds to the reflection of the smooth metallic structure followed by a resonant (time) dispersion component. Figure 2.6 shows the time-domain response of a Coke can after correcting for the unwanted reflections from the hallway structures and after deconvolution of the antenna effects [36]. Figure 2.7 shows the corresponding frequency-domain response, which is not flat with some frequencies emphasized. These frequencies correspond to the resonant frequencies observed in the time-domain response.

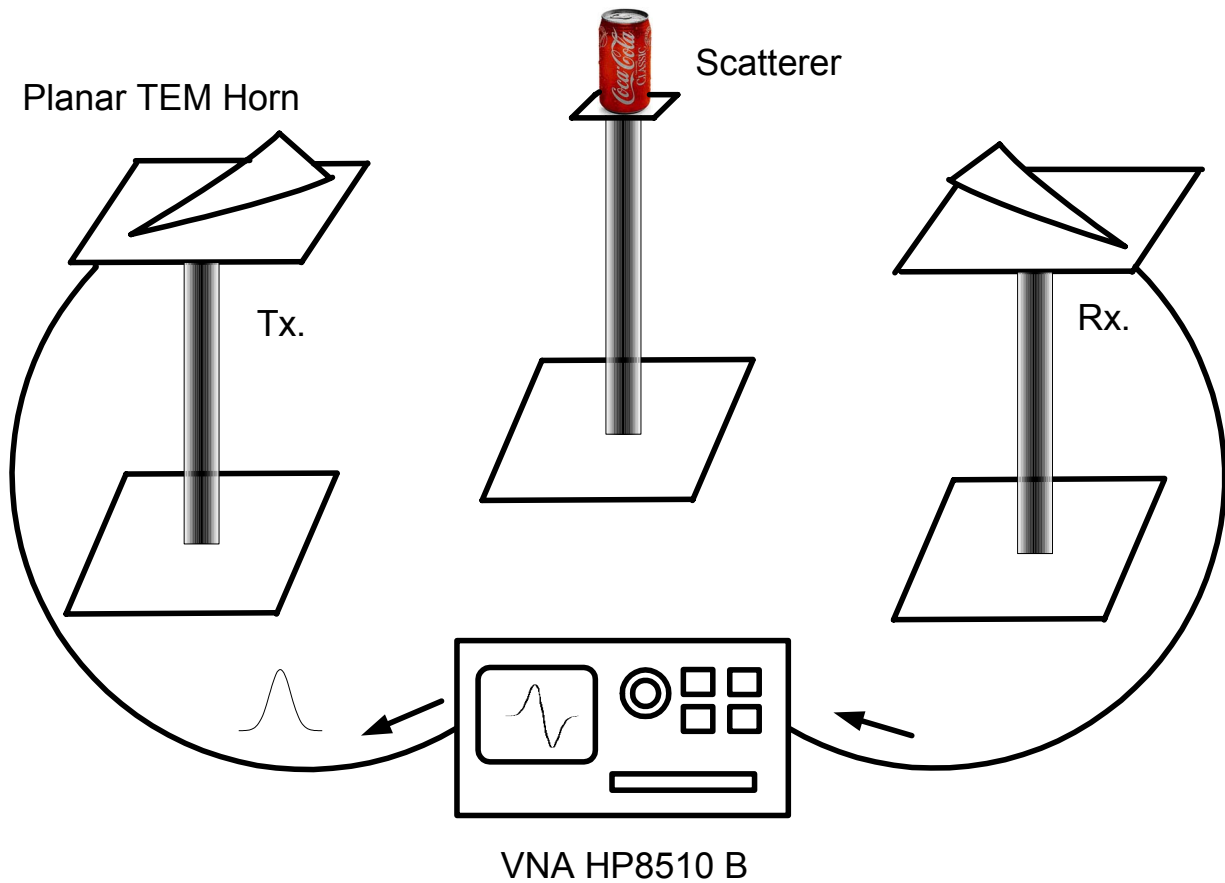


Figure 2.5 A measurement setup in a hallway environment with an empty Coke[®] can as a scatterer illuminated using two planar TEM horn antennas. The measured data were collected using a VNA HP8510 over a frequency range of 400 MHz to 12 GHz.

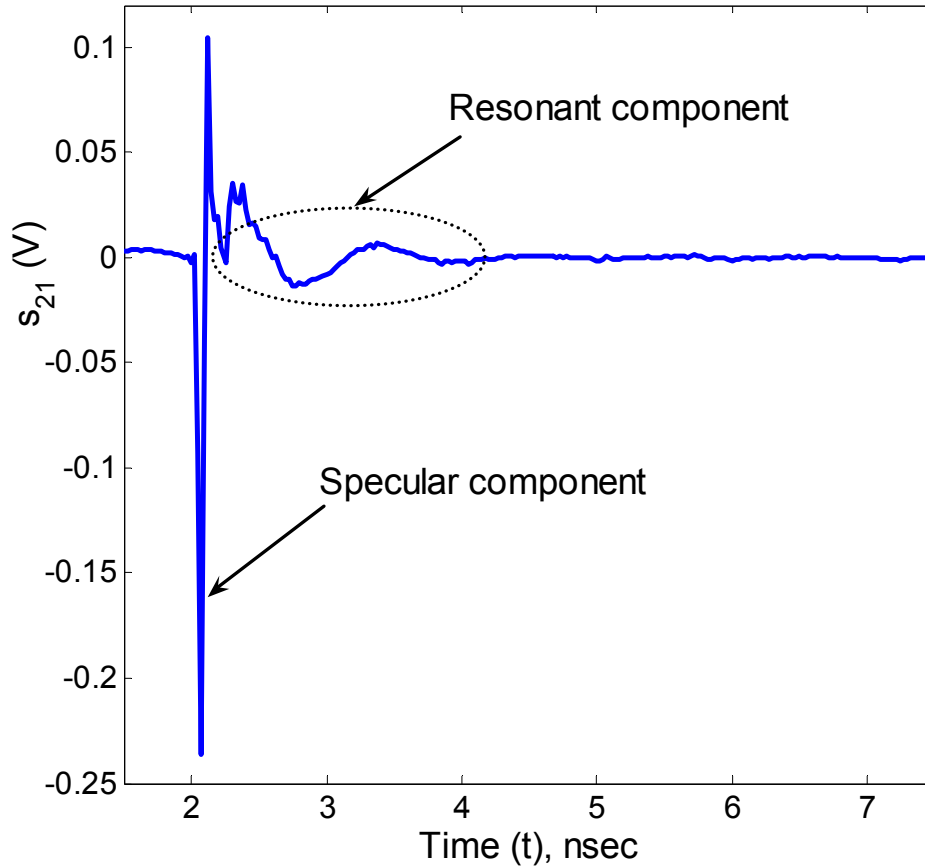


Figure 2.6 Time-domain response of a scatterer (Coke[®] can) due to a 50 pico-second Gaussian pulse excitation. The scatter response is corrected for unwanted reflections from the hallway structures and deconvolved of the antenna response.

The time-domain response of most finite dimensional objects with smooth surfaces (without edges) exhibits damped resonance. The resonant dispersion is visible in the response from smooth finite dimensional objects and it extends the pulse over a time-duration of 2–4 nsec. The resonant dispersive nature of the scatterer response can be modeled as frequency selective filtering that magnifies certain frequency components. However, there is no frequency dependent delay as is observed in frequency (phase) dispersion.

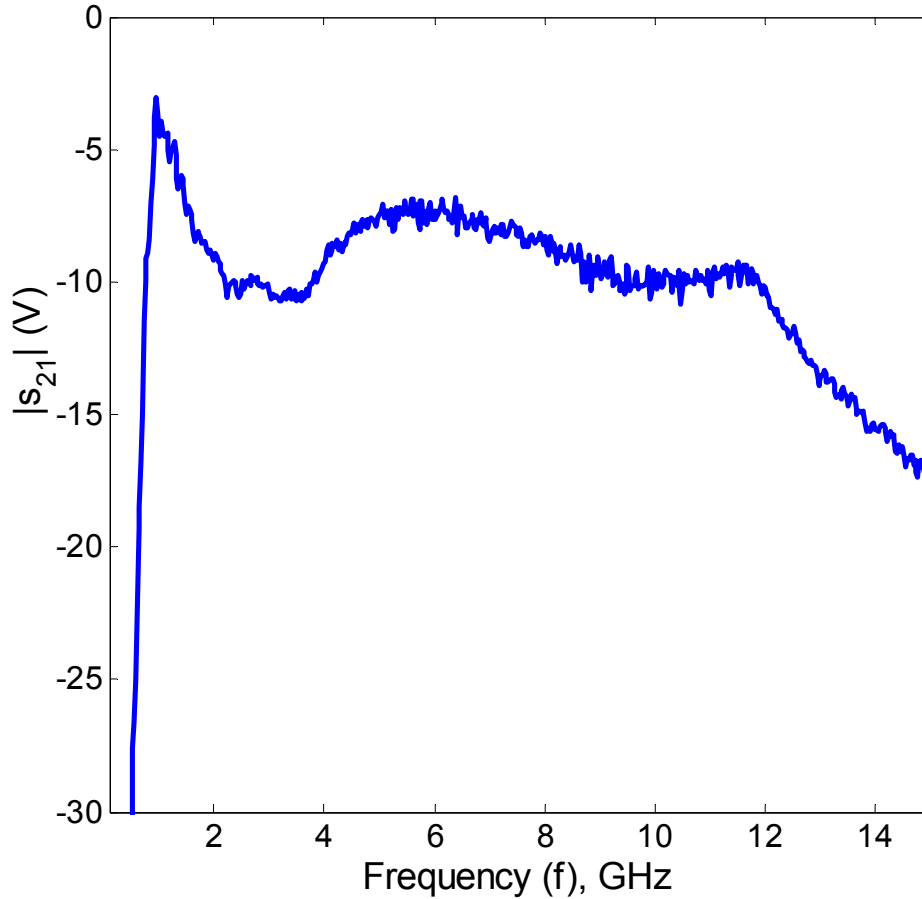


Figure 2.7 Frequency amplitude response of a scatterer (Coke[®] can) due to a 50 pico-second Gaussian pulse excitation.

2.2.3 Multipath Channel Dispersion

Multipath dispersion, defined as the time spreading of the transmitted signal observed at the receiver due to the multipath phenomena [29, 37], is the dominant of the three dispersion phenomena. Multipath dispersion spreads the pulse over a much longer time interval compared to the frequency and resonant dispersion as seen in Fig. 2.9 for a typical indoor environment.

Multipath dispersion can be viewed as the characteristic feature of a wireless channel, which causes the transmitted signal to arrive at the receiver with different delays due to the multipath phenomena. A multipath dispersive channel can be quantified in terms of the RMS delay spread, which is defined as the square root of the second central moment of the power delay profile [9, 38]. For wideband signals with symbol duration smaller than the delay spread,

channel dispersion causes inter-symbol interference (ISI) and, thus, limits the capacity of UWB systems.

The impulse response of a dispersive channel can be observed with measured power delay profiles (PDP) of the dispersive wireless channel using a channel sounding technique [29, 39]. Channel dispersion spreads the signal energy over several tens of nanoseconds, corresponding to several feet of separation between the first and the last significant multipath in the indoor environment. To illustrate multipath dispersion, the power delay profile of an indoor hallway environment is shown in Fig. 2.8 at discrete instants of time. Planar TEM horn antennas were mounted on pedestal at a height of 0.83 m and separated by a distance of 3.1 m (10.2 ft.). The indoor hallway environment is described in detail in Section 5.2.3.

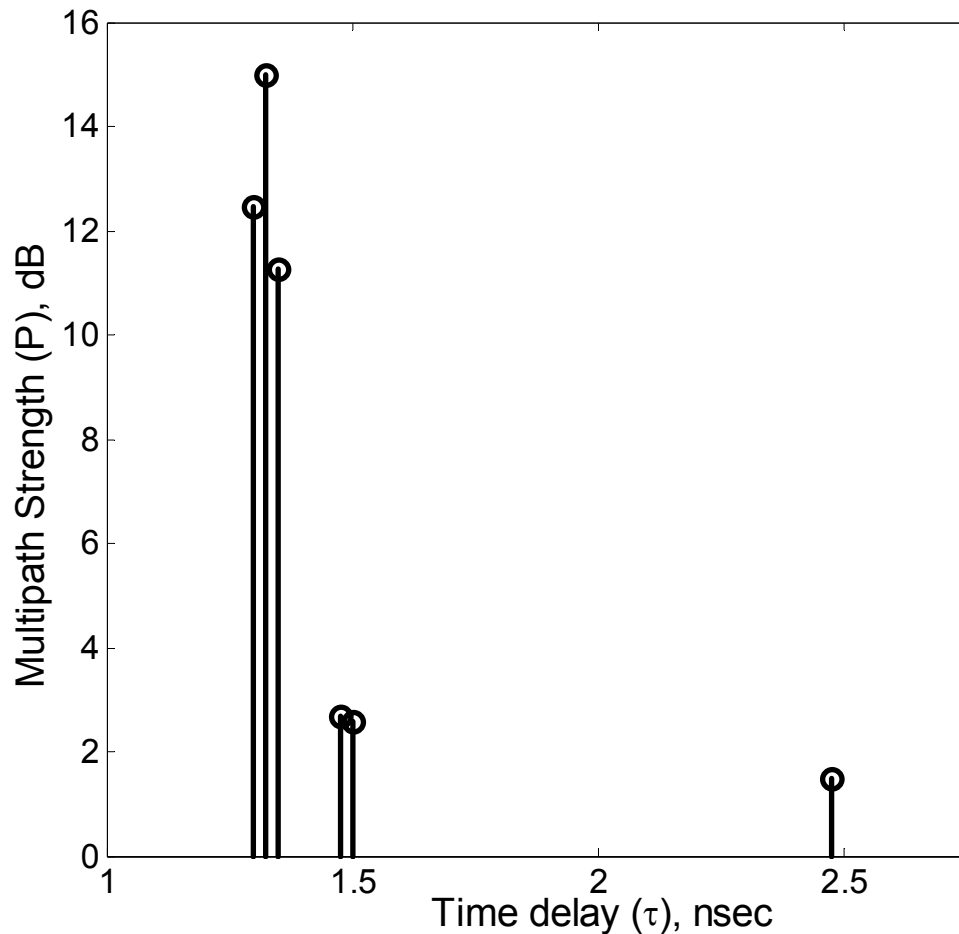


Figure 2.8 Measured Power Delay Profile of an indoor hallway environment using a VNA HP 8510B and two planar TEM horn antennas placed at a distance of 3.1 m (10.2 ft.), using 0.83 m antenna height within a frequency of 100 MHz to 12 GHz.

The RMS delay spread of the channel also depends on the directivity and the heights of the transmitting and receiving antennas. The type of scenario (line-of-sight or obstructed) and the range of operation also affect the delay spread. The multipath dispersive nature of the channel can be modeled as a tapped delay line.

2.3 Comparison of Frequency, Resonant and Multipath Dispersions

Ultra-wideband communication systems employ Gaussian shaped nano-second pulses to achieve high data rates (in excess of 100 Mbps) over a short distance. The pulse width of a Gaussian shaped UWB pulse ranges from few hundreds of Pico-seconds (to cover entire 3.1 GHz – 10.6 GHz band) to 2 nano-seconds (covering the minimum UWB bandwidth of 500 MHz). In the previous section, dispersion phenomena was described and classified into three categories:

- iv. Frequency (phase) dispersion: caused by frequency dependent delay
- v. Resonant dispersion: caused by ringing response from scatterers
- vi. Multipath dispersion: caused by multipath propagation and well characterized by RMS delay spread.

In comparison to sub-nanosecond UWB pulses, resonant and frequency dispersion are significant, as seen in Fig. 2.9. Multipath dispersion dominates for large indoor environments; however, for office or room sized indoor channels, other dispersive mechanisms cannot be ignored. It is interesting to note that the frequency dispersion is on the order of 2–8 nsec, resonant (time) dispersion is on the order of few hundreds of Pico-seconds to few nanoseconds (up to 4 nsec), and multipath dispersion is on the order of 1–30 nsec for a typical office environment [Cra02]. The widely perceived notion that channel (multipath) dispersion limits the data rate is not completely correct. Frequency and resonant dispersion can also be responsible for limiting the data rates in UWB communication systems.

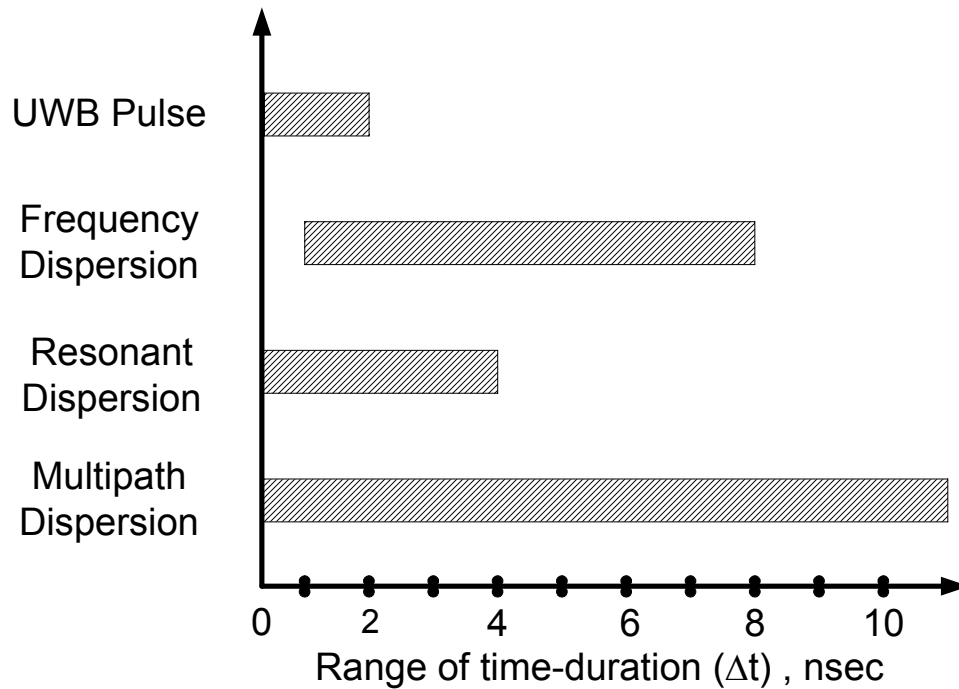


Figure 2.9 Comparison of the time-dispersion in nano-second of the three dominant dispersive phenomena in a typical indoor environment. The time duration of a typical UWB pulse (150 ps to 2 ns, corresponding to the application frequency range of 7 GHz and 500 MHz, respectively) is also shown for reference.

2.4 Dispersive Characteristics of UWB Propagation Channels

The dispersive characteristics of the UWB propagation channel are best understood by employing the scattering center approach. Electrically large (size $\gg \lambda$) physical objects that scatter the incident electromagnetic field can be resolved into various canonical structures that are frequency dependent. The scattering center approach permits modeling of the resonant dispersion because the scatter response has frequency dependency. In fact, by employing the scatter center approach, the channel characterization problem is converted to a scatter object characterization problem [40].

Hurst and Mittra [24] employed time-domain analysis to decompose electrically large objects into several frequency dependent scattering centers. Qiu [37] reported the temporal dispersive characteristics of UWB pulsed systems to distinguish the contributions of different multipath components. Measurements performed in the 2 – 2.67 GHz band [17] validated the scatter center theory; that is, the total received signal can be decomposed into various frequency

dependent scatter centers. Further investigations were reported that describe frequency dependent multipath channel effects [36, 38, 40].

Improved receiver designs will be required in the future to combat the distortions introduced by the dispersive wireless channel. Prior research in dispersive channel characterization has focused only on multipath dispersion. Neither simulation nor measurement results have been reported that characterize resonant dispersion for ultra-wideband wireless communication systems. At present, there is no comprehensive treatment of channel dispersion applied to wireless communication systems.

Accurate characterization of UWB channels is important for proper design of receiver systems. UWB systems will operate with a bandwidth that significantly exceeds conventional channel measurement and modeling techniques. UWB channels can be classified into two main categories: indoor and outdoor. The indoor UWB channel, just like most wideband indoor channels, is short-distance and characterized by high scatterer density. In contrast, the UWB outdoor channel is long-range with medium scatter density. In the following sub-sections, a brief overview of the dispersive characteristics of both the outdoor and the indoor UWB channels is presented.

2.4.1 UWB Outdoor Channel

UWB outdoor channel characterization in a rural area was first reported in 1997 based on measurement results with a bandwidth of 1.3 GHz [41]. The UWB channel characterization in [41], like most conventional channel characterizations, reported propagation loss and forest-vegetation loss. The UWB outdoor channel exhibits multipath dispersion with an increase in RMS delay spread from 31 ns to 49 ns as the transmitter-receiver distance increased from 3 m to 15 m. In order to investigate the amount of degradation introduced by the multipath channel, [41] proposed the concept of an Infinite RAKE receiver, which would, ideally, completely match the reference signal to the received signal waveform.

Schiavone et al. [42] presented simulation results to characterize an UWB outdoor channel for a dense forest environment using a combination of ray tracing and Finite Difference Time Domain (FDTD) methods. This combination of methods permits inclusion of the dielectric constants of the trees, antenna polarizations and separations, while simultaneously reducing the complexity of the simulation task. Data available from measurements and simulations illustrate

that up to a distance of 150 ft., horizontal polarization produced better signal-to-noise values compared to vertical polarization for the frequency range of 3.1 to 10.6 GHz. Large-scale propagation characteristics of UWB signals are investigated and reported in [43]. The lognormal fading is observed with standard deviation of 6 dB when the path loss exponent remains constant at about 2.7 in outdoor environments [43].

The outdoor UWB channel exhibits resolvable multipath components with expected delays ranging from 13 ns to 63 ns for a separation of 15 m. For outdoor UWB systems, with small pulse durations on the order of few nanoseconds, allows high resolution to distinguish closely arriving multipath components. The multipath dispersive nature of the wideband wireless channel is briefly discussed in [44-46]. However, none of these papers offer any insight in to the frequency or temporal dispersive nature of the UWB outdoor channel.

2.4.2 UWB Indoor Channel

Significant work has been reported on characterization of indoor wideband channels, with [47] providing an exceptionally good summary of the significant contributions. Narrowband characterization of an indoor channel [44, 45] shows that for measurements conducted over the frequency range of 850 MHz to 5.8 GHz, the path loss due to propagation through floors and walls is independent of the frequency. However, the frequency selective delay or resonant response of the walls or floors was not investigated.

Wideband characterization of indoor channel has been limited to investigating the multipath dispersive nature of the indoor channel. Time-domain, ultra-wideband multipath channel investigations [12, 47-49], report following important features of an indoor UWB channel:

- The contributions of multipath components due to diffraction are much smaller than that of multipath components due to reflection.
- Energy in horizontally polarized multipath components is comparable to the vertically polarized rays for vertically polarized transmit antenna.
- Significant pulse waveform distortion occurs due to diffraction and scattering off the objects with negligible distortion due to reflection.
- Higher order multiple reflections contribute to the received signal energy with diminishing intensities and can be neglected for orders higher than three.

For an indoor UWB channel, multipath signal components arriving early exhibit little frequency dependence [36], indicating that the multipath components that arrive late are more distorted than those that arrive early. For high-resolution measurements, time-adjacent multipath component amplitudes exhibit strong correlation due to scattering off the same object [22, 46]. For a line-of-sight (LOS) indoor environment, the direct LOS component amplitude is uncorrelated with the amplitude of a multipath component that arrives with a delay of more than 16 nsec [50]. For the obstructed indoor environment, multipath components with delay differences in excess of 25 nsec exhibit uncorrelated amplitude [51]. For a highly dense scattering environment, uncorrelated amplitudes of the multipath components indicate scattering off different objects with uncorrelated time of arrival at the receiver. The amplitude of the multipath components is strongly correlated to the time of arrival because greater path lengths indicate higher attenuation.

Multipath dispersive characteristics of an indoor channel show that the number of resolvable multipath components increases not only with increasing range but also with decreasing receiver threshold (or increasing sensitivity of the receiver). The received signal in the indoor environment appears to consist of groups of multipaths called clusters. Measurements by Saleh and Valenzuela [52] conducted at 1.5 GHz using 10 ns pulses show that the time of arrival of the clusters as well as the rays within the clusters has a Poisson distribution (with different parameters). The general structure (wall, floor, etc...) and dimension of the indoor environment determine the number of resolvable clusters, while the individual scatterers close to the indoor structures are responsible for the individual rays received within clusters. Pulse broadening due to multiple multipaths arriving within a cluster indicates multipath dispersion [52].

The rms-delay spread (τ_{rms}), to be defined in (3.5), is a measure of the multipath dispersion introduced by the channel. It offers a useful means to determine the performance of wireless communication systems in an indoor multipath environment.

2.5 Chapter Summary

Pulse distortion due to various types of dispersion reduces the output SNR of the matched filter receiver and thus, limits the achievable data-rate capacity in UWB communication systems. A

brief overview of wireless propagation mechanisms, namely reflection, diffraction and scattering are presented from the perspective of dispersion. The response of the scatterers combined with the multipath mechanism requires thorough investigation. Based on the observations and applications, different fields of science have different definitions of dispersion. Section 2.2 presents definitions and classification of various dispersive phenomena. Based on these underlying phenomena, dispersion is classified into frequency (wavelength dependent delay) dispersion, resonant (ringing response) dispersion and, multipath dispersion. A comparison of the dispersive phenomena is presented in Section 2.3.

In Section 2.4, an overview of the dispersive characteristics of the outdoor and the indoor UWB channels indicates that multipath mechanism and narrowband path loss issues have been much emphasized. Work on the separation of multipath components within a cluster makes a significant contribution towards investigation of the other dispersive mechanisms. This chapter provides a groundwork for the UWB dispersive channel modeling through understanding how the channel spreads the transmit signal energy in time. Scattering wave propagation mechanisms, especially the response of scattering objects to ultra-wideband pulse excitation, have not been comprehensively investigated. The objective of the following chapter is to build upon existing channel model to include resonant dispersion mechanism in order to compensate for dispersive distortion. Characterization and modeling of scatterer response contributes to reliable design and deployment of UWB receivers.

References

- [1] A. Rajeswaran, V. S. Somayazulu, and J. R. Foerster, "RAKE performance for a pulse based UWB system in a realistic UWB indoor channel," *Proceedings of the IEEE International Conference on Communications, ICC '03* vol. 4, pp. 2879-2883, May 2003.
- [2] H. Zhang, T. Udagawa, T. Arita, and M. Nakagawa, "Home entertainment network: combination of IEEE 1394 and ultra wideband solutions," *Proceedings of the IEEE Conference on Ultra Wideband Systems and Technologies*, pp. 141-145, May 2002.
- [3] G. G. Joshi, W. A. Davis, and W. L. Stutzman, "Ultra-wideband (UWB) channel dispersion: classification and modeling," *Proceedings of the IEEE Antennas and Propagation Society International Symposium*, vol. 1B, pp. 702-705, July 2005.
- [4] A. F. Molisch, "Ultrawideband propagation channels-theory, measurement, and modeling," *IEEE Transactions on Vehicular Technology*, vol. 54 (5), pp. 1528-1545, Sept. 2005.
- [5] F. Sagnard, T. Quiniou, G. El Zein, and G. Thevenin-Foray, "Wide-band characterization of building materials for propagation modeling : analysis of dispersion phenomena," *Proceedings of the 59th IEEE Vehicular Technology Conference, VTC-Spring '04*, vol. 1, pp. 239-243, May 2004.
- [6] J. P. Hermand, "Model-based matched filter processing for delay-Doppler measurement in a multipath dispersive ocean channel," *Proceedings of OCEANS '93*, vol. 1, pp. I306-I311, Oct. 1993.
- [7] J. P. Hermand and W. I. Roderick, "Acoustic model-based matched filter processing for fading time-dispersive ocean channels: theory and experiment," *IEEE Journal of Oceanic Engineering*, vol. 18 (4), pp. 447-465, Oct. 1993.
- [8] R. C. Qiu, "A generalized time domain multipath channel and its application in ultra-wideband (UWB) wireless optimal receiver design-Part II: physics-based system analysis," *IEEE Transactions on Wireless Communications*, vol. 3 (6), pp. 2312-2324, Nov. 2004.
- [9] T. S. Rappaport, *Wireless Communications: Principles and Practice*, 2nd ed. Upper Saddle River, N.J.: Prentice Hall PTR, 2002.
- [10] J. Lavergnat and M. Sylvain, *Radio Wave Propagation: Principles and Techniques*. New York, NY: John Wiley & Sons, Inc., 2000.
- [11] Y. Yao, "A time-domain ray model for predicting indoor wideband radio channel propagation characteristics," *Proceedings of the 6th IEEE International Conference on Universal Personal Communications Record*, vol. 2, pp. 848-852, Oct. 1997.

- [12] R. Yao, W. Zhu, and Z. Chen, "An efficient time-domain ray model for UWB indoor multipath propagation channel," *Proceedings of the 58th IEEE Vehicular Technology Conference, VTC Fall '03*, vol. 2, pp. 1293-1297, Oct. 2003.
- [13] W. L. Stutzman and G. A. Thiele, *Antenna theory and design*, 2nd ed. New York: J. Wiley, 1998.
- [14] H. L. Bertoni, *Radio Propagation for Modern Wireless Systems*. Upper Saddle River, NJ: Prentice Hall Inc., 2000.
- [15] R. G. Kouyoumjian and P. H. Pathak, "High frequency diffraction, focus on ray methods," *Proceedings of IEEE Antennas and Propagation Society International Symposium*, vol. 3, pp. 1638, July 2000.
- [16] J. D. Parsons, *The Mobile Radio Propagation Channel*, 2nd ed. New York, NY: John Wiley & Sons Inc., 2000.
- [17] R. C. Qiu, "A study of the ultra-wideband wireless propagation channel and optimum UWB receiver design," *IEEE Journal on Selected Areas in Communications*, vol. 20 (9), pp. 1628-1637, Dec. 2002.
- [18] S. Y. Seidel and T. S. Rappaport, "A ray tracing technique to predict path loss and delay spread inside buildings," *Proceedings of IEEE Global Telecommunications Conference, GLOBECOM '92*, vol. 2, pp. 649-653, Dec. 1992.
- [19] S. Seidel, K. Schaubach, T. Tran, and T. Rappaport, "Research in site-specific propagation modeling for PCS system design," *Proceedings of 43rd IEEE Vehicular Technology Conference*, pp. 261-264, May 1993.
- [20] S. Y. Seidel and T. S. Rappaport, "Site-specific propagation prediction for wireless in-building personal communication system design," *IEEE Transactions on Vehicular Technology*, vol. 43 (4), pp. 879-891, Nov. 1994.
- [21] C. F. Yang, B. C. Wu, and C. J. Ko, "A ray-tracing method for modeling indoor wave propagation and penetration," *IEEE Transactions on Antennas and Propagation*, vol. 46 (6), pp. 907-919, June 1998.
- [22] H. Hashemi, "The indoor radio propagation channel," *Proceedings of the IEEE*, vol. 81 (7), pp. 943-968, July 1993.
- [23] I. T. Fung and T. Sarkar, "Experimental determination of resonant frequencies by transient scattering from conducting spheres and cylinders," *IEEE Transactions on Antennas and Propagation*, vol. 32 (9), pp. 914-918, Sept. 1984.
- [24] M. Hurst and R. Mittra, "Scattering center analysis via Prony's method," *IEEE Transactions on Antennas and Propagation*, vol. 35 (8), pp. 986-988, Aug. 1987.

- [25] M. Morgan, "Time-domain scattering measurements," *IEEE Antennas and Propagation Society Newsletter*, vol. 26 (4), pp. 4-9, Aug. 1984.
- [26] J. D. Kraus, *Electromagnetics*, 4th ed. New York: McGraw-Hill, 1992.
- [27] R. C. Dixon, *Spread Spectrum Systems with Commercial Applications*. New York, NY: John Wiley & Sons Inc., 1994.
- [28] S. Haykin, *Adaptive Filter Theory*, 4th ed. Upper Saddle River, NJ: Prentice Hall Inc., 2001.
- [29] W. C. Jakes and IEEE Communications Society., *Microwave Mobile Communications*. Piscataway, NJ: IEEE Press, 1993.
- [30] W. C. Y. Lee, *Mobile Communications Engineering: Theory and Applications*, 2nd ed. New York: McGraw-Hill, 1998.
- [31] T. W. Hertel and G. S. Smith, "On the dispersive properties of the conical spiral antenna and its use for pulsed radiation," *IEEE Transactions on Antennas and Propagation*, vol. 51 (7), pp. 1426-1433, July 2003.
- [32] S. Licul and W. A. Davis, "A comparison between a cavity backed spiral and a resonant monopole - an ultra-wideband consideration," *Proceedings of the IEEE International Symposium on Antennas and Propagation*, vol. 4, pp. 486-489, June 2003.
- [33] S. Licul and W. A. Davis, "Unified frequency and time-domain antenna modeling and characterization," *IEEE Transactions on Antennas and Propagation*, vol. 53 (9), pp. 2882-2888, Sept. 2005.
- [34] H. G. Schantz, "Dispersion and UWB antennas," *Proceedings of the International Workshop on Ultra Wideband Systems, Joint UWBST & IWUWBS '04*, pp. 161-165, May 2004.
- [35] FCC, "Authorization of Ultrawideband Technology, First Report and Order," Federal Communications Commission, Washington D.C. FCC 02-48, Feb. 14th 2002.
- [36] R. C. Qiu and I-T. Lu, "Multipath resolving with frequency dependence for wide-band wireless channel modeling," *IEEE Transactions on Vehicular Technology*, vol. 48 (1), pp. 273-285, Jan. 1999.
- [37] R. C. Qiu, "A theoretical study of the ultra-wideband wireless propagation channel based on the scattering centers," *Proceedings of the 48th IEEE Vehicular Technology Conference, VTC '98*, vol. 1, pp. 308-312, May 1998.
- [38] R. C. Qiu and I. T. Lu, "A novel approach with superresolution and path frequency dependence for channel modeling and application in CDMA cellular system," *Proceedings of IEEE Wireless Communication System Symposium*, pp. 27-32, Nov. 1995.

- [39] R. C. Qiu and I. T. Lu, "A novel model of time-dispersion multipath channel for wideband CDMA systems," *Proceedings of 5th IEEE International Conference on Universal Personal Communications*, vol. 1, pp. 350-354, Oct. 1996.
- [40] R. C. Qiu and I. T. Lu, "Wideband wireless multipath channel modeling with path frequency dependence," *Proceedings of IEEE International Conference on Communications, ICC '96*, vol. 1, pp. 277-281, June 1996.
- [41] M. Z. Win, F. Ramirez-Mireles, R. A. Scholtz, and M. A. Barnes, "Ultra-wide bandwidth (UWB) signal propagation for outdoor wireless communications," *Proceedings of 47th IEEE Vehicular Technology Conference*, vol. 1, pp. 251-255, May 1997.
- [42] G. Schiavone, P. Wahid, R. Palaniappan, J. Tracy, E. van Doorn, and B. Lonske, "Outdoor propagation analysis of ultra wide band signals," *Proceedings of IEEE Antennas and Propagation Society International Symposium*, vol. 2, pp. 999-1002, June 2003.
- [43] Q. Zeng, "Suitability of some propagation models to analyse interference from ultra wideband transmitters in outdoor environments," *Proceedings of IEEE Conference on Ultra Wideband Systems and Technologies*, pp. 488-492, Nov. 2003.
- [44] D. M. J. Devasirvatham, C. Banerjee, R. R. Murray, and D. A. Rappaport, "Four-frequency radiowave propagation measurements of the indoor environment in a large metropolitan commercial building," *Proceedings of Global Telecommunications Conference, GLOBECOM '91*, vol. 2, pp. 1282-1286, Dec. 1991.
- [45] D. M. J. Devasirvatham, M. J. Krain, D. A. Rappaport, and C. Banerjee, "Radio propagation measurements at 850 MHz, 1.7 GHz and 4 GHz inside two dissimilar office buildings," *Electronics Letters*, vol. 26 (7), pp. 445-447, July 1990.
- [46] H. Hashemi, "Impulse response modeling of indoor radio propagation channels," *IEEE Journal on Selected Areas in Communications*, vol. 11 (7), pp. 967-978, July 1993.
- [47] D. Cassioli, M. Z. Win, and A. F. Molisch, "The ultra-wide bandwidth indoor channel: from statistical model to simulations," *IEEE Journal on Selected Areas in Communications*, vol. 20 (6), pp. 1247-1257, Aug. 2002.
- [48] R. J. M. Cramer, M. Z. Win, and R. A. Scholtz, "Evaluation of the multipath characteristics of the impulse radio channel," *Proceedings of the 9th IEEE International Symposium on Personal, Indoor and Mobile Radio Communications*, vol. 2, pp. 864-868, Sept. 1998.
- [49] R. A. Scholtz, R. J. M. Cramer, and M. Z. Win, "Evaluation of the propagation characteristics of ultra-wideband communication channels," *Proceedings of IEEE Antennas and Propagation Society International Symposium*, vol. 2, pp. 626-630, June 1998.

- [50] S. Y. Seidel, K. Takamizawa, and T. S. Rappaport, "Application of second-order statistics for an indoor radio channel model," *Proceedings of the 39th IEEE Vehicular Technology Conference*, vol. 2, pp. 888-892, May 1989.
- [51] T. S. Rappaport, S. Y. Seidel, and K. Takamizawa, "Statistical channel impulse response models for factory and open plan building radio communicate system design," *IEEE Transactions on Communications*, vol. 39 (5), pp. 794-807, May 1991.
- [52] A. Saleh and R. Valenzuela, "A Statistical Model for Indoor Multipath Propagation," *IEEE Journal on Selected Areas in Communications*, vol. 5 (2), pp. 128-137, Feb. 1987.

Chapter 3 – Overview of Ultra-Wideband Channel Dispersion Modeling

Ultra-wideband (UWB) systems are defined by the FCC [1] as systems with absolute signal bandwidth exceeding 500 MHz or with a relative -20 dB bandwidth greater than 25%. A large signal bandwidth ranging from 500 MHz to 7.5 GHz promises tremendous advancement in indoor communications [2, 3], ground penetrating radar [4-6], and bio-medical applications [7-9]. Accurate channel characterization and modeling for ultra-wideband applications is important for system design. The previous chapter presented an overview of ultra-wideband channel for indoor and outdoor communications. Moreover, the observed dispersion phenomena were classified into multipath, frequency (phase) and resonant dispersion. This chapter presents an overview of UWB communications channel models with emphasis on dispersion modeling. Although the focus of this dissertation is to model dispersion in UWB communication systems the dispersion models are also applicable for other UWB systems such as buried landmine detection and breast tumor imaging.

Communication channel models are proposed based on a combination of empirical data and a reasonable physics-based explanation. Communication systems design requires accurate information on received signal strength and the waveform. Large-scale channel modeling provides necessary information on the received signal strength, which is used for coverage planning and link-budget analysis [10]. Small-scale channel modeling is necessary to estimate the received signal waveform, which is used for receiver architecture design [11]. Communication channel models are proposed based on following approaches [12]:

- (a) Analytical Physics-based modeling
- (b) Deterministic channel modeling,
- (c) Statistical channel modeling based on empirical data, and
- (d) A hybrid statistical-deterministic channel modeling

Various types of UWB communication channel scenarios such as outdoors vs. indoors, line-of-sight vs. obstructed, and hallway vs. office environment influence the choice of a channel modeling approach. The simplest approach is to use an analytical formula such as Friis' free space transmission equation to determine channel characteristics without any measurements or simulations. This approach is overly simplistic and does not provide accurate modeling of the UWB communications channel. Availability of resources also plays an important role in the choice of approach. An empirical channel modeling approach is the most accurate and site-specific, but is an expensive undertaking in terms of resources and time.

Other channel modeling approaches lie in between the analytical and the empirical channel modeling approaches. A simplified but sufficiently accurate approach is a deterministic ray-tracing method that uses high frequency approximation for wave propagation. Deterministic modeling requires large computing resources and environment information to simulate a complex propagation scenario. A further simplification is achieved by using statistical parameters determined from pilot empirical data that completely describe the channel. A brief comparison of analytical, statistical, and deterministic channel modeling techniques is presented in Table 3-1.

This chapter begins with a brief discussion of large-scale channel models in Section 3.1 for ultra-wideband communications. A brief overview of analytical, statistical, and deterministic path loss channel models is presented. Frequency dependent path loss effects observed for ultra-wideband communications is also briefly discussed. Small-scale UWB channel models are described in Section 3.2 with deterministic ray-tracing methods and statistical impulse response models described in Section 3.2.1 and Section 3.2.2, respectively.

Traditionally, small-scale channel modeling emphasizes multipath dispersion phenomenon because it is observed to be the dominant channel effect for conventional wireless and mobile communications. Section 3.3 describes various hybrid channel-modeling approaches that combine statistical and deterministic modeling to include frequency dependent channel effects. Moreover, it allows frequency-dependent modeling and permits a trade-off between

required accuracy and available computing resources [13, 14]. Limitations of all conventional UWB channel models in modeling frequency (phase) dispersion as well as resonant dispersion is briefly discussed. Finally, Section 3.4 summarizes important ultra-wideband channel modeling issues presented in this chapter.

Table 3-1 Comparison of Channel Modeling Approaches

<i>Characteristics</i>	<i>UWB Channel Modeling Approaches</i>		
	<i>Analytical</i>	<i>Statistical (based on experiments)</i>	<i>Deterministic</i>
(a) Computational Requirement	None	Low	Very High
(b) Environment Specification Requirement	Little	Low	Detailed site information
(c) Physical Basis	Approximate	None/Low	High
(d) Complexity	None	Low/High	Very High
(e) Accuracy	Poor	Good	Very Good

3.1 Large-Scale UWB Channel Models

Large-scale channel modeling provides information on the received signal strength necessary for planning and estimating service coverage. Large-scale channel models describe signal attenuation in terms of the path loss (P_L), path loss exponent (γ), and standard deviation of shadow fading (σ) [15]. A brief overview of analytical, statistical, and deterministic path loss channel models is presented for ultra-wideband (UWB) communications. Frequency dependent path loss effects observed for ultra-wideband communications is also briefly discussed. Because the emphasis of this dissertation is to characterize dispersion, which is a wideband phenomenon, a brief discussion of narrowband path loss channel models is presented.

3.1.1 Analytical UWB Path Loss Channel Modeling

Analytical path loss channel models provide an overly simplified channel characterization that is employed in the initial planning of wireless-service coverage. This approach is widely used for determining an estimate of cell coverage for mobile cellular communications [16]. This approach, however, is usually followed by deterministic or measured channel characterization for more accurate channel analysis. For example, the Friis' free-space transmission equation provides an analytical expression to predict the received signal strength for conventional narrowband communication systems [17]. Recently, the standards task group for UWB Wireless Personal Area Network (WPAN) has proposed a free-space path-loss model based on the Friis' formula [18]. The UWB path loss in free-space, which is actually the propagation spreading loss, is given by [18]

$$L = \left(4\pi d / \lambda\right)^2 \quad (3.1)$$

where the wavelength λ corresponds to the center frequency $f_c = 6.85$ GHz for 3.1 – 10.6 GHz UWB communications band. Note that the presence of wavelength λ in (3.1) is because of the implicit assumption that the antennas have constant gain. The UWB path loss in free-space given by (3.1) can be interpreted erroneously as frequency dependent path loss [19]. The choice of constant gain versus constant aperture antennas at transmit and receive ends of a UWB communication link influences the estimation of the path loss [20].

The UWB path loss in free-space, proposed by the standards task group for UWB Wireless Personal Area Network (WPAN), is an example of analytical UWB path loss channel modeling. Although the free-space propagation spreading loss is widely accepted as path loss, path loss should not be interpreted as frequency-dependent. Comparison of pulse shape measured at various distances in a line-of-sight (LOS) scenario showed negligible variations, indicating that path loss does not introduce frequency dependent pulse distortion [21]. UWB path loss in free-space environment is always frequency independent while the received signal power can be frequency dependent [19-21].

Since the emphasis of this dissertation is to model frequency-dependent dispersive phenomena, interested readers are encouraged to see [19-22] for further information on analytical path loss models in ultra-wideband communication systems.

3.1.2 Statistical UWB Path Loss Channel Modeling

Extensive research efforts have reported path loss characteristics for ultra-wideband (UWB) communication links for outdoor as well as indoor environments [22-28]. Path loss channel statistics, calculated from pilot experiments, are described using a few statistical parameters. This approach, which uses empirically determined path loss propagation parameters, is also called parametric modeling [29]. Large-scale propagation parameters such as the mean path loss (P_L), path loss exponent (γ) and standard deviation of shadow fading (σ) are stochastically modeled based on the measured data. Table 3-2 summarizes statistical path loss models for UWB communications reported in literature.

Table 3-2 Overview of Statistical UWB Path Loss Channel Models reported in literature

<i>Measurement Method</i>	<i>Frequency Range (GHz)</i>	<i>Environment (Scenario)</i>	<i>Distance Range (m)</i>	<i>Parameters Statistically Analyzed</i>	<i>Reference</i>
Sweep Frequency using Network Analyzer	4.375 – 5.625	Residential (LOS & NLOS)	1 – 15	P_L, γ, σ	AT&T Labs-Research, [26, 28]
	2 – 8	Residential & Commercial (LOS & NLOS)	0.8 – 10.5	P_L, γ, σ	AT&T Labs-Research, WINLab, & Harvard Univ. [27, 30]
	1 – 11	Corridor & Office (LOS & NLOS)	1 – 12	P_L	Whyless Consortium [31, 32]
	0.1 – 12	Office & Hallway (LOS & NLOS)	1 – 14	P_L, γ, σ	Virginia Tech [22, 23]
	1 – 13	Indoor (LOS & NLOS)	4 – 14	P_L, γ, σ	Acorde Comm. & Univ. de Cantabria [33]
Time domain Pulse Method	1.25 – 2.75	Office (LOS & NLOS)	9 – 23	P_L, γ, σ	Time Domain Corp. [34]
	BW* = 1.3 GHz	Office (LOS & NLOS)	5 – 18	P_L, γ, σ	AT&T Labs-Research, [35, 36]
	BW = 1.3 GHz	Outdoor Forest	3 – 18.3	P_L	Univ. of Southern California & Time Domain Systems [3]
	0.1 – 12	Office & Hallway (LOS & NLOS)	1 – 14	P_L, γ, σ	Virginia Tech [24]

* BW: Bandwidth
 P_L : mean path loss,
 γ : path loss exponent, and
 σ : standard deviation of shadow fading

The above mentioned statistical path loss models assume that path loss is frequency independent. However, the wide UWB signal bandwidth requires careful examination, which is discussed in the next section on deterministic large-scale channel modeling. Parametric UWB path loss channel modeling is based on extensive empirical data collected using either of the two measurement methods: sweep-frequency method using vector network analyzer or time-domain channel sounding method using pulse generator [22].

3.1.3 Deterministic UWB Path Loss Channel Modeling

Deterministic channel modeling using ray-tracing and site-specific information is a popular approach to calculate service-coverage for indoor communications [37, 38]. It offers accurate modeling of the environment but requires specific information about the environment and significant computing resources to simulate a complex propagation scenario. Most deterministic channel modeling techniques use ray-tracing methods such as Geometrical Optics (GO), which is a high-frequency approximation for wave propagation [39]. Ray-tracing combined with diffraction modeling techniques such as the Geometrical Theory of Diffraction (GTD) and the Uniform Theory of Diffraction (UTD) accurately model diffraction mechanisms [40].

Ray-tracing methods have been widely used to model large-scale path loss characteristics of indoor environment for conventional narrowband and wideband systems [41-44]. However, application of ray-tracing methods to ultra-wideband communications has shown that path loss varies with frequency because of frequency-dependent dispersion mechanisms [40, 45]. This frequency dependency of path loss leads to pulse distortion in the time domain [46, 47]. Table 3-3 summarizes deterministic path loss modeling using time domain ray-tracing methods combined with UTD for UWB communications reported in literature.

The list of popular UWB deterministic channel models in Table 3-2 is not comprehensive. Several studies have reported and analyzed frequency dependent distortion of ultra-wideband pulses, but have not addressed the frequency dependent large-scale channel propagation characteristics [46-49]. It is beyond the scope of this dissertation to provide a detailed discussion of narrowband path loss channel models. The emphasis of this dissertation is to characterize dispersion, which is a wideband phenomenon modeled by small-scale channel parameters. Thus, the remainder of the chapter focuses on the UWB wideband impulse response channel models.

Table 3-3 Ultra-wideband (UWB) Large-Scale Channel Characterization using Deterministic Ray-Tracing Methods reported in literature

<i>Environment (Scenario)</i>	<i>Frequency Range (GHz)</i>	<i>Parameters Investigated</i>	<i>Method</i>	<i>Reference:</i>
Indoor (single room, room-to-room)	3.1 – 10.6	Path Loss, and Pulse Distortion	TD-UTD	Microsoft Research & Tsinghua Univ. [45, 50]
Indoor (office)	1 – 6.5	Path Loss, and BER	TD-UTD	Jiangsu Univ. [51]
Indoor & Outdoor	-	Path Loss, & Distortion	UTD	LCST/IETR & SIRADEL, Rennes [52]
Outdoor Farm (LOS & obstructed)	7.5 GHz (bandwidth)	Path Loss, and Service Coverage	3-D Ray Tracing	Freescale Semiconductors [53]
Indoor / Outdoor	5 GHz (Bandwidth)	Path Loss, and Power Spectral Density	2-Ray UTD	Comm. Research Center, Ottawa [54]

3.2 Small-Scale UWB Channel Modeling

Small-scale channel modeling provides information necessary for efficient receiver design. The small-scale channel characteristics are extracted from several impulse response realizations either collected from measurements or using deterministic ray-tracing methods. Most small-scale UWB channel models extend the conventional channel model frequency limits to characterize the time-delay channel dispersion in terms of mean excess delay, maximum excess delay, RMS delay spread, and the number of paths. This section discusses the conventional wideband channel models applied to ultra-wideband communication systems as well as any novel small-scale UWB models.

The geometrical properties of the transmitter, receiver, and scatterers define the multipath characteristics of a physical environment. Multipath effects lead to time-delay dispersion for wideband signals [16, 55-57]. Site-specific measurements and modeling approaches are becoming popular based on geometrical and deterministic models. Section 3.2.1 provides a brief discussion on the deterministic UWB channel models highlighting the advantages and disadvantages of various ray-tracing methods. Section 3.2.2 gives an overview of impulse

response based stochastic channel modeling along with the original Turin's impulse response channel model [58] and various modifications.

3.2.1 Deterministic UWB Small-Scale Channel Modeling

Deterministic channel modeling approaches accurately model the channel, but require detailed site-specific structural information of the environment such as the geometrical information of the environment, electromagnetic properties of interacting surfaces and discrete scatterers as well as the position of the transmitting and receiving antennas. Moreover, deterministic modeling requires large computing resources to simulate a complex propagation scenario. Some of the commonly used deterministic channel-modeling tools are summarized below.

3.2.1.1 Ray-tracing Modeling Method

Ray-tracing methods employ the high frequency approximation based on Geometrical Optics (GO) principles to model the received signal waveform as a superposition of significant rays arriving at the receiver [59]. This method is based on *Fermat's Principle*, which states that a signal modeled by a ray follows the shortest path connecting from the transmitter to the receiver [55]. Reflection, refraction, and diffraction depend solely on the geometric properties of the local region of the object and the incident electromagnetic field in the immediate neighborhood of the point of interaction.

The two popular approaches to ray tracing are: (a) *Image method*, and (b) *Brute-force* method [39]. The Image method produces images at all reflecting planes and its computational complexity increases exponentially with the increase in the number of the reflecting planes of the environment. In the Brute-force ray tracing method, a finite set of rays is transmitted in selected directions based on the range and the environment. The accuracy of the model depends on the number of rays launched. Propagation mechanisms such as reflection and refraction are accounted for using the Geometrical Optics (GO). The GO approach does not account for the diffraction rays, which is accounted for using the Geometrical Theory of Diffraction (GTD) [60].

3.2.1.2 Geometric Theory of Diffraction (GTD) Modeling Method

It is well known that scatterers with abrupt boundaries such as edges produce diffraction rays, which illuminate the receiver in the shadow region [16]. The GTD method is a field-based

method, which has been improvised to provide reliable solutions to the diffraction problem at low frequencies. The GTD method assumes that the diffracted ray obeys Fermat's principle and follows the shortest optical path. The diffracted field is the product of the incident field and the diffraction coefficient $\overline{\overline{D}}(f)$ determined in the immediate neighborhood of interaction and is given by [55]

$$E_D(f) = E_{inc}(f) A \overline{\overline{D}}(f) e^{-j2\pi f\tau} \quad (3.2)$$

where $\overline{\overline{D}}(f)$ is the dyadic diffraction coefficient, A and τ are the amplitude and delay of the diffraction field. The GTD method can be used to solve a variety of diffraction problems that involves knife-edge, wedge, vertex, and many other canonical structures. However, the GTD method is not accurate in the shadow boundary region and when the observer is too close to the diffracting edge [59]. Under such conditions accurate field estimate can be obtained using the Uniform Theory of Diffraction (UTD), which is discussed in the next sub-section.

3.2.1.3 Uniform Theory of Diffraction (UTD)

The Geometric Theory of Diffraction (GTD) method has a singularity at the transition between the illuminated and the shadowed region, and hence, cannot be applied near the boundary [55]. The Uniform Theory of Diffraction (UTD) overcomes this limitation of GTD by making the diffraction coefficient continuous at the shadow boundary such that the magnitude of the total field at the boundary is half the value in the illuminated region [59].

Combining the diffraction modeling using UTD with the ray tracing permits inclusion of frequency dependent diffraction effects. Indoor as well as outdoor hybrid UWB channel models have been proposed that combine ray – tracing methods with the Uniform Theory of Diffraction (UTD) [52]. This hybrid approach, called time-domain UTD, computes the impulse responses of each ray and combines the contributions at the receiver [12]:

$$h_c(t, \tau) = \sum_{n=1}^N a_n(t) F_n(t, \tau) \otimes \delta(\tau - \tau_n) \quad (3.3)$$

where $F_n(t, \tau)$ denotes the time varying distortion factor due to the frequency dependent interaction of the n^{th} multipath component with the respective scatterer. Assuming the channel to

be time-invariant compared to the data rate, the time dependency can be dropped for the impulse response of the n th multipath given by

$$h_{c,n}(\tau) = a_n F_n(\tau) \quad (3.4)$$

Once the diffraction field is determined in the frequency domain using UTD and the delay τ_n is determined using the ray-tracing methods, the channel impulse response is created by combining the impulse response of each ray with their respective delays:

$$h_C(\tau) = \sum_{n=1}^N h_{c,n}(\tau - \tau_n) \quad (3.5)$$

Yao, et al. [45, 50, 61, 62] developed a hybrid deterministic UWB multipath channel model based upon the time-domain uniform theory of diffraction (TD-UTD) method. The overall channel impulse response can be shown as the summation of different multipath components exhibiting different propagation mechanisms as

$$\begin{aligned} h_C(\tau) &= h_{LOS}(\tau) + h_r(\tau) + h_d(\tau) \\ &= h_{LOS}(\tau) + E_{inc} \left| A_r(s^r) \right| \bar{r}(\tau_r) + E_{inc} \left| A_d(s^d) \right| \bar{d}(\tau_d) \end{aligned} \quad (3.6)$$

where $h_C(\tau)$, $h_{LOS}(\tau)$, $h_r(\tau)$, and $h_d(\tau)$ are the complete, LOS, reflected, and diffracted multipath channel impulse response, respectively; $A_r(s^r)$ and $A_d(s^d)$ indicate the spreading factor of the waveform due to reflection and diffraction respectively. The time-domain dyadic reflection coefficient $\bar{r}(\tau_r)$ is given by (2.2), and the diffraction coefficient $\bar{d}(\tau_r)$ is similarly expressed. The incident field E_{inc} corresponds to the normalized transmitted impulse.

The combined UTD and ray tracing based UWB channel model [52] provides an efficient way to find significant rays from the transmitter to the receiver and to determine the response of scatterers using ray tracing and UTD, respectively. Measurements have revealed that the transmitted UWB signals arrive in clusters [22, 26, 35]. A hybrid model has been proposed that combines the deterministic approach of ray tracing for identifying clusters and Rayleigh distribution for clutter within the clusters [31]. Table 3-4 summarizes small-scale ultra-wideband (UWB) channel characterization efforts reported in the literature using deterministic methods.

Table 3-4 Ultra-wideband (UWB) Small-Scale Channel Characterization using Deterministic Ray-Tracing Methods reported in literature

<i>Environment (Scenario)</i>	<i>Method</i>	<i>Pulse Duration (psec)</i>	<i>Distance Range (m)</i>	<i>Small-Scale Parameters Investigated</i>	<i>Reference:</i>
Indoor (office, LOS & NLOS)	3D ray tracing	100	6 – 10	Num. of multipaths N_M , RMS delay spread τ_{rms} , Power Delay Profile, Angle of Arrival (AoA)	UMIST, Manchester UK [63, 64]
Indoor (office, residential)	Time-domain Uniform Theory of Diffraction (TD-UTD)	110	3 – 10	Num. of multipaths N_M , Multipath strength (P_m), Multipath propagation delay (τ_m)	Microsoft Research Asia & Tsinghua Univ. [45, 50, 61]
Outdoor (farm, LOS)	3D ray tracing	133	5 – 75	Num. of multipaths N_M , Channel Impulse Response, RMS delay spread τ_{rms}	Freescale Semiconductors [65]
Indoor (office)	TD-UTD	500	3.18	Num. of multipaths N_M , Multipath strength (P_m), Multipath propagation delay (τ_m)	Jiangsu Univ. [51]
Outdoor (urban and forest)	Combined Ray-tracing and FDTD	500 ($f_c^* = 1.9$ GHz)	1 – 45.8	Num. of multipaths N_M , Multipath strength (P_m), Multipath propagation delay (τ_m)	Univ. of Central Florida [66, 67]
Indoor & Outdoor	Combined Ray-tracing and UTD	1000	15 – 30	Channel Impulse Response	LCST/IETR & SIRADEL, Rennes [52]

* f_c^* : center frequency

Deterministic small-scale modeling approaches accurately model multiple reflections and diffractions between floors, ceiling, walls and objects in an indoor environment. Statistical channel models cannot address waveform distortion. Unlike statistical modeling, deterministic methods permit treating each propagation mechanism separately. Deterministic methods can determine small-scale modeling parameters such as the number of multipaths N_M , strength (P_m) and propagation delay (τ_m) of each multipath component.

3.2.2 Statistical UWB Small-Scale Channel Modeling

The receiver design is based on the nature of the received signal waveform and this requires wideband channel characterization in terms of channel impulse response. The impulse response completely models the wideband characteristics of the channel. Accurate modeling of a wireless channel requires either expensive site-specific measurements or time-consuming deterministic solution. A cost effective alternative is to use statistical channel models based on empirical data. This section provides an overview of statistical UWB small-scale channel models and highlights their limitations in characterizing various dispersive phenomena observed in UWB communication systems.

Turin [58] first proposed modeling a wireless channel in terms of a filter that can be completely defined by its impulse response. Since then the wideband wireless multipath channel has been modeled as a linear time-varying filter. The impulse response modeling of the channel assumes that the channel has infinite bandwidth, with the communication system bandwidth limiting the overall bandwidth [68, 69]. Impulse response characterization of a wideband wireless channel provides enough information about the channel so that the receiver response can be matched to the channel response. A general form for impulse response of a time-invariant wireless channel is given by

$$h(\tau) = \sum_{n=1}^N a_n e^{j\theta_n} \delta(\tau - \tau_n) \quad (3.7)$$

where: N is the number of clusters (multipath components) that can be resolved

a_n is the amplitude of the n^{th} multipath component. Statistically, it can be represented by Rayleigh, Rician, Nakagami, and other types of distributions.

θ_n is the phase of the n^{th} multipath component. Statistically, the phase of the first multipath component distribution can be modeled as uniform $[0, 2\pi)$, with inter-arrival time modeled by Gaussian increments.

τ_n is the time-varying delay of the n^{th} multipath component. Statistically, the time-of-arrival can be represented by Poisson Model, Modified Δ -K Poisson Model, or Weibull Model.

Turin's impulse response channel model in (3.7) offers information only on the multipath time dispersive nature of the channel. Angle of arrival (AoA) information is not available from

the impulse response because it requires spatial domain sampling using multiple receive antennas. Moreover, information on the channel dispersion due to frequency dispersion and resonant dispersion is not available from Turin's channel model. The following sections present an overview of modified Turin's stochastic impulse response channel models that are extended to model UWB propagation channel.

3.2.2.1 Stochastic Tapped-Delay-Line Channel Model

Wideband transmission of short-time pulses results in a received signal consisting of a series of attenuated, delayed and phase-shifted echoes of the transmitted pulse, as modeled in (3.7). For the UWB application, modified Turin's channel models have been used to characterize UWB propagation channel. The stochastic tapped-delay-line UWB channel model is the first statistical small-scale channel model proposed for UWB communications [36]. It models the power delay profile for indoor environments as a single exponential decay based on the rms delay spread and path gains calculated from measured impulse responses. This model does not include the concept of multipaths arriving in clusters and is consistent with the single-cluster case of the Saleh-Valenzuela (SV) indoor channel model [70]. It models the time-decay constant distribution as lognormal. With the temporal axes quantized into bins of width 2 nsec, the average received power and the received power in each bin follows Exponential and Gamma distributions, respectively [36].

3.2.2.2 Saleh-Valenzuela (SV) UWB Impulse Response Channel Model

Measurements have revealed that the transmitted UWB pulses arrive in clusters at the receiver [22, 26, 35]. Saleh and Valenzuela [70] proposed a modification to the Turin's mathematical model of (3.7) to accommodate the observed phenomenon of clustering of received rays due to reflection or diffraction from different surfaces of the same scattering object. The modified impulse response, also referred to as double exponential decay model, models the clusters and the rays within each cluster as a separate exponential decay model given by [70]

$$h(\tau) = \sum_{n=1}^N \sum_{k=1}^K a_{nk} e^{j\theta_{nk}} \delta(\tau - T_n - \tau_{nk}) \quad (3.8)$$

where: N (K) is the number of clusters (multipath components within clusters) that can be resolved; a_{nk} , θ_{nk} , and $\tau_{n,k}$ are the amplitude, phase and time-delay of the k^{th} multipath component

of the n^{th} cluster. T_n is the arrival time of the n^{th} cluster. For most indoor office environments 2 – 5 clusters have found for ultra-wideband (UWB) applications [71].

The stochastic model proposed by the IEEE 802.15.3a standardization group is the Saleh-Valenzuela (SV) UWB model with four distinct environments [18]: (a) short distance (1-4 m) line-of-sight (LOS), (b) short distance (1-4 m) non line-of-sight (NLOS), (c) NLOS for distances 4-10 m, and (d) heavy multipath environment. Table 3-5 summarizes some of the well-known UWB small-scale statistical channel models reported in literature. For further details, interested readers are referred to [12, 72].

Table 3-5 Statistical Small-Scale Channel Characterization reported in literature for Ultra-wideband (UWB) Communications

<i>Small-Scale Model Parameters</i>	<i>Environment (Scenario)</i>	<i>Statistical Characterization</i>
Power Delay Profile (PDP)	Indoor Office (LOS & NLOS)	Exponential decay with excess delay [36]
	Indoor (LOS & NLOS)	Double exponential decay model [31, 71]
Time Decay Constant (TDC)	Indoor Office (NLOS)	Lognormal distribution [2, 36]
Number of Multipaths	Indoor (LOS & NLOS)	Rayleigh distribution [73]
RMS Delay Spread	Indoor Office & Residential (LOS & NLOS)	Normal distribution [73, 74]
Path Amplitudes	Indoor (LOS & NLOS)	Nakagami distribution [35]
		Rice distribution [75]
		Gamma distribution [35, 36]
		Lognormal distribution [18]
		POCA and NAZU [76]
Path Inter-arrival Times within a cluster	Indoor Office (LOS & NLOS)	Poisson distribution [18]
		Double Poisson distribution [77]

When the fractional bandwidth of the transmitted signal is very large the frequency dependency of the a_n (resonant dispersion) and τ_n (frequency dispersion) become an important

issue. The statistical UWB small-scale channel models listed in Table 3-5 that are based on the impulse response channel model do not address the frequency dependent channel dispersion effects, which is addressed in the next sub-section.

3.3 Frequency-dependent UWB Channel Modeling

The received ultra-wideband (UWB) signal consists of various multipath components, each of which includes the interaction effect of the transmitted UWB signal with the surrounding scatterers [62]. Most small-scale channel models proposed for ultra-wideband (UWB) communications examine only multipath dispersion. There is a significant amount of research reported in literature for modeling the geometrical distribution of scatterers in a typical indoor or outdoor environment [37, 38, 78, 79]. However, there has been little effort to model the responses of the scatterers to incident wideband electromagnetic pulses. Interaction of the transmitted UWB signal and the surrounding objects results in pulse distortion as observed at the receiver.

Before the advent of ultra-wideband communications, most wireless applications were relatively narrowband, within which the scatterer response could be assumed to be frequency independent. Although such postulation of the scatterer response holds for narrowband signals, it is not valid for ultra-wideband signals because the scatterer response varies over the frequency of interest. The conventional channel models validated for wireless applications with bandwidth of 200 kHz – 5 MHz do not consider the impact of distortion visible in UWB systems with bandwidths up to 7 GHz.

Propagation mechanisms such as the refraction, diffraction and scattering from dielectric objects show frequency dependence. The frequency dependence over the entire UWB band and resulting pulse distortion of commonly used building materials has been reported in [21, 80]. Dispersion effects can also be seen in the frequency domain in the channel transfer function, given by the Fourier transform of the channel impulse response

$$\begin{aligned}
 H(\omega) &= F\{h(\tau)\} = \sum_{n=1}^N a_n e^{j\theta_n} e^{-j\omega\tau_n} \\
 &= |H(\omega)| e^{j\Phi(\omega)}
 \end{aligned}
 \tag{3.9}$$

The frequency amplitude response of the channel $|H(\omega)|$ must remain flat over the entire ultra-wideband communications band, i.e. 3.1 – 10.6 GHz. Unequal emphasis of certain frequency components by the channel distorts the UWB pulse in the time domain. Similarly, the phase response $\Phi(\omega)$ must be linear over the signal bandwidth to achieve constant group delay, which is given by

$$\tau_g(\omega) = - \frac{d \Phi(\omega)}{d \omega} \quad (3.10)$$

If the group delay τ_g is not constant over the signal bandwidth, it indicates that different frequency components of the signal undergo different delays, causing what is commonly known as phase or frequency dispersion. A measure of phase dispersion is the rate of change of group delay with respect to the frequency over the bandwidth of interest as given by

$$D_p(\omega) = \left| \frac{d \tau_g(\omega)}{d \omega} \right| = \left| \frac{d^2 \Phi(\omega)}{d \omega^2} \right| \quad (3.11)$$

This section examines various types frequency-dependent UWB channel models and their limitations in modeling all the three types of dispersion phenomena described in the previous chapter. Section 3.3.1 briefly discusses hybrid statistical and deterministic channel models that incorporate frequency dependent response of dielectric objects [31]. Section 3.3.2 presents a frequency dependent scatter center channel model [46, 81, 82] that time-gates the received signal into signals arriving from various scatter centers having different frequency dependency.

3.3.1 Frequency domain Autoregressive (AR) Channel Model

The autoregressive (AR) channel modeling approach models the frequency response of the UWB channel $H(f)$ at a location using an AR process given by [74]

$$H(f_n) - \sum_{i=1}^K a_i H(f_{n-i}) = W(f_n) \quad (3.12)$$

where $H(f_n)$ is the n th sample of the frequency response, $W(f_n)$ is complex white noise, K and a_i are the order and parameters of the model, respectively. This approach includes frequency dependent channel effects requires only a small model-order ($K = 2$) to model the UWB channel with sufficient accuracy [74].

3.3.2 Frequency-dependent Scatter Center Channel Modeling

The frequency dependent scatter center channel model [81] is a significant step toward comprehensive treatment of dispersion for UWB communications. It is based on the concept that the total scattered signal available at the receiver can be modeled as signals arriving from localized frequency dependent mechanisms called as equivalent scattering centers [83]. Each scatter center response can be modeled with an equivalent frequency dependent amplitude and time delay. This approach casts the channel-modeling problem in the form of bistatic radar target modeling [81]. The Uniform Theory of Diffraction (UTD), Method of Moments (MoM) or the Finite Difference Time Domain (FDTD) approach can be used to model scattering from objects [46]. Qiu proposed a scatter center UWB channel model where the frequency domain transfer function is [81]

$$H(\omega) = \sum_{n=1}^N a_n e^{j\theta_n} \left(\frac{\omega}{\omega_c} \right)^{\alpha_n} e^{-j\omega\tau_n} \quad (3.13)$$

where N is the number of resolvable scatter center responses; a_n , θ_n and τ_n denote the amplitude, phase and time-delay of the n^{th} scattered signal; ω_c is a reference (center) frequency; and α_n denotes frequency dependency parameter that is calculated using GTD or UTD. In the time domain, the corresponding impulse response is

$$h(\tau) = \sum_{n=1}^N a_n e^{j\theta_n} (\tau - \tau_n)^{(\alpha_n - 1)} U(\tau - \tau_n) \quad (3.14)$$

where $U(\bullet)$ is Heavyside unit step function, and α_n is the frequency dependent distortion parameter. Since scattered signals arrive with different time delays, time gating permits differentiation of various scatter centers at the receiver to determine α_n for each path. The frequency dependency parameter α_n can be extracted using super-resolution algorithms such as MUSIC, Prony's method or Matrix Pencil Method. If all the scattered signals are frequency independent, i.e. α_n is zero for all arriving paths, then (3.13) and (3.14) reduce to Turin's channel model [58] given by

$$H(\omega) = \sum_{n=1}^N a_n e^{j\theta_n} e^{-j\omega\tau_n} \Leftrightarrow h(\tau) = \sum_{n=1}^N a_n e^{j\theta_n} \delta(\tau - \tau_n) \quad (3.15)$$

The frequency dependency parameter α_n and the time delay τ_n can be combined to form a single parameter called as complex travel-time [46], given by

$$T_n = \tau_n + j \alpha_n \quad (3.16)$$

where the frequency dependency parameter α_n and the time delay τ_n can be extracted accurately using a modified SVD Eigen-Matrix Pencil Method even for multiple rays arriving in a small time interval at the receiver [46].

The scatter center UWB channel model given by (3.13) and (3.14) includes scattering and diffraction effects that are frequency dependent. A significant limitation of this approach is the exponential modeling term that can be applied to model canonical structures like edges and wedges. This approach cannot accurately model resonant responses from complex structures commonly found in indoor environment.

3.4 Chapter Summary

Wideband wireless communication systems are susceptible to distortion from various dispersion phenomena. Multipath dispersion is especially problematic for UWB applications because of the frequency dependent scattering from various objects [21, 84]. Scattering from various objects distorts the transmitted UWB pulse resulting in poor performance of correlation based matched filter receivers [85].

Most UWB channel models have been proposed by simply extending conventional wideband channel models. This chapter presented a brief overview of various UWB channel models with special emphasis on frequency dependent UWB channel dispersion models. Section 3.1 discussed analytical, statistical, and deterministic large-scale path loss channel models for ultra-wideband communications. Frequency dependency of large-scale channel model was also discussed for parameters such as the path loss (P_L), path loss exponent (γ), and standard deviation of shadow fading (σ).

Section 3.2 discussed deterministic ray-tracing methods and statistical impulse response small-scale UWB channel models. This section discussed conventional wideband channel models applied to ultra-wideband communication systems as well as few novel UWB small-scale channel models.

The received ultra-wideband (UWB) signal consists of various multipath components, each of which includes the interaction effect of the transmitted UWB signal with the surrounding scatterers [62]. Interaction of the transmitted UWB signal and the surrounding objects results in pulse distortion as observed at the receiver. Section 3.3 described various hybrid channel-modeling approaches that combine statistical and deterministic modeling to include frequency dependent channel effects. Limitations of all conventional UWB channel models in modeling all identified dispersion mechanisms [85] was briefly discussed. Propagation mechanisms such as the refraction, diffraction and scattering from dielectric objects show frequency dependence.

Review of various channel models in the literature indicates that sufficient research has been conducted to accurately characterize the distribution of scatterers in a given environment. However, little effort has been made to characterize the response of these scatterers to incident wideband electromagnetic pulses. The next chapter attempts to contribute towards understanding and modeling the responses of scatterers using measurements.

References

- [1] FCC, "Authorization of Ultrawideband Technology, First Report and Order," Federal Communications Commission, Washington D.C. FCC 02-48, February 14 2002.
- [2] R. J. M. Cramer, M. Z. Win, and R. A. Scholtz, "Evaluation of the multipath characteristics of the impulse radio channel," *Proceedings of the 9th IEEE International Symposium on Personal, Indoor and Mobile Radio Communications*, vol. 2, pp. 864-868, Sep. 1998.
- [3] M. Z. Win, F. Ramirez-Mireles, R. A. Scholtz, and M. A. Barnes, "Ultra-wide bandwidth (UWB) signal propagation for outdoor wireless communications," *Proceedings of the 47th IEEE Vehicular Technology Conference, VTC '97*, vol. 1, pp. 251-255, May 1997.
- [4] V. Kovalenko, A. Yarovoy, and L. P. Ligthart, "Waveform Based Detection of Anti-Personnel Landmines with an UWB Radar," *Proceedings of the IEEE International Conference on Ultra-Wideband*, pp. 644-649, Sep. 2005.
- [5] Y.-J. Park, S.-B. Cho, K.-H. Kim, and D.-G. Youn, "Development of an ultra wideband ground penetrating radar (UWB GPR) for nondestructive testing of underground objects," *Proceedings of the IEEE Antennas and Propagation Society International Symposium*, vol. 2, pp. 1279-1282, June 2004.
- [6] J. D. Taylor, *Introduction to Ultra-Wideband Radar Systems*. Boca Raton: CRC Press, 1995.

- [7] E. M. Staderini, "UWB radars in medicine," *IEEE Aerospace and Electronic Systems Magazine*, vol. 17 (1), pp. 13-18, Jan. 2002.
- [8] A. E. C. Tan and M. Y. W. Chia, "UWB radar transceiver and measurement for medical imaging," *Proceedings of IEEE International Workshop on Biomedical Circuits and Systems*, pp. S3/1-9-12, Dec. 2004.
- [9] B. Zhou, W. Shao, and G. Wang, "On the resolution of UWB microwave imaging of tumors in random breast tissue," *Proceedings of IEEE Antennas and Propagation Society International Symposium*, vol. 3A, pp. 831-834, July 2005.
- [10] T. S. Rappaport, *Wireless Communications: Principles and Practice*, 2nd ed. Upper Saddle River, N.J.: Prentice Hall PTR, 2002.
- [11] G. L. Stüber, *Principles of mobile communication*, 2nd ed. Boston: Kluwer Academic, 2001.
- [12] A. F. Molisch, "Ultrawideband propagation channels-theory, measurement, and modeling," *IEEE Transactions on Vehicular Technology*, vol. 54 (5), pp. 1528-1545, Sep. 2005.
- [13] K. T. Lam and A. K. Y. Lai, "Hybrid UTD/statistical technique for indoor radio propagation modeling," *Proceedings of Asia-Pacific Microwave Conference, APMC '97*, vol. 3, pp. 1221-1224, Dec. 1997.
- [14] C. P. Michaelides and A. R. Nix, "Accurate high-speed urban field strength predictions using a new hybrid statistical/deterministic modelling technique," *Proceedings of 54th IEEE Vehicular Technology Conference, VTC Fall '01*, vol. 2, pp. 1088-1092, Oct. 2001.
- [15] J. D. Parsons, *The Mobile Radio Propagation Channel*, 2nd ed. New York, NY: John Wiley & Sons Inc., 2000.
- [16] W. C. Y. Lee, *Mobile communications engineering : theory and applications*, 2nd ed. New York: McGraw-Hill, 1998.
- [17] W. C. Y. Lee, *Mobile Cellular Telecommunications : Analog and Digital Systems*, 2nd ed. New York: McGraw-Hill, 1995.
- [18] A. F. Molisch, J. R. Foerster, and M. Pendergrass, "Channel models for ultrawideband personal area networks," *IEEE Wireless Communications Magazine*, vol. 10 (6), pp. 14-21, Dec. 2003.
- [19] S. Licul, "Ultra-Wideband Antenna Characterization and Modeling," in *Bradley Dept. of Electrical and Computer Engineering*. Ph.D Dissertation: Virginia Polytechnic Institute and State University, Blacksburg, 2004.
- [20] B. M. Donlan, "Ultra-wideband Narrowband Interference Cancellation and Channel Modeling for Communications," in *Bradley Department of Electrical and Computer*

- Engineering*. Master's Thesis: Virginia Polytechnic Institute and State University, Blacksburg, 2005.
- [21] A. H. Muqaibel, "Characterization of Ultra Wideband Communication Channels," in *Bradley Dept. of Electrical and Computer Engineering*. Ph.D Dissertation: Virginia Polytechnic Institute and State University, Blacksburg, 2003.
 - [22] R. M. Buehrer, W. A. Davis, A. Safaai-Jazi, and D. Sweeney, "Characterization of the ultra-wideband channel," *Proceedings of IEEE Conference on Ultra Wideband Systems and Technologies*, pp. 26-31, Nov. 2003.
 - [23] A. Bayram, A. M. Attiya, A. Safaai-Jazi, and S. M. Riad, "Frequency-domain measurement of indoor UWB propagation," *Proceedings of IEEE Antennas and Propagation Society International Symposium*, vol. 2, pp. 1303-1306, June 2004.
 - [24] A. H. Muqaibel, A. Safaai-Jazi, A. M. Attiya, A. Bayram, and S. M. Riad, "Measurement and characterization of indoor ultra-wideband propagation," *Proceedings of IEEE Conference on Ultra Wideband Systems and Technologies*, pp. 295-299, Nov. 2003.
 - [25] A. Di Francesco, M. Di Renzo, and R. Minutolo, "Sounding and modelling of the ultra wide-band channel in outdoor scenarios," *Proceedings of 2nd International Workshop on Networking with Ultra Wide Band*, pp. 20-24, July 2005.
 - [26] S. S. Ghassemzadeh, R. Jana, C. W. Rice, W. Turin, and V. Tarokh, "Measurement and modeling of an ultra-wide bandwidth indoor channel," *IEEE Transactions on Communications*, vol. 52, pp. 1786-1796, Oct. 2004.
 - [27] S. S. Ghassemzadeh, L. J. Greenstein, A. Kavcic, T. Sveinsson, and V. Tarokh, "UWB indoor path loss model for residential and commercial buildings," *Proceedings of 58th IEEE Vehicular Technology Conference, VTC Fall '03*, vol. 5, pp. 3115-3119, Oct. 2003.
 - [28] S. S. Ghassemzadeh and V. Tarokh, "UWB path loss characterization in residential environments," *Proceedings of IEEE Radio Frequency Integrated Circuits (RFIC) Symposium*, pp. 501-504, June 2003.
 - [29] H. Hashemi, "The indoor radio propagation channel," *Proceedings of the IEEE*, vol. 81, pp. 943-968, July 1993.
 - [30] S. S. Ghassemzadeh, L. J. Greenstein, T. Sveinsson, A. Kavcic, and V. Tarokh, "UWB Delay Profile Models for Residential and Commercial Indoor Environments," *IEEE Transactions on Vehicular Technology*, vol. 54, pp. 1235-1244, July 2005.
 - [31] J. Kunisch and J. Pamp, "Measurement results and modeling aspects for the UWB radio channel," *Proceedings of IEEE Conference on Ultra Wideband Systems and Technologies*, pp. 19-23, May 2002.

- [32] J. Kunisch and J. Pamp, "An ultra-wideband space-variant multipath indoor radio channel model," *Proceedings of IEEE Conference on Ultra Wideband Systems and Technologies*, pp. 290-294, Nov. 2003.
- [33] A. Alvarez, G. Valera, M. Lobeira, R. Torres, and J. L. Garcia, "New channel impulse response model for UWB indoor system simulations," *Proceedings of the 57th IEEE Vehicular Technology Conference, VTC Spring '03*, vol. 1, pp. 1-5, Apr. 2003.
- [34] S. M. Yano, "Investigating the ultra-wideband indoor wireless channel," *Proceedings of 55th IEEE Vehicular Technology Conference, VTC Spring '02*, vol. 3, pp. 1200-1204, May 2002.
- [35] D. Cassioli, M. Z. Win, and A. F. Molisch, "The ultra-wide bandwidth indoor channel: from statistical model to simulations," *IEEE Journal on Selected Areas in Communications*, vol. 20, pp. 1247-1257, Aug. 2002.
- [36] D. Cassioli, M. Z. Win, and A. F. Molisch, "A statistical model for the UWB indoor channel," *Proceedings of 53rd IEEE Vehicular Technology Conference, VTC Spring '01*, vol. 2, pp. 1159-1163, May 2001.
- [37] S. Seidel, K. Schaubach, T. Tran, and T. Rappaport, "Research in site-specific propagation modeling for PCS system design," *Proceedings of 43rd IEEE Vehicular Technology Conference*, pp. 261-264, May 1993.
- [38] S. Y. Seidel and T. S. Rappaport, "A ray tracing technique to predict path loss and delay spread inside buildings," *Proceedings of IEEE Global Telecommunications Conference, GLOBECOM '92*, vol. 2, pp. 649-653, Dec. 1992.
- [39] T. K. Sarkar, J. Zhong, K. Kyungjung, A. Medouri, and M. Salazar-Palma, "A survey of various propagation models for mobile communication," *IEEE Antennas and Propagation Magazine*, vol. 45, pp. 51-82, June 2003.
- [40] R. J. Luebbers, W. A. Foose, and G. Reyner, "Comparison of GTD propagation model wide-band path loss simulation with measurements," *IEEE Transactions on Antennas and Propagation*, vol. 37, pp. 499-505, Apr. 1989.
- [41] G. German, Q. Spencer, L. Swindlehurst, and R. Valenzuela, "Wireless indoor channel modeling: statistical agreement of ray tracing simulations and channel sounding measurements," *Proceedings of IEEE Conference on Acoustics, Speech, and Signal Processing, ICASSP '01*, vol. 4, pp. 2501-2504, May 2001.
- [42] R. A. Valenzuela, S. Fortune, and J. Ling, "Indoor propagation prediction accuracy and speed versus number of reflections in image-based 3-D ray-tracing," *Proceedings of 48th IEEE Vehicular Technology Conference, VTC '98*, vol. 1, pp. 539-543, May 1998.
- [43] R. Valenzuela, "A ray tracing approach to predicting indoor wireless transmission," *Proceedings of 43rd IEEE Vehicular Technology Conference, VTC '93*, pp. 214-218, May 1993.

- [44] R. A. Valenzuela, "Ray tracing prediction of indoor radio propagation," *Proceedings of 5th IEEE International Symposium on Personal, Indoor and Mobile Radio Communications*, vol. 1, pp. 140-144, Sept. 1994.
- [45] R. Yao, G. Gao, Z. Chen, and W. Zhu, "UWB multipath channel model based on time-domain UTD technique," *Proceedings of IEEE Global Telecommunications Conference, GLOBECOM '03*, vol. 3, pp. 1205-1210, Dec. 2003.
- [46] R. C. Qiu and I.-T. Lu, "Multipath resolving with frequency dependence for wide-band wireless channel modeling," *Vehicular Technology, IEEE Transactions on*, vol. 48, pp. 273-285, Jan. 1999.
- [47] R. C. Qiu and I. T. Lu, "Wideband wireless multipath channel modeling with path frequency dependence," *Proceedings of IEEE International Conference on Communications, ICC 96*, vol. 1, pp. 277-281, June 1996.
- [48] R. C. Qiu, Z. Chenming, and L. Qingchong, "Physics-based pulse distortion for ultra-wideband signals," *IEEE Transactions on Vehicular Technology*, vol. 54, pp. 1546-1555, Sept. 2005.
- [49] R. C. Qiu, "A generalized time domain multipath channel and its application in ultra-wideband (UWB) wireless optimal receiver design-Part II: physics-based system analysis," *IEEE Transactions on Wireless Communications*, vol. 3, pp. 2312-2324, Nov. 2004.
- [50] R. Yao, W. Zhu, and Z. Chen, "An efficient time-domain ray model for UWB indoor multipath propagation channel," *Proceedings of 58th IEEE Vehicular Technology Conference, VTC Fall '03*, vol. 2, pp. 1293-1297, Oct. 2003.
- [51] H. Xu and G. Wang, "Study on UWB channel modeling and UWB-IR system performance in a typical indoor environment," *Proceedings of International Conference on Wireless Communications, Networking and Mobile Computing*, vol. 1, pp. 349-352, Sept. 2005.
- [52] B. Uguen, E. Plouhinec, Y. Lostanlen, and G. Chassay, "A deterministic ultra wideband channel modeling," *Proceedings of IEEE Conference on Ultra Wideband Systems and Technologies*, pp. 1-5, May 2002.
- [53] C. A. Corral, S. Emami, and G. Rasor, "A weighted multiple-frequency method for ultra-wideband outdoor coverage prediction," *Proceedings of the 2nd IEEE Consumer Communications and Networking Conference, CCNC '05*, pp. 461-465, Jan. 2005.
- [54] Q. Zeng, "Suitability of some propagation models to analyse interference from ultra wideband transmitters in outdoor environments," *Proceedings of IEEE Conference on Ultra Wideband Systems and Technologies*, pp. 488-492, Nov. 2003.
- [55] H. L. Bertoni, *Radio Propagation for Modern Wireless Systems*. Upper Saddle River, NJ: Prentice Hall Inc., 2000.

- [56] H. Hashemi, "Impulse response modeling of indoor radio propagation channels," *IEEE Journal on Selected Areas in Communications*, vol. 11, pp. 967-978, Sept. 1993.
- [57] W. C. Jakes and IEEE Communications Society., *Microwave mobile communications*. Piscataway, NJ: IEEE Press, 1993.
- [58] G. Turin, "On the estimation in the presence of noise of the impulse response of a random, linear filter," *IEEE Transactions on Information Theory*, vol. 3, pp. 5-10, Jan. 1957.
- [59] W. L. Stutzman and G. A. Thiele, *Antenna theory and design*, 2nd ed. New York: J. Wiley, 1998.
- [60] R. Luebbers, "Propagation prediction for hilly terrain using GTD wedge diffraction," *IEEE Transactions on Antennas and Propagation*, vol. 32, pp. 951-955, Sept. 1984.
- [61] R. Yao, Z. Chen, and Z. Guo, "An efficient multipath channel model for UWB home networking," *Proceedings of IEEE Radio and Wireless Conference*, pp. 511-516, Sept. 2004.
- [62] Y. Yao, "A time-domain ray model for predicting indoor wideband radio channel propagation characteristics," *Proceedings of the 6th IEEE International Conference on Universal Personal Communications Record*, vol. 2, pp. 848-852, Oct. 1997.
- [63] Z. Yongwei, "Ultra-wide bandwidth channel analysis in time domain using 3-D ray tracing," *Proceedings of High Frequency Postgraduate Student Colloquium*, pp. 189-194, Sept. 2004.
- [64] Z. Yongwei and A. K. Brown, "Ultra-wide bandwidth communication channel analysis using 3-D ray tracing," *Proceedings of the 1st International Symposium on Wireless Communication Systems*, pp. 443-447, Sept. 2004.
- [65] S. Emami, C. A. Corral, and G. Rasor, "Ultra-wideband outdoor channel modeling using ray tracing techniques," *Proceedings of the 2nd IEEE Consumer Communications and Networking Conference, CCNC '05*, pp. 466-470, Jan. 2005.
- [66] G. Schiavone, R. Palaniappan, and P. Wahid, "Study of ultra-wide band signal propagation in urban environments," *Proceedings of IEEE Antennas and Propagation Society International Symposium*, vol. 3, pp. 346-349, June 2002.
- [67] G. Schiavone, P. Wahid, R. Palaniappan, J. Tracy, E. van Doorn, and B. Lonske, "Outdoor propagation analysis of ultra wide band signals," *Proceedings of IEEE Antennas and Propagation Society International Symposium*, vol. 2, pp. 999-1002, June 2003.
- [68] K. Feher, *Wireless Digital Communications: Modulation and Spread Spectrum Applications*. Upper Saddle River, N.J.: Prentice-Hall PTR, 1995.

- [69] A. F. Molisch, *Wideband Wireless Digital Communications*. Upper Saddle River, NJ: Prentice Hall, 2000.
- [70] A. Saleh and R. Valenzuela, "A Statistical Model for Indoor Multipath Propagation," *IEEE Journal on Selected Areas in Communications*, vol. 5, pp. 128-137, Feb. 1987.
- [71] S. Venkatesh, J. Ibrahim, and R. M. Buehrer, "A new 2-cluster model for indoor UWB channel measurements," *Proceedings of IEEE Antennas and Propagation Society International Symposium*, vol. 1, pp. 946-949, June 2004.
- [72] Z. Irahauten, H. Nikookar, and G. J. M. Janssen, "An overview of ultra wide band indoor channel measurements and modeling," *IEEE Microwave and Wireless Components Letters*, vol. 14, pp. 386-388, Aug. 2004.
- [73] C. Prettie, D. Cheung, L. Rusch, and M. Ho, "Spatial correlation of UWB signals in a home environment," *Proceedings of IEEE Conference on Ultra Wideband Systems and Technologies*, pp. 65-69, May 2002.
- [74] S. S. Ghassemzadeh, R. Jana, C. W. Rice, W. Turin, and V. Tarokh, "A statistical path loss model for in-home UWB channels," *Proceedings of IEEE Conference on Ultra Wideband Systems and Technologies*, pp. 59-64, May 2002.
- [75] V. Hovinen, M. Hamalainen, and T. Patsi, "Ultra wideband indoor radio channel models: preliminary results," *Proceedings of IEEE conference on Ultra Wideband Systems and Technologies*, pp. 75-79, May 2002.
- [76] H. Zhang, T. Udagawa, T. Arita, and M. Nakagawa, "A statistical model for the small-scale multipath fading characteristics of ultra wideband indoor channel," *Proceedings of IEEE Conference on Ultra Wideband Systems and Technologies*, pp. 81-85, May 2002.
- [77] C.-C. Chong, Y. Kim, and S.-S. Lee, "A statistical based UWB multipath channel model for the indoor environments WPAN applications," *Proceedings of IEEE Intelligent Vehicles Symposium*, pp. 525-530, June 2005.
- [78] M. R. Arias and B. Mandersson, "An approach of the geometrical-based single bounce elliptical channel model for mobile environments," *Proceedings of the 8th International Conference on Communication Systems, ICCS '02*, vol. 1, pp. 11-16, Nov. 2002.
- [79] S. Y. Seidel and T. S. Rappaport, "Site-specific propagation prediction for wireless in-building personal communication system design," *IEEE Transactions on Vehicular Technology*, vol. 43, pp. 879-891, Nov. 1994.
- [80] A. Muqaibel, A. Safaai-Jazi, A. Bayram, and S. M. Riad, "Ultra wideband material characterization for indoor propagation," *Proceedings of IEEE Antennas and Propagation Society International Symposium*, vol. 4, pp. 623-626, June 2003.

- [81] R. C. Qiu, "A theoretical study of the ultra-wideband wireless propagation channel based on the scattering centers," *Proceedings of the 48th IEEE Vehicular Technology Conference, VTC '98*, vol. 1, pp. 308-312, May 1998.
- [82] R. C. Qiu and I. T. Lu, "A novel approach with superresolution and path frequency dependence for channel modeling and application in CDMA cellular system," *Proceedings of IEEE Wireless Communication System Symposium*, pp. 27-32, Nov. 1995.
- [83] M. McClure, R. C. Qiu, and L. Carin, "On the superresolution identification of observables from swept-frequency scattering data," *IEEE Transactions on Antennas and Propagation*, vol. 45, pp. 631-641, Apr. 1997.
- [84] A. Bayram, A. M. Attiya, A. Safaai-Jazi, and S. M. Riad, "Frequency-domain measurement of indoor UWB propagation," *Proceedings of IEEE Antennas and Propagation Society International Symposium*, vol. 2, pp. 1303-1306, 2004.
- [85] G. G. Joshi, W. A. Davis, and W. L. Stutzman, "Ultra-wideband (UWB) channel dispersion: classification and modeling," *IEEE Antennas and Propagation Society International Symposium*, vol. 1B, pp. 702-705, July 2005.

Chapter 4 – Scatterer Response Modeling and Pole-Dispersion UWB Channel Model

The previous chapter presented various conventional ultra-wideband (UWB) channel models and discussed their limitations in modeling dispersion mechanisms that distort the transmitted UWB pulse. This chapter presents a novel channel model for ultra-wideband communication systems that incorporates known dispersion effects observed in sub nano-second pulse communications. The proposed pole-dispersion UWB channel model is an original contribution that extends the general impulse response based multipath channel model to include resonant dispersion [1]. The proposed pole-dispersion UWB channel model includes resonant scatterer response to accurately model channel-dispersion effects observed in ultra-wideband applications.

The time-domain response of the scatterers is modeled using the Singularity Expansion Method (SEM), which is a numerical method that has found widespread application in radar target identification, ground penetration radar for buried landmine detection and breast tumor detection [2, 3]. A 50 pico-second pulse (corresponding to a bandwidth of 20 GHz) illuminates scatterers and the time-domain responses are analyzed and modeled using the SEM approach. The chapter begins with a brief discussion of the Singularity Expansion Method (SEM) in Section 4.1. The SEM approach models the time-domain response of the induced surface currents of a scatterer due to incident UWB pulse with a weighted sum of complex exponentials (damped sinusoids) [4].

Section 4.2 reviews various numerical techniques used for determining the complex poles and residues including the frequency domain search method [5], Prony's method [6], and the

Matrix Pencil Method (MPM) [7]. Both the Prony's method and the Matrix Pencil Method have been applied with limited success in determining the SEM parameters from the measured time-domain scatterer response [8-10].

Wave scattering propagation mechanisms are difficult to analyze, especially for arbitrarily shaped scattering objects [11]. Section 4.2 briefly describes the measured transient response analysis of scatterers using an example of a conducting hemispherical scatterer over a ground plane. The measured time-domain response of the hemisphere over the ground plane is post-processed to remove unwanted reflections from the environment and is deconvolved with the antenna response. Time gating of the resultant response from deconvolution is used to separate the specular and the late-time resonant dispersion components.

Section 4.3 presents modeling of the responses from scatterers of canonical shapes to an incident ultra-wideband pulse. The canonical scatterers include a sphere, a cylinder, a reflecting surface, and an edge. Experimental results are presented in this section with validation of scatterer responses addressed in the next chapter.

The pole-dispersion UWB channel model is proposed in Section 4.4. Section 4.5 presents a summary of important issues addressed in this chapter.

4.1 Scatter Response Modeling using the Singularity Expansion Method (SEM)

The Singularity Expansion Method (SEM) is a mathematical modeling approach used to model the scatterer response to an incident wideband pulse [4]. The SEM modeling approach was proposed in 1971 to solve electromagnetic interaction problems such as transient response of a finite dimensional scatterer to incident impulse-like signal [2, 4]. The SEM represents the transient response from scatterers as a sum of complex exponentials using all of the following: natural frequencies (poles), natural modes, coupling coefficients, and the early-time entire function due to the presence of the incident waveform [4]. The scatterer response as a function of time and scatterer location and orientation with respect to the incident waveform is given by [4]

$$y(\bar{r}, t) = \sum_{\alpha=1}^{\infty} \eta_{\alpha}(\bar{i}, s_{\alpha}) \nu_{\alpha}(\bar{r}) e^{s_{\alpha} t} u(t) + C(\bar{i}, s_{\alpha}) \quad (4.1)$$

where $s_{\alpha} = \sigma_{\alpha} + j\omega_{\alpha}$ represents the natural frequency (complex pole) that depends on the scatterer geometry and composition; ν_{α} represents the natural modes of the scatterer at the

natural frequencies and depends on the scatterer location and orientation; η_α represents the coupling coefficients that determine the strength of the natural modes at the natural frequencies, and depends on the polarization characteristics of the incident wave. The entire function $C(s_\alpha)$ is present during the early-time response due to the presence of the incident waveform and is insignificant for the late-time scatterer-response analysis.

Exact characterization of a finite dimensional scatterer-response requires an infinite number of natural frequencies [5, 11]. However, due to the band-limited nature of incident waveform, the response is accurately modeled using only the most dominant complex poles, P in number. The above expression is further simplified by combining the natural mode and the coupling coefficients into complex residues corresponding to complex poles. The late time response (response after the incident wave has passed) can now be represented by a weighted sum of complex exponentials and is given by [12]

$$y(t) = \sum_{\alpha=1}^P R_\alpha e^{s_\alpha t} \Leftrightarrow Y(\omega) = \sum_{\alpha=1}^P \frac{R_\alpha(\varphi, \theta)}{s - s_\alpha} \quad (4.2)$$

where R_α is the complex aspect angle dependent residue and P is the number of dominant poles used to characterize the transient response of the scatterer. The poles must be complex conjugate pairs in order for the response $y(t)$ to be real valued. The value of P is determined by the noise sensitivity of the measurement system [13-16]. In the complex frequency plane, this representation is equivalent to a transfer function given by a ratio of two polynomials, whose roots are the system poles and zeros.

If the scatterer response is sampled at a sufficiently high frequency, such that N samples are available at time intervals of T , then [10, 17, 18]

$$\begin{aligned} y_n = y(nT + T_L) &= \sum_{\alpha=1}^P R_\alpha e^{s_\alpha(nT)} \quad n = 0, 1, \dots, N \\ &= \sum_{\alpha=1}^P R_\alpha z_\alpha^n \end{aligned} \quad (4.3)$$

where T_L , the beginning of the late time response, is sufficiently large to allow the pulse excitation to damp out. The natural frequencies, or the poles of the scatterer response, are given by [10, 17, 18]

$$z_\alpha = e^{s_\alpha T} = e^{(\sigma_\alpha + j\omega_\alpha)T} \quad (4.4)$$

The problem now reduces to estimating the number of natural resonances P , the poles $\{s_\alpha\}$, and the corresponding residues $\{R_\alpha\}$ [17]. A variety of methods can be applied to solve this problem; the three most prominent approaches are: (a) Frequency domain search technique [5, 19, 20], (b) Time domain Prony's method [6, 10, 13, 21], and (c) Matrix pencil method [7, 9, 17, 22]. The frequency domain search is the earliest known method for extracting the natural resonances or singularities from the scatterer response. This method was based on an iterative search procedure in the complex frequency plane and was used successfully to model the response of thin wires to an incident wideband pulse [5]. Prony's method has been applied successfully to scatterer response recorded at a high signal-to-noise ratio (SNR) [6]. In comparison, the matrix pencil method is more robust and has been demonstrated to be effective even in the presence of noise [9]. These techniques are briefly discussed in more detail in the following subsections.

4.1.1 Frequency Domain Search Method

The frequency domain search was the earliest method for determining the natural resonances or singularities of a scatterer through an iterative search procedure. The frequency domain search method involves solving the following integral equation [5, 23]

$$\int_V \bar{\Gamma}(\bar{r}, \bar{r}'; s) \bullet \bar{J}(\bar{r}'; s) dv' = \bar{F}(\bar{r}; s) \quad (4.5)$$

where $\bar{\Gamma}$ is the kernel of the integral equation, \bar{J} is the scatterer response current density, and \bar{F} is the forcing function. The natural frequency s_α and the natural mode v_α satisfy the following equation

$$\int_V \bar{\Gamma}(\bar{r}, \bar{r}'; s_\alpha) \bullet v(\bar{r}') dv' = 0 \quad (4.6)$$

Using the method of moments approach, the above equation can be converted to the following matrix equation [23]

$$\bar{\Gamma}_{n,m}(s_\alpha) \bullet (v_n)_\alpha = 0_n \quad (4.7)$$

The kernel matrix $\bar{\Gamma}$ that satisfies the above equation has to be singular at natural frequencies s_α . Thus, the natural frequencies can be determined from the following expression [23]

$$\det(\bar{\Gamma}_{n,m}(s_\alpha)) = 0_n \quad (4.8)$$

The frequency domain search method essentially determines the natural frequencies of an object or scatterer by searching for complex frequencies s_α that force the determinant of the $\bar{\Gamma}$ matrix to zero. Based on the knowledge of the natural frequencies, natural modes can be determined using (4.7). This approach though accurate is not computationally efficient and hence slow. Before the introduction of the Prony's method and the Matrix pencil method, this approach was successfully used to determine the singularities of various thin wire and spherical scatterers [5].

4.1.2 Time Domain Prony's Method

R. Prony [24] solved a thermal expansion problem of fluids by representing a series of equally spaced time sampled data using a weighted sum of exponentials. It involves solving two $N \times N$ systems of linear equations and an N^{th} order polynomial, where N is the number of singularities required to accurately represent the equally spaced time sampled data [10]. After the singularity expansion method (SEM) was introduced, Prony's algorithm was quickly applied to the problem of the singularities (complex poles) of a 1-m dipole antenna using a Gaussian pulse excitation [6]. Prony's method requires $N = 2P$ number of equally spaced time sampled electric field response to determine P complex poles and P corresponding residues, where the number of poles is either known *a priori* or is overestimated.

The first step in determining the complex poles using the Prony's method is to solve P equations derived from (4.3) for coefficient matrix $[\mathbf{B}]$ shown in matrix notation as [6]

$$[\mathbf{B}]_{Px1} = [\beta_{P-1} \quad \beta_{P-2} \quad \cdots \quad \beta_0]_{Px1}^T = [Y_{P-1}]_{PxP}^+ [Y_P]_{Px1} \quad (4.9)$$

where $[\cdot]^+$ indicates Moore-Penrose pseudo inverse [25] and the data matrices $[Y_{P-1}]$ and $[Y_P]$ from uniformly sampled time-domain response are given by

$$\begin{aligned}
[Y_{P-1}] &= \begin{bmatrix} y_{P-1} & y_{P-2} & \cdots & y_0 \\ y_P & y_{P-1} & \cdots & y_1 \\ \vdots & \vdots & \ddots & \vdots \\ y_{N-2} & y_{N-3} & \cdots & y_{P-1} \end{bmatrix}_{PxP, N=2P} \\
[Y_P] &= [-y_P \quad -y_{P+1} \quad \cdots \quad -y_{N-1}]_{Px1, N=2P}^T
\end{aligned}$$

Once the coefficients $[\beta_i], i = 1, 2, \dots, P$ are known, the following P^{th} order equation can be solved to determine $[z_i], i = 1, 2, \dots, P$

$$\sum_{i=1}^P \beta_i z^i = 0 \quad (4.10)$$

The complex poles are then extracted from $[z_i], i = 1, 2, \dots, P$ using the following expression

$$s_i = \frac{\ln(z_i)}{T} \quad i = 1, 2, \dots, P \quad (4.11)$$

The uniformly sampled time-domain response of finite-dimensional scatterers as a weighted sum of complex exponentials given by (4.3) can be shown in a matrix formulation as

$$[Y]_{Px1} = [R]_{Px1} [Z]_{PxP} \quad (4.12)$$

where $[Y]$ is the time-domain response vector, $[R]$ is a vector of residues corresponding to the complex poles arranged in the matrix form $[Z]$, given by

$$[Z] = \begin{bmatrix} 1 & 1 & \cdots & 1 \\ z_1 & z_2 & \cdots & z_P \\ \vdots & \vdots & \ddots & \vdots \\ z_1^{(P-1)} & z_2^{(P-1)} & \cdots & z_P^{(P-1)} \end{bmatrix}_{PxP} \quad (4.13)$$

Finally, the corresponding residues are determined by solving P equations for $[R]$ shown by the following matrix notations [6]

$$[R]_{Px1} = [Z]_{PxP}^+ [Y]_{Px1} \quad (4.14)$$

where

$$[R] = [R_1 \quad R_2 \quad \cdots \quad R_{P-1}]_{Px1}^T$$

$$[Y] = [y_1 \quad y_2 \quad \cdots \quad y_{P-1}]_{P \times 1}^T$$

A significant limitation to Prony's method is that it merely provides a least-square fit to a set of finite data and does not guarantee that the determined poles represent the scatterer or object under examination [10]. Moreover, there are two possible limitations affecting the reliable estimation of the poles and residues:

- (a) Incorrect estimation of the number of poles P , and
- (b) Estimation error due to noisy data.

The SEM approach requires an *a priori* knowledge or an estimate of the number of dominant poles. Although overestimating the number of poles P leads to spurious poles with small magnitudes because of the ill-conditioned problem, the effect is not severe. A poor estimate of this can lead to inaccurate results. In comparison, underestimating the number of poles P introduces large errors. Hence, the first problem is easily avoided by overestimating the number of poles and then employing the Singular Value Decomposition (SVD) to determine the dominant poles.

The SEM approach is a weighted sum of complex sinusoids. But noise cannot be modeled as a sum of sinusoidal terms, so the SEM approach cannot model noise accurately, introducing error in estimating the location of singularities. Position estimation of poles in the complex plane and the corresponding residue estimation of weak poles with small residues are severely affected by noise.

4.1.3 Matrix Pencil Method

The matrix pencil method is the most useful of all methods in the parameterization of scatterer transient response. The advantage of this method lies in its low sensitivity to noise and simplicity of computation. In 1962, Gantmakher [26] defined a linear combination of two functions as the *pencil of function* with a parameter λ given by

$$f(x, \lambda) = g(x) + \lambda h(x) \quad (4.15)$$

The *matrix pencil* derives its name from the matrix formulation of the pencil of function expression given by (4.15). Formulating the measured time-domain scatterer response in terms of a matrix pencil allows solving for the complex poles from a generalized eigenvalue problem approach [7]. The matrix pencil method first defines the matrix pencil as a linear combination of

two square matrices ($\mathbf{Y}_1 - z\mathbf{Y}_2$) [22], where z is a scalar and the two square matrices from equally spaced time samples $\{y_n\}$ of the scatterer response are given by

$$[\mathbf{Y}_1] = \begin{bmatrix} y_1 & y_2 & \cdots & y_L \\ y_2 & y_3 & \cdots & y_{L+1} \\ \vdots & \vdots & \ddots & \vdots \\ y_{N-L} & y_{N-L+1} & \cdots & y_{N-1} \end{bmatrix}_{(N-L) \times L} \quad (4.16)$$

$$[\mathbf{Y}_2] = \begin{bmatrix} y_0 & y_1 & \cdots & y_{L-1} \\ y_1 & y_2 & \cdots & y_L \\ \vdots & \vdots & \ddots & \vdots \\ y_{N-L-1} & y_{N-L} & \cdots & y_{N-2} \end{bmatrix}_{(N-L) \times L} \quad (4.17)$$

The parameter L denotes the length of the data window and is called the matrix pencil parameter. The matrix pencil ($\mathbf{Y}_1 - \lambda\mathbf{Y}_2$) has a rank P , if $P \leq L \leq N - P$. The eigenvalues of the matrix pencil $\{\lambda = z_\alpha, \text{ where } \alpha = 1, 2, \dots, P\}$, reduce the rank of the matrix pencil to $P - 1$. If $\{v_\alpha\}$ are the corresponding eigenvectors then

$$[\mathbf{Y}_1]v_\alpha = z_\alpha[\mathbf{Y}_2]v_\alpha \quad \Rightarrow \quad \left\{ [\mathbf{Y}_2]^+[\mathbf{Y}_1] - z_\alpha[\mathbf{I}_P] \right\} v_\alpha = [\mathbf{0}] \quad (4.18)$$

where the poles, or natural frequencies, $\{z_\alpha\}$ can be easily obtained by determining the eigenvalues of the matrix product $\mathbf{Y}_2^+ \mathbf{Y}_1$, and $[\cdot]^+$ indicates the matrix pseudo inverse [25]. The corresponding residues $\{R_\alpha\}$ are obtained using the least squares approach, once the poles are known, using the following relationship

$$\begin{bmatrix} R_1 \\ R_2 \\ \vdots \\ R_P \end{bmatrix} = \begin{bmatrix} 1 & 1 & \cdots & 1 \\ z_1 & z_2 & \cdots & z_P \\ \vdots & \vdots & \ddots & \vdots \\ z_1^{(N-1)} & z_2^{(N-1)} & \cdots & z_P^{(N-1)} \end{bmatrix}^{-1} \begin{bmatrix} y_0 \\ y_1 \\ \vdots \\ y_{N-1} \end{bmatrix} \quad (4.19)$$

A modified matrix pencil method known as the Total Least-Squares Matrix Pencil method (TLSMP) [22] can be used to estimate the natural resonances from the transient data recorded for multiple aspect angles (directions). This method provides a single estimate of all the poles using all the transient data recorded for multiple aspect angles because the poles are aspect

independent. However, the residues are different for each pole in each recorded aspect direction, indicating that the contribution of the poles to scatterer response is different for different look angles. Moreover, the method does not perform an average to determine the poles, which is known to degrade the pole estimation. When the signal-to-noise ratio (SNR) of measured time-sampled data for the different look direction are different, averaging introduced noise in pole estimation due to low SNR data.

The next section describes the analysis of the measured time-domain response of scatterers using an example of a conducting hemisphere over a ground plane. The post processing to remove unwanted reflections, antenna effects and pole-residue extraction using the Matrix Pencil Method (MPM) are described.

4.2 Time-domain Scatter Response Measurement and Analysis

Scattering from arbitrarily shaped objects can be described in terms of scattering from canonically shaped scattering centers [13, 27]. The signal scattered from an object with P scattering centers can be decomposed into P signals, each of which can be represented using poles and residues. This section briefly describes the measured transient response analysis of scatterers using an example of a conducting hemispherical scatterer over a ground plane.

Section 4.2.1 briefly describes the measurement setup that is used to record time-domain response of canonically shaped scatterers. The measurement setup description is provided in Section 5.2 in association with validating the scatterer response using the singularity expansion method (SEM). The measurements were conducted using planar TEM Horn antenna as an illuminator and another one as a receiving antenna with the canonical objects mounted over a 1.2 m x 1.2 m (4 ft. x 4 ft.) ground plane. The scatterer response data were recorded using an HP8510 vector network analyzer (VNA) in the Virginia Tech Antenna Group (VTAG) facility.

Section 4.2.2 describes the analysis of the measured time-domain response of a 15.2 cm (6 inch) diameter hemisphere over a ground plane. The measured time-domain response of the hemisphere over the ground plane is post-processed to remove unwanted reflections from the environment and is deconvolved with the antenna response. Time gating of the resultant response from deconvolution is used to separate the specular and the late-time resonant dispersion components. The data collected through transient measurements were post-processed to obtain

poles and residues using the Least Squares Prony's algorithm and the Matrix Pencil Method discussed in Section 4.1.2 and Section 4.1.3, respectively.

4.2.1 Measurement Setup

This section briefly describes scatter response measurement using an example of a conducting hemispherical of diameter 15.2 cm (6 inch) on a ground plane. The next section describes the post processing of the measured time-domain response of the hemisphere over the ground plane to remove unwanted reflections from the environment and the antenna effects.

The scatterer-response measurement setup uses two planar horn antennas mounted on diagonal corners of a 1.2 m x 1.2 m square ground surrounded by absorbers as shown in Fig. 1. Data were collected using a VNA-HP8510, deconvolved with the line-of-sight (LOS) antenna response, and post-processed using the Least-Squares (LS) Prony's algorithm. The edge of the ground plane was covered with absorber to reduce diffraction from the edge and subsequent scattering from the surrounding environment.

The time spacing between successive samples was chosen to satisfy the Nyquist criterion. That is, the time spacing or resolution is 25 psec, corresponding to a 40 GHz sampling frequency, which is twice the highest frequency of the incident pulse of width 50 psec (corresponds to 20 GHz signal bandwidth). Multiple measurements were recorded and averaged to improve the signal-to-noise ratio (*SNR*). An averaging operation on 1024 repetitive measurements improves the *SNR* by approximately 30 dB, which is sufficient for accurate estimation of the poles and residues [6].

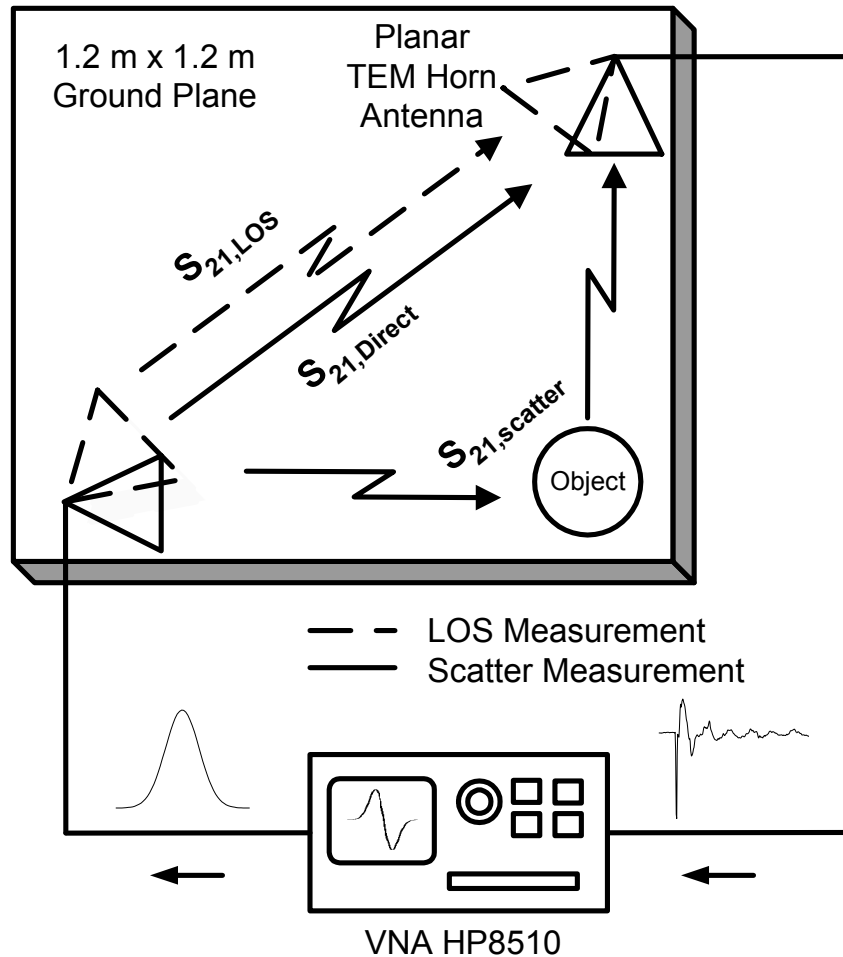


Figure 4.1 Time-domain scatterer response measurement setup using planar TEM horn antennas on a 1.2 m x 1.2 m square ground surrounded by absorber using a VNA-HP8510.

4.2.2 Measured Scatterer Response Data Analysis

This section describes the analysis of the measured time-domain response of a 6-inch diameter hemisphere over a ground plane. The measured time-domain response is post-processed to remove unwanted reflections from the environment and is deconvolved with the antenna response. The antenna time-domain response is deconvolved using the measured $s_{21,LOS}$ scatter parameter that corresponds to an unobstructed line-of-sight (LOS) scenario.

The antennas are aimed toward the corner with the test object as shown in Fig. 4.1. The test objects are placed in the corner at a distance of 0.71 m (28 inch) from the antenna feed point. A final measurement of parameter s_{21} was made with antennas pointed toward the corner without

the test object, which was then used to subtract the effect of the surrounding environment. This procedure in time domain is formulated as follows:

$$S_{21, scattered} = S_{21, data (with scatterer)} \text{ deconvolved by } S_{21, LOS} \quad (4.20)$$

$$S_{21, direct} = S_{21, data (no scatterer)} \text{ deconvolved by } S_{21, LOS} \quad (4.21)$$

$$S_{21, canonical} = S_{21, scattered} - S_{21, direct} \quad (4.22)$$

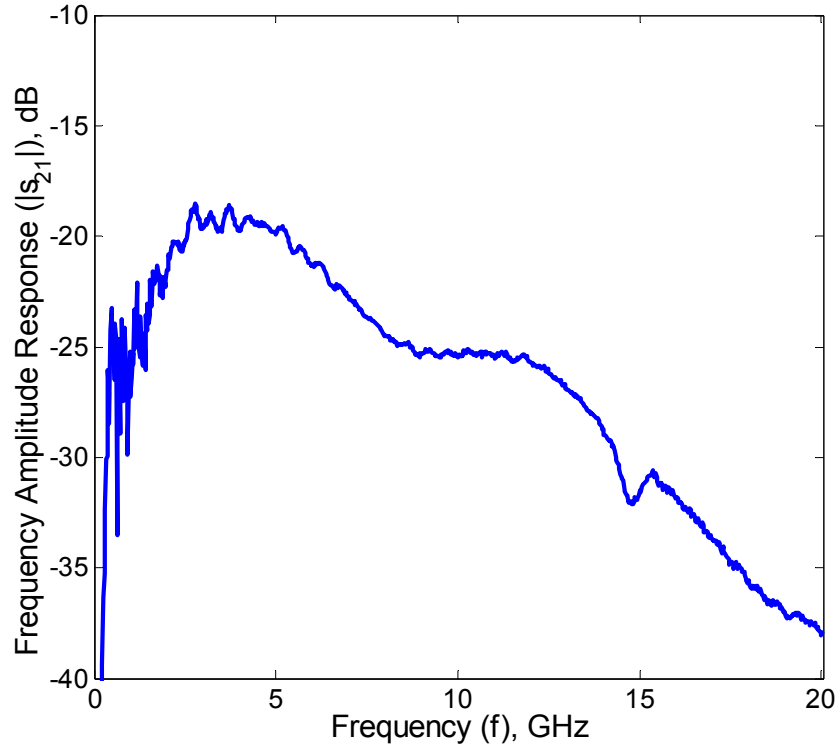
where the s quantities are the associated scattering parameters (s_{21}) corresponding to different experiment setups. The first step is to record the line-of-sight (LOS) response between the two planar TEM horn antennas, which is used to deconvolve the antenna response. The deconvolution operation of time domain s_{21} parameters is performed using division operation in the frequency domain as

$$S_{21, scattered}(\omega) = S_{21, data (with scatterer)}(\omega) / S_{21, LOS}(\omega) \quad (4.23)$$

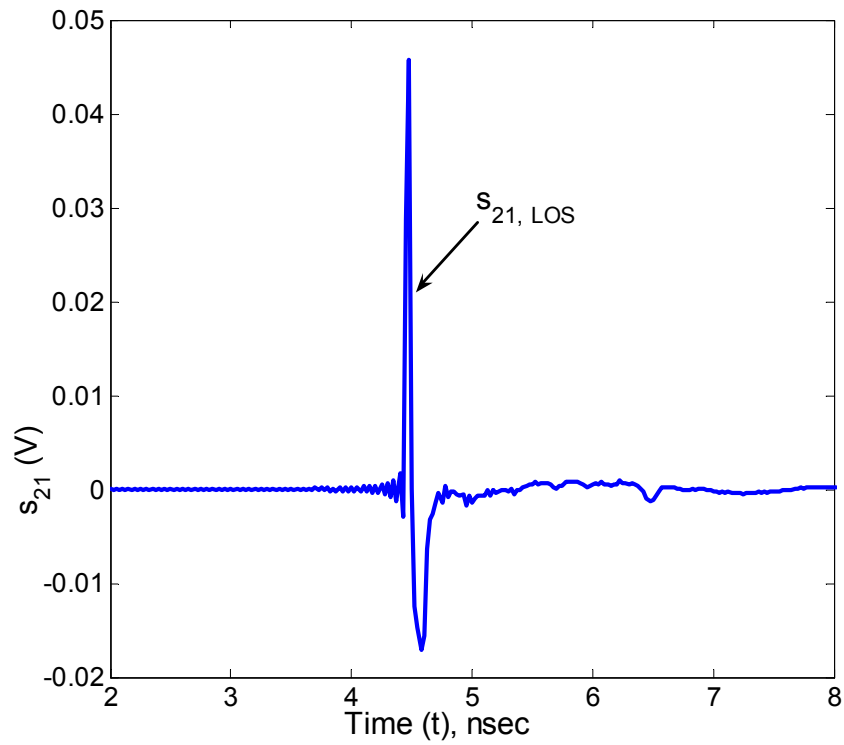
$$S_{21, direct}(\omega) = S_{21, data (no scatterer)}(\omega) / S_{21, LOS}(\omega) \quad (4.24)$$

The frequency amplitude response and the time domain impulse response for the LOS link between the two planar horn antennas are shown in Fig. 4.2. The approximate distance between the feed points of the two antennas along the scattering path is 1.35 m (4.5 ft.), corresponding to a delay of 4.5 nsec when the HP 8510 is triggered. The $s_{21, LOS}$ data is the s_{21} scatter parameter recorded for the line-of-sight (LOS) measurement scenario.

The next step is to orient the two antennas toward the scatterer located at a corner on the ground plane and to record the s_{21} scattering parameter. The measured s_{21} parameter after deconvolution with $s_{21, LOS}$, called $s_{21, scattered}$, is shown in Fig. 4.3. The direct pulse observed in $s_{21, scattered}$ response is observed at the same delay as the $s_{21, LOS}$. The scattered pulse is observed after a delay of 1 nsec.



(a) Frequency-domain amplitude response



(b) Time domain response

Figure 4.2 Frequency amplitude and time-domain response of the line-of-sight (LOS) link between two planar horn antennas ($s_{21,LOS}$).

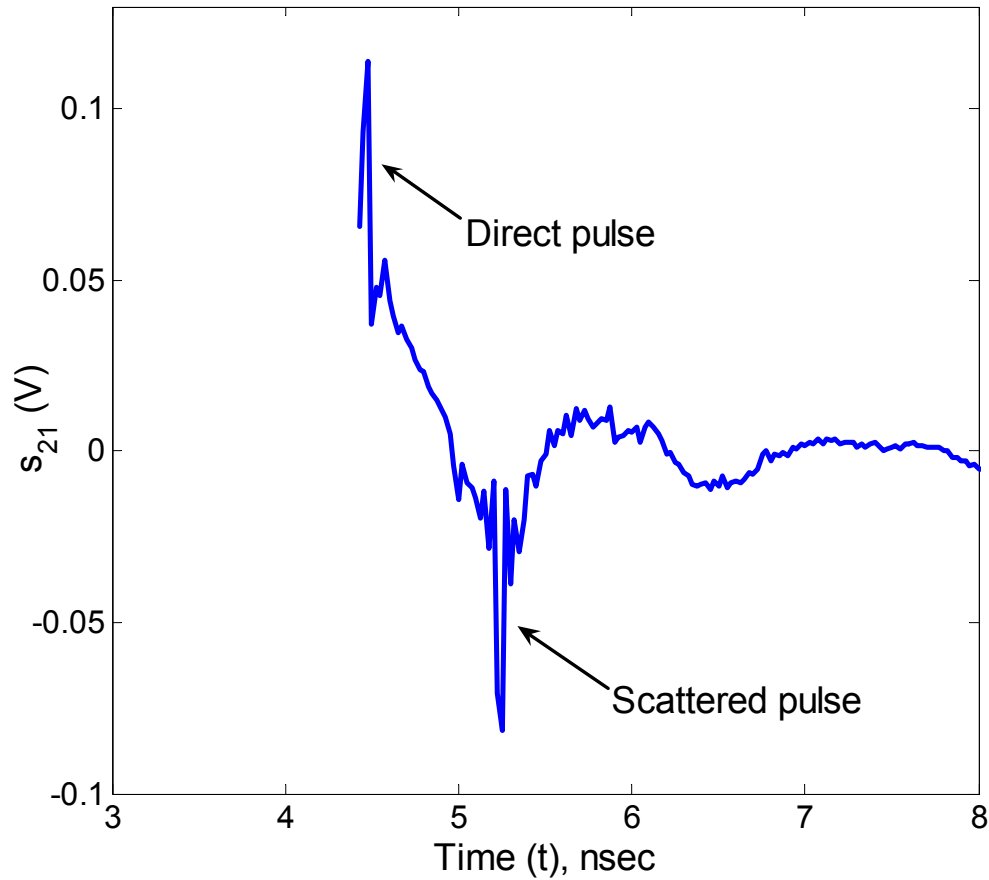


Figure 4.3 Time domain response when the two horn antennas are oriented toward a 15.2 cm (6 inch) diameter conducting hemispherical scatterer on a ground plane, deconvolved by the LOS impulse response using (4.23).

The s_{21} scatter parameter is recorded with the scatterer removed. This measures the direct component $s_{21,Direct}$, which is then subtracted from the $s_{21,scattered}$ data previously recorded. The resultant $s_{21,canonical}$ data corresponds to the scattered impulse response of the canonical object under investigation. As an example, the frequency amplitude response and the time domain scattered response of a 15.2 cm (6 inch) diameter conducting hemispherical scatterer mounted on a ground plane are shown in Fig. 4.4. For a positive pulse excitation, the specular-reflection component of the scatterer response is inverted in polarity. At the end of the specular component, an exponential decaying dispersive component is observed. This dispersive response is the late-time response of the scatterer due to the excitation of natural modes. Fig. 4.4 shows that the specular reflection component and the resonant dispersion component can be separated using time gating of the isolated scatter response.

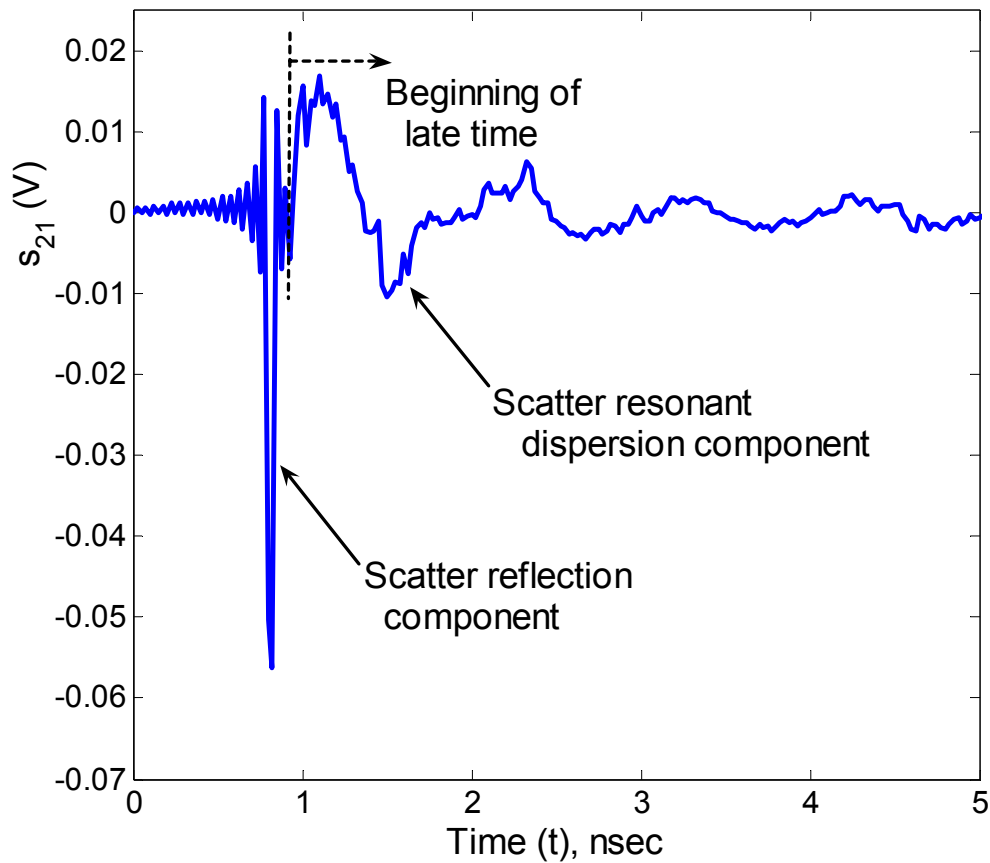


Figure 4.4 Measured time-domain response of a 15.2 cm (6 inch) diameter hemisphere mounted on a ground plane deconvolved with antenna response using (4.22), (4.23), and (4.24).

The late time response of the scatterer at the end of the specular (reflection) component can be modeled as a weighted sum of complex exponentials, i.e. complex poles and residues, using the singularity expansion method (SEM). The next section presents the extraction of complex poles and residues from the late time response of canonically shaped scatterers using the Matrix Pencil Method.

4.2.3 Pole-Residue Extraction using the Matrix Pencil Method (MPM)

The previous section presented post processing of the measured data to remove the unwanted reflections and antenna effects. The time-domain response of the isolated scatterer indicated a specular reflection component and a resonant dispersion component that can be separated using time gating of the scatterer response. This section demonstrates extraction of complex poles and

residues from the late time response of a conducting hemisphere over a ground plane using the Matrix Pencil Method.

The late time response of a conducting hemisphere of 15.2 cm (6 inch) diameter over a 1.2 m x 1.2 m ground plane is evenly sampled in time. Two $\{(N - L) \times L\}$ matrices $[\mathbf{Y}_1]$ and $[\mathbf{Y}_2]$ are generated from equally spaced time samples of the scatterer response as given by (4.16) and (4.17). The complex poles of the scatterer response are given by the eigenvalues of the matrix product $\mathbf{Y}_2^+ \mathbf{Y}_1$, where $[\cdot]^+$ indicates the Moore-Penrose pseudo inverse [25].

It is difficult to estimate the exact number of poles P_{exact} required to model the time-domain scatterer response without apriori information. If the number of estimated poles P is larger than the exact number of poles contained in the data ($P > P_{exact}$), then the matrix pencil algorithm generates extraneous poles in addition to the actual poles. However, if the number of estimated poles P is less than the exact number of poles contained in the data ($P < P_{exact}$), then the estimated pole values using the matrix pencil algorithm may deviate significantly from the actual pole values. The number of estimated poles P is chosen to be 50 (meaning 25 pairs of complex conjugate or real poles) so as to satisfy the matrix pencil formulation given by $P \leq L \leq (N - P)$, where $N = 120$ and $L = 70$.

Figure 4.5 shows 25 pairs of complex conjugate poles of a conducting hemisphere of diameter 15.2 cm (6 inch) over a ground plane. The complex poles are estimated using both the Matrix Pencil Method (MPM) and the Least Squares Prony's Method. The real and imaginary axes are scaled by (a/c) , where a is the radius of the hemisphere and c is the speed of light. Identical pole values were obtained using the Least Squares Prony's Method. In the remainder of this dissertation, the Matrix Pencil Method (MPM) is used because of its robustness in presence of noise and its computational simplicity. Once the poles are known, the corresponding residues $\{R_\alpha\}$ are solved using the least squares approach given by (4.19).

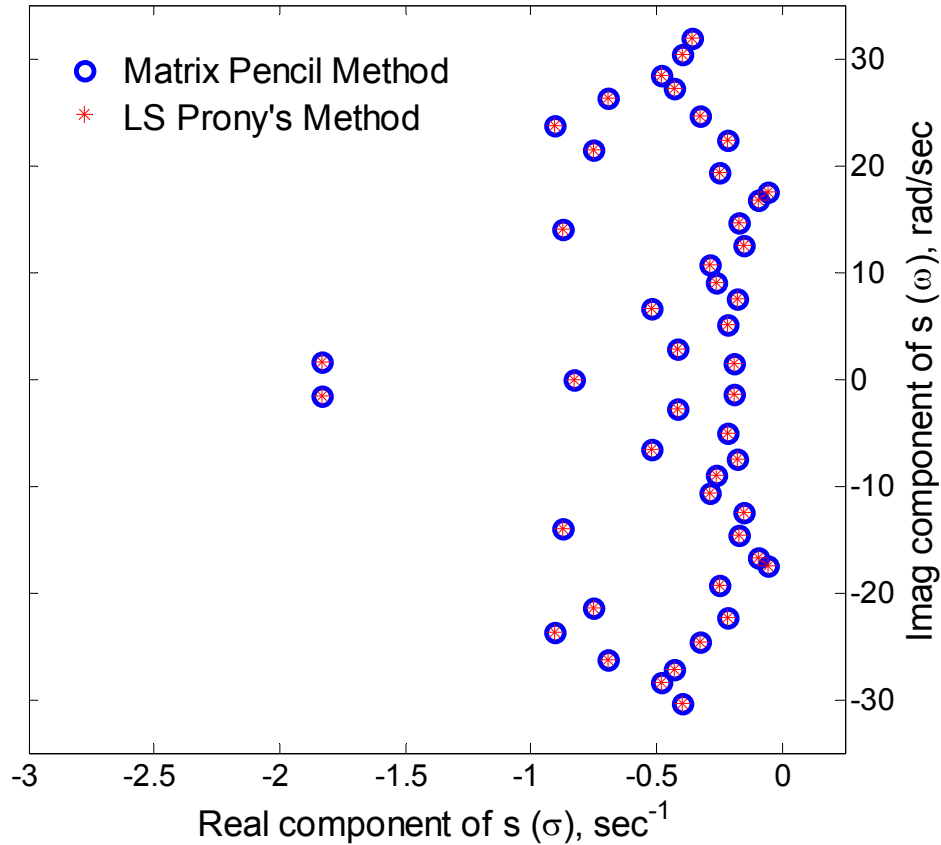


Figure 4.5 Estimated 25 pairs of complex conjugate poles of a conducting hemisphere of diameter 15.2 cm (6 inch) mounted on a 1.2 m x 1.2 m ground plane as shown in Fig. 4.1. The complex poles are estimated using the matrix pencil algorithm and the least squares Prony's method. The real and imaginary axes are scaled by (a/c) , where a is the radius of the hemisphere and c is the speed of light.

A number of estimated poles larger than $P = 50$ results in spurious poles. Singular value decomposition (SVD) of the matrix $[\mathbf{Y}_1]$ can be used to estimate only the strong poles [28]. The singular values of 50 estimated poles normalized with the maximum value are shown in Fig. 4.6. Note that only 2 pairs of complex conjugate poles have a relatively large singular value compared to the SVD values of the other poles. However, this approach results in too few a number of estimated poles and that is not sufficient for scatter response modeling. An alternate approach in determining dominant poles using the residue amplitude and the energy content of the poles is presented in Section 5.3.

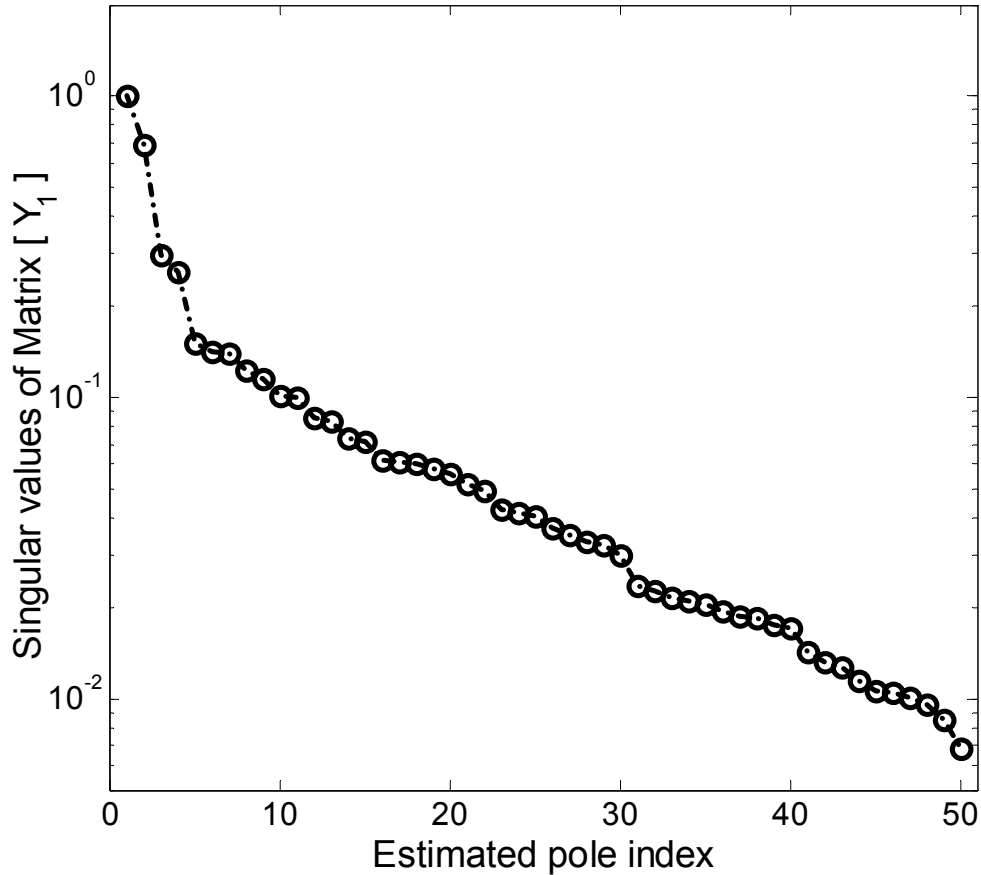


Figure 4.6 Singular value decomposition of the matrix $[Y_1]$ given by (4.13) for the case of a conducting hemisphere of diameter 15.2 cm (6 inch) mounted on a 1.2 m x 1.2 m ground plane as shown in Fig. 4.1. The complex poles are estimated using the matrix pencil algorithm and the least squares Prony's method.

Generally, the response from antennas and scatterers has simple poles [6]. Double poles can occur if the excitation signal itself has double poles, e.g. ramp signal. Because a Gaussian pulse of few pico second duration was used in this investigation, simple poles are assumed in the remainder of the discussion. The complex pole positions are indicative of the scatterer size and structure and can be used as scattering signature of the canonical object. The next section presents time-domain responses and pole-residue signatures of various canonical objects.

4.3 Pole-Residue Scattering Signatures of Canonical Structures

The late time response of scatterers can be modeled using the singularity expansion method (SEM). The complex poles and the corresponding residues can be used as the scattering signature because they completely describe the scatterer response. This section presents the

complex poles and residues for canonically shaped scatterers such as sphere, and a cylinder, using the Matrix Pencil Method (MPM).

4.3.1 Spherical Scatterer

A conducting hemisphere of diameter 15.2 cm (6 inch) is mounted over a 1.2 m x 1.2 m ground plane as shown in Fig. 4.1. The image of the hemisphere in the ground plane produces an effective spherical scatterer in free space. The 25 pairs of complex conjugate poles used to estimate the transient scatterer response are shown in Fig. 4.5. However, the transient response can be estimated with fair accuracy using only 6 pairs of dominant poles as shown in Fig. 4.7.

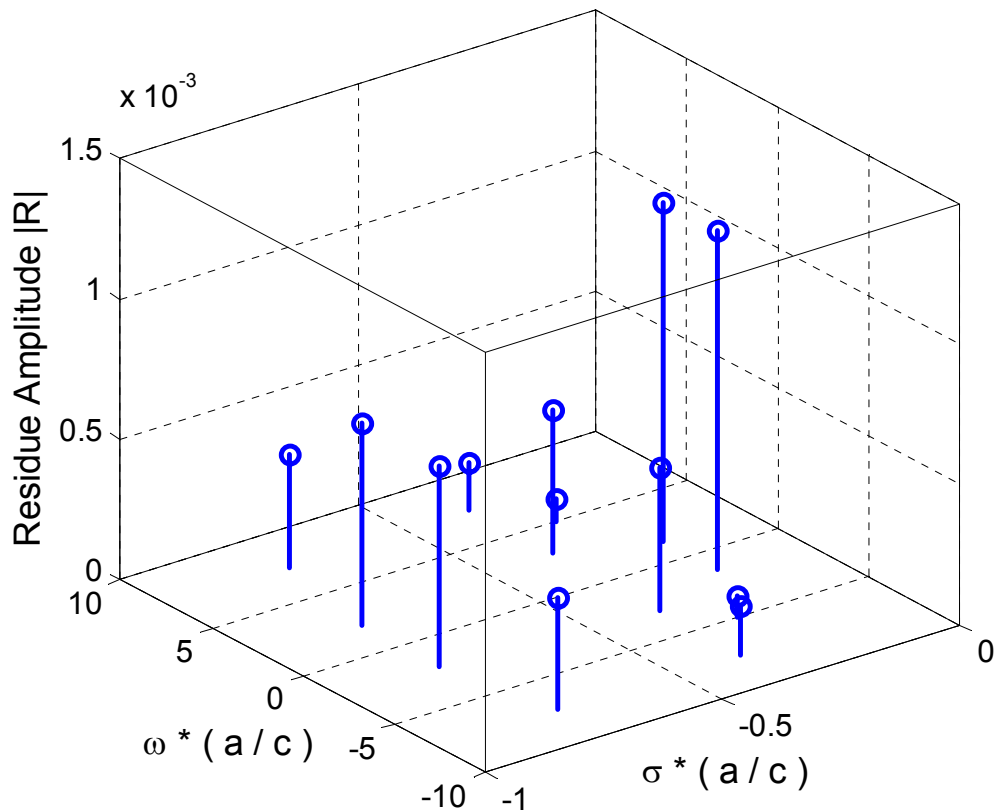


Figure 4.7 Estimated dominant poles and residues of a 15.2 cm (6 inch) diameter hemisphere over a 1.2 m x 1.2 m ground plane based on the energy content of the poles using the Matrix Pencil method.

The dominant poles are selected based on the energy content of the poles as described in Section 5.1.2. The energy content of these 6 pairs of dominant poles combined constitutes about

91% of the total energy in the scatter response. Introduction of additional poles did not improve the transient response and hence, only 6 pairs of dominant poles were selected. The estimated transient response using only these 6 pairs of dominant poles is shown in Fig. 4.8. Although the time domain response is accurately modeled using all the 25 pole pairs (not shown for figure clarity), the 6 pairs of dominant poles model the scatterer response with sufficient accuracy as seen in Fig. 4.8.

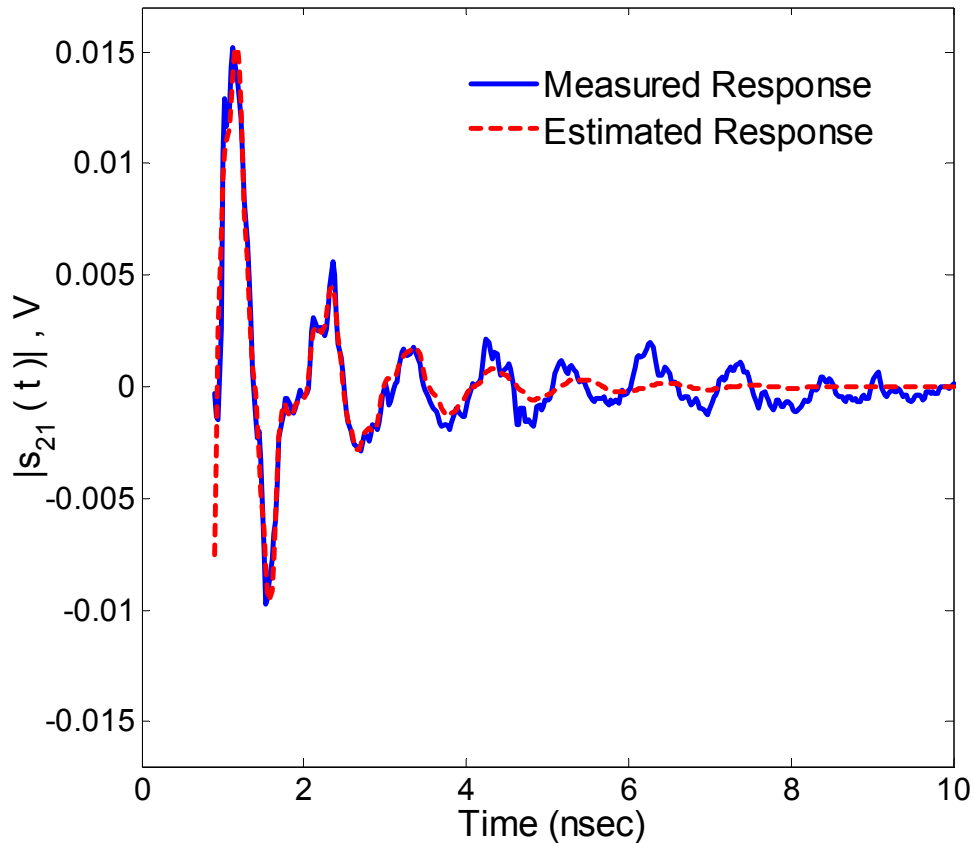
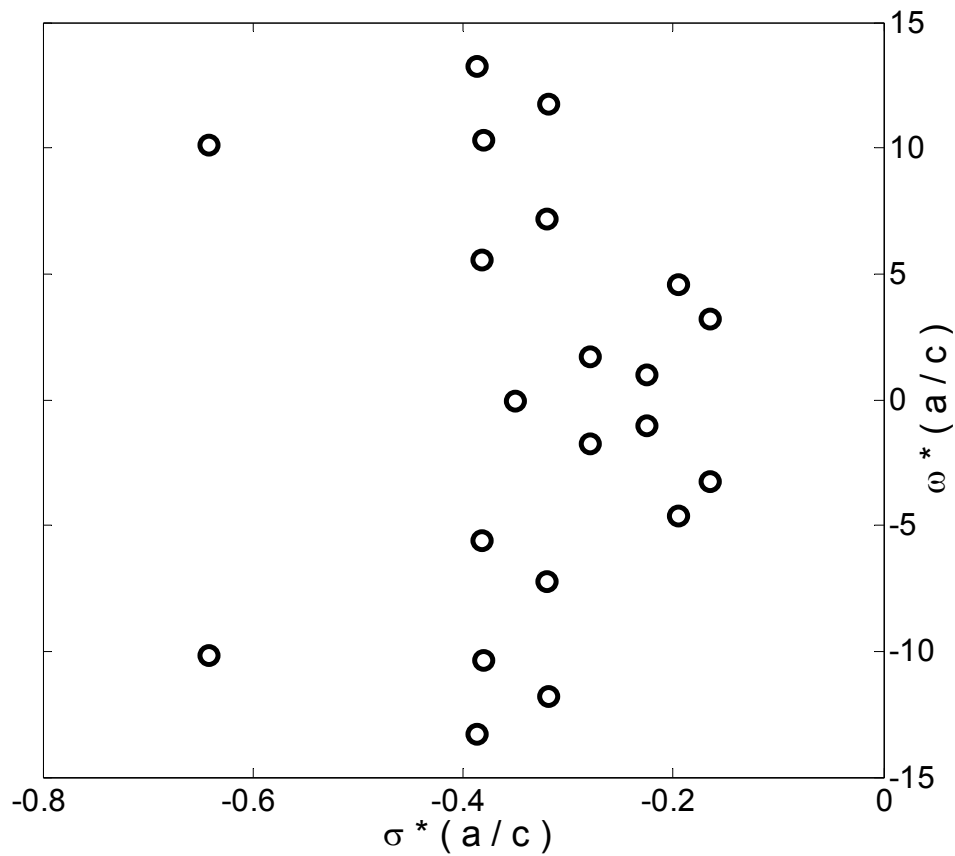


Figure 4.8 Comparison of the estimated transient response using only the 6 pairs of dominant poles shown in Fig. 4.7 and the measured late time response of a 15.2 cm (6 inch) diameter hemisphere over a 1.2 m x 1.2 m ground plane.

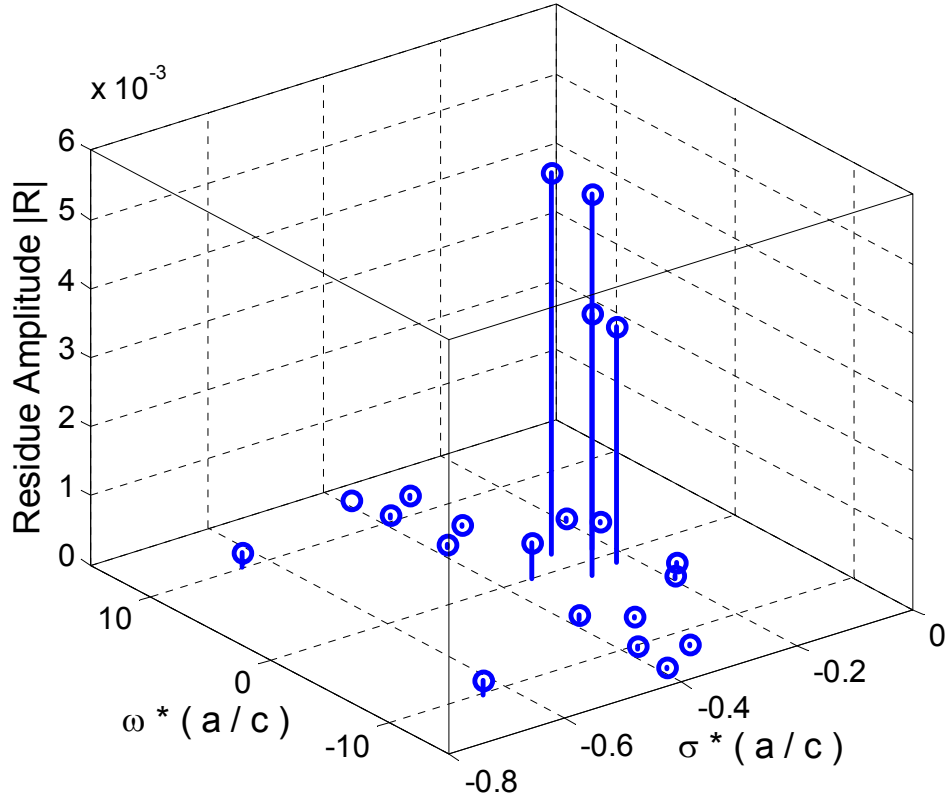
4.3.2 Cylindrical Scatterer

The time domain scatter response of cylindrically shaped canonical objects was measured and the data processed to extract scatter signatures in terms of poles and residues. The conducting cylinder of height 25.4 cm (10 inches) and a base diameter of 10.2 cm (4 inches) was mounted at the object location on the 1.2 m x 1.2 m ground plane as shown in Fig. 4.1. The transient

response of the cylinder is similar to the response of sphere, consisting of a specular component followed in time by a resonant component. The dominant poles extracted from the s_{21} response of this cylinder using the Matrix Pencil method are shown in Fig. 4.9 (a). Figure 4.9 (b) shows the estimated 10 pairs of dominant complex poles and their corresponding residue values. The combined energy content of these 10 pairs of dominant poles constitutes about 93% of the total energy in the late time response of the cylinder. Because additional poles did not improve the transient response, only 10 pairs of dominant poles were selected. These 10 pairs of dominant poles accurately represent the scatter response from the conducting cylinder as seen in Fig. 4.10.



(a) Estimated dominant complex poles based on the energy content of the poles.



(b) Estimated dominant complex poles and the corresponding residue amplitude

Figure 4.9 Scatter signature of a conducting cylinder of base diameter 10.2 cm (4 inch) and height 25.4 cm (10 inch). Axes scaled by (a/c) where a is the base radius of the cylinder and c is the speed of light.

A novel pole-dispersion channel model is proposed for ultra-wideband (UWB) communications in the next section. The proposed pole-dispersion channel model includes the scatter signature in terms of poles and residues as described in this section for sample scatterers with spherical and cylindrically shaped canonical scatterers. Scatterer response is accurately modeled by illuminating the scatterer with a 50 pico-second pulse corresponding to a bandwidth of 20 GHz.

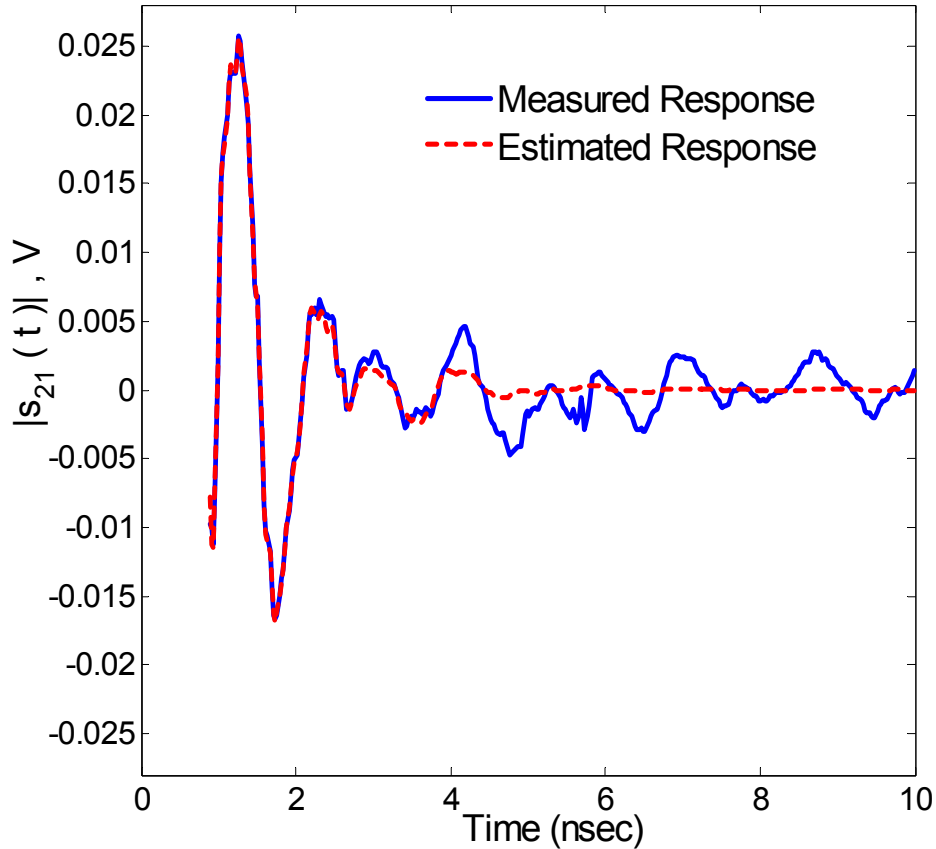


Figure 4.10 Comparison of the estimated transient response using only the 10 pairs of dominant poles shown in Fig. 4.9 to the measured late time response of a conducting cylinder of base diameter 10.2 cm (4 inch) and height 25.4 cm (10 inch).

4.4 Pole-Dispersion UWB Channel Model

The impulse response of a wireless channel can be statistically modeled to include multipath dispersion using distributions for the time-delay, amplitude and phase of the received multipath components [29, 30]. The widely used Turin's impulse response channel model [31] is frequency independent and hence, cannot model channel dispersion, which is a frequency dependent phenomena. A novel pole-dispersion channel model is proposed for ultra-wideband (UWB) communications that includes scatterer response to incident wideband UWB pulse. The proposed UWB channel model is an original contribution that incorporates the frequency-dependent scatter response modeled using the Singularity Expansion Method (SEM). The proposed channel model for ultra-wideband applications permits implementation of optimum matched filtering.

Experimental results demonstrating superior performance of the proposed pole-dispersion channel model compared to the conventional channel models is presented in Chapter 8. The

scatter response analyzed using the Matrix Pencil method to extract the pole-residue scatter signatures. The proposed channel model can be used to provide guidelines for UWB receiver design that compensates for the dispersive nature of the channel. This will result in maximum achievable signal-to-noise ratio for correlation-based matched filter receiver.

The proposed model is based on the generalized stochastic channel model that decouples the channel impulse response into components given as

$$h(t, \tau) = \sum_{n=1}^N A_n(t; \tau - \tau_n) \quad (4.25)$$

where N is the random number of multipaths, A_n is the frequency-dependent complex scatter amplitude, t is the observation time, and τ is the multipath delay. Turin first suggested a simple impulse response channel model [31] based on the generalized stochastic channel model that represents the channel impulse response as a sum of N impulses given by

$$h(t, \tau) = \sum_{n=1}^N a_n(t) e^{j\theta_n(t)} \delta(\tau - \tau_n) \quad (4.26)$$

where amplitude $a_n(t)$ is modeled stochastically by Rayleigh, Rician, Weibull, Nakagami, Suzuki or other distributions. The phase $\{\theta(t)\}$ distribution is assumed to be uniform. Multipath time-delay τ is modeled stochastically by a standard Poisson or a modified Poisson (Δ -K) distribution [32].

Simulation results presented in [33] demonstrate that late arriving multipath components exhibit more dispersive distortion, indicating that there is correlation between the time-of-arrival (TOA) and the amount of dispersion. Moreover, received multipath components exhibit different frequency dependencies because of interactions with scatterers. The scatter center-based frequency-dependent channel model is a significant step towards incorporating frequency dependent scatter response by extending Turin's channel model to investigate diffraction related distortion [34]. The objective is to further extend Turin's channel model to incorporate resonant dispersion from finite dimensional scatterers for inclusion in UWB channel propagation modeling. The response from each scatterer is modeled using the Singularity Expansion Method (SEM) approach with poles and residues. The response of finite dimensional objects to a wideband incident pulse can be characterized by using the SEM, which models the scattered response from objects as sum of damped sinusoids given by (4.2).

The resonant dispersion channel model proposed here builds on the generalized multipath channel model of (3.5) and the SEM based pole-residue scatterer model of (4.3) and is

$$h_c(\tau) = \sum_{n=1}^N \left\{ a_n e^{j\theta_n} \delta(\tau - \tau_n) + \sum_{m=1}^P R_{n,m}(\Omega_f, \Omega_r) e^{s_{n,m}(\tau - \tau_n - \Delta t_p)} u(\tau - \tau_n - \Delta t_p) \right\} \quad (4.27)$$

where N is the number of multipath components, a_n is magnitude of the multipath specular component, θ is phase shift introduced by the reflection of the UWB pulse, τ_n indicates the time-delay of the n th multipath component, P is the number of poles (even number) used to characterize the late time response of the n th scatterer, Ω_i and Ω_r are the incident and reflection aspect angles, Δt_p indicates the pulse width and the m th pole and residue of the n th scatterer are given by $s_{n,m}$ and $R_{n,m}$, respectively.

If different multipath components from different scattering centers can be isolated at the receiver, then each scattering center can be represented in two components: the specular multipath component and the resonant dispersion component. The first half of the proposed pole-dispersion channel model is the impulse response channel model that models the specular reflections off the scattering objects. The second half is based on the singularity expansion method (SEM) that models the resonant response of the scattering objects. The resonant response modeling using the SEM allows a time-delay equivalent to the incident pulse width after the specular reflection. This time-delay allows for the incident pulse to pass the scatterer. This ensures late time response modeling of the scatterer response.

The n th multipath component scattered from a finite dimensional object and arriving at the receiver with delay τ_n is represented in terms of a specular component and a late time component that is modeled using P number of poles (s_α) and residues (R_α). The poles and residues can be extracted using Prony's or Matrix Pencil Method. Chapter 5 presents a validation of the pole-residue dispersion characterization from scatterer response by comparing the scatterer response of canonical structures to known analytical results.

4.5 Chapter Summary

This chapter presented a novel pole-dispersion channel model for ultra-wideband wireless applications. The proposed pole-dispersion channel model includes resonant and multipath dispersion effects observed in sub nano-second UWB pulse communications. Advances in the

proposed channel modeling technique will benefit UWB radar target identification, ground penetration radar for buried landmine detection and breast tumor detection.

A brief introduction of the Singularity Expansion Method (SEM) was presented before the proposed pole-dispersion UWB channel model because the model includes SEM based scatterer response modeling. Various numerical techniques used for determining the pole-residue scatter signatures such as the frequency domain search method, Prony's method, and the Matrix Pencil Method (MPM) were discussed in Section 4.1.

Transient response analysis is explained in Section 4.2 using an example of a conducting hemispherical scatterer over a ground plane. The measurement setup, post-processing to remove unwanted reflections and antenna effects, and time gating to separate the late-time resonant dispersion component is described in detail. Section 4.3 presents modeling of the responses from scatterers of canonical shapes to an incident ultra-wideband pulse. The canonical scatterers include a sphere, and a cylinder. Validation of the measured scatterer responses is addressed in the next chapter.

A novel pole-dispersion channel model was proposed in Section 4.4 for ultra-wideband (UWB) communications that includes scatterer response to incident wideband UWB pulse. If multipath components from the scattering centers can be isolated at the receiver, then each scattering center can be represented individually in terms of poles and residues.

References

- [1] G. G. Joshi, W. A. Davis, and W. L. Stutzman, "Ultra-wideband (UWB) channel dispersion: classification and modeling," *Proceedings of IEEE Antennas and Propagation Society International Symposium*, vol. 1 (B), pp. 702-705, July 2005.
- [2] C. E. Baum, "On the Singularity Expansion Method for the Solution of Electromagnetic Interaction Problems," *Interaction Notes #88, AFRL Directed Energy Directorate*, Dec. 1971.
- [3] C. E. Baum, E. J. Rothwell, K. M. Chen, and D. P. Nyquist, "The singularity expansion method and its application to target identification," *Proceedings of the IEEE*, vol. 79 (10), pp. 1481-1492, Oct. 1991.
- [4] C. E. Baum, "The Singularity Expansion Method," in *Transient Electromagnetic Fields*, L. B. Felsen, Ed. New York: Springer-Verlag, 1976.
- [5] F. Tesche, "On the analysis of scattering and antenna problems using the singularity expansion technique," *IEEE Transactions on Antennas and Propagation*, vol. 21 (1), pp. 53-62, Jan. 1973.
- [6] M. Van Blaricum and R. Mittra, "A technique for extracting the poles and residues of a system directly from its transient response," *IEEE Transactions on Antennas and Propagation*, vol. 23 (6), pp. 777-781, Nov. 1975.
- [7] T. K. Sarkar and O. Pereira, "Using the matrix pencil method to estimate the parameters of a sum of complex exponentials," *IEEE Antennas and Propagation Magazine*, vol. 37 (1), pp. 48-55, Jan. 1995.
- [8] K. S. Cho and J. T. Cordaro, "Calculation of the Singularity Expansion Method Parameters from the Transient Response of a Thin Wire," *Interaction Notes #379, AFRL Directed Energy Directorate*, Sept. 1979.
- [9] Y. Hua and T. K. Sarkar, "Matrix pencil method for estimating parameters of exponentially damped/undamped sinusoids in noise," *IEEE Transactions on Acoustics, Speech, and Signal Processing*, vol. 38 (5), pp. 814-824, May 1990.
- [10] A. Poggio, M. VanBlaricum, E. Miller, and R. Mittra, "Evaluation of a processing technique for transient data," *IEEE Transactions on Antennas and Propagation*, vol. 26 (1), pp. 165-173, Jan. 1978.
- [11] L. B. Felsen and N. Marcuvitz, *Radiation and Scattering of Waves*. Piscataway, NJ: IEEE Press, 1994.
- [12] D. Moffatt and K. Shubert, "Natural resonances via rational approximants," *IEEE Transactions on Antennas and Propagation*, vol. 25 (5), pp. 657-660, Sep. 1977.

- [13] M. Hurst and R. Mittra, "Scattering center analysis via Prony's method," *IEEE Transactions on Antennas and Propagation*, vol. 35 (8), pp. 986-988, Aug. 1987.
- [14] M. Morgan, "Time-domain scattering measurements," *IEEE Antennas and Propagation Society Newsletter*, vol. 26 (4), pp. 4-9, Aug. 1984.
- [15] M. A. Morgan and B. W. McDaniel, "Transient electromagnetic scattering: data acquisition and signal processing," *IEEE Transactions on Instrumentation and Measurement*, vol. 37 (2), pp. 263-267, June 1988.
- [16] M. A. Morgan and N. J. Walsh, "Ultra-wide-band transient electromagnetic scattering laboratory," *IEEE Transactions on Antennas and Propagation*, vol. 39 (8), pp. 1230-1234, Aug. 1991.
- [17] R. S. Adve, T. K. Sarkar, O. M. C. Pereira-Filho, and S. M. Rao, "Extrapolation of time-domain responses from three-dimensional conducting objects utilizing the matrix pencil technique," *IEEE Transactions on Antennas and Propagation*, vol. 45 (1), pp. 147-156, Jan. 1997.
- [18] T. Sarkar, D. Weiner, V. Jain, and S. Dianat, "Impulse response determination in the time domain-Theory," *IEEE Transactions on Antennas and Propagation*, vol. 30 (4), pp. 657-663, July 1982.
- [19] R. G. Madonna, P. J. Scheno, G. H. Vilaridi, C. Hom, and J. Scannepieco, "Scattering, Resonance, Creeping Wave, Traveling Wave and All That: UWB Measurements of Various Targets," in *Ultra-Wideband, Short-Pulse Electromagnetics*, vol. 1, H. L. Bertoni, L. Carin, and L. B. Felsen, Eds. New York: Plenum Press, 1993.
- [20] L. Pearson, "A note on the representation of scattered fields as a singularity expansion," *IEEE Transactions on Antennas and Propagation*, vol. 32 (5), pp. 520-524, May 1984.
- [21] R. Carriere and R. L. Moses, "High resolution radar target modeling using a modified Prony estimator," *IEEE Transactions on Antennas and Propagation*, vol. 40 (1), pp. 13-18, Jan. 1992.
- [22] T. K. Sarkar, P. Sheeyun, K. Jinhwan, and S. M. Rao, "Application of the matrix pencil method for estimating the SEM (singularity expansion method) poles of source-free transient responses from multiple look directions," *IEEE Transactions on Antennas and Propagation*, vol. 48 (4), pp. 612-618, Apr. 2000.
- [23] J. Cordaro and W. Davis, "Time-domain techniques in the singularity expansion method," *IEEE Transactions on Antennas and Propagation*, vol. 29 (3), pp. 534-538, Mar. 1981.
- [24] R. Prony, "Essai experimental et analytique sur les lois de la dilatabilite de fluids elastiques et sur celles de la force expansion de la vapeur e l'alkool, a differents temperatures," *Journale L'Ecole Polytech*, vol. 1, pp. 24-76, 1795.

- [25] W. H. Beyer, *CRC Handbook of Mathematical Sciences*. West Palm Beach, FL: CRC Press, 1978.
- [26] F. R. Gantmakher, *The Theory of Matrices*, vol. 1, 2nd ed. New York: Chelsea, 1989.
- [27] R. C. Qiu, "A theoretical study of the ultra-wideband wireless propagation channel based on the scattering centers," *Proceedings of the 48th IEEE Vehicular Technology Conference, VTC '98*, vol. 1, pp. 308-312, May 1998.
- [28] Y. Hua and T. K. Sarkar, "On SVD for estimating generalized eigenvalues of singular matrix pencil in noise," *IEEE Transactions on Signal Processing*, vol. 39 (4), pp. 892-900, Apr. 1991.
- [29] H. Hashemi, "Impulse response modeling of indoor radio propagation channels," *IEEE Journal on Selected Areas in Communications*, vol. 11 (7), pp. 967-978, July 1993.
- [30] H. Hashemi, "The indoor radio propagation channel," *Proceedings of the IEEE*, vol. 81 (7), pp. 943-968, July 1993.
- [31] G. Turin, "On the estimation in the presence of noise of the impulse response of a random, linear filter," *IEEE Transactions on Information Theory*, vol. 3 (1), pp. 5-10, Mar. 1957.
- [32] J. H. Reed, *Software radio : a modern approach to radio engineering*. Upper Saddle River, NJ: Prentice Hall, 2002.
- [33] R. C. Qiu and I.-T. Lu, "Multipath resolving with frequency dependence for wide-band wireless channel modeling," *IEEE Transactions on Vehicular Technology*, vol. 48 (1), pp. 273-285, Jan. 1999.
- [34] R. C. Qiu, "A study of the ultra-wideband wireless propagation channel and optimum UWB receiver design," *IEEE Journal on Selected Areas in Communications*, vol. 20 (9), pp. 1628-1637, Dec. 2002.

This page intentionally left blank.

Chapter 5 – Validation of Scatterer Response

The previous chapter presented the pole-dispersion channel model for ultra-wideband communication systems, which incorporates known dispersion effects for sub nano-second pulse communications. The proposed model is an extension of the Turin's multipath channel model to include dispersion from scatterer response. This chapter validates the pole-residue dispersion characterization from scatterer response, which is modeled using the Singularity Expansion Method (SEM) [1, 2]. The pole-residue dispersion characteristics of scatterer response are validated through comparison of the estimated complex-pole positions from measured data and the complex-pole positions available analytically for canonical objects. Two types of canonical scatterers are used for comparison of the measured and the analytically determined complex poles: a conducting sphere and a thin wire scatterer.

The chapter begins with a brief discussion of approximate analytical expressions for pole-residue characterization of a conducting sphere and a thin wire scatterer. The Mie series [3] solution offers an analytical solution to the response of a sphere to ultra-wideband pulse excitation. A comprehensive review of the Mie series solution is beyond the scope of this dissertation, so a simplified and approximate method is proposed in Section 5.1.1 for a conducting sphere based on Chen and Westmoreland's research [4]. An analytical solution to the response of a thin wire scatterer is available as an eigenvalue solution of the time-domain scattering equations cast in the form of a matrix difference equation [5]. Section 5.1.2 presents a brief overview of the thin wire response determined as a series of damped exponentials obtained from the eigenvalue solution of the matrix difference equation.

Three types of experiment setups are used to measure responses of canonical structures for ultra-wideband pulse excitation with increasing level of reality. Section 5.2 briefly describes the three experimental setups. The first experimental setup uses a 1.2 m x 1.2 m ground-plane; the second setup is inside an anechoic chamber; and the third setup is inside a hallway.

The accuracy of the estimated pole-residue dispersion characteristics from measured responses is limited by measurement noise and hardware setup errors. Low signal-to-noise ratios in measured scatterer response, especially at higher frequencies, result in spurious poles [6]. Moreover, the position deviations occur in the complex s -plane of the estimated poles corresponding to the true poles [7, 8]. Dominant poles based on the magnitude of residues and the energy content are selected and compared to the theoretically determined poles. Section 5.3 presents an overview of the dominant pole selection process using a sample measured time-domain response of a hemisphere over a ground plane.

The scatter response from the canonical sphere is validated using all the three sets of measured data. The first uses a conducting hemisphere over a ground plane, the second uses conducting spheres of various radii inside an anechoic chamber and the third uses a single metallic sphere in a hallway scenario. Section 5.4 presents a comparison of the complex pole-position data available from these experimental setups and the theoretically determined complex poles for conducting sphere.

Similar to the canonical sphere, the scatter response from thin wire scatterer is validated using two sets of experiments: one with thin wires of various lengths and thicknesses inside an anechoic chamber and the other with a thin wire in a hallway environment as part of an indoor communication scenario. Section 5.5 presents a comparison of the complex pole-position data available from these two experimental setups and the theoretically determined complex poles for thin wire scatterer. Finally, Section 5.6 summarizes the important observations and contributions presented in this chapter.

5.1 Analytical Response of Canonical Objects

An important step to proposing the novel pole-dispersion channel model for ultra-wideband communication systems is to validate dispersion modeling. The pole-dispersion channel model incorporates known dispersion effects and includes dispersion due to scatterer response. This

section presents analytically determined complex pole-positions for two types of canonical objects: a conducting sphere and a thin wire scatterer.

The scatterer response in terms of pole-residue dispersion signature is better represented in the Laplace domain rather than the Fourier domain because the Laplace domain signature is indicative of both the resonant frequency and the damping rate. The Laplace transform of a continuous time function $f(t)$ given by [9]

$$L[f(t)] = F(s) = \int_0^{\infty} e^{-st} f(t) dt \quad (5.1)$$

where $s = \sigma + j\omega$ is the complex frequency, σ is the damping coefficient (sec^{-1}) and ω is the radial frequency (radians/sec). The complex frequency domain is a Cartesian co-ordinate representation of the complex frequency s with the real axis indicating the position of the real component (σ) of the complex frequency s and the imaginary axis indicating the position of the imaginary component (ω). For example, complex frequency $s_1 = \sigma_1 + j\omega_1$ is located in the complex frequency domain as shown in Fig. 5.1.

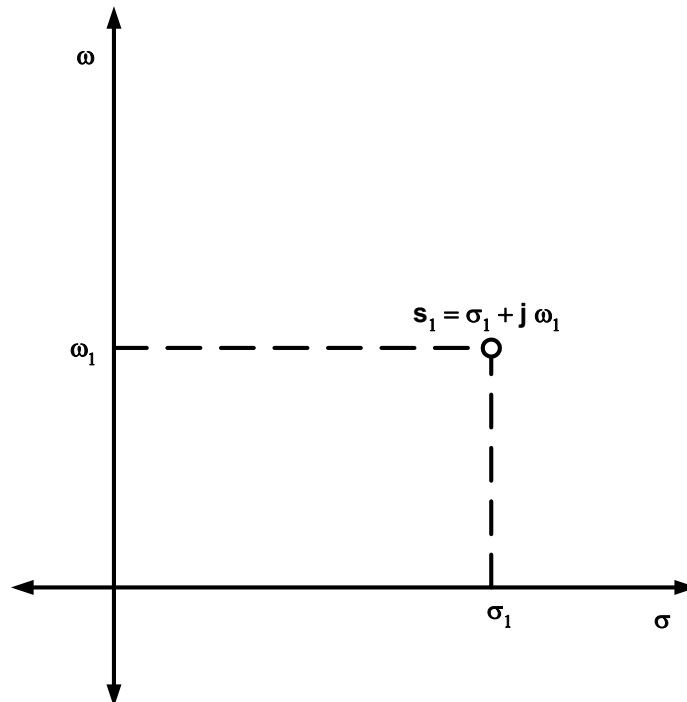


Figure 5.1 Complex frequency domain representation of complex frequency $s_1 = \sigma_1 + j\omega_1$

Section 5.1.1 presents a brief discussion on an approximate analytical expression for pole-residue characterization of a conducting sphere using a simplified and approximate Mie

series [10] solution. Section 5.1.2 briefly discusses an efficient method used to determine the analytical complex poles of a thin wire scatterer by casting the scatter response in terms of a matrix eigenvalue problem.

5.1.1 Pole-Residue Dispersion Signature of a Conducting Sphere

The impulse response of a spherically shaped scatterer can be determined by solving the Mie series [10-12]. The Mie series was developed by Gustav Mie in 1908 to characterize scattering of light by spherical particles [13]. However, sophisticated numerical methods are required to solve the Mie series for a general dielectric spherical scatterer. A simplified but approximate method [14] based on the Singularity Expansion Method (SEM) offers reasonably accurate pole-residue characterization of a conducting sphere. The pole-dispersion channel model is developed based on the empirical results of a conducting canonical sphere, providing an acceptable simplified approach.

The approximate solution of the Mie series [4] for a conducting sphere of arbitrary radius ‘ a ’ is obtained by first examining the backscattered field. Consider an incident field of a pulse excitation in time domain incident on a conducting sphere given by

$$\vec{E}_{inc}(t) = \hat{x} \delta\left(t - \left(\frac{z+a}{c}\right)\right) \quad (5.2)$$

The field of an impulse excitation propagates in the z direction and is polarized in the x direction. The backscatter response is well represented in the Laplace domain, which is given by (5.1). The Laplace transform of the incident pulse excitation on a conducting sphere is given by

$$\vec{E}_{inc}(s) = L[\vec{E}_{inc}(t)] = \hat{x} e^{-as/c} e^{-sR \cos(\theta)/c} \quad (5.3)$$

A simplified solution to the backscattered field from a conducting sphere in Laplace domain is given by [4]

$$\vec{E}_{backscattered}(s) = -\hat{x} \frac{a}{2R} e^{-s(R-a)/c} H(s) \quad (5.4)$$

where $H(s)$ is the sphere transfer function given by [4]

$$H(s) = \sum_{n=1}^{\infty} \frac{(2n+1)\zeta^{2n}}{f_n(\zeta)g_n(\zeta)} \quad (5.5)$$

where $\zeta = (a/c) \cdot s$ are the complex poles normalized by the radius of the sphere. The complex poles of the transfer function $H(s)$ of a conducting sphere are obtained by solving for the roots of the functions $f_n(\zeta)$ and $g_n(\zeta)$, which are given by [4]

$$f_n(\zeta) = \sum_{\beta=0}^n \frac{(n+\beta)!}{\beta!(n-\beta)!} \frac{1}{2^\beta} \zeta^{n-\beta} \quad (5.6)$$

$$g_n(\zeta) = \sum_{\beta=0}^n \frac{(n+\beta)!}{\beta!(n-\beta)!} \frac{1}{2^\beta} (\beta+\zeta) \zeta^{n-\beta} \quad (5.7)$$

The natural resonances of a conducting sphere are obtained by solving equations (5.6) and (5.7) for the normalized complex poles ζ . Fig. 5.2 shows the roots $s_n^f = \sigma_n^f + j\omega_n^f$ and $s_n^g = \sigma_n^g + j\omega_n^g$ of these equations, which group into branches. The first branch and the odd number of branches of normalized complex poles are obtained by solving $g_n(\zeta)$. Similarly, the second branch and even number of branches of roots are obtained by solving $f_n(\zeta)$. For simplicity, only the first two branches are plotted in Fig. 5.2. Moreover, the complex poles of these first two branches dominate the scatter response of the sphere due to their proximity to the imaginary axis in the complex s-plane (i.e. less negative damping coefficients).

The solution of Mie series to calculate the scatter response of a dielectric spherical scatterer is a non-trivial problem because of the sophisticated numerical methods required to solve the problem [4]. The above approximate solution to the Mie series for conducting sphere [4] is reasonably accurate for the first two branches as shown in Table 5-1. The exact complex poles of a conducting sphere are obtained from [14], which solves the Mie series based on the approach proposed in [13]. The approximate pole positions in Table 5-1 were computed using (5.6) and (5.7). There is excellent agreement between the exact results from the literature and the approximate method for this case. This serves as a validation of the approach.

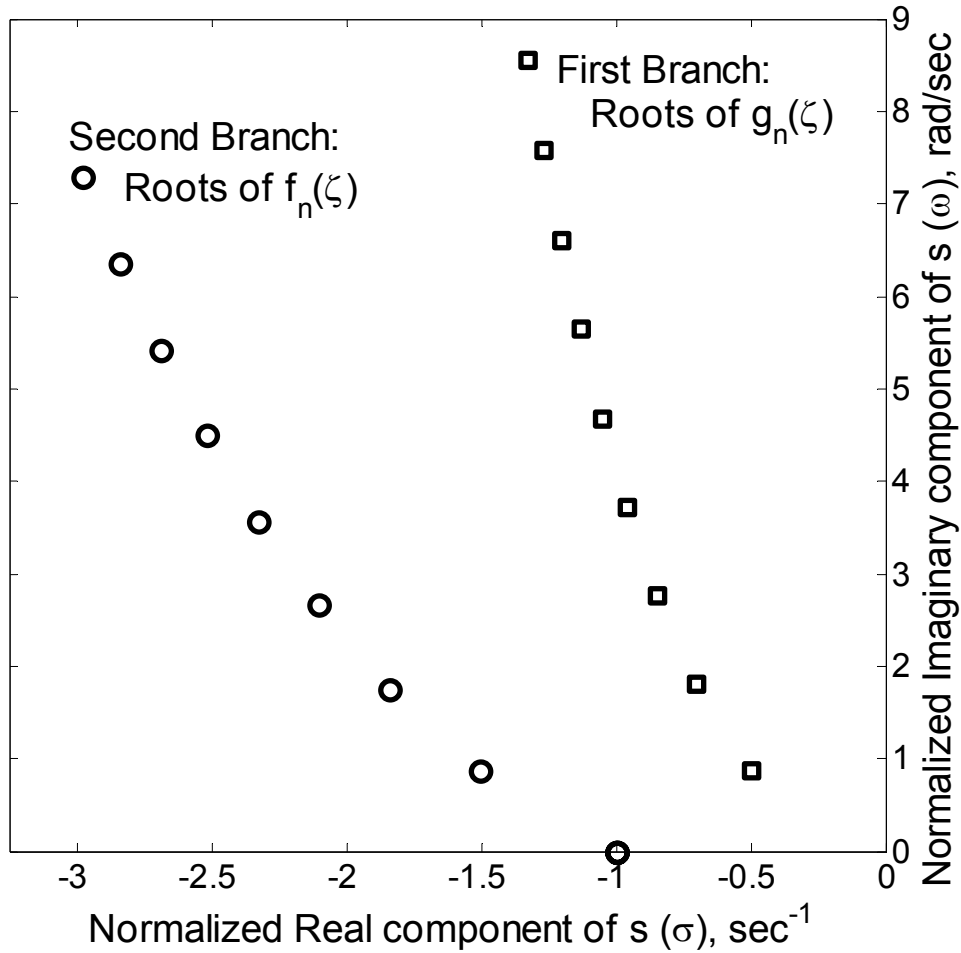


Figure 5.2 Approximate complex poles $s_n^f = \sigma_n^f + j\omega_n^f$ and $s_n^g = \sigma_n^g + j\omega_n^g$ of a conducting sphere computed using the Singularity Expansion Method (SEM) of (5.6) and (5.7). The axes are normalized by the factor a/c , where a is the sphere radius and c is the speed of light.

Table 5-1 Comparison of the Approximate Complex Poles of a Conducting Sphere [4] to the Exact Complex Poles [14] obtained by Solving the Mie Series

<i>Pole #</i>	<i>Exact Pole Position</i>	<i>Approximate Pole Position</i>
1	$-0.50000 \pm j 0.86603$	$-0.50000 \pm j 0.86600$
2	$-0.70196 \pm j 1.80740$	$-0.70200 \pm j 1.80700$
3	$-0.84286 \pm j 2.75786$	$-0.84300 \pm j 2.75800$
4	$-0.95423 \pm j 3.71478$	$-0.95400 \pm j 3.71500$

5.1.2 Pole-Residue Dispersion Signature of a Thin Wire Scatterer

The impulse response of a thin wire scatterer can be analytically determined by a variety of methods [15-17]. The eigenvalues approach outlined in [5] is used to determine the analytical solution to the response of a thin wire scatterer, because of its numerical simplicity. The time-domain scattering equation of a thin wire scatterer is cast in the form of a matrix eigenvalue problem. The solution of this eigenvalue problem offers natural frequencies (complex poles) and corresponding residue amplitudes, similar to the Singularity Expansion Method (SEM).

The analytical approach outlined here bypasses the step of computing the time-domain response of the thin wire scatterer and proceeds directly determining the pole-residue characteristics. Using the thin-wire approximation for the current I on the wire, the electric field integral equation for a thin wire can be written as [5]

$$\frac{\partial}{\partial t} E_z^{inc}(z, t) = -\frac{L}{\varepsilon} \int_0^L \frac{1}{8\pi^2 R} \bullet I(z', t - |z - z'|/c) dz' \quad (5.8)$$

where $E_z^{inc}(z, t)$ is the incident field corresponding to an impulse excitation propagating in the z direction, ε is the dielectric constant, L is the length of the thin wire, and I is the excited current. The current I can be discretized temporally and spatially over the thin wire as [5]

$$I(z, t) \cong \sum_{m=-\infty}^{\infty} \sum_{n=1}^N I_{mn} P_{\Delta}(ct - m\Delta) P_{\Delta}(z - n\Delta) \quad (5.9)$$

where I_{mn} is the current element over the differential region defined by $(m\Delta, n\Delta)$, N is the number of differential elements over the length of the thin wire, and P_{Δ} is a unit pulse of width $\Delta_t = \Delta/c$. Equation (5.9) when substituted in (5.8) can be put in the following form [5]

$$I_{m+1} = \sum_{i=0}^N A_i I_{m-i} + F_m, \quad m = 1, 2, 3, \dots \quad (5.10)$$

where I_m represents the spatial current element at the m^{th} elemental length of the thin wire, A_i are sparse matrices that relate the spatial components of I_m , and F_m is the forcing function. After the incident field has passed, F_m is zero and the I_{m+1} term can be expanded in a power series form as given by

$$I_{m+1} = Z_{\alpha}^{m+1} v_{\alpha}, \quad m = 1, 2, 3, \dots \quad \text{and} \quad F_m = 0 \quad (5.11)$$

$$= \left(e^{s_{\alpha} \Delta_t} \right)^{m+1} v_{\alpha}, \quad m = 1, 2, 3, \dots \quad (5.12)$$

where $s_\alpha = \sigma_\alpha + j\omega_\alpha$ is the α^{th} complex pole and \mathbf{v}_α is the vector that describes the corresponding natural mode. The complex poles must exist as real or as complex-conjugate pairs because the time-domain response given by (5.10) is real. Substituting (5.12) into (5.10) for $F_m = 0$, we obtain

$$\left(e^{s_\alpha \Delta_t}\right)^{m+1} \mathbf{v}_\alpha = \sum_{i=1}^N A_i \left(e^{s_\alpha \Delta_t}\right)^{m-i} \mathbf{v}_\alpha \quad (5.13)$$

Equation (5.13) can be re-arranged into following form for all complex poles s_α

$$\left(I - \sum_{i=0}^N A_i \left(e^{s_\alpha \Delta_t}\right)^{-(i+1)} \right) \mathbf{v}_\alpha = 0 \quad (5.14)$$

where I is the $N \times N$ identity matrix and the number of time samples equal the number of spatial samples (i.e., $M = N$). Equation (5.14) can be written in matrix form. Let X_m be a state vector and Φ be a state transition matrix defined as [5]

$$X_m^T = \left[I_m^T, I_{m-1}^T, \dots, I_{m-N}^T \right] \quad (5.15)$$

$$\Phi = \begin{bmatrix} A_0 & A_1 & A_2 & \dots & A_N \\ I & 0 & 0 & \dots & \vdots \\ \vdots & I & 0 & \dots & \vdots \\ \vdots & \vdots & \vdots & \ddots & \vdots \\ 0 & 0 & 0 & \dots & 0 \end{bmatrix} \quad (5.16)$$

where $[\cdot]^T$ indicates transpose operation and it follows that [5]

$$X_{m+1} = \Phi X_m, \quad m \geq 1 \quad (5.17)$$

If the eigenvalues of the matrix Φ are assumed to be distinct, then the eigenvalues and the corresponding eigenvectors are given by [5]

$$Z_\alpha = e^{s_\alpha \Delta_t} = \text{eigen}(\Phi), \quad \alpha = 1, 2, \dots, N \quad (5.18)$$

$$E_\alpha^T = \left[\mathbf{v}_\alpha^T, Z_\alpha^{-1} \mathbf{v}_\alpha^T, \dots, Z_\alpha^{-N} \mathbf{v}_\alpha^T \right], \quad \alpha = 1, 2, \dots, N \quad (5.19)$$

This demonstrates that the eigenvalues Z_α of the Φ matrix yield the complex poles given by $Z_\alpha = \exp(s_\alpha \Delta t)$ and the corresponding first N components of the eigenvectors of matrix Φ are the corresponding un-normalized natural mode vectors [5]. Thus, the complex poles and their corresponding residues are determined by casting the thin wire scatter response in terms of an eigenvalues problem.

The complex poles of the thin wire scaled by the length L and the speed of light c as found from the eigenvalue analysis of matrix Φ , given by (5.18), are plotted in Figure 5.3. These complex poles in the s -plane form the scatter signature of the thin wire scatterer. The measured scatter response of thin wires of various lengths is processed using the Matrix Pencil Method (MPM) to extract complex poles. These complex poles are scaled by the respective lengths of the thin wires and compared to the analytically determined complex poles shown in Fig. 5.3.

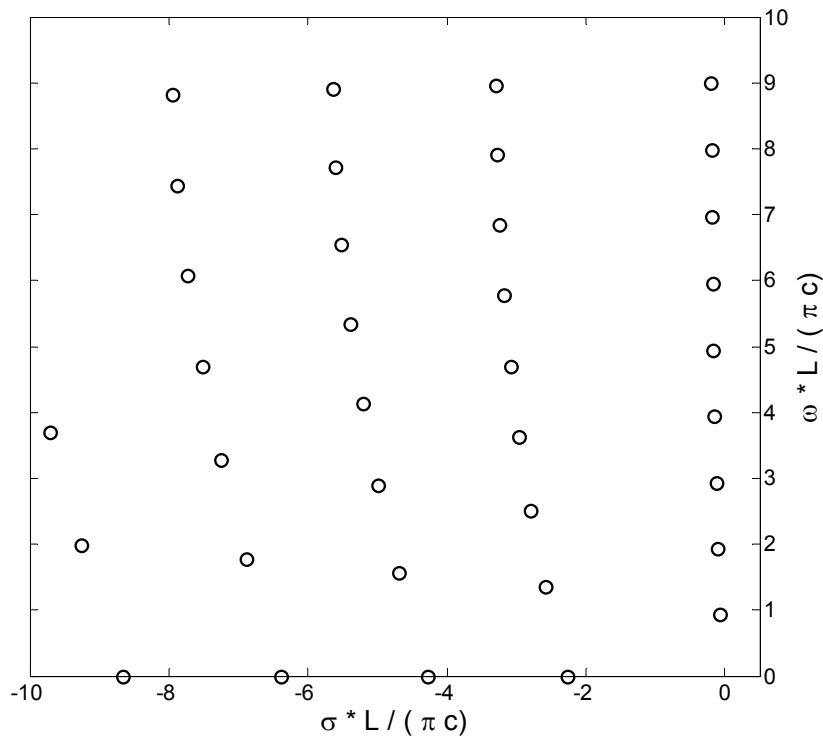


Figure 5.3 Analytically determined complex poles of a thin wire scatterer using the eigenvalue approach (5.18) [5].

5.2 Validation Experiment Setup

The scatterer response for arbitrary scatterers is validated using canonically shaped scatterers such as conducting spheres and thin wires. Three types of experiment setups are used to measure responses of canonical structures for ultra-wideband pulse excitation. These three types of experiment setups are chosen to reflect increasing level of actual propagation environment situations. Section 5.2.1 describes the first experimental setup, which uses a ground plane with planer TEM horn antennas. This was the initial setup used in investigating the ultra-wideband channel dispersion and is useful for its simplicity. The second experimental setup is inside an anechoic chamber and is described in Section 5.2.2. This setup is more focused towards measuring the time-domain scatterer response of arbitrary shape and size. This setup is also very effective in mitigating interference from other RF and microwave sources. The final experimental setup uses a realistic indoor UWB channel and is described in Section 5.2.3. Table 5-2 summarizes the three validation experiment setups including the types of antenna used, the range of frequencies and the canonical objects investigated.

Table 5-2 Three types of Validation Experiment Setups

<i>Experiment Scenario</i>	<i>Antennas</i>	<i>Frequency Range (GHz)</i>	<i>Canonical Objects</i>	<i>Comments</i>
1. Scatter over a ground plane	Planar flat TEM horn antennas	0.05 – 20.05	Hemisphere ($D = 15.2$ cm)	<ul style="list-style-type: none"> • Best SNR • Ground Plane limits size • Does not support all canonical shapes
2. Inside an anechoic chamber	Planar curved TEM horn antennas	0.05 – 12.00	Spheres ($D = 10.2, 12.7, 15.2$ cm), and Thin Wires ($L = 29, 46, 64$ cm)	<ul style="list-style-type: none"> • Good SNR • Object size limited by chamber dimensions • Supports all canonical shapes
3. Inside a hallway	Planar curved TEM horn antennas	0.05 – 12.00	Sphere ($D = 15.2$ cm), and Thin Wire ($L = 27$ cm)	<ul style="list-style-type: none"> • Poor SNR • Object size limited by hallway dimensions • Supports all canonical shapes

5.2.1 Canonical Objects over a Ground Plane

The first of the three types of validation experiment setups is simplest in terms of the required time-to-setup and the resources. In this type of scatterer-response measurement setup, canonical scatterers were investigated using two flat planar horn antennas mounted on diagonal corners of a 1.2 m x 1.2 m (4' x 4') square ground plane surrounded by absorber as shown in Fig. 5.4. The data were collected using a vector network analyzer VNA-HP8510. The measured scatterer responses were deconvolved with the line-of-sight (LOS) antenna response, and post-processed using the Least-Squares (LS) Prony's algorithm as outlined in Chapter 4.

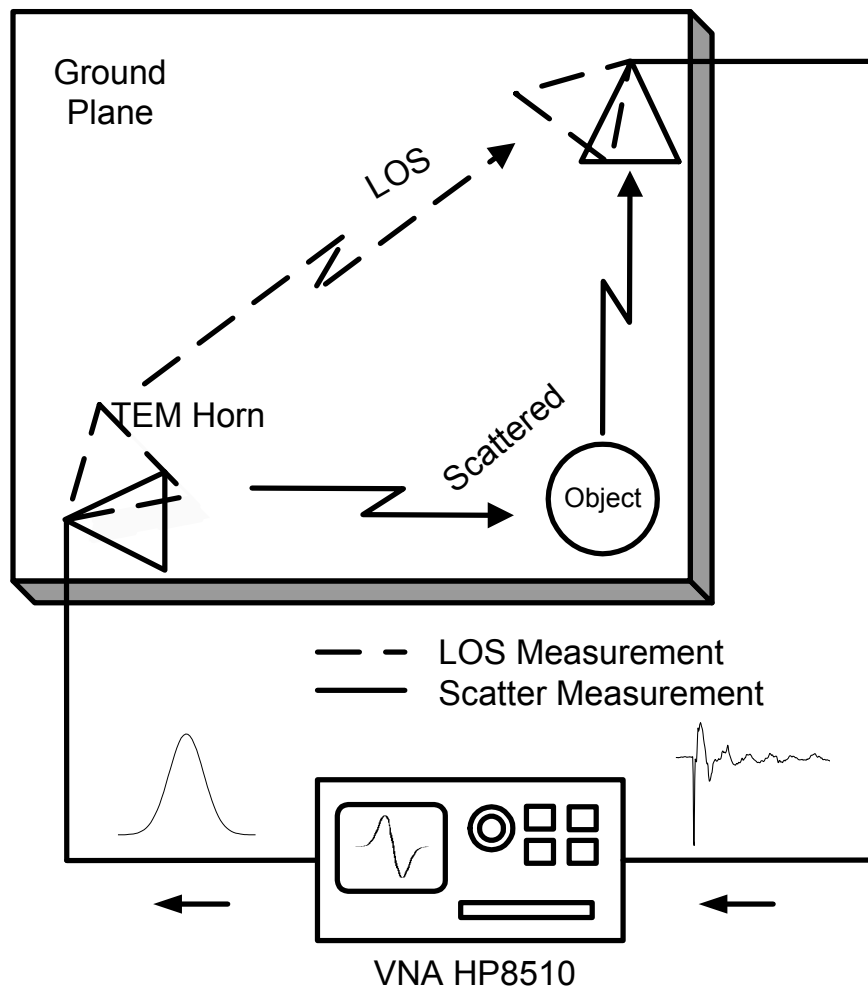


Figure 5.4 Validation experiment setup for Scenario # 1 using two flat planar horn antennas mounted on diagonal corners of a 1.2 m x 1.2 m square ground plane.

The edge of the ground plane was covered with absorber to reduce diffraction from the edge as well as to reduce scattering from the surrounding environment. A hemisphere of diameter 15.2 cm (6 inch) is investigated within a frequency range of 50 MHz – 20.05 GHz. The time resolution of the Gaussian pulse excitation is 25 psec corresponding to 40 GHz of sampling frequency. Data for each frequency step of 50 MHz were recorded using a vector average of 1024 measurements. Since the signal-to-noise ratio (SNR) increases by 3 dB for every doubling of the number of measurements, an average of 1024 measurements leads to an improvement in SNR of approximately 30 dB.

This simple setup, however, limits the types of canonical structures that can be used to validate the measured scatterer response. Moreover, only a small canonical scatterer can be used because the time-delay difference between the scatterer response and the edge of the ground-plane has to be sufficient to allow time gating. A single hemisphere of diameter 15.2 cm was used, permitting scatter measurements with very high signal-to-noise ratios (SNR).

5.2.2 Canonical Objects inside an Anechoic Chamber

This validation experiment setup is used to overcome the size and symmetry limitations of using a ground plane. Moreover, this setup is also very effective in mitigating interference from other RF and microwave sources. In this type of scatterer-response measurement setup, various types of canonical scatterers such as metallic spheres of various sizes and thin wires of various lengths were mounted on a pedestal inside an anechoic chamber. Two curved planar horn antennas were used in a bi-static radar configuration to record the s_{21} parameter for the scatterer response as shown in Fig. 5.5. The data were collected using a VNA-HP8510, deconvolved with the line-of-sight (LOS) antenna response, and post-processed using the Least-Squares (LS) Matrix Pencil Method (MPM).

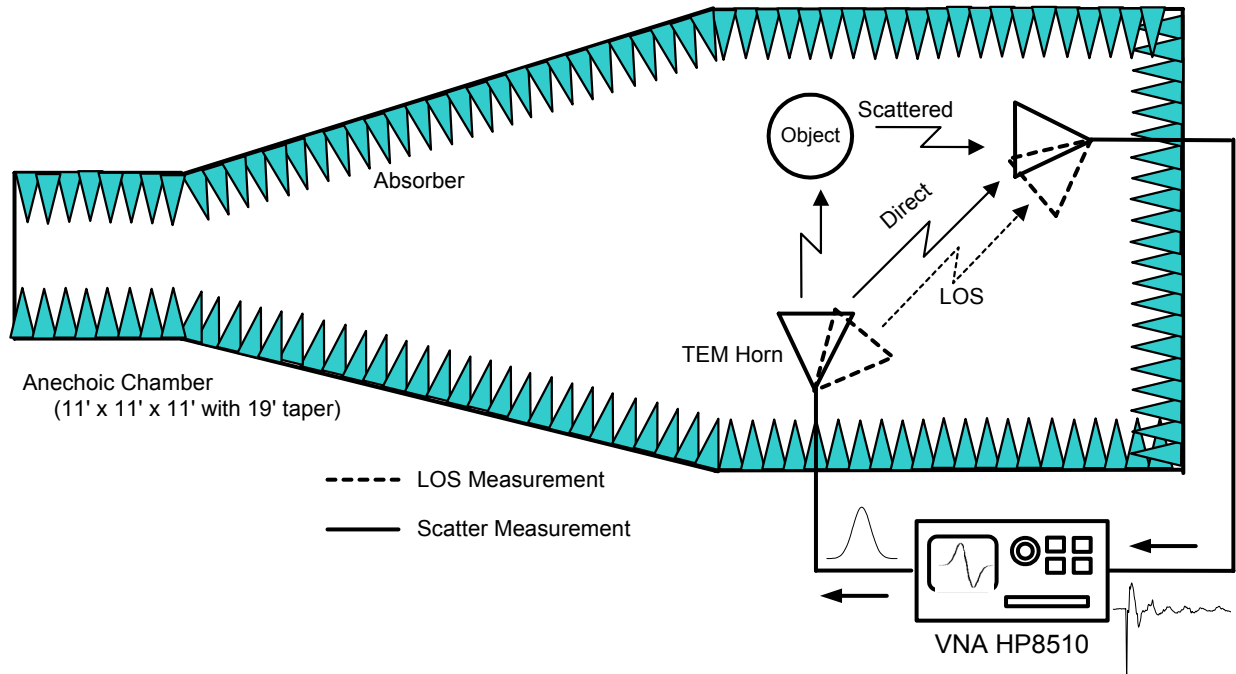


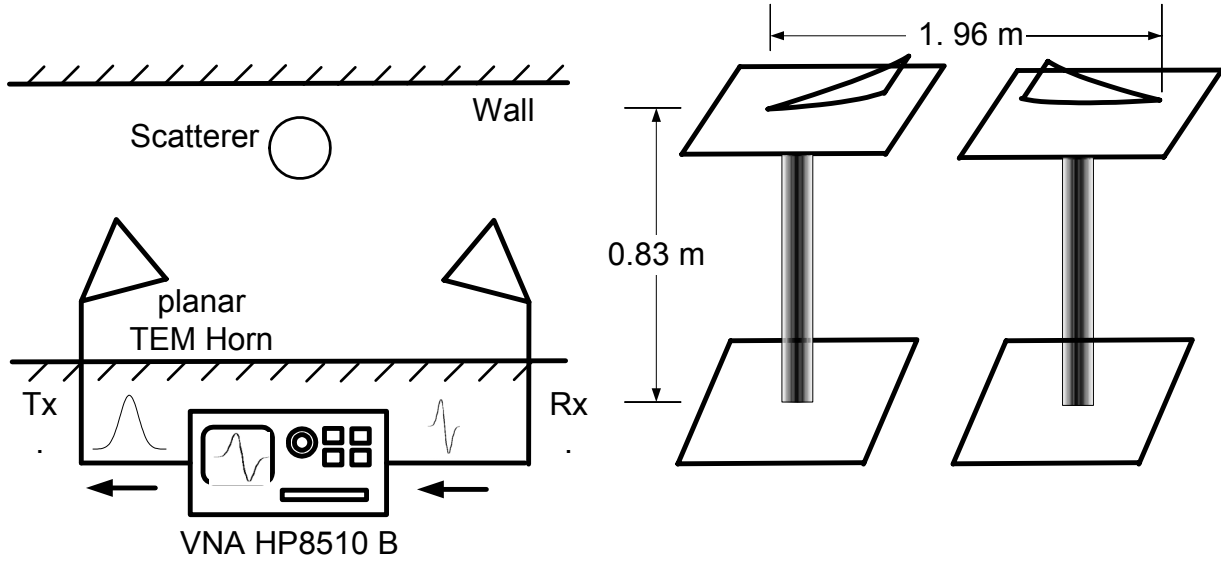
Figure 5.5 Validation experiment setup for Scenario # 2 using two curved planar TEM horn antennas mounted on pedestals inside an anechoic chamber of dimensions 3.35 m x 3.35 m x 3.35 m with 5.79 m taper (11' x 11' x 11' with 19' taper).

Using this setup, data for each frequency step of 50 MHz were recorded using a vector average of 1024 measurements, which resulted in an SNR range of 10 – 20 dB. The chamber dimensions did not limit the types of canonical structures that were used to validate the measured scatterer response. Canonical structures of various sizes and lengths were measured and validated through comparison with theoretical data. The operating bandwidth of the curved planar TEM horn antennas limited the frequency range from 50 MHz – 12 GHz.

5.2.3 Canonical Objects inside an Indoor Hallway Environment

This final validation experiment setup is most realistic in terms of an actual ultra-wideband (UWB) communication scenario. In this type of scatterer-response measurement setup, a single thin wire scatterer and a single metallic sphere were mounted on a pedestal in a hallway environment on the 6th floor of Whittemore Hall, Virginia Tech, as shown in Fig. 5.6 (a). Similar to the setup inside an anechoic chamber, two curved planar TEM horn antennas were used in a bi-static radar configuration to record the s_{21} parameter for the scatterer response. The data were

collected using a VNA–HP8510B and deconvolved with the line-of-sight (LOS) antenna response, which was measured as shown in Fig. 5.6 (b).



(a) Scatterer Response Measurement Setup (b) Line-of-Sight Response Measurement

Figure 5.6 Scatterer response validation experiment setup for Scenario # 3 using two curved planar TEM horn antennas mounted on pedestals inside a hallway

The available signal-to-noise ratios (SNR) from this setup are poor due to losses in the cable and due to unavoidable scattering from the floor, ceiling and the walls. A metallic sphere of diameter 15.2 cm (6 inch) and a thin wire scatterer of length 27 cm (10.6 inch) were used to validate the scatterer responses. The hallway dimensions permitted time gating of the desired response from the scatterers, thus avoiding reflections from the hallway structures.

5.3 Dominant Complex Poles from Measured Scatter Responses

Measurement noise limits the accuracy of the pole-residue dispersion characteristics estimation from measured responses. Noise in measured scatterer response results in spurious poles and deviation in the position of the actual poles in the complex s-plane [6-8]. For validation process, dominant poles based on the magnitude of residues and the energy content are selected and compared to the theoretically determined poles. In the remainder of the dissertation, dominant poles based on the energy content are used for the pole-dispersion channel model analysis. The dominant pole selection based on the residue magnitude and the energy content of the estimated

poles is described in Sections 5.3.1 and 5.3.2, respectively, for the measurement response of a hemisphere.

The dominant pole selection process is illustrated using a measured response of a conducting hemisphere of diameter 15.2 cm (6 inch) mounted over a ground plane. The experimental scatterer response data available from this ground plane measurement setup described in Section 5.2.1 are analyzed using the Matrix Pencil Method (MPM). This section presents an overview of the dominant pole selection process.

The scatterer-response of a 15.2 cm diameter hemisphere mounted over a ground plane is s_{21} scatter parameter measured using a VNA–HP8510 vector network analyzer. The measured s_{21} response was deconvolved with the antenna line-of-sight response and analyzed using the Matrix Pencil Method (MPM) to determine the complex poles. All the 23 complex poles (found using the method described in Section 4.1.3) used to characterize the scatter response are shown in Fig. 5.7. Note that only the complex poles lying in the upper left half of the complex s -plane are shown because for real time-domain response, the estimated poles are either real or occur in complex conjugate pairs. The scatter signature in terms of pole-position in the s -plane is normalized by the factor $g = a/c \log_e 10$, where a is the radius of the sphere and c is the speed of propagation of EM waves.

Using fewer than all the 23 pairs of complex conjugate poles reduces computational complexity. Moreover, all the 23 pairs of estimated poles do not correspond to actual poles. Some of the estimated poles are spurious poles due to noise. A comparison of all the 23 estimated poles to the analytically determined poles of a conducting sphere, as calculated in Section 5.1.1, shows that most of the estimated poles are spurious poles as seen in Fig. 5.8.

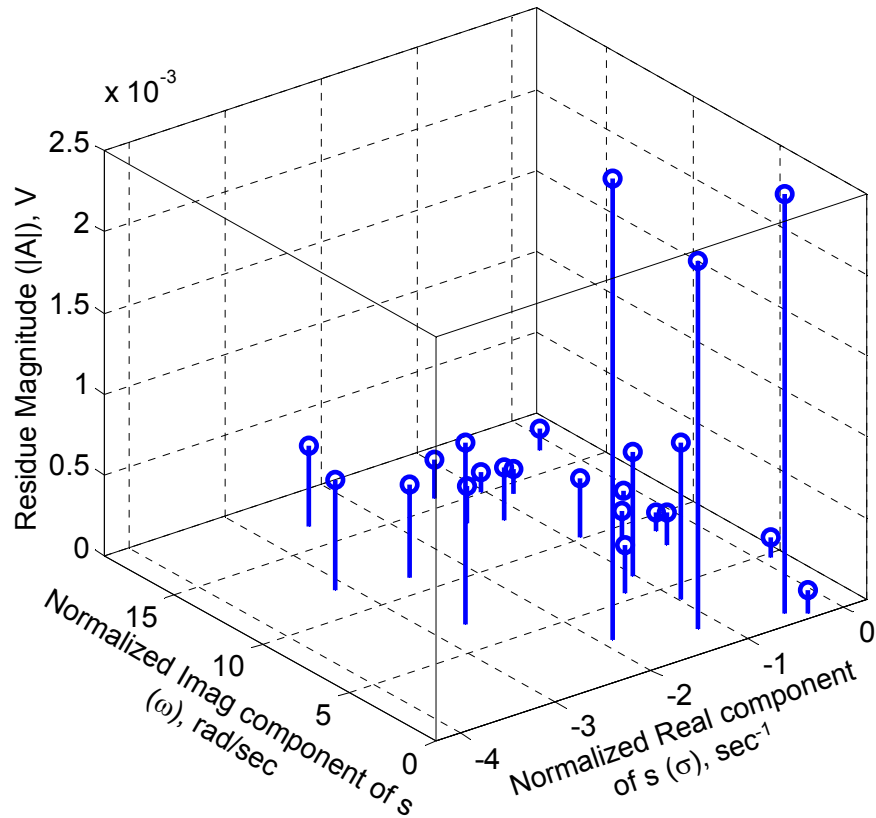


Figure 5.7 All 23 estimated complex poles and their corresponding residues used to characterize a 15.2 cm diameter hemisphere mounted over a ground plane. The s_{21} scatter parameter measured with VNA-HP8510 was used to compute the complex poles using the Matrix Pencil Method (MPM) of Section 4.1.3. The real and imaginary axes are normalized by the factor $g = a/c \log_e 10$, where a is the sphere radius and c is the speed of light.

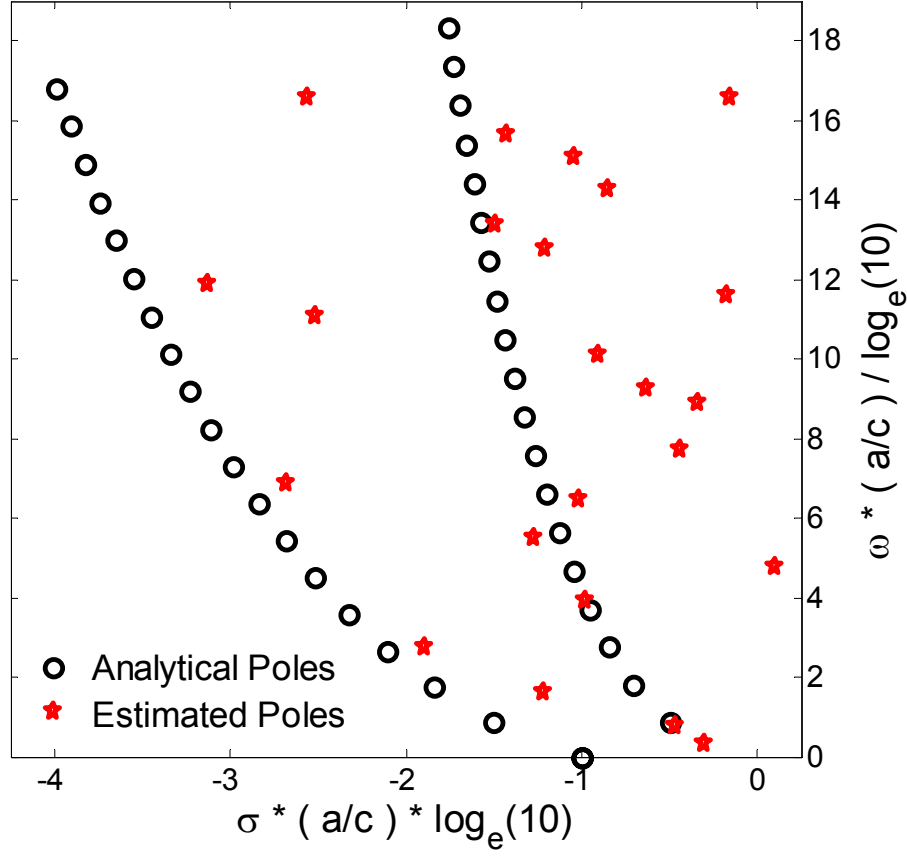


Figure 5.8 All 23 estimated complex poles of a 15.2 cm diameter hemisphere mounted over a ground plane for Scenario # 1 compared to the poles of a conducting sphere analytically determined from (5.18) [4].

5.3.1 Dominant Complex Poles based on Residue Magnitude

Using dominant poles based on the residue magnitude or the pole energy prevents selecting and comparing spurious poles to the actual poles. Dominant poles s_D based on the magnitude of residues are selected by choosing the complex pole-pairs with their corresponding residues above a threshold as given by

$$s_D = s(A_s > A_{Threshold}) \quad (5.20)$$

where $s = \sigma + j\omega$ is the complex pole, operation $[\cdot]^*$ indicates complex conjugation and $A_{Threshold}$ indicates the magnitude threshold chosen to determine the dominant poles. Figure 5.9 shows the dominant complex poles of a 15.2 cm diameter hemisphere over a ground plane having the magnitude of the corresponding residues greater than a threshold of $A_{thresh} = 8e^{-4}$. Note that only

five dominant poles based on the residue magnitude are sufficient to represent the response of a conducting sphere in free space or a hemisphere over a ground plane.

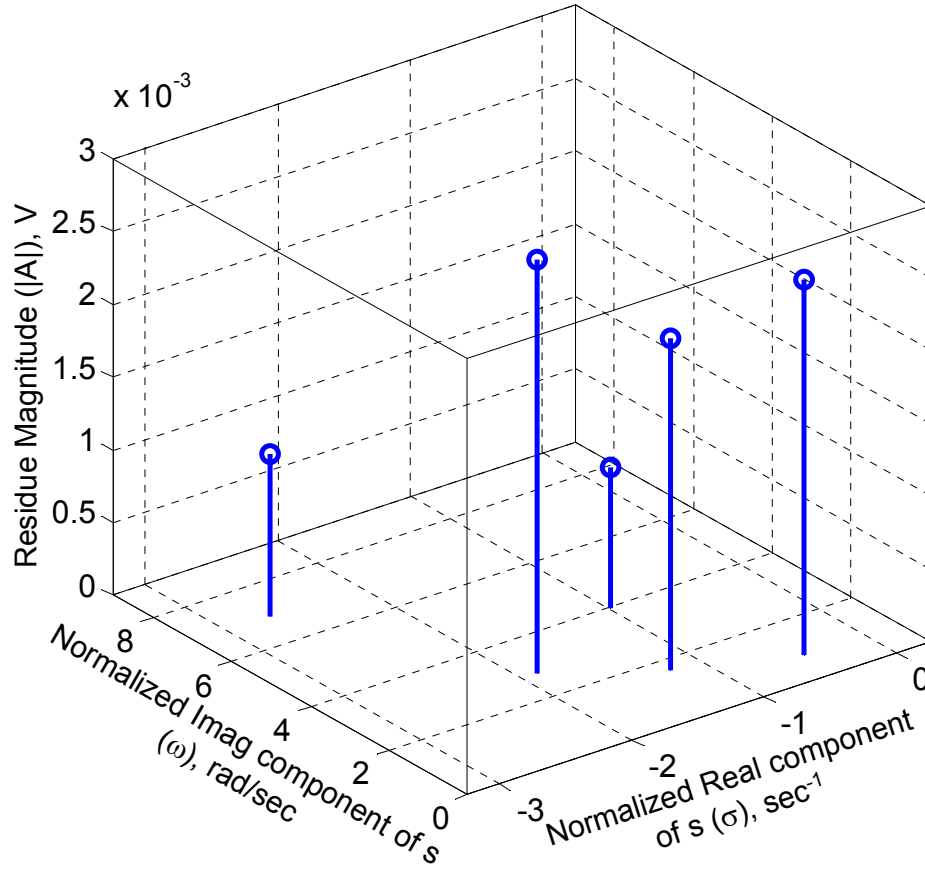


Figure 5.9 The dominant complex poles of a 15.2 cm diameter hemisphere over a ground plane selected from poles in Fig. 5.8 for residue magnitudes greater than a threshold of $A_{thresh} = 8e^{-4}$. The real and imaginary axes are normalized by the factor $g = a/c \log_e 10$, where a is the sphere radius and c is the speed of light.

5.3.2 Dominant Complex Poles based on Pole Energy content

Dominant poles s_D based on the energy content of the poles are selected by choosing the complex pole-pairs with their corresponding energy above a threshold given by

$$s_D = s \left(\int_{t=0}^{\infty} \left| A_s e^{(\sigma+j\omega)t} + A_s^* e^{(\sigma-j\omega)t} \right|^2 dt > E_{Threshold} \right) \quad (5.21)$$

where $E_{Threshold}$ indicates the energy threshold chosen to determine the dominant poles. The upper time limit for integration is limited by the finite duration of the measured scatterer response.

Figure 5.10 shows the dominant poles selected based on their energy content greater than a threshold of $E_{Threshold} = 1e^{-4}$.

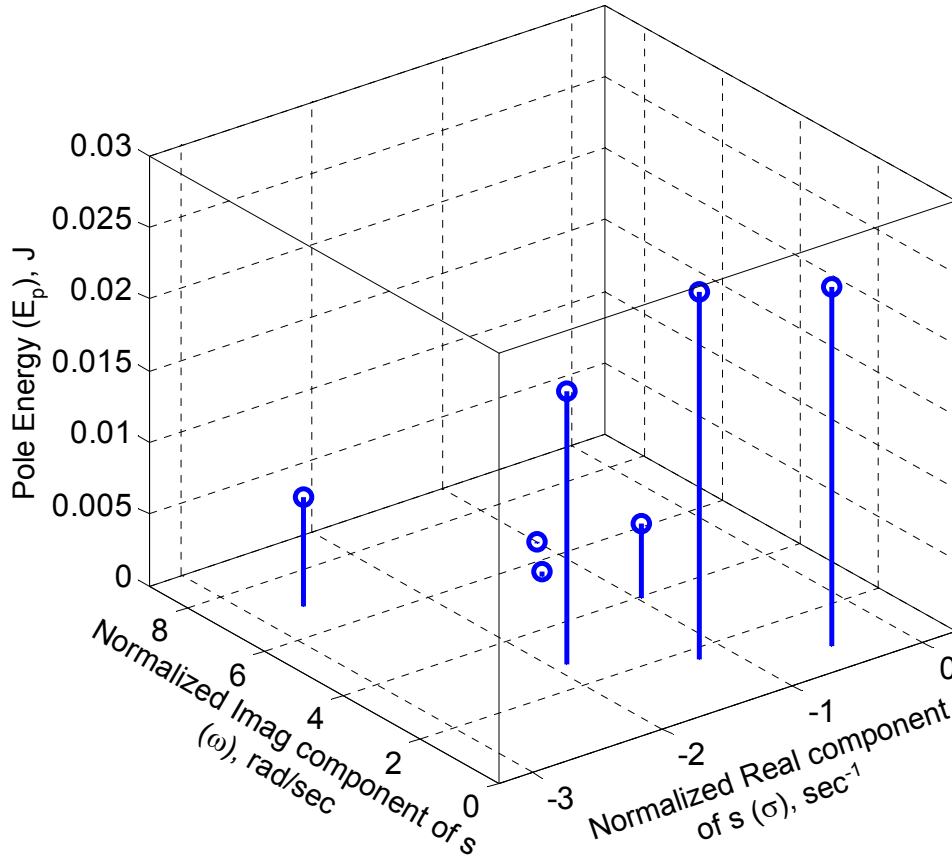


Figure 5.10 The dominant complex poles of a 15.2 cm diameter hemisphere over a ground plane selected from the poles in Fig. 5.8 for energy greater than a threshold of $E_{Threshold} = 1e^{-4}$. The real and imaginary axes are normalized by the factor $g = a/c \log_e 10$, where a is the sphere radius and c is the speed of light.

Note that there are 5 poles selected based on the residue magnitude and 7 poles selected based on the pole energy criteria. Thus, this section presents an overview of the dominant pole selection process using a sample measurement of a 15.2 cm diameter hemisphere over a ground plane. The scatter response validation is presented in the next section where these dominant poles are compared to the analytically determined poles.

5.4 Scatter Response Validation using Canonical Sphere

In this section, the dominant natural resonances (complex poles) of conducting spheres, selected based on the criteria presented in the previous section, are compared to the analytical complex poles described in Section 5.1.1. The scatter-signature comparison in terms of pole-position in the s-plane is first demonstrated for the hemisphere over a ground plane in Section 5.4.1. In Section 5.4.2, the complex-pole position is compared for the spheres of various sizes inside an anechoic chamber.

5.4.1 Conducting Hemisphere over a Ground-Plane

In this sub-section, the scatter signature in terms of dominant pole-position in the s-plane, extracted from the measured impulse response of a 15.2 cm diameter hemisphere mounted over a ground plane, is compared to the analytically derived pole-positions. The comparison of pole-position in the s-plane between the measured poles normalized by the factor $a/c \log_e 10$ and the analytical poles is shown in Fig. 5.11. Only the dominant measured poles based on the residue magnitude and energy criteria are compared with the theoretically determined poles.

Note that the measured dominant complex poles offer a reasonably accurate match to the analytically determined poles. The dominant complex poles allow characterization of the scatterer response using fewer parameters: 5 pairs of complex conjugate poles based on the magnitude of their corresponding residues and 7 pairs of complex conjugate poles based on their energy content.

The dominant measured complex poles also model the late-time response of the scattered field from the hemisphere with reasonable accuracy as seen in Fig. 5.12. However, the accuracy of the time-domain impulse response characterization is reduced as seen in Fig. 5.12, which compares the measured late-time response of a 15.2 cm diameter hemisphere over a ground plane for the estimated response using all the 23 pairs of complex conjugate poles to the estimated response using the 5-pairs of dominant complex poles based on the magnitude of the residues and the estimated response using the 7-pairs of dominant complex poles based on their energy content. In the remainder of this dissertation, dominant complex conjugate poles will be used to characterize the resonant dispersion from scatterers because it allows fairly accurate characterization of the scatterer response using fewer parameters.

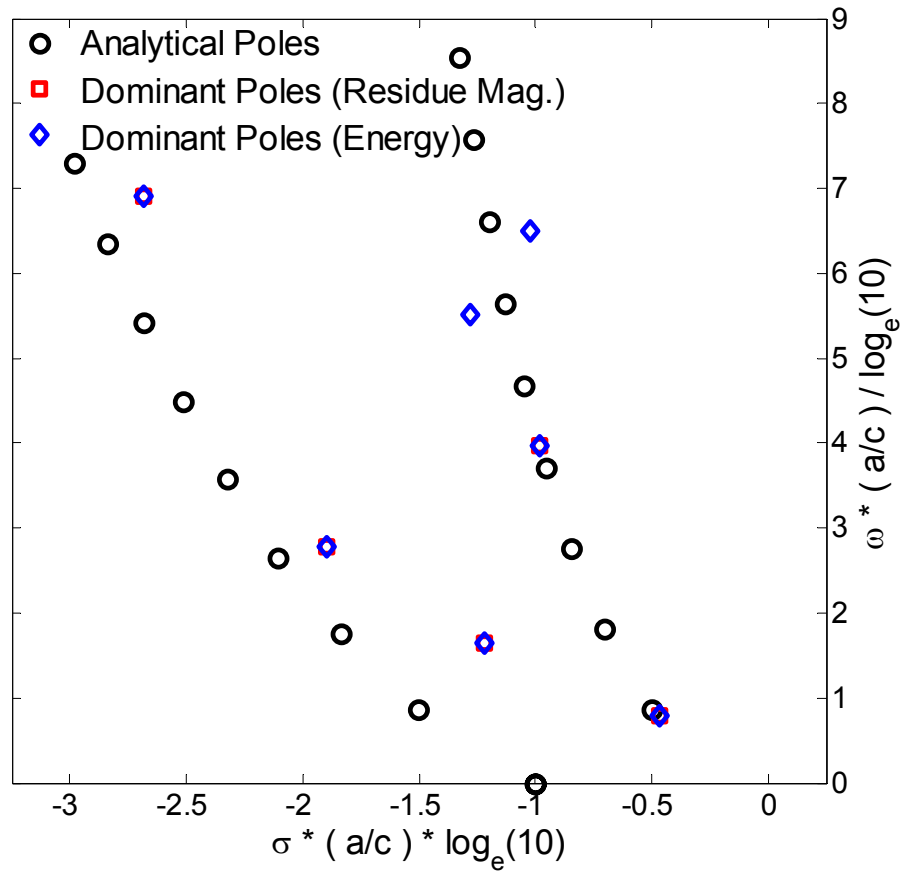


Figure 5.11 Comparison of scatter signature in terms of complex-pole position in the s-plane between the dominant measured poles of a 15.2 cm (6-inch) hemisphere over a ground plane in Scenario # 1 normalized by the factor $g = a/c \log_e 10$ and the analytical poles obtained by solving (5.6) and (5.7). The dominant poles are based on the magnitude of the residue (square) and the energy content (star).

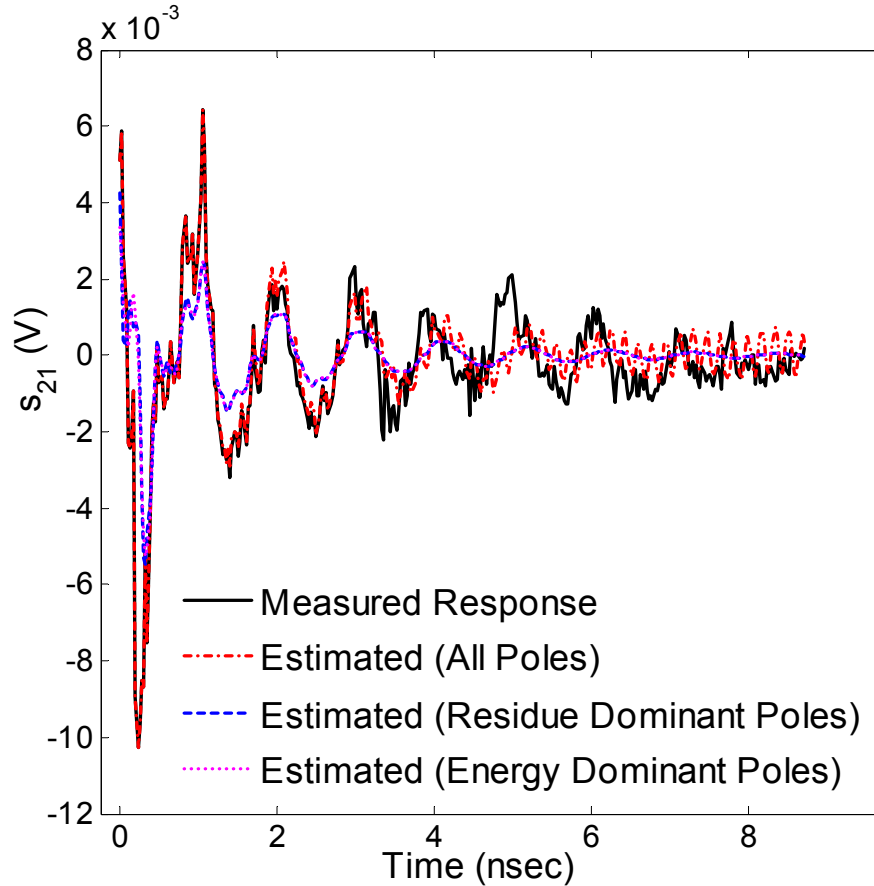


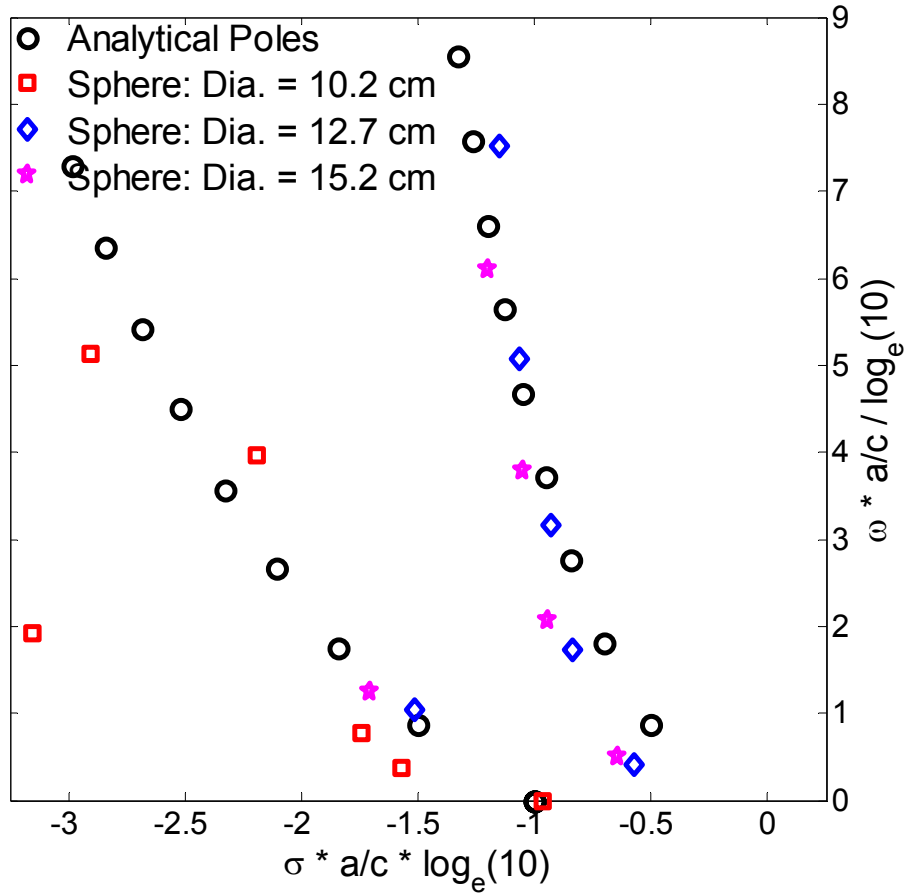
Figure 5.12 Measured (solid) and estimated late-time impulse response of a 15.2 diameter hemisphere over a ground plane using all poles (dash-dot), dominant poles based on the magnitude of the residues (dash), and dominant poles based on the energy content (dotted)

5.4.2 Conducting Spheres inside an Anechoic Chamber

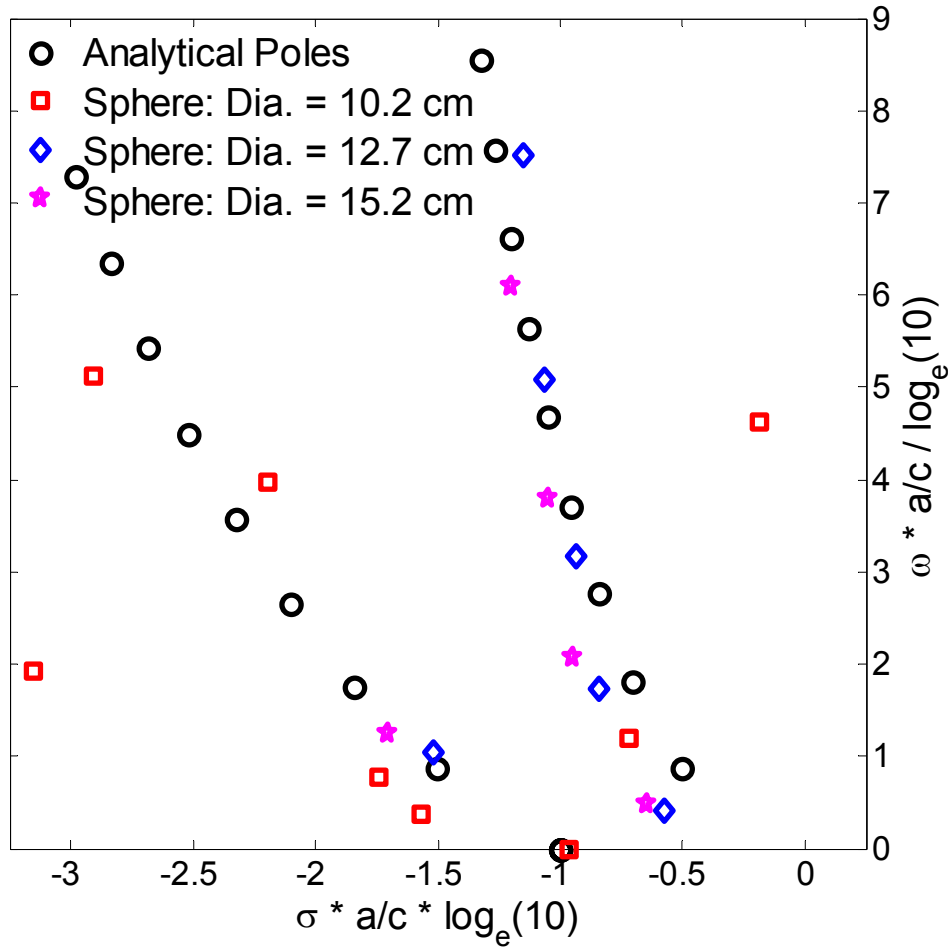
The dominant poles extracted from the measured impulse response of 10.2 cm (4 inch), 12.7 cm (5 inch) and 15.2 cm (6 inch) diameter conducting spheres inside an anechoic chamber matched the analytical scatter signature of a conducting sphere in terms of pole-position in the s -plane. A comparison between the measured poles normalized by the factor $a/c \log_e 10$ and the analytical poles is shown in Fig. 5.13 (a) for dominant poles determined based on the residue magnitude and in Fig. 5.13 (b) for dominant poles determined based on the energy content.

The dominant measured poles of the first branch for each conducting sphere with a different diameter offer a reasonably close match to the first branch of analytically determined complex poles determined from (5.7). A comparison between the second branch of measured

poles and the analytical poles showed a close match for low frequency poles with some deviation for higher frequency poles. The deviation of the measured complex poles can be attributed to higher noise levels and lower signal-to-noise ratios at higher frequencies [6-8].



(a) Dominant poles selected based on the magnitude of the residue



(b) Dominant poles selected based on the energy content

Figure 5.13 Comparison of scatter signature in terms of complex-pole position in the s-plane between the measured dominant poles of 10.2 cm, 12.7 cm and 15.2 cm diameter conducting spheres inside an anechoic chamber in Scenario # 2 normalized by the factor $g = a/c \log_e 10$ and the analytical poles obtained by solving (5.6) and (5.7). The dominant poles are selected based on the magnitude of the residue (5.20) and the energy content (5.21).

5.4.3 Conducting Sphere inside an Indoor Hallway Environment

The measured time-domain response of a 15.2 cm (6 inch) diameter metallic sphere inside an indoor hallway (Scenario # 3) was analyzed using the MPM and the dominant poles were extracted based on (5.20) and (5.21). These dominant poles based on the residue magnitude and the pole-energy content matched the analytical scatter signature of a conducting sphere in terms of pole-position in the s-plane. A comparison between the measured poles normalized by the

factor $a/c \log_e 10$ and the analytical poles is shown in Fig. 5.14 for both types of dominant poles determined based on the residue magnitude and the energy content.

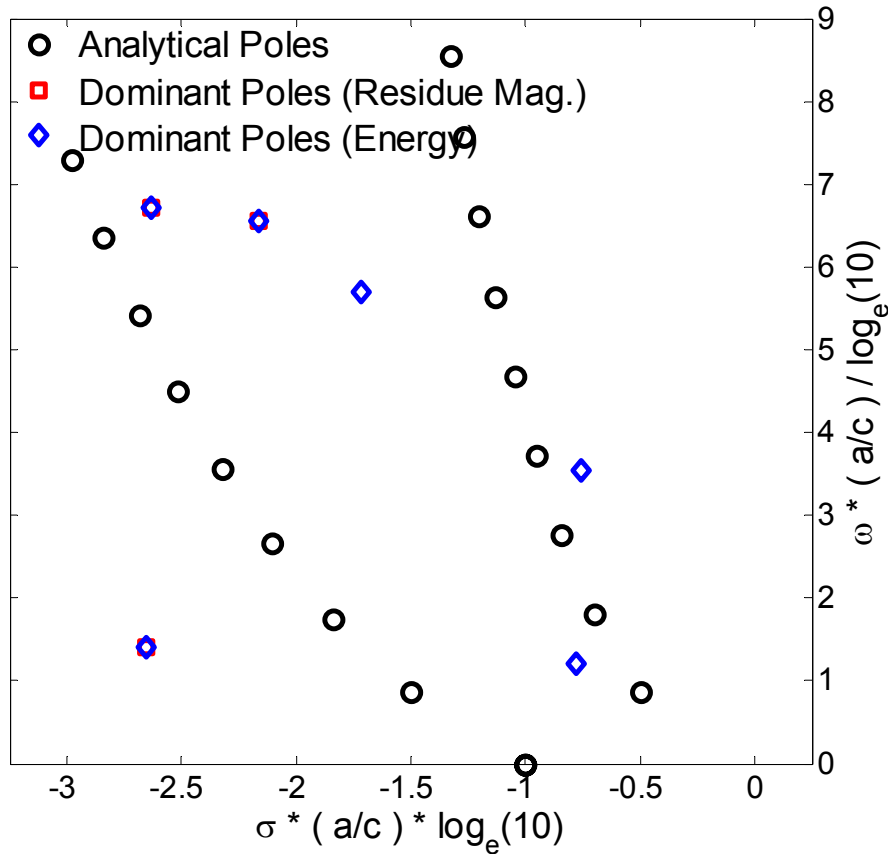


Figure 5.14 Comparison of scatter signature in terms of complex-pole position in the s-plane between the measured dominant poles of 15.2 cm diameter conducting sphere inside an indoor hallway (Scenario # 3) normalized by the factor $g = a/c \log_e 10$ and the analytical poles obtained by solving (5.6) and (5.7). The dominant poles are selected based on the magnitude of the residue (5.20) and the energy content (5.21).

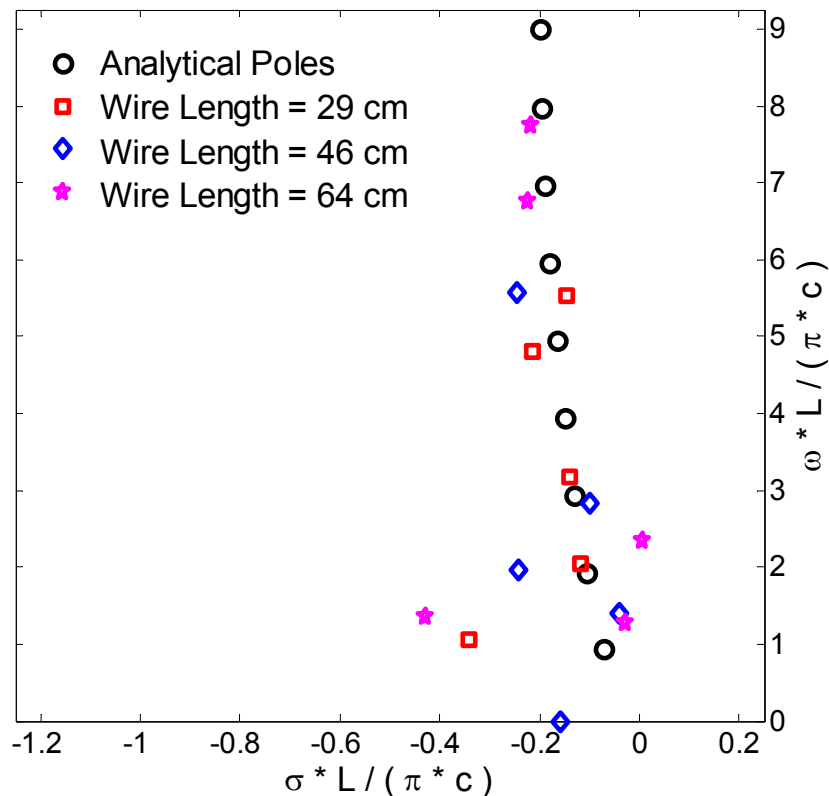
The dominant measured poles of the first branch for each conducting sphere with a different diameter offer a close match to the first branch of analytically determined complex poles. Significant deviation from the actual pole position is observed compared to the previous two cases of hemisphere over a ground-plane and spheres inside an anechoic chamber. The available signal-to-noise ratios (SNR) from this setup are poor due to losses in the cable and due to unavoidable scattering from the floor, ceiling and the walls. The beginning of the late time and the duration of sphere response were chosen to avoid reflections from the hallway structures.

5.5 Scatter Response Validation using Thin Wire Scatterers

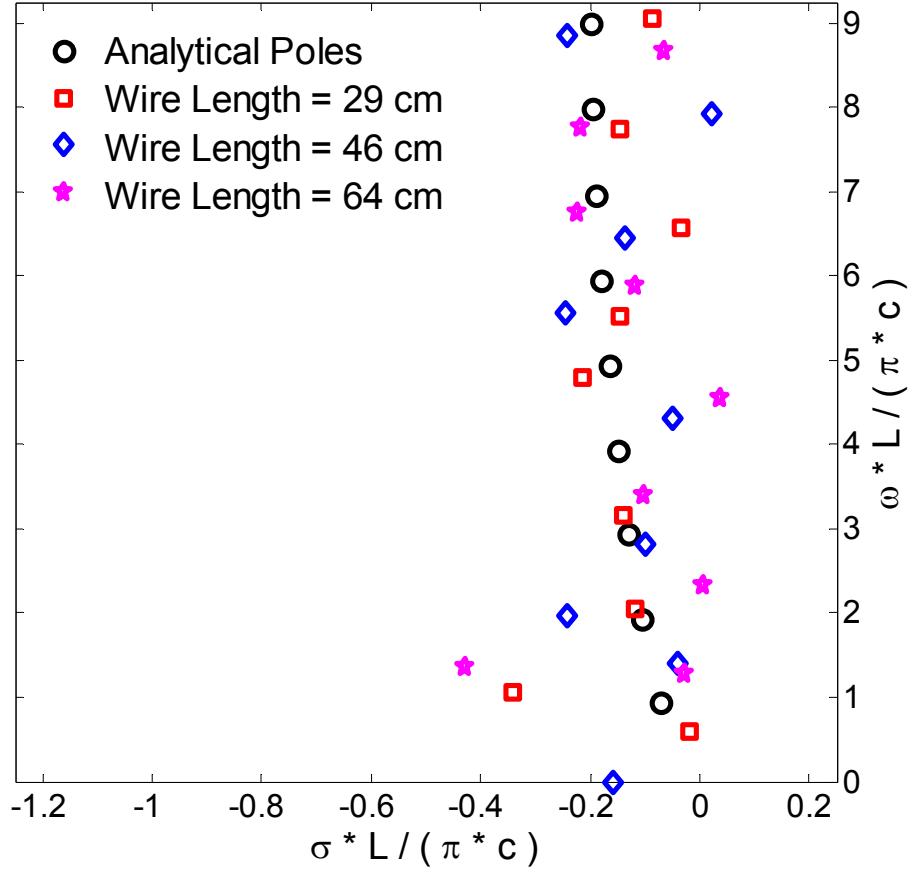
In this section, the dominant natural resonances (complex poles) of thin wire scatterers, selected based on the criteria of (5.20) and (5.21), are compared to the analytical complex poles of a thin wire scatterer described in Section 5.1.2. The scatter-signature comparison in terms of pole-position in the s-plane is first demonstrated for thin wires of various lengths inside an anechoic chamber in Section 5.5.1. In Section 5.5.2, the complex-pole position is compared for a thin wire of length 13 cm inside an indoor hallway environment.

5.5.1 Thin Wire Scatterer Inside an Anechoic Chamber

In this sub-section, the scatter signature in terms of dominant pole-position in the s-plane, extracted from the measured time-domain response normalized by the factor $L / (\pi \bullet c)$ of thin wire scatterers of lengths 29 cm, 46 cm, and 64 cm are compared to the analytically derived pole-positions in Fig. 5.15.



(a) Dominant poles selected based on the magnitude of the residue.



(b) Dominant poles selected based on the energy content.

Figure 5.15 Comparison of scatter signature in terms of complex-pole position in the s-plane between the measured dominant poles of 29 cm, 46 cm and 64 cm length thin wire scatterers inside an anechoic chamber in Scenario # 2 normalized by the factor $h = L / (\pi \bullet c)$ and the analytical poles obtained by solving (5.18). The dominant poles are selected based on the magnitude of the residue (5.20) and the energy content (5.21).

Figure 5.15 (a) plots dominant poles determined based on the residue magnitude as given by (5.20) using a threshold of $A_{thresh} = 8e^{-4}$. Similarly, Fig. 5.15 (b) plots dominant poles determined based on the energy content as given by (5.21) using a threshold of $E_{threshold} = 1e^{-4}$. Note that only the first branch is observed because the high damping coefficient for higher branches leads to poles with less energy content. The dominant measured poles offer a reasonably close match to the first branch of analytically determined complex poles.

5.5.2 Thin Wire Scatterer inside an Indoor Hallway Environment

The dominant poles extracted from the measured time-domain response of a 27 cm length thin wire scatterer inside an indoor hallway scenario matched the analytical scatter signature of a conducting sphere in terms of pole-position in the s-plane. A comparison between the measured poles normalized by the factor $L / (\pi \bullet c)$ and the analytical poles is shown in Fig. 5.16 for both types of dominant poles determined based on the residue magnitude and the energy content. Again only the first branch is observed with the estimated dominant poles offering a good match to the analytically determined poles. The available signal-to-noise ratios (SNR) from this setup are poor resulting in significant deviation from the actual pole position compared to the measured results from an anechoic chamber.

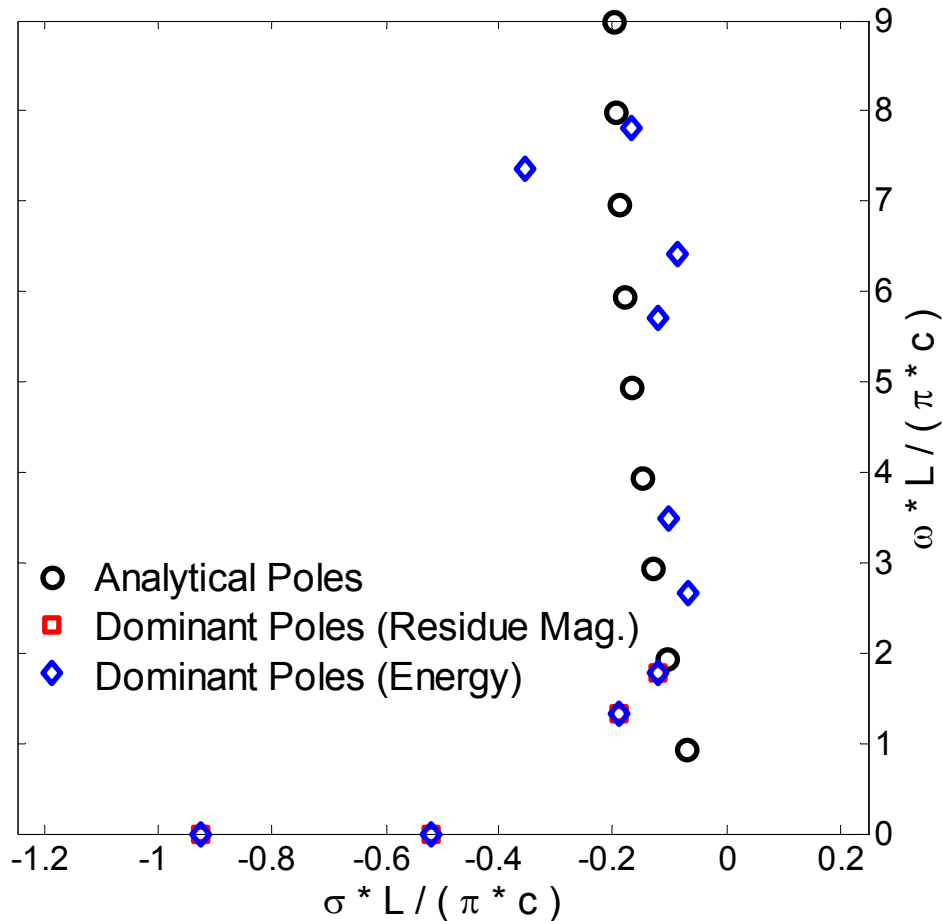


Figure 5.16 Measured dominant complex poles of a 27 cm length thin wire scatterer of thickness 0.125 inch inside an anechoic chamber

5.6 Chapter Summary

In support of the proposed pole-dispersion channel model for ultra-wideband communication systems, this chapter validates the pole-residue dispersion characterization from scatterer response, which is modeled using the Singularity Expansion Method (SEM). The pole-residue dispersion characteristics of scatterer response are validated through comparison of the estimated complex-pole positions from measured data and the complex-pole positions available analytically for two types of canonical objects: a conducting sphere and a thin wire scatterer. Some important observations include:

- A simplified and approximate method for determining the analytical expressions for pole-residue characterization of a conducting sphere and a thin wire scatterer are briefly discussed; see Section 5.1.
- Three types of experiment setups are used to measure responses of canonical structures for ultra-wideband pulse excitation; see Table 5-1 and Section 5.2.
- Dominant poles based on the magnitude of residues and the energy content are selected and compared to the theoretically determined poles; see Section 5.3. The dominant pole selection process prevents selecting and comparing spurious poles to the theoretical poles.
- The scatter response from the canonical sphere is validated using all the three sets of experiments: first with a conducting hemisphere over a ground plane, second with conducting spheres of various radii inside an anechoic chamber, and third using a single sphere in a hallway environment; see Section 5.4.
- The scatter response from thin wire scatterer is validated using two sets of experiments: one with thin wires of various length and thickness inside an anechoic chamber and the other with a thin wire in a hallway environment as part of an actual indoor communication scenario; see Section 5.5.
- The dominant measured poles for a conducting hemisphere, spheres of various sizes and thin wire scatterers of various lengths provided a reasonably close match to the analytically determined complex poles; see Fig. 5.11 to 5.16.

Validated scatterer responses pave way for advances in the statistical characterization of the pole-residue dispersion parameters.

References

- [1] C. E. Baum, "On the Singularity Expansion Method for the Solution of Electromagnetic Interaction Problems," *Interaction Notes #88, AFRL Directed Energy Directorate*, Dec. 1971.
- [2] C. E. Baum, E. J. Rothwell, K. M. Chen, and D. P. Nyquist, "The singularity expansion method and its application to target identification," *Proceedings of the IEEE*, vol. 79 (10), pp. 1481-1492, Oct. 1991.
- [3] G. Mie, "Beitra ge zur Optik truber Medien, speziell kolloidaler Metallo sungen," *Annals of Physics*, vol. 25 (3), pp. 377-445, [An English translation is available as G. Mie, "Contributions to the optics of turbid media, particularly of colloidal metal solutions," Royal Aircraft Establishment Library, Her Majesty's Stationery Office, London, Feb. 1976], Mar. 1908.
- [4] K. M. Chen and D. Westmoreland, "Impulse Response of a Conducting Sphere Based on Singularity Expansion Method," *Proceedings of the IEEE*, vol. 69 (6), pp. 747 - 750, June 1981.
- [5] J. Cordaro and W. Davis, "Time-domain techniques in the singularity expansion method," *IEEE Transactions on Antennas and Propagation*, vol. 29 (3), pp. 534-538, Mar. 1981.
- [6] A. Poggio, M. VanBlaricum, E. Miller, and R. Mittra, "Evaluation of a processing technique for transient data," *IEEE Transactions on Antennas and Propagation*, vol. 26 (1), pp. 165-173, Jan. 1978.
- [7] Y. Hua and T. K. Sarkar, "Matrix pencil method for estimating parameters of exponentially damped/undamped sinusoids in noise," *IEEE Transactions on Acoustics, Speech, and Signal Processing*, vol. 38 (5), pp. 814-824, May 1990.
- [8] D. A. Ksienski and T. M. Willis, "Numerical Methods of Noise Reduction for Frequency Domain SEM," *Mathematics Notes #81, AFRL Directed Energy Directorate* Oct. 1984.
- [9] W. H. Beyer, *CRC Standard Mathematical Tables and Formulae*, 29th ed., pp. 416-425, Boston: CRC Press, 1991.
- [10] R. F. Harrington, *Time Harmonics Electromagnetics*. New York: McGraw-Hill, 1961.
- [11] M. A. Morgan and B. W. McDaniel, "Transient electromagnetic scattering: data acquisition and signal processing," *IEEE Transactions on Instrumentation and Measurement*, vol. 37 (2), pp. 263-267, June 1988.
- [12] R. Weyker and D. Dudley, "Identification of resonances of an acoustically rigid sphere," *IEEE Journal of Oceanic Engineering*, vol. 12 (2), pp. 317-326, Apr. 1987.

- [13] G. C. Gaunaurd, H. Uberall, and A. Nagl, "Complex-frequency poles and creeping-wave transients in electromagnetic-wave scattering," *Proceedings of the IEEE*, vol. 71 (1), pp. 172-174, Jan. 1983.
- [14] J. M. Pond, "Determination of SEM Poles from Frequency Responses," *Interaction Notes #408, AFRL Directed Energy Directorate*, July 1981.
- [15] K. S. Cho and J. T. Cordaro, "Calculation of the Singularity Expansion Method Parameters from the Transient Response of a Thin Wire," *Interaction Notes #379, AFRL Directed Energy Directorate*, Sept. 1979.
- [16] K. Mei, "On the integral equations of thin wire antennas," *IEEE Transactions on Antennas and Propagation*, vol. 13 (3), pp. 374-378, Mar. 1965.
- [17] F. Tesche, "On the analysis of scattering and antenna problems using the singularity expansion technique," *IEEE Transactions on Antennas and Propagation*, vol. 21 (1), pp. 53-62, Jan. 1973.

This page intentionally left blank.

Chapter 6 – Fuzzy Pole Characterization of Scatterer Response

Time-domain characterization based on the Singularity Expansion Method (SEM) has been a popular approach to model scatterer-response for ultra-wideband ground penetration radar (UWB-GPR) [1] and target identification [2, 3]. Recently, the SEM approach has also found widespread acceptance in tumor detection [4-6] by representing the time-domain response of malignant tumors in terms of complex poles. However, noise limits achievable benefits for these applications. Early research in SEM emphasized the accuracy of various extraction methods and techniques for noisy time-domain data [7-9]. So far, the singular value decomposition (SVD) is the only approach used to reduce the effect of noise and to represent complex poles in the presence of noise with a small number of equivalent poles [10].

This chapter presents an alternate approach to the pole-residue dispersion characterization of scatterer response in terms of a small number of equivalent poles termed ‘fuzzy poles’. Analytical scatterer responses of a straight wire are analyzed for fuzzy characterization at various noise levels. Measured scatterer responses of a straight wire and a conducting sphere are evaluated to extract equivalent ‘fuzzy poles’. A modified fuzzy clustering approach is proposed as a solution to overcome the effect of noise, which has not been previously considered. The original contribution is the demonstration that the estimated fuzzy poles offer a close match to the actual poles determined from the simulated data for a thin wire scatterer. The time-domain response is analyzed using the Matrix Pencil Method (MPM) [11, 12] and the fuzzy poles are computed using the modified Unsupervised Optimal Fuzzy Clustering (UOFC) algorithm [13].

This chapter begins with a brief discussion of noise effects on the estimation of complex poles in Section 6.1. Some interesting observations on the estimated complex poles in the presence of noise are highlighted and analyzed. A comprehensive review of the UOFC algorithm is beyond the scope of this dissertation, but a brief introduction is presented in Section 6.2. The Fuzzy Hyper-Volume (F_{HV}) and the Partition Density (P_D) performance parameters are used to estimate the optimal number of fuzzy poles. Another original contribution is a modification of the UOFC algorithm to offer a closer match of the fuzzy poles to the actual poles using the pole energy. The modified UOFC algorithm and improvement in fuzzy pole representation are described in Section 6.3. Computed fuzzy poles for the simulated response of a thin wire scatterer for various noise levels are presented in Section 6.4. The measured time-domain response of a thin wire and a conducting sphere are analyzed using MPM and UOFC to estimate their respective fuzzy poles are also evaluated. Finally, Section 6.5 summarizes the important observations and contributions presented in this chapter.

6.1 Effect of Noise on Complex Pole Estimation

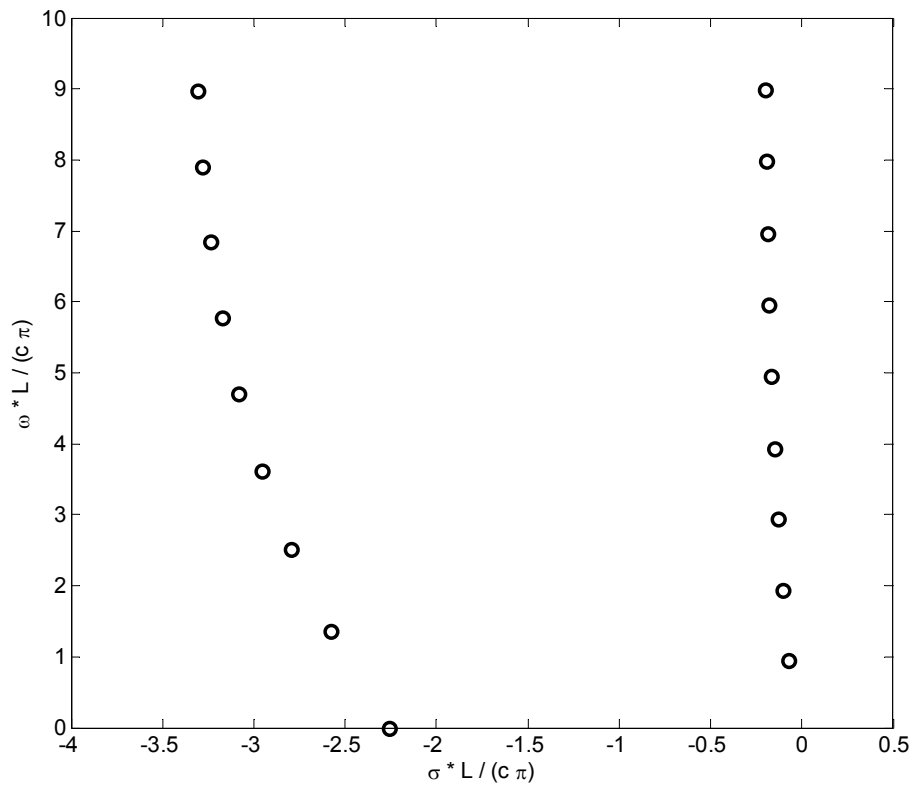
The singularity expansion method (SEM) permits representation of the late time response of a scatterer as a sum of complex exponentials. The complex poles, also known as the singularities and natural resonances, are indicative of the scatterer size and are used as a target signature in the complex s -plane. However, the application of SEM approach to target identification and classification has limited benefits due to the presence of noise. Low signal-to-noise ratios corresponding to high noise levels in measured scatterer response, especially at higher frequencies, result in spurious poles and deviation in the position of the poles in the complex s -plane [14]. Noise not only results in the estimation of spurious poles but also results in the estimation of incorrect values of corresponding residues. Percentage error in estimation of complex poles in a noisy environment is briefly discussed in [15]. Noise also makes it difficult to determine the actual number of poles needed to characterize the TD signature.

An analytically determined response for a thin wire scatterer is used to investigate the effect of noise on the estimated complex poles [16]. The thin wire scatterer considered for this example has a length L and a radius r such that $r/L = 0.01$. The parameters that describe the thin wire scatterer response to the incident pulse in the broadside direction are given in Table 6.1. The

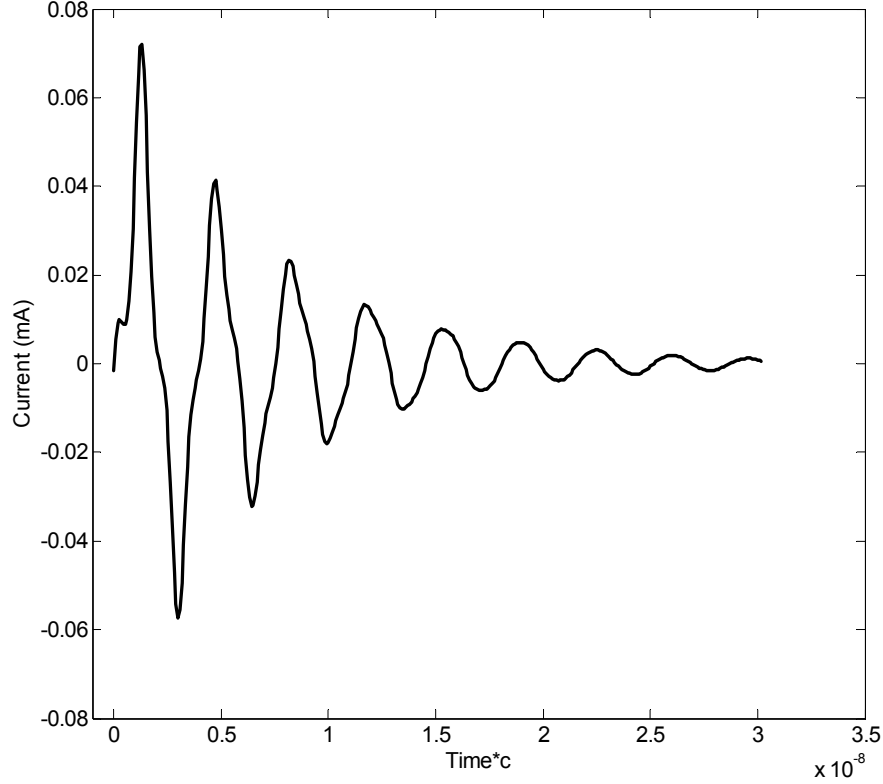
analytically determined complex poles for a thin wire scatterer are shown in Fig. 6.1(a) and the corresponding noiseless time-domain response determined from these complex poles is shown in Fig. 6.1(b).

Table 6-1 Thin Wire Scatterer Response Example

<i>Parameters</i>	<i>Value / Symbol</i>
Length	L
Radius	$r (= 0.01 \cdot L)$
Conductivity	∞
Incident Signal	Heavyside Pulse
Direction of Incidence	Broadside
Current distribution	Sinusoidal (thin wire approximation)



(a) Complex poles



(b) Time-domain response

Figure 6.1 Analytically determined complex poles and the corresponding noiseless time-domain response of the thin wire scatterer described in Table 6.1.

The energy of the analytically determined noiseless waveform is computed as an integral over a predefined time window. For discrete samples of the time-domain signal, the signal energy (E_s) is computed as a sum of squares of sample values with the lower limit corresponding to the beginning of the late time as

$$E_s = \int_{T_L}^{\infty} |y(t)|^2 dt \Rightarrow \sum_{k=1}^K |y(T_L + kT_S)|^2 \quad (6.1)$$

where $y(t)$ is the noisy time-domain response, K is number of samples (sufficiently large to capture the signal energy) and, T_S is the sample duration. Additive Gaussian noise with zero mean and variance σ_n^2 is added to the signal to study noise effects for a desired signal-to-noise ratio (SNR) given by

$$SNR = 10 \log_{10} \left[\frac{E_s}{\sigma_n^2} \right] dB \quad (6.2)$$

A noisy time-domain response of a thin wire scatterer corrupted with a noise level corresponding to 5 dB SNR is shown in Fig. 6.2. The $SNR = 5$ dB value is selected to demonstrate that complex poles cannot be reliably extracted using the Matrix Pencil extraction method (MPM). In fact, MPM can estimate the complex poles to a reasonable accuracy only for $SNR > 20\text{--}25$ dB [15]. The complex poles estimated using the MPM for a single snapshot of the noisy data with 5 dB SNR is shown in Fig. 6.3. The abscissa and the ordinate in Fig. 6.3 indicate the real and imaginary parts, respectively, of the estimated complex poles scaled by the factor $L/(c \cdot \pi)$, where L is the length of the thin wire scatterer and c is the speed of light.

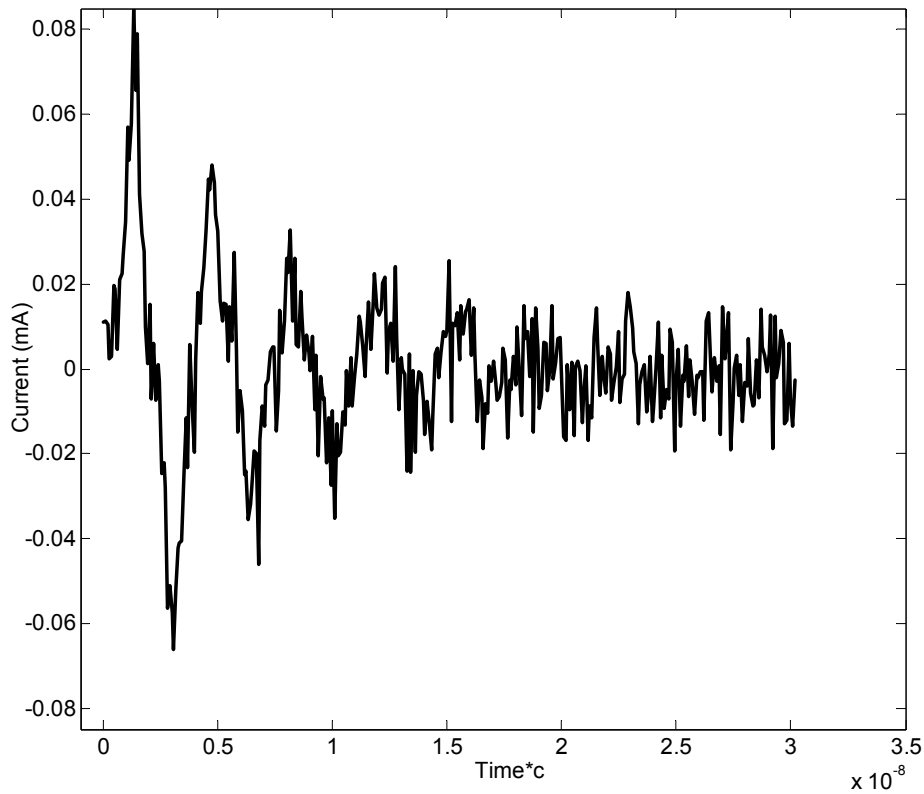


Figure 6.2 Time-domain response of the thin wire scatterer of Table 6.1 corrupted with a noise level corresponding to 5 dB SNR .

Note that the second and higher layers of complex poles are very difficult to estimate due to the large value of the corresponding damping coefficients (σ). The MPM is able to extract only the first layer of complex poles that dominates the time-domain response. Moreover, only the dominant lower-frequency poles are estimated with reasonable accuracy with significant estimation error for higher-frequency poles as seen by comparison to the analytical poles [17].

Fig. 6.3 demonstrates the limitation of MPM in estimating complex poles from a single realization with low SNR . To further support this conclusion, 91 realizations of the noisy TD response with 5 dB SNR were performed and, all the estimated poles using MPM are shown on the same plot in Fig. 6.4 and compared to the actual poles. The following phenomena are observed in Fig. 6.4(a):

- Pole positions in the s -plane deviate due to noise. For no noise conditions, i.e. $SNR > 70$ dB all the estimated poles exactly match to the analytical poles (not shown).
- An ensemble of spurious poles provides no information on the actual number of poles present. Fig. 6.4 shows dominant poles for each of the 91 realizations.
- The estimated residues corresponding to the spurious poles have incorrect values resulting in a poor match to the time-domain response (not shown).

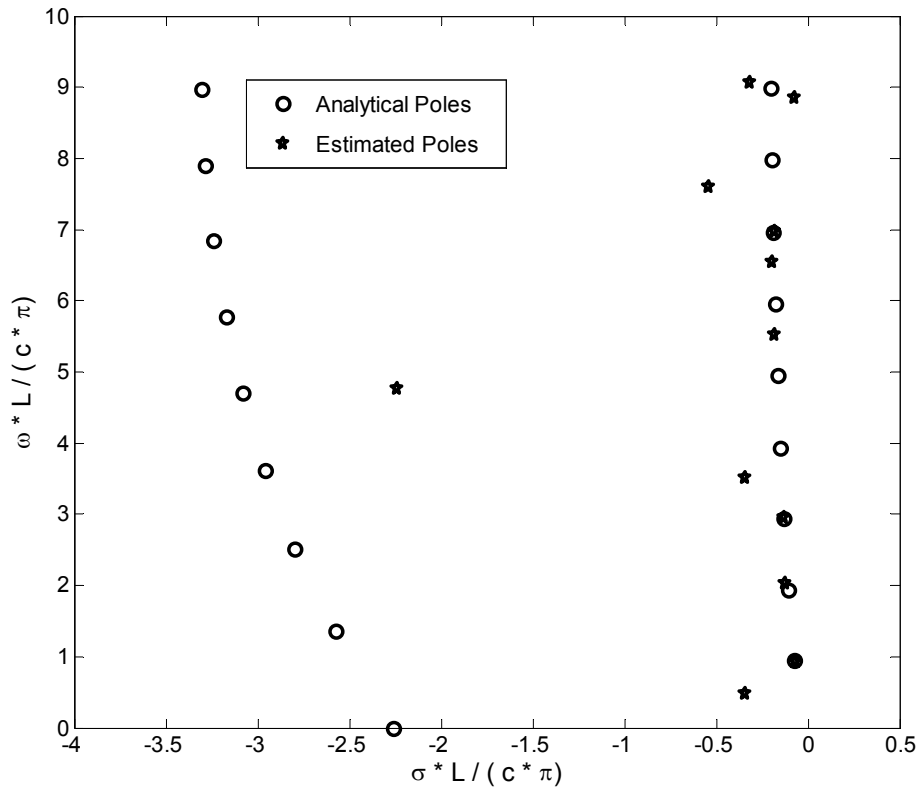
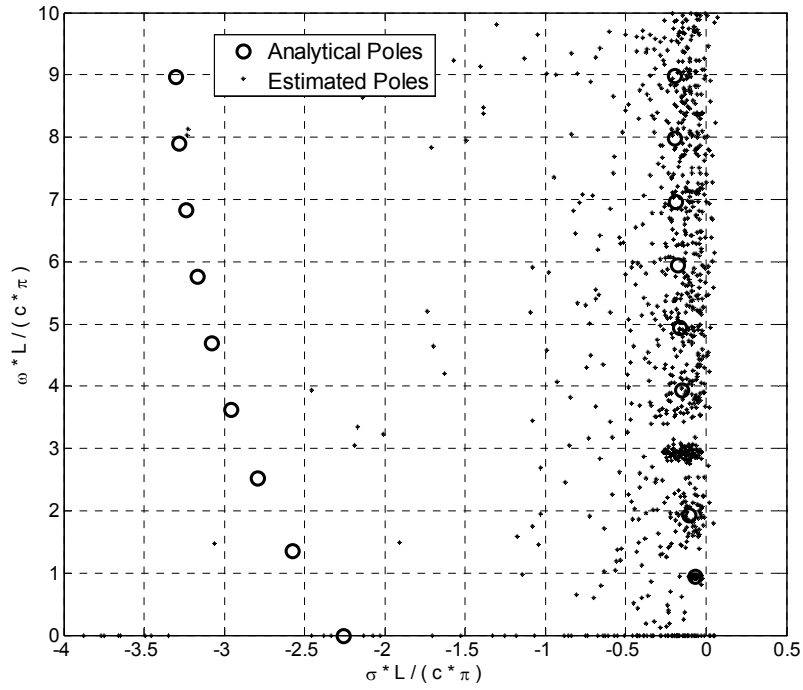
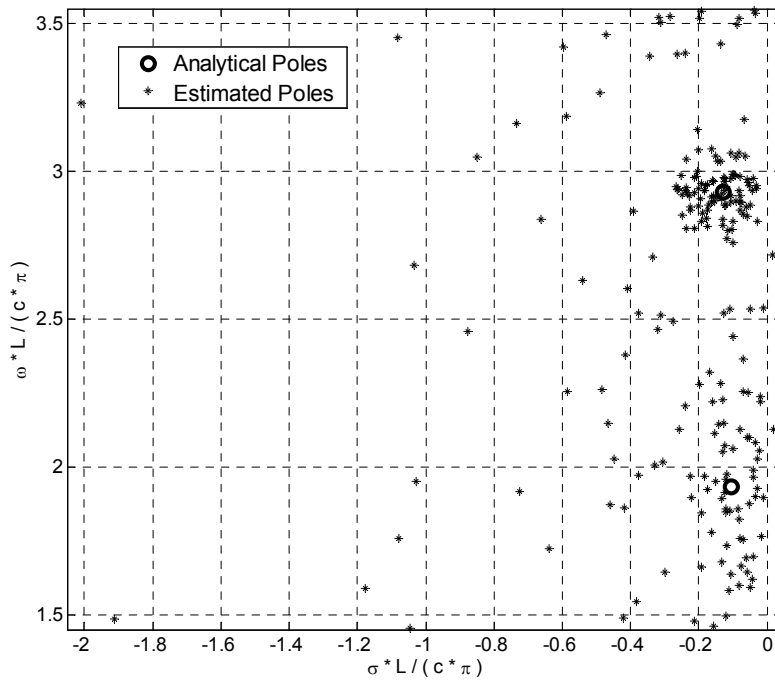


Figure 6.3 The estimated complex poles for a single snapshot of the noisy data with 5 dB SNR using the MPM for the thin wire scatterer of Table 6.1.



(a) Upper left s-plane view



(b) Zoomed view of (a)

Figure 6.4 The estimated complex poles for all the 91 snapshots or realizations of the noisy data with 5 dB SNR using the MPM for the thin wire scatterer of Table 6.1.

A close examination of Fig. 6.4(a) using the zoomed view as shown in Fig. 6.4(b) leads to following observations:

- The estimated complex poles for multiple realizations of a noisy time-domain response form clusters around the actual poles.
- The energy content of the poles within the cluster is nearly equal and reduces with distance from the cluster (not shown).

The above observations suggest a different approach in estimating the true complex poles in which each of the observed clusters is represented with corresponding cluster centroids. Hence, the problem of representing a noisy scatterer response with few poles reduces to determining the cluster centroids, also termed ‘fuzzy poles’. In the next section, the fuzzy poles are computed using the modified Unsupervised Optimal Fuzzy Clustering (UOFC) algorithm [18].

6.2 The Unsupervised Optimal Fuzzy Clustering (UOFC) Algorithm

The Unsupervised Optimal Fuzzy Clustering Algorithm belongs to a family of blind fuzzy clustering algorithms that do not require any a-priori information on the number of clusters present. The UOFC algorithm based on the performance parameter values estimates the number of cluster centers required to provide optimal representation. In order to optimize the cluster center representation, the UOFC algorithm combines two sub-algorithms [19]: (a) the Fuzzy K-Means (FKM) algorithm, and (b) the Fuzzy modification of Maximum Likelihood Estimation (FMLE) algorithm.

An overview of the proposed solution to the problem of representing a noisy scatterer response with cluster centers (‘fuzzy poles’) is shown in Fig. 6.5. It is assumed that the complex poles for multiple realizations are already computed. These estimated poles of a noisy scatterer response form a two-dimensional data set in the complex s -plane. The following steps summarize the approach to determining the fuzzy poles:

1. Compute the mean and standard deviation of the entire data set (all the two-dimensional complex pole vectors estimated for N realizations or repetitions, here $N = 91$).
2. Place the first cluster center at the mean position.

3. Place another cluster center several multiples of the computed standard deviation from the mean position. Ideally this cluster center position should be equidistant from all the data points.
4. Considering the given cluster center positions as a starting point, apply the FKM algorithm to provide initial estimates of the cluster centers (see Section 6.2.1).
 - a. First compute the membership function or values u_{kn} for all the estimated poles
 - b. Update the cluster center positions based on the data points and their new determined membership values
 - c. Iterate steps 4.a and 4.b until there is no perceptible change in the membership values
5. Use the cluster center positions computed by the FKM algorithm as initial estimates of the FMLE algorithm and refine the decision on fuzzy poles (see Section 6.2.2).
 - a. Initialize the exponential distance measures $d_e^2(c_k, x_n)$ equal to the final Euclidean distances $d^2(c_k, x_n)$ computed by the FKM algorithm.
 - b. Compute the posterior probability $h(k/x_n)$
 - c. Compute the a-priori probability P_k
 - d. Compute the exponential distance measures $d_e^2(c_k, x_n)$ for each of the estimated complex poles and clusters.
 - e. Update the cluster center positions based on the data points and their new determined posterior probabilities
 - f. Iterate steps 5.b to 5.e until there is no perceptible change in the posterior probability values
6. Compute and store the performance parameters namely (a) the Fuzzy Hyper Volume (F_{HV}), and (b) the Partition Density (P_D).
7. Repeat steps 3 to 6 up to a chosen upper limit of cluster centroids or fuzzy poles.

The Fuzzy K-Means (FKM) algorithm is the cornerstone of the entire solution. The following subsection briefly discusses the FKM algorithm.

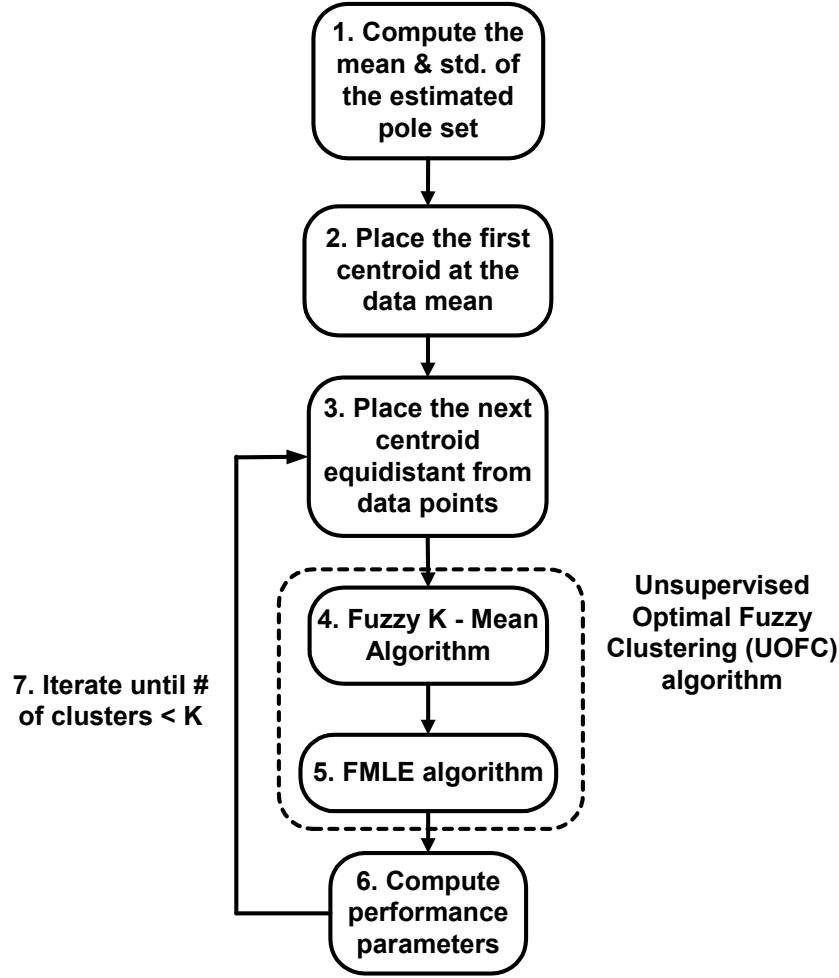


Figure 6.5 A flow diagram of the proposed solution to the problem of representing a noisy scatterer response with cluster centroids (‘fuzzy poles’) using the Unsupervised Optimal Fuzzy Clustering (UOFC) algorithm.

6.2.1 Fuzzy K–Means (FKM) Algorithm

The Fuzzy K-Means (FKM) algorithm is the main clustering algorithm that partitions the 2-D estimated poles in the complex s -plane into clusters. The Fuzzy K-Means algorithm seeks to minimize a least-square cost function given by the following expression by choosing the cluster centroids $[c_k]$ [17]:

$$J_q(U, [c_k]) = \sum_{n=1}^{N_d} \sum_{k=1}^{N_c} u_{kn}^q d^2(c_k, x_n) \quad (6.3)$$

where the exponent q can have a value > 1 (here chosen as 2), N_d and N_c are the number of data points and the number of clusters, respectively. The objective is to minimize the sum of the

product of Euclidean distance between the estimated poles & the fuzzy centroids $d^2(c_k, x_n)$ and the membership values u_{kn} ($0 \leq u_{kn} \leq 1$). In fuzzy analysis, each data point is given a membership value with respect to each of the clusters. If the membership value of a data point for a given cluster is close to unity – it indicates that the data point strongly belongs to the given cluster [18, 19]. And similarly, membership values close to zero indicate that the data point is less likely to belong to the given cluster. Hence, membership values in a fuzzy analysis indicate a soft measure of partitioning.

The first step is to choose the initial cluster center values, which were determined using the first three steps illustrated in Fig. 6.5. The next step (Step 4.a) is to apply FKM algorithm that first computes the membership function or values u_{kn} for all the estimated poles given by the following expression [19]:

$$u_{kn} = \frac{[d^2(c_k, x_n)]^{-1/(q-1)}}{\sum_{k=1}^{N_c} [d^2(c_k, x_n)]^{-1/(q-1)}} \quad 0 \leq u_{kn} \leq 1 \quad (6.4)$$

Note that these membership values are a function of distance only. Later in Section 6.3, the energy of the estimated poles will be included. Once the membership values are known, the next step (Step 4.b) is to update the cluster center positions based on the data points and their membership values given by [19]:

$$c_k = \frac{\sum_{m=1}^{N_d} u_{km}^q \cdot x_m}{\sum_{m=1}^{N_d} u_{km}^q} \quad \text{for } k = 1, 2, \dots, N_c \quad (6.5)$$

The process of determining the membership values and the cluster centroids is iterated until the increment change in the membership values is small as given by

$$\max_{kn} = |u_{kn}^i - u_{kn}^{i-1}| < \varepsilon \quad (6.6)$$

where u_{kn}^i indicates the membership values at the i^{th} iteration. Thus, the FKM algorithm iteratively searches for fuzzy poles by minimizing a cost function as in a constrained optimization problem. These estimates of the fuzzy poles are used as initial conditions by the FMLE algorithm to refine the decision. The next section briefly outlines the FMLE algorithm.

6.2.2 Fuzzy modification of the Maximum Likelihood Estimation (FMLE)

The FMLE algorithm is very robust to the variations in the number of clusters and the cluster densities. It is a non-linear algorithm that can become unstable if it does not have “good” initial estimates. Hence, the final estimates of the fuzzy poles as calculated by the FKM algorithm are used as initial values for this algorithm. It is similar to the FKM algorithm with two main exceptions:

- (a) It uses posterior probability instead of membership values
- (b) It uses exponential distance measure instead of the Euclidean distance measure.

The Euclidean distances $d^2(c_k, x_n)$ as computed by the FKM algorithm corresponding to the final estimated fuzzy poles are used as the initial exponential distance measures $d_e^2(c_k, x_n)$ (Step 5.a). The posterior probability $h(k/x_n)$, which indicates the likelihood of a given data point X_n belonging to the cluster k , is then computed (Step 5.b) as given by [19]:

$$h(k/x_n) = \frac{[d_e^2(c_k, x_n)]^{-1/(q-1)}}{\sum_{k=1}^{N_c} [d_e^2(c_k, x_n)]^{-1/(q-1)}} \quad (6.7)$$

Based on the posterior probabilities for each data point and the given cluster set, a-priori probability P_k is calculated (Step 5.c) which indicates what is the likelihood of occurrence of cluster k [13]

$$P_k = \frac{1}{N_d} \sum_{n=1}^{N_d} h(k/x_n) \quad (6.8)$$

The next step (Step 5.d) is to determine the exponential distance measures for each of the estimated complex poles and clusters. This exponential distance function used in the FMLE algorithm optimizes the decision in a small local region in the complex s -plane. It optimizes the partitioning of the estimated poles into clusters and is given by [19]

$$d_e^2(c_k, x_n) = \frac{[\det(F_k)]}{P_k} e^{[(c_k - x_n)^T F_k^{-1} (c_k - x_n)/2]} \quad (6.9)$$

where the Fuzzy Covariance Matrix F_k for the k^{th} cluster is given by [19]

$$F_k = \frac{\sum_{n=1}^{N_d} h(k/x_n) [(c_k - x_n)(c_k - x_n)^T]}{\sum_{n=1}^{N_d} h(k/x_n)} \quad (6.10)$$

The final step (Step 5.e) is to compute the new centroids [19] and iterate (by returning to Step 5.b) until there is no perceptible change in the value of the posterior probability

$$c_k = \frac{\sum_{m=1}^{N_d} h^q(k/x_n) \cdot x_m}{\sum_{m=1}^{N_d} h^q(k/x_n)} \quad \text{for } k = 1, 2, \dots, N_c \quad (6.11)$$

Thus, the first phase (FKM algorithm) of the UOFC algorithm provides blind tracking of the initial fuzzy poles and the next sequential phase (the FMLE algorithm) provides optimal partitioning of the estimated poles into the clusters. This permits characterization of target or scatterer signatures using fewer complex poles in presence of noise. Hence, advances in fuzzy pole representation will provide an alternative approach to scatterer response modeling for noisy measured data.

6.2.3 Performance Parameters for Fuzzy Clustering

The objective of the UOFC algorithm is to optimally partition the given set of estimated poles into clusters. The ‘optimal partitioning criteria’ seeks to maximize/minimize the computed performance parameters based on the following requirements [19]:

- (a) Well-defined clusters with clear spacing between the clusters in the s-plane
- (b) Clusters on average occupy minimum area in the s-plane
- (c) Clusters on average have maximum number of estimated poles in the vicinity of the cluster centroid.

Based on the above-mentioned criteria, the following two performance parameters provide information for optimal partitioning of the estimated poles:

- (a) The Fuzzy Hyper Volume (F_{HV}), and
- (b) The Partition Density (P_D)

6.2.3.1 Fuzzy Hyper Volume (FHV)

F_{HV} is a measure of the amount of space occupied by the clusters on average in the complex s-plane. Since this algorithm was developed to support any N -dimensional data set, the corresponding performance parameter is an N -dimensional Fuzzy Hyper Volume. For our case it is simply a 2-D area in the complex s-plane. Because a smaller area is occupied in the s-plane, there will be a closely packed cluster and a low value of the F_{HV} . Thus, the objective is a low value for F_{HV} , which is computed by [13]

$$F_{HV} = \sum_{k=1}^{N_c} [\det(F_k)]^{1/2} \quad (6.12)$$

where F_k is given by (6.10). The F_{HV} for each cluster size from 2 to 15 (a pre-defined upper limit) of the data set shown in Fig. 6.4 is computed and plotted in Fig. 6.6. Since lower F_{HV} values are indicative of a distinct cluster, the number of clusters corresponding to the minimum value of F_{HV} is the optimal number of clusters. The F_{HV} for estimated poles of a thin wire scatterer response with 5 dB SNR, shown in Fig. 6.6 indicates that the optimal number of clusters and hence, fuzzy poles needed to represent the noisy data, is 10.

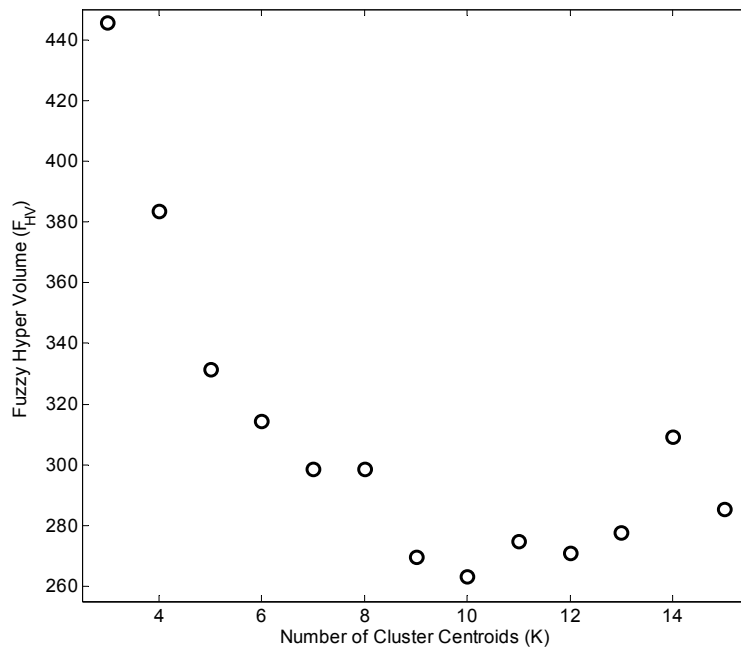


Figure 6.6 Fuzzy Hyper Volume (F_{HV}) for increasing number of clusters from 2 to 15, computed for the 2-D estimated complex poles shown in Fig. 6.4 for the example of Table 6.1.

6.2.3.2 Partition Density (PD)

The UOFC algorithm uses partition density (P_D) to determine the optimal number of clusters. The partition density is a measure of the average number of data points within a cluster per unit area in s-plane and is given by [13]

$$P_D = \frac{\sum_{n=1}^{N_d} \sum_{k=1}^{N_c} u_{kn}}{\sum_{k=1}^{N_c} [\det(F_k)]^{1/2}} \quad \forall x_n \in \{x_n : (c_k - x_n)^T F_k^{-1} (c_k - x_n) < 1\} \quad (6.13)$$

where F_k is given by (6.10). Higher density values are indicative of the presence of a distinct cluster, so the number of clusters corresponding to the maximum value of P_D is the optimal number of clusters. The P_D for estimated poles of a thin wire scatterer response with 5 dB SNR, shown in Fig. 6.7 indicates that the optimal number of clusters needed to represent the noisy data is 10. This optimal value is valid only up to the upper limit of pre-selected cluster size. In the remainder of this chapter, Partition Density (P_D) is used as the parameter to determine the optimal number of clusters needed to represent the estimated poles of a noisy TD response.

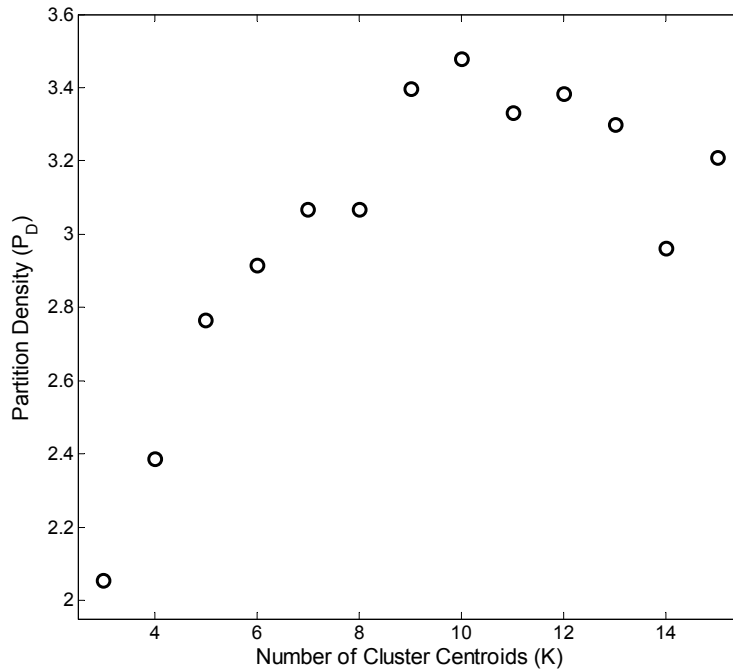


Figure 6.7 Partition Density (P_D) for the number of clusters from 2 to 15 computed for the data points shown in Fig. 6.4 using (6.13) for the example of the thin wire scatterer of Table 6.1.

6.3 Modified UOFC Algorithm

The Unsupervised Fuzzy Optimal Clustering (UOFC) algorithm is based only on geometrical in s-plane. It determines the geometrical cluster centers, which may not give accurate results if there are one or more spurious poles of low amplitude but far from actual pole positions. These spurious poles can shift the geometrical cluster center away from the actual pole location. In order to achieve more accurate estimation of actual poles using the fuzzy pole estimates, the UOFC algorithm was modified to include the pole energy.

The energy content of the poles was observed in test calculations to be similar for estimated poles within the cluster about the actual poles and reduced with distance from the actual poles. The membership values u_{kn} are indicative of the cluster to which the estimate poles belong, so the expression to compute the membership values in the UOFC algorithm is modified to include the pole energy content

$$u_{kn} = \frac{[d^2(c_k, x_n) \cdot E_n]^{1/(q-1)}}{\sum_{k=1}^{N_c} [d^2(c_k, x_n) \cdot E_n]^{1/(q-1)}} \quad 0 \leq u_{kn} \leq 1 \quad (6.14)$$

where E_n indicates the energy content of the estimated poles given by (5.21) and normalized for each realization. The original FKM algorithm uses membership values that depend only on the Euclidean distance.

We introduced an additional weighting based on the pole energy that improved the estimation of the actual poles. Fig. 6.8 compares the estimated fuzzy cluster centers and fuzzy cluster centroids (calculated using the modified UOFC algorithm with energy weighting) to the actual poles for the thin wire scatterer. The fuzzy cluster centers and centroids were calculated for the estimated poles of the 5 dB SNR time-domain response shown in Fig. 6.2. The optimal number of 10 computed fuzzy poles (cluster centers & centroids) as determined from methods in Section 6.2.3 match closely to the actual poles. As expected, modifying the algorithm to include the pole energy as an additional weighting factor results in a better estimate of the actual poles.

For each realization, the maximum pole energy value of the estimated poles is normalized to unity. This forces the membership values of the strong poles (i.e. those with large energy content) to remain unchanged, with only the membership values of the weak poles reduced. This reduces the weighting of the weak poles in determining the fuzzy cluster centroids. For very

strong poles, the clusters are tight and implementing the modified UOFC algorithm does not offer any further advantage. However for weak poles, the cluster centroids compared to the cluster centers are closer to the actual pole in the s-plane.

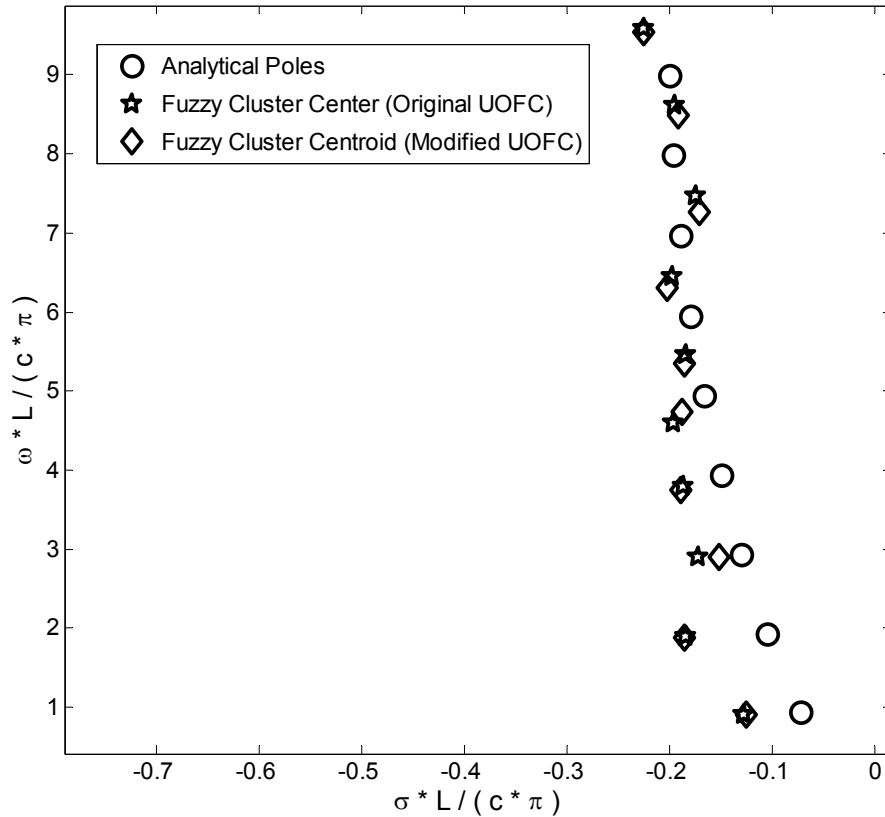


Figure 6.8 Computed fuzzy cluster centers and cluster centroids (using modified UOFC algorithm for the estimated poles shown in Fig. 6.4 and the optimal cluster size shown in Fig. 6.7 for the example of a thin wire scatterer described in Table 6.1.

Figure 6.9 compares the impulse responses estimated from the fuzzy cluster centers and centroids with the actual noiseless response. The averaged waveform over $N = 91$ realizations was used to determine the residues for the fuzzy poles. Observe that the impulse response computed from fuzzy centers and centroids are identical. This is because the strong poles dominate the TD behavior and both the original and the modified UOFC algorithms presented identical fuzzy poles. Although the estimation of the weak poles was improved using the modified UOFC algorithm, it did not reflect in the TD response.

In the remainder of this chapter, fuzzy cluster centroids will be used for fuzzy pole representation.

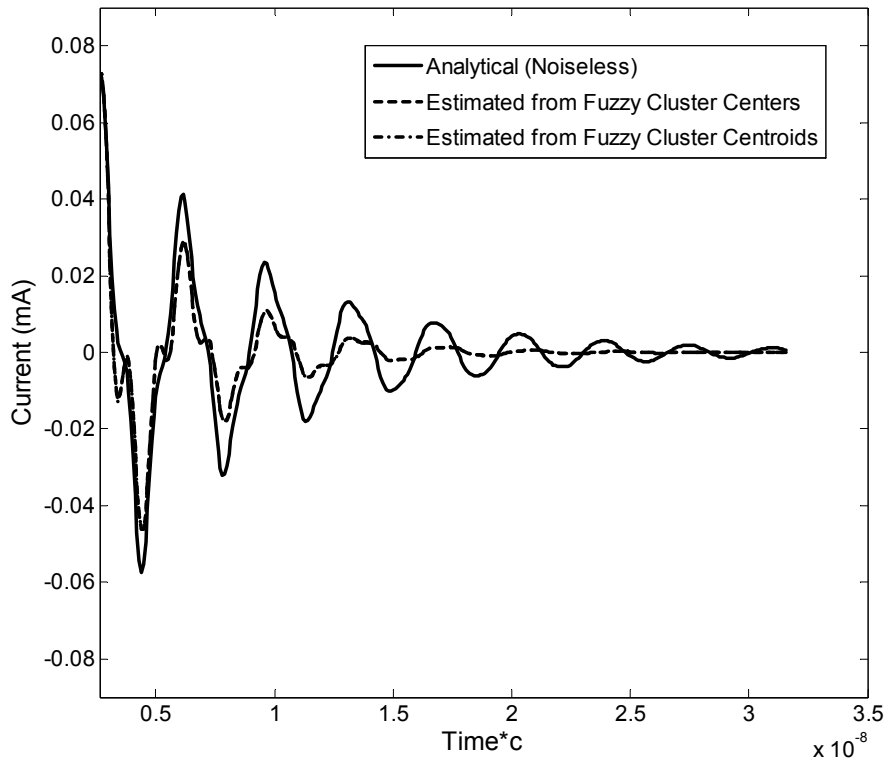


Figure 6.9 Estimated time-domain responses using fuzzy cluster centers and cluster centroids (using modified UFOC algorithm with pole-energy weighting) for the estimated poles shown in Fig. 6.4 and optimal cluster size of 10 as shown in Fig. 6.7 for the example of a thin wire scatterer described in Table 6.1.

6.4 Simulation and Measurement Results

The fuzzy analysis method described in the previous section was found to produce good results for the example of a thin wire scatterer described in Table 6.1. The near-accurate estimation of the actual poles using the fuzzy clustering approach, demonstrated in Section 6.3 for 5 dB *SNR* signal, motivates the investigation of fuzzy pole representation for various noise levels. Next, we analyze simulated as well as measured data to represent estimated poles of a noisy time-domain response in terms of fuzzy poles. First, the simulated results for two extreme cases of noise levels are discussed in Section 6.4.1. Section 6.4.2 presents fuzzy analysis of the measured time-domain response of a thin wire of length 27 cm using the MPM and the modified UFOC algorithm. This measured data is corrupted with noise to allow fuzzy analysis. Section 6.4.3 presents fuzzy pole representation of measured response of a conducting sphere.

6.4.1 Fuzzy Analysis of the Simulated Response of a Thin Wire Scatterer

Simulated response of the thin wire scatterer [20] was corrupted with additive Gaussian noise to achieve a SNR of 5 dB in Section 6.1. The estimated poles using the MPM for 91 snapshots of the noisy TD response were analyzed using the modified UOFC algorithm. This subsection demonstrates the estimation of the optimal number of clusters based on the maximization of the partition density for two extreme noise levels.

Optimal values of $N = 4$ and 9 were observed for the number of clusters for noise levels corresponding to $SNR = 50$ dB and 10 dB, respectively, as shown in Fig. 6.10. This plot provides information on how the noise level affects the optimal choice of the number of clusters. Observe that as the noise level rises (i.e. the SNR drops), the optimal value shifts to a higher number. This is because as the noise level increases more clusters are visible, increasing the optimal value of number of clusters. This phenomenon is expected because up to a certain noise level the clusters are more distinct and then gradually the spurious poles spread in the s -plane.

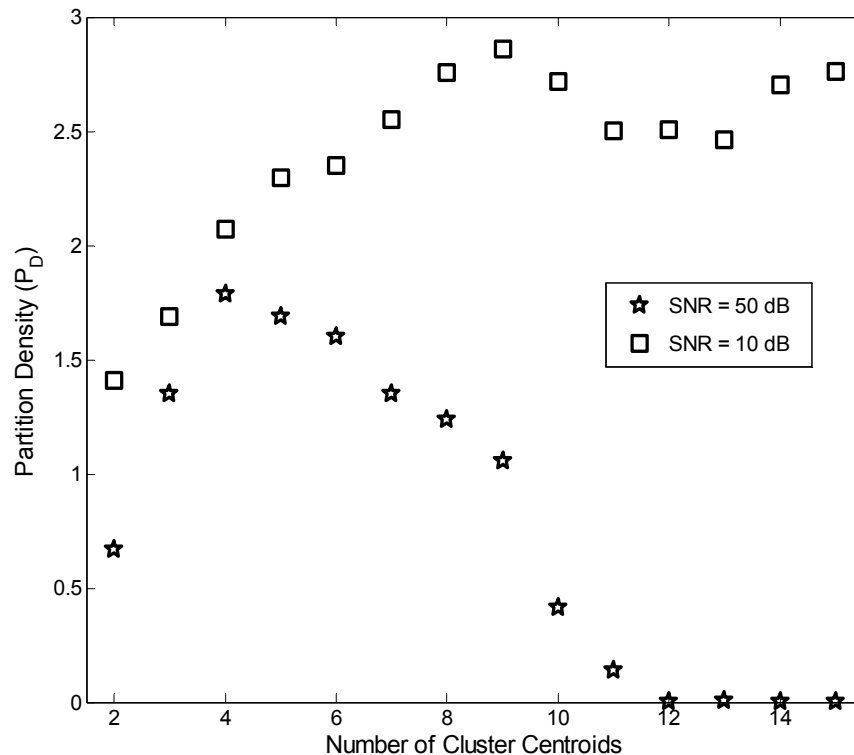


Figure 6.10 Partition Density (P_D) for increasing number of clusters from 2 to 15 computed for simulated response of a thin wire for two levels of noise corresponding to 50 dB and 10 dB SNR for the example of a thin wire scatterer described in Table 6.1.

At high noise levels, the value of the optimal number of poles fluctuated. However, for large number of realizations or snapshots of the noisy response these fluctuations can be reduced. Hence, for low *SNR* values (say, under 10–15 dB) more samples are required to average out the fluctuations in the Partition density values.

Based on the optimal number of fuzzy poles determined in Fig. 6.10, Fig. 6.11 shows the fuzzy poles for simulated response of a thin wire for two levels of noise corresponding to 50 dB and 10 dB *SNR*. The fuzzy cluster centroids or fuzzy poles match closely to the actual poles for data with high *SNR* (i.e. 50 dB) because the clusters are distinct. Even at low *SNR* (i.e. 10 dB) the fuzzy poles estimated using the blind algorithm offers a fairly good match. Another interesting observation is that as the noise level increases spurious poles appear and move the cluster to the left of the actual pole. This results in the estimation of the cluster centroid or the fuzzy poles with a larger damping rate value.

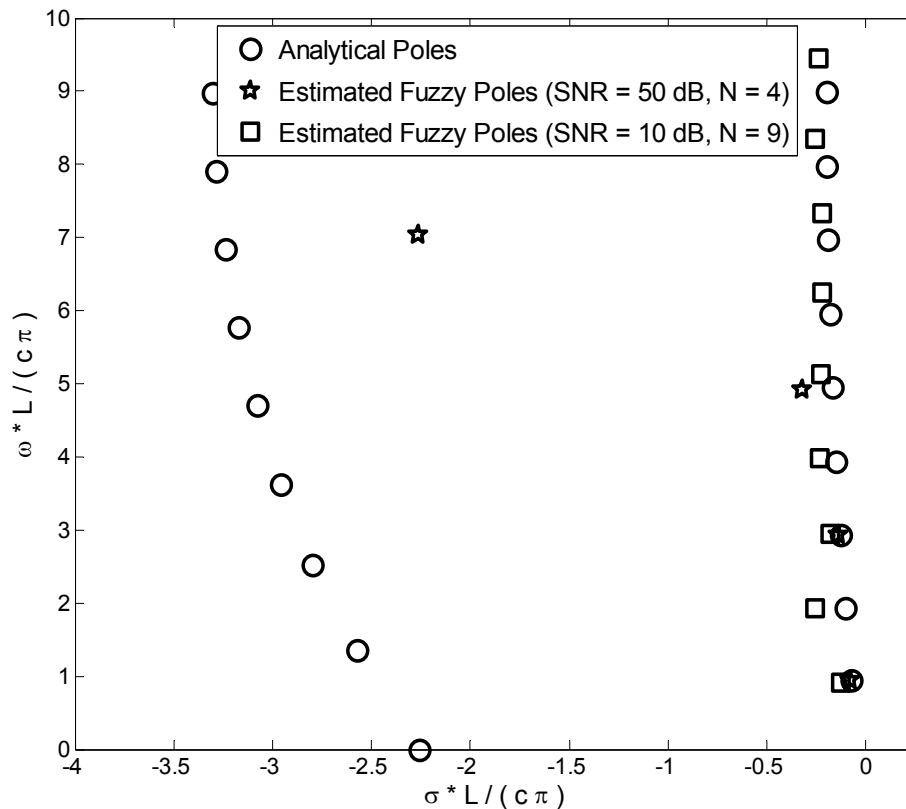


Figure 6.11 Estimated fuzzy poles of a thin wire scatterer of Table 6.1 for two levels of noise corresponding to 50 dB and 10 dB *SNR*.

The increased damping rate is observed in the impulse response estimated from the fuzzy poles for low SNR as shown in Fig. 6.12. Note that as the noise level increases, the impulse response damps faster. This is because the noise offsets the estimated fuzzy poles slightly to the left in the s -plane, resulting in a greater damping rate given by the real part of the complex fuzzy poles.

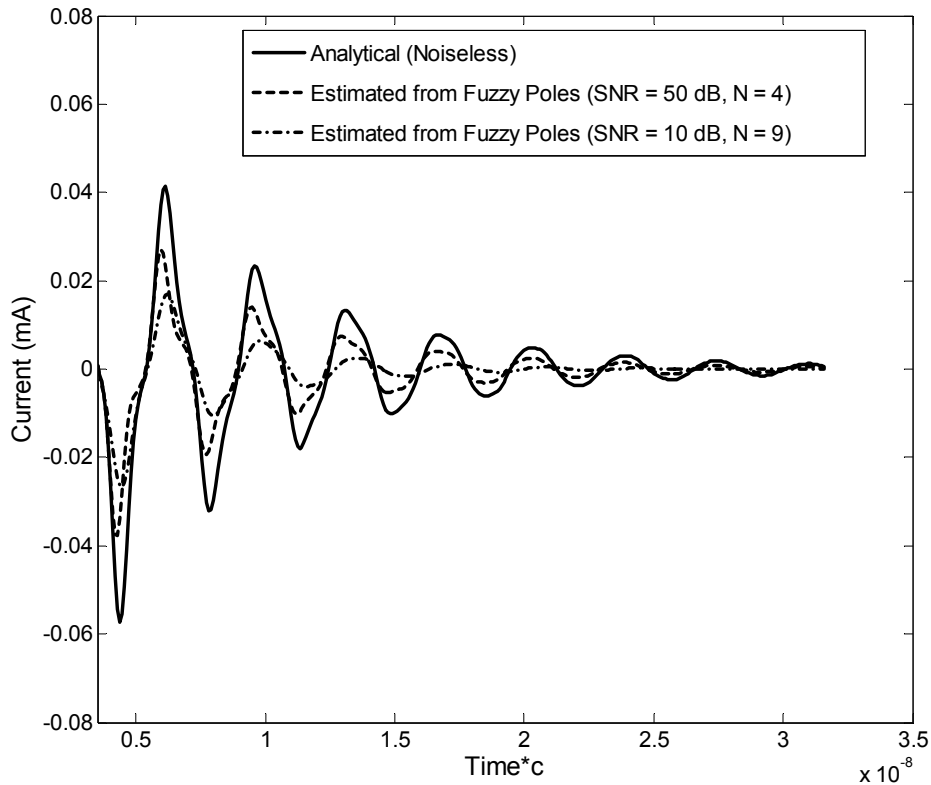


Figure 6.12 Estimated response of a thin wire scatterer of Table 6.1 using the fuzzy poles shown in Fig. 6.11 for two levels of noise corresponding to 50 dB and 10 dB SNR .

6.4.2 Fuzzy Analysis of the Measured Response of a Thin Wire

Response of a thin wire scatterer of length $L = 27$ cm and diameter $d = 0.1$ cm in a controlled environment was measured for various levels of noise corresponding to different averaging factors available on a vector network analyzer (VNA). The measurement setup using the VNA, described in Chapter 4, was used to record the frequency domain response. The averaging function in VNA uses vector addition that improves the SNR by 3 dB with every doubling of the averaging factor. The response of a thin wire scatterer of length 27 cm recorded with an

averaging factor (AF) of 4096 is processed using method outlined in Section 4.1. The estimated complex poles using the Matrix Pencil Method (MPM) are compared to the analytically determined poles of a thin wire scatterer in Fig. 6.13. Only the dominant poles as determined by the pole energy content in Section 5.2 are chosen. These dominant poles are observed to match closely to the first branch of analytically determined poles. Due to high damping factor, the estimated poles from the measured response are not observed for second and higher branches.

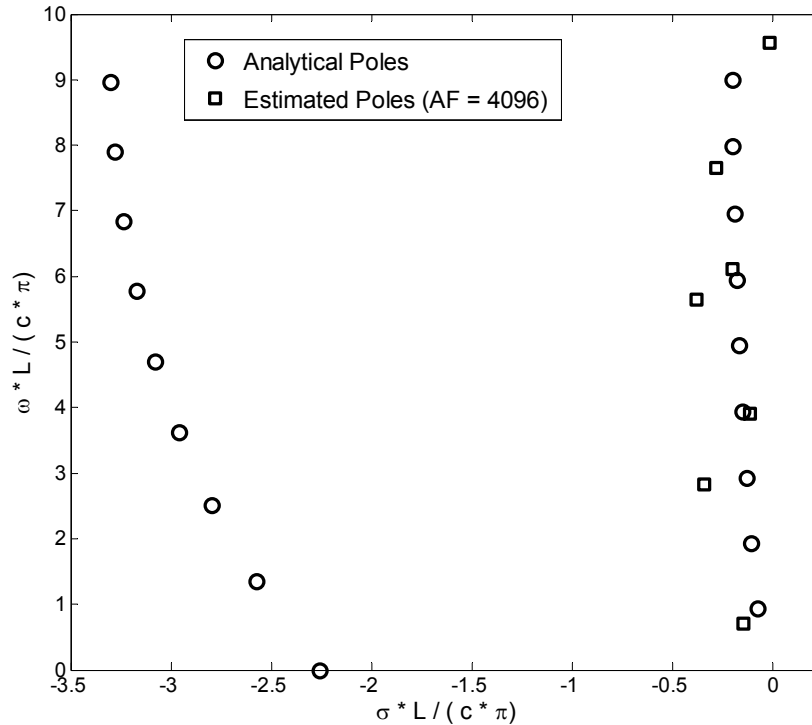


Figure 6.13 Analytically determined and estimated poles from a measured response of a thin wire scatterer of length $L = 27$ cm and diameter $d = 0.1$ cm using the VNA and MPM for an averaging factor (AF) of 4096.

The averaging factor (AF) was reduced to 256 and 11 snapshots of the noisy TD response were recorded. Reduction in the AF from 4096 to 256 (a factor of 16) results in reduction of SNR by 12 dB, i.e. the equivalent noise level increased by 12 dB. The estimated complex poles using the MPM for 11 snapshots of the noisy TD response were analyzed using the modified UFOFC algorithm to calculate the fuzzy poles. Analytically determined poles, estimated poles for all the 11 snapshots of the measured response and the fuzzy poles of a thin wire scatterer of length $L = 27$ cm are shown in Fig. 6.14.

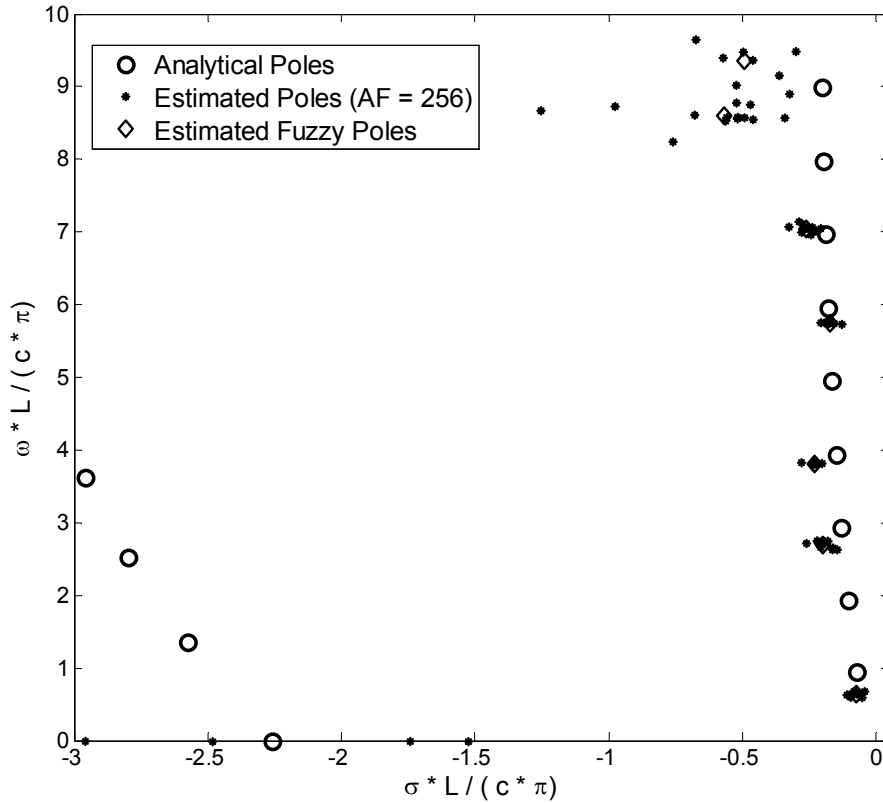


Figure 6.14 A comparison of analytically determined poles, estimated poles from 11 snapshots of a noisy measured response of a thin wire scatterer of length $L = 27$ cm and diameter $d = 0.1$ cm with $AF = 256$ and the computed fuzzy poles using the modified UOFC algorithm.

The estimated poles corresponding to the measured response with 12 dB noise formed clusters and the optimally determined fuzzy poles offered a close match to the actual poles. The optimal number of fuzzy poles was determined to be 7 corresponding to the maximum value of the partition density (P_D) as shown in Fig. 6.15.

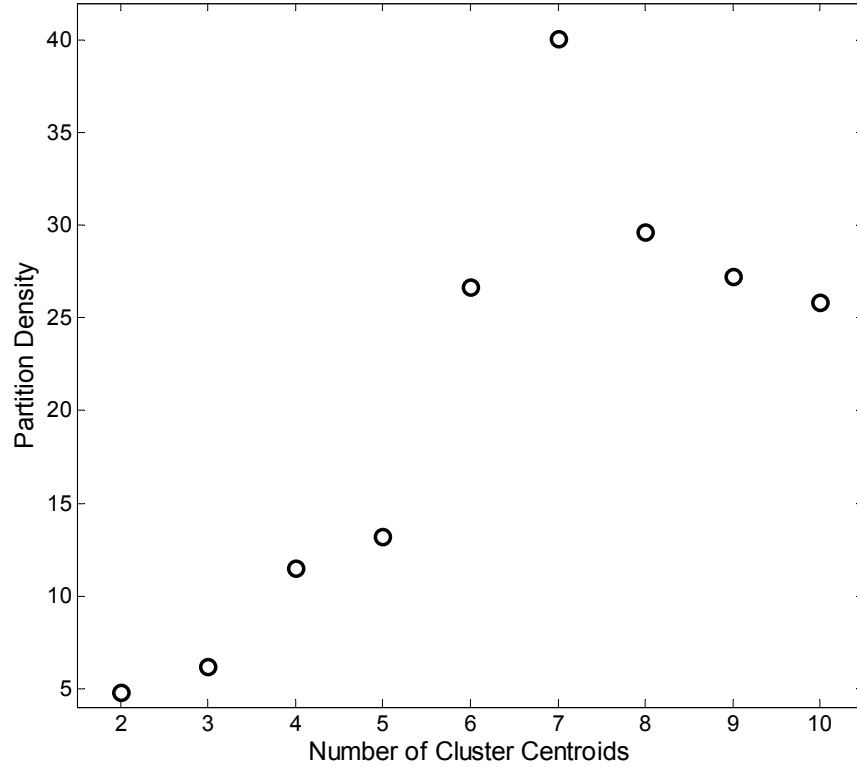


Figure 6.15 Partition Density (P_D) for increasing number of clusters from 2 to 10 computed for the measured response of a thin wire of length $L = 27$ cm and diameter $d = 0.1$ cm for 12 dB of noise corresponding to $AF = 256$.

Similarly, fuzzy poles were optimally determined from all the estimated poles of 11 snapshots of measured thin wire scatterer response for an $AF = 16$. A further reduction in the AF from 256 to 16 results in reduction of SNR by 12 dB, i.e. the noise level increased by a factor of 24 dB in comparison to the AF of 4096. Fig. 6.16 compares the theoretically determined poles to the estimated poles for $AF = 4096$, estimated fuzzy poles for $AF = 256$ and 16. Following observations can be recorded from Fig. 6.16:

- a. The estimated fuzzy poles from noisy data offer a close match to the actual poles.
- b. As expected, increase in noise level by 12 dB shifted the estimated fuzzy poles for $AF = 16$ to the left of the fuzzy poles for $AF = 256$.
- c. The fuzzy poles corresponding to $AF = 256$ offer a better estimate of the actual poles than the estimated poles corresponding to $AF = 4096$.

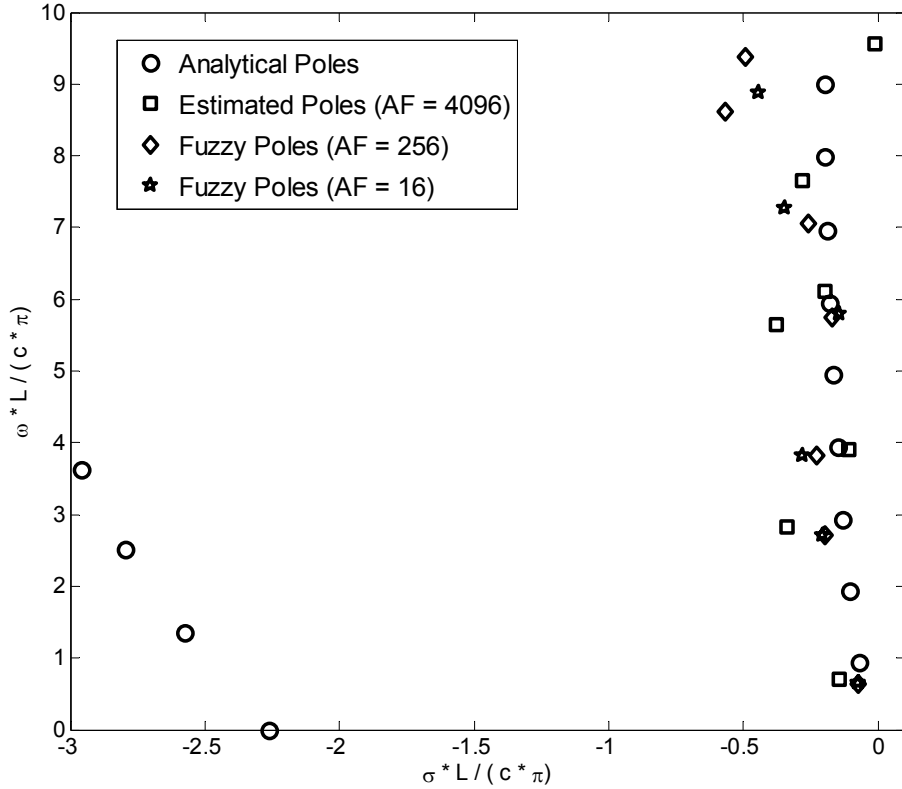


Figure 6.16 Comparison of estimated poles for $AF = 4096$ and fuzzy poles for $AF = 256$ & 16 determined from the measured response of the thin wire scatterer of length 27 cm and diameter $d = 0.1$ cm to the analytically determined poles [16].

6.4.3 Fuzzy Analysis of the Measured Response of a Conducting Sphere

Similar to the results presented in the previous section for a thin wire scatterer, the measured response of a conducting sphere was analyzed for various levels of noise corresponding to different averaging factors available on a vector network analyzer (VNA). An identical measurement setup as described in Chapter 4 was used to record the frequency domain response of the conducting sphere of diameter $d = 15.25$ cm (6 inch).

Measurements were recorded in three sets. The first measurement set consists of a single snapshot of measured response with an averaging factor $AF = 4096$. Since the signal-to-noise ratio (SNR) is difficult to measure, assume the SNR corresponding to this measured data as SNR_{Ref} . The single measured response is analyzed using the MPM to determine the complex poles. The second measurement set consists of 11 snapshots of the measured response with $AF = 256$ corresponding to a SNR of $[SNR_{Ref} - 12]$ dB. The third measurement set consists of 11

snapshots of the measured response with $AF = 16$ corresponding to a SNR of $[SNR_{Ref} - 24]$ dB. The estimated poles using the MPM determined for 11 snapshots of the noisy TD response corresponding to the second and the third sets were analyzed using the modified UOFC algorithm to calculate the fuzzy poles. Fig. 6.17 compares the theoretically determined poles [21] to the estimated poles for $AF = 4096$ and estimated fuzzy poles for $AF = 256$ and $AF = 16$ for a conducting sphere of diameter 6 inches.

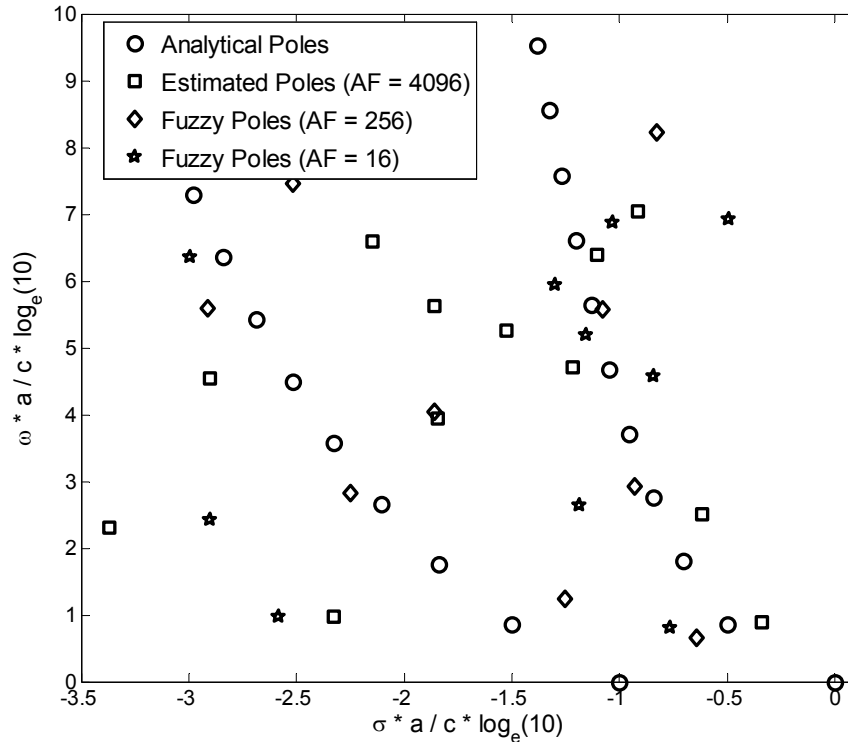


Figure 6.17 Comparison of estimated poles for $AF = 4096$ and fuzzy poles for $AF = 256$ & 16 determined from the measured response of a conducting sphere of diameter $d = 15.25$ cm to the analytically determined poles [21].

All observations recorded for the thin wire scatterer case in the previous section are also seen here for the case of a conducting sphere. The estimated fuzzy poles from noisy data (-12 and -24 dB SNR relative to the SNR_{Ref} corresponding to the $AF = 4096$) offered a close match to the actual poles. Increase in noise level shifted the estimated fuzzy poles for $AF = 16$ to the left of the fuzzy poles for $AF = 256$. The fuzzy poles corresponding to $AF = 256$ offered an improved estimate of the actual poles of a conducting sphere compared to the estimated poles for $AF = 4096$.

6.5 Chapter Summary

This chapter presented fuzzy poles representation of the estimated complex poles of a noisy time-domain scatterer response. Cluster formations of complex poles around the actual poles in the s -plane are exploited to offer an improved estimation of the actual poles. In this chapter, a modified fuzzy clustering approach is proposed as a solution to determine the optimal representation of the noisy data using fuzzy cluster centroids also termed ‘fuzzy poles’. The near-accurate estimation of the actual poles using the fuzzy clustering approach is demonstrated using $SNR = 5$ dB time-domain response of a simulated thin wire scatterer described in Table 6.1.

The Unsupervised Fuzzy Optimal Clustering (UOFC) algorithm determines the geometrical cluster centers, which may not give accurate results if there are one or more spurious poles far from actual pole positions. We introduced an additional weighting based on the energy content of poles that improved the estimation of the actual poles; see Fig. 6.8. The Matrix Pencil Method (MPM) and the modified Unsupervised Optimal Fuzzy Clustering (UOFC) algorithm are used to process the noisy time domain response to determine fuzzy poles. Simulated results for two extreme cases of noise levels indicate that with increasing noise levels the optimal number of clusters needed to represent the noisy data increases. Measured time domain responses of a thin wire of length $L = 27$ cm and a conducting sphere of diameter $d = 15.25$ cm were also analyzed using the MPM and the modified UOFC algorithm for various noise levels.

The calculated fuzzy poles with increasing levels of noise move to the left in the complex s -plane, resulting in the corresponding time response with larger damping rate. The modified UOFC algorithm applied to multiple snapshots of a noisy measured response of a thin wire and a conducting sphere illustrated that the fuzzy poles offer a closer match to the actual poles compared to the poles estimated from a single realization with higher SNR . Advances in fuzzy characterization have promising applications in target identification, which uses noisy time-domain UWB radar response.

References

- [1] F. Guanyou and Z. Zhongzhi, "Measurement and numerical calculation about the resonance properties of objects buried in a lossy half-space," *Proceedings of Asia-Pacific Microwave Conference, APMC '97* vol. 3, pp. 1021-1024, Dec. 1997.
- [2] C. E. Baum, E. J. Rothwell, K. M. Chen, and D. P. Nyquist, "The singularity expansion method and its application to target identification," *Proceedings of the IEEE*, vol. 79 (10), pp. 1481-1492, Oct. 1991.
- [3] M. A. Morgan, "Target I.D. using natural resonances," *IEEE Potentials*, vol. 12 (4), pp. 11-14, Dec. 1993.
- [4] M. El-Shenawee, "Resonant spectra of Malignant breast cancer tumors using the three-dimensional Electromagnetic Fast multipole model," *IEEE Transactions on Biomedical Engineering*, vol. 51 (1), pp. 35-44, Jan. 2004.
- [5] E. C. Fear, X. Li, S. C. Hagness, and M. A. Stuchly, "Confocal microwave imaging for breast cancer detection: localization of tumors in three dimensions," *IEEE Transactions on Biomedical Engineering*, vol. 49 (8), pp. 812-822, Aug. 2002.
- [6] E. C. Fear and M. Okoniewski, "Confocal microwave imaging for breast tumor detection: application to a hemispherical breast model," *IEEE International Microwave Symposium Digest, MTT-S '02* vol. 3, pp. 1759-1762, June 2002.
- [7] R. Carriere and R. L. Moses, "High resolution radar target modeling using a modified Prony estimator," *IEEE Transactions on Antennas and Propagation*, vol. 40 (1), pp. 13-18, Jan. 1992.
- [8] Y. Hua and T. K. Sarkar, "Matrix pencil method for estimating parameters of exponentially damped/undamped sinusoids in noise," *IEEE Transactions on Acoustics, Speech, and Signal Processing*, vol. 38 (5), pp. 814-824, May 1990.
- [9] M. VanBlaricum and R. Mittra, "Problems and solutions associated with Prony's method for processing transient data," *IEEE Transactions on Antennas and Propagation*, vol. 26 (1), pp. 174-182, Jan. 1978.
- [10] Y. Hua and T. K. Sarkar, "On SVD for estimating generalized eigenvalues of singular matrix pencil in noise," *Signal Processing, IEEE Transactions on*, vol. 39 (4), pp. 892-900, Apr. 1991.
- [11] T. K. Sarkar and O. Pereira, "Using the matrix pencil method to estimate the parameters of a sum of complex exponentials," *IEEE Antennas and Propagation Magazine*, vol. 37 (1), pp. 48-55, Jan. 1995.
- [12] T. K. Sarkar, P. Sheeyun, K. Jinhwan, and S. M. Rao, "Application of the matrix pencil method for estimating the SEM (singularity expansion method) poles of source-free

- transient responses from multiple look directions," *IEEE Transactions on Antennas and Propagation*, vol. 48 (4), pp. 612-618, Apr. 2000.
- [13] I. Gath and A. B. Geva, "Unsupervised optimal fuzzy clustering," *IEEE Transactions on Pattern Analysis and Machine Intelligence*, vol. 11 (7), pp. 773-780, July 1989.
- [14] A. Poggio, M. VanBlaricum, E. Miller, and R. Mittra, "Evaluation of a processing technique for transient data," *IEEE Transactions on Antennas and Propagation*, vol. 26 (1), pp. 165-173, Jan. 1978.
- [15] S. Licul, "Ultra-Wideband Antenna Characterization and Modeling," in *Electrical and Computer Engineering*, vol. Ph.D Dissertation Blacksburg: Virginia Polytechnic Institute and State University, 2004.
- [16] J. Cordaro and W. Davis, "Time-domain techniques in the singularity expansion method," *IEEE Transactions on Antennas and Propagation*, vol. 29 (3), pp. 534-538, Mar. 1981.
- [17] J. C. Bezdek, *Pattern Recognition with Fuzzy Objective function Algorithms*. New York: Plenum Press, 1981.
- [18] J. C. Bezdek and S. K. Pal, "Chapter 1: Fuzzy Models for Pattern Recognition - Background, Significance and Key Points," in *Fuzzy Models for Pattern Recognition*, J. C. Bezdek and S. K. Pal, Eds. New York: IEEE Press, 1991, pp. 1-27.
- [19] A. B. Geva and D. H. Kerem, "Forecasting generalized epileptic seizures from the EEG signal by wavelet analysis and dynamic unsupervised fuzzy clustering," *IEEE Transactions on Biomedical Engineering*, vol. 45 (10), pp. 1205-1216, Oct. 1998.
- [20] K. S. Cho and J. T. Cordaro, "Calculation of the Singularity Expansion Method Parameters from the Transient Response of a Thin Wire," *Interaction Notes #379, AFRL Directed Energy Directorate*, Sept. 1979.
- [21] K. M. Chen and D. Westmoreland, "Impulse Response of a Conducting Sphere Based on Singularity Expansion Method," *Proceedings of the IEEE*, vol. 69 (6), pp. 747 - 750, June 1981.

This page intentionally left blank.

Chapter 7 – Statistical Characterization of Scatterer Response

Noise severely limits scatterer response characterization from measured transient data using the Singularity Expansion Method (SEM). For typical noise levels in measured transient data, only the complex poles with least damping coefficient can be estimated with reasonable accuracy [1]. Moreover, the higher order poles within the first layer are severely corrupted by noise, resulting in the estimation of only a few pairs of dominant complex conjugate poles. Early research focused on pre-filtering the noisy data through optimal combining [2-4] because direct estimation of natural resonances (poles) and natural modes (residues) from the noisy transient response lead to inaccurate results.

In Chapter 6, a fuzzy approach was proposed to circumvent the effect of noise. Cluster formation about the actual poles due to noise was exploited to represent the noisy transient response with a small number of fuzzy poles. Simulated as well as measured results demonstrated a close match of the estimated fuzzy poles to the actual poles of thin wire and conducting sphere scatterers. This estimation can be further improved by incorporating the statistical behavior of the estimated poles in presence of noise. Clustering algorithms can be applied to determine the estimated poles about the actual poles. The probability distribution of the estimated poles within the cluster permits using the estimate as the starting point for the fuzzy pole analysis. The overall objective to improve pole estimation in presence of noise using both the fuzzy analysis and the statistical analysis approach is outlined in Fig. 7.1.

The statistical characterization of complex pole positions in the s-plane has direct application in determining the classification criteria for target identification [5, 6]. Investigations

of noise effects on pole estimation for various extraction techniques [7-9] briefly discussed the deviations in pole estimation for various noise levels. The importance and need for statistical characterization was identified [10] to understand and improve pole estimation in presence of noise for target identification and classification problems. Surprisingly, the statistical distribution in terms of a probability density function (*pdf*) or a cumulative density function (*CDF*) of the estimated poles in the complex s-plane has not been investigated. After identifying the optimal number of clusters in the complex s-plane as shown in Fig. 7.1, there are two options: estimate the fuzzy poles or estimate the statistical mean values within each cluster.

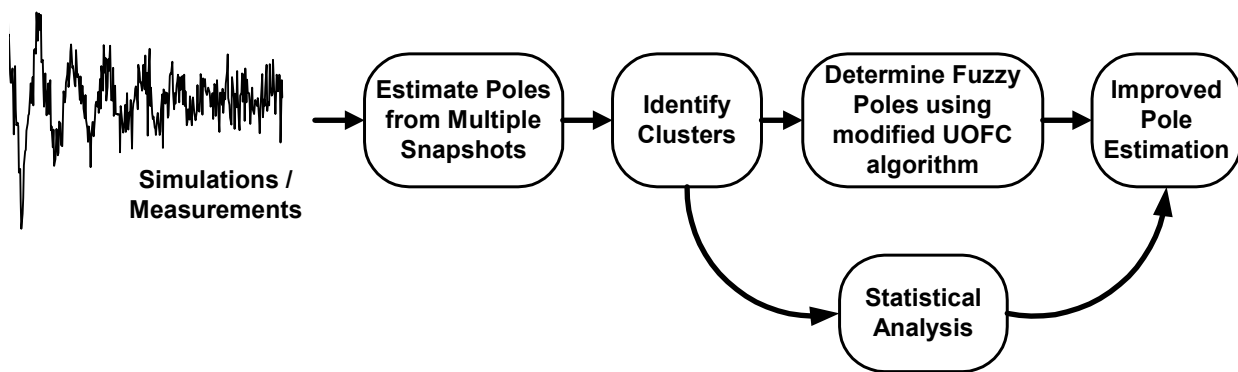


Figure 7.1 Outline of an approach to improve pole estimation from noisy data using both the fuzzy and the statistical analysis.

This chapter presents a comprehensive statistical modeling of the estimated complex poles in the s-plane. Scatter responses of a straight wire are numerically analyzed for different noise levels. The clustering algorithm used in the previous chapter is applied here to identify distinct clusters of estimated poles about the actual poles. A curve fit is applied to the histogram of real and imaginary components of the estimated complex poles within the cluster. Based on the estimated statistical parameters such as the mean and the standard deviation, the probability density functions are plotted for various noise levels. The original contribution of this work is a joint distribution of the real and imaginary components of the estimated poles in the complex s-plane. This joint distribution of the real and imaginary components, or equivalently the 2-D distribution in the s-plane, offers valuable insight in to the noise susceptibility of the poles. The time-domain response is analyzed using the Matrix Pencil Method (MPM) [11, 12] and the statistical curve fits are computed using the ‘dfitool’ available in Matlab[®] 7.0.1 Statistical toolbox.

This chapter begins with a brief discussion of the framework for the statistical analysis in Section 7.1. Three dominant pairs of complex conjugate poles are identified. These poles with different residue amplitudes show different susceptibility to noise. Hence, an important contribution in terms of a novel idea of pole energy to noise ratio (E_p/N_o) is presented in Section 7.1.3. The modified Unsupervised Optimal Fuzzy Clustering (UOFC) algorithm used in the previous chapter is applied here to identify distinct clusters of estimated poles about the dominant poles of a thin wire scatterer.

The statistical analysis is presented in Section 7.2 beginning with a brief discussion of the best-fit distribution, which was found to be the Student's t-distribution. The real and imaginary components of the estimated poles are analyzed separately and their distribution for a chosen E_p/N_o value is presented. The argument that E_p/N_o parameter completely defines the distribution is also discussed. Section 7.3 presents the computed standard deviation and degrees of freedom values for different signal to noise ratios (SNR). A joint distribution of the real and imaginary components of a thin wire for the first branch is presented in Section 7.4. Section 7.4.3 compares the fuzzy approach to the statistical approach (which uses fuzzy clustering) in terms of pole estimation accuracy. Finally, Section 7.5 summarizes the important observations and contributions presented in this chapter.

7.1 Framework for Statistical Analysis of Estimated Poles

Limited investigation of noise effects on pole estimation has revealed that higher order poles are more susceptible to noise than are lower order poles [2-4, 13]. However, this observation offers no insight into which parameters are responsible for accurate estimation of pole positions. The objective of this section is to identify and develop a framework for statistical analysis of pole estimation. An analytically determined response for a thin wire scatterer is used to meet this objective [14]. The proposed framework for the statistical analysis of pole estimation in the complex s-plane for different levels of noise is shown in Fig. 7.2.

The statistical analysis is performed on the real and imaginary components of a single pole. The first step (Step #1) is the statistical analysis, which is presented in Section 7.1.1, is to select any one of the dominant poles of a scatterer. In particular, the analytically determined response for a thin wire scatterer as outlined in Table 6-1 is often used [14].

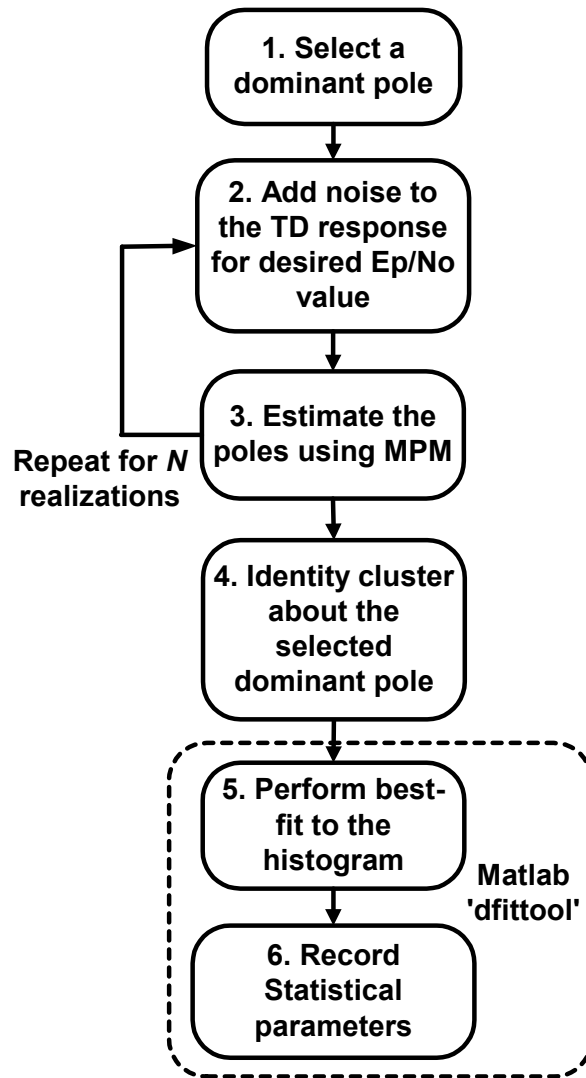


Figure 7.2 The flow diagram of the proposed framework to statistically analyze the real and imaginary components of the estimated complex poles of noisy transient response.

The pole estimation process depends not only on the noise level but also on the energy content of the pole under study. Thus, instead of using the signal-to-noise ratio (SNR) of the entire waveform, a new parameter called the pole energy to noise ratio (E_p/N_o) is introduced in Section 7.1.3. The second step (Step #2) is to determine the noise level corresponding to the desired E_p/N_o value and add it to the waveform, as demonstrated in Chapter 6. Step #3 estimates the complex poles using the Matrix Pencil Method (MPM) and was discussed in Chapter 4.

Prior to the statistical analysis, cluster formation about the desired dominant pole is determined using the modified Unsupervised Optimal Fuzzy Clustering (UOFC) algorithm,

which constitutes Step # 4. This process is presented in Section 7.1.4. The next two steps (Step # 5 and 6) involve statistical curve fitting to the histogram of the real and imaginary components of the estimated poles. These steps are discussed in detail in Section 7.2.

7.1.1 Dominant Poles of a Thin Wire Scatterer

An analytically determined response for a thin wire scatterer is used to statistically investigate the effect of various parameters on the estimation of complex poles [14], which is outlined in Table 6-1. The estimated complex poles of the noiseless time-domain response of a thin wire scatterer using the Matrix Pencil Method (MPM) are shown in Fig. 7.3. Only odd natural modes are observed due to the symmetry of the excitation from broadside direction. Note that the MPM accurately estimates the odd harmonic poles of the thin wire scatterer in absence of noise.

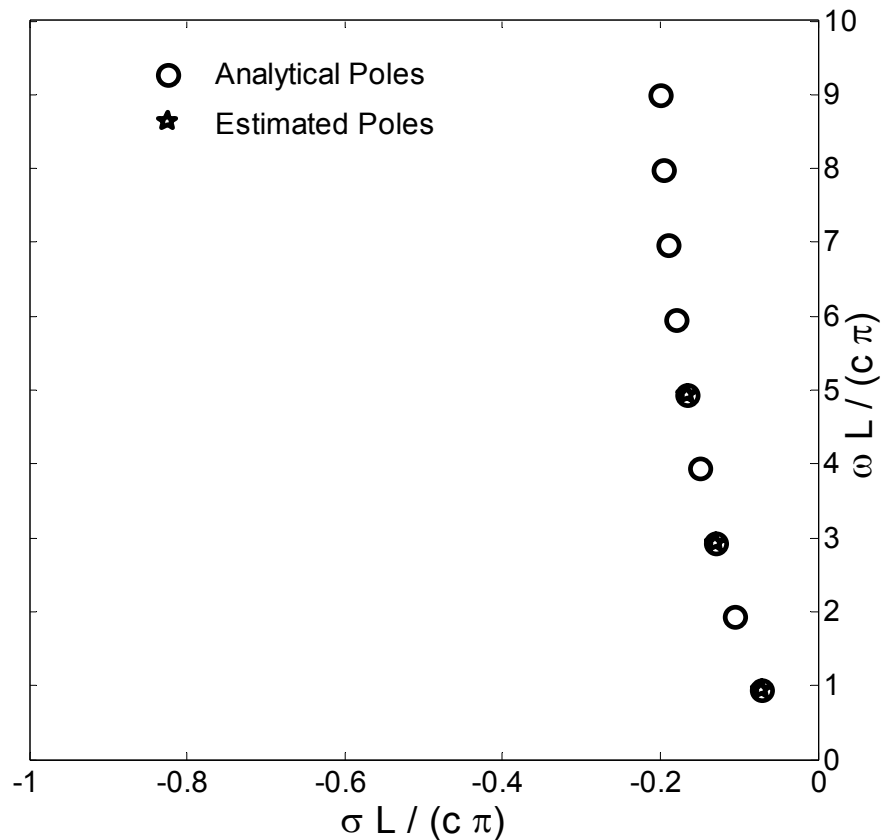


Figure 7.3 Estimated complex poles using MPM compared to the analytically determined complex poles for a noiseless time-domain response of a thin wire scatterer [14] (described in Table 6-1).

A close observation of Fig. 7.3 shows the dominant odd harmonic poles of 1st, 3rd and 5th order that correspond to the 1st, 3rd and 5th half wavelength resonances as given by

$$n \frac{\omega L}{c \cdot \pi} = n \frac{2 \cdot \pi \cdot f \cdot L}{c \cdot \pi} = n \frac{L}{\lambda/2}, \quad n=1,3, \text{ and } 5 \quad (7.1)$$

where L is the length of the thin wire and c is the speed of light. Note that the corresponding complex conjugate pairs of these estimated poles are not shown. The three dominant pairs of complex conjugate poles characterize the time domain response of the thin wire scatterer to significant accuracy as shown in Fig. 7.4.

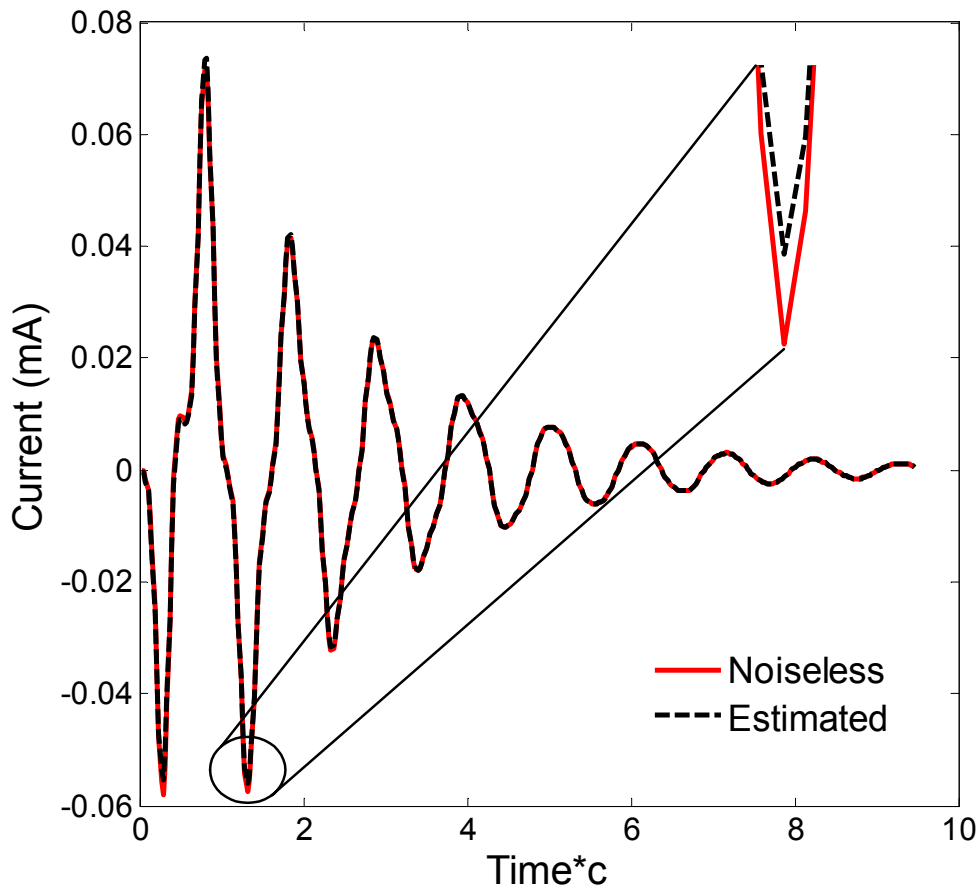


Figure 7.4 Comparison of the estimated TD response using only the three dominant pairs of complex conjugate poles shown in Fig. 7.3 to the analytically determined noiseless response of a thin wire scatterer [14] (described in Table 6-1). Inset picture: zoomed view of the comparison demonstrating a small deviation of the estimated response from the analytical response.

The inset portion of Fig. 7.4 is a zoomed view, which shows a small deviation from the analytical response using only the three dominant pairs of poles identified in Fig. 7.3. The

corresponding residue amplitudes of the three dominant pair of complex conjugate poles is shown in Fig. 7.5, which clearly demonstrates that the strength of the dominant poles decreases as the pole order increases (from 1 to 3 to 5). The decrease in the pole strength for higher order poles is responsible for the higher susceptibility of pole estimation to noise. Fig. 7.6 shows the estimated complex poles using the MPM for 91 realizations of the time domain response of a thin wire scatterer with a signal-to-noise ratio $SNR = 25$ dB. The signal-to-noise ratio (SNR) is defined using (6.2)

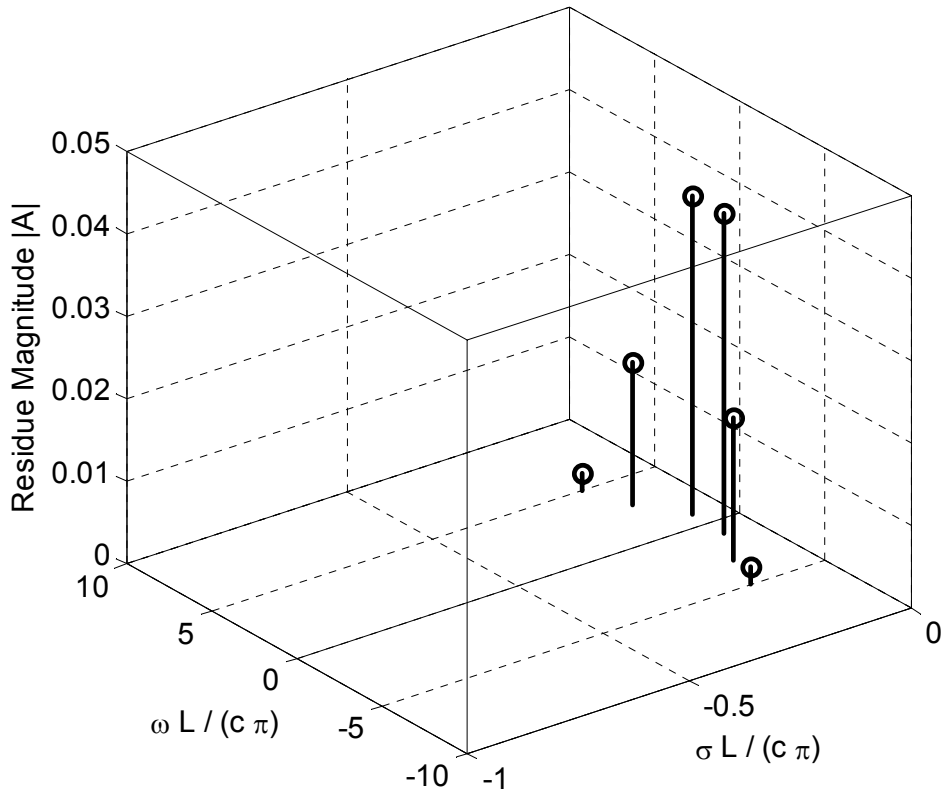


Figure 7.5 Residues of the three dominant pairs of complex conjugate poles identified and shown in Fig. 7.2.

In Fig. 7.6, the first dominant pole is estimated accurately with all estimates matching closely to the actual pole position in the s -plane. Moreover, the pole estimation accuracy decreases as the pole order increases, because higher order poles (i.e. the third and the fifth order poles) have significantly lower strength compared to the first dominant pole. Interestingly, the estimated poles form clusters around the actual poles, which can be exploited to investigate the distribution of the estimated poles about the actual poles.

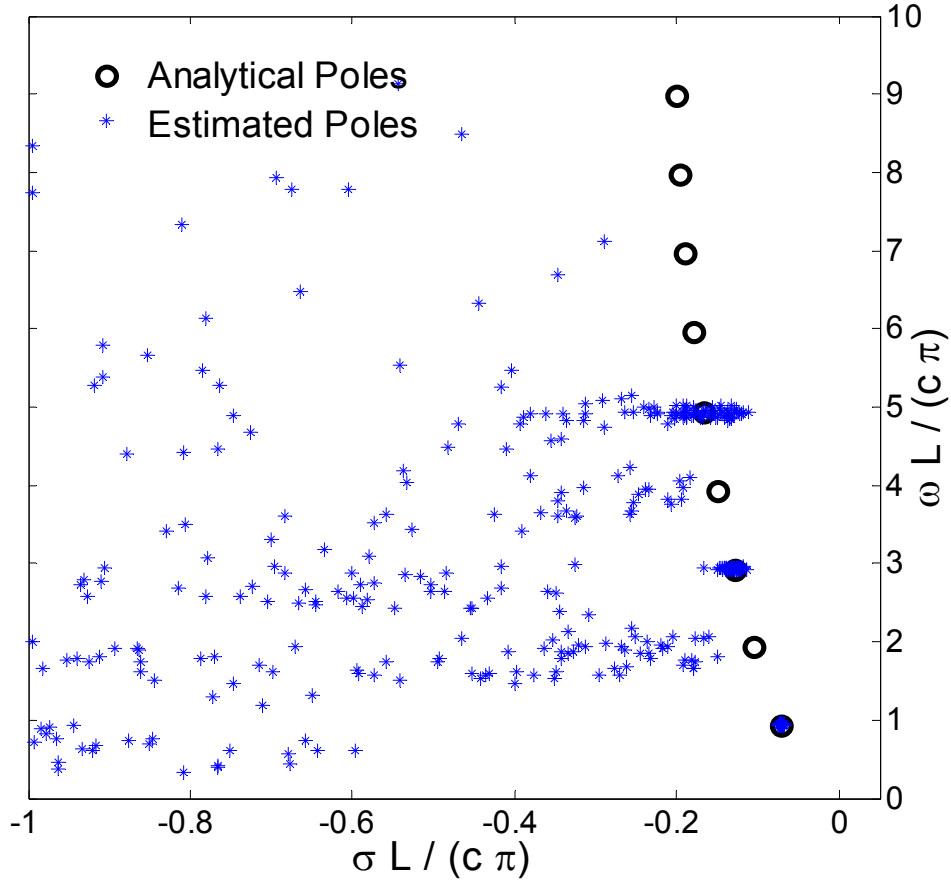


Figure 7.6 The estimated complex poles for 91 realizations of the noisy TD response with $SNR = 25$ dB using the MPM for the example of a thin wire scatterer [14] (described in Table 6-1).

7.1.2 Pole Energy to Noise Ratio (E_p/N_o)

It is insufficient to define the pole strength only in terms of the corresponding residue amplitude. The accuracy of the pole estimation process for a particular pair of complex conjugate poles depends on the following factors:

- Residue amplitude $\{ |A_n(\phi, \theta)| \}$, which in turn depends on
- Signal strength, i.e. the signal energy content as given by equation (6.3)
- Aspect angle of excitation $\{ \Omega(\phi, \theta) \}$
- Damping coefficient or the real component of the complex pole $\{ \sigma \}$
- Noise power spectral density (PSD)

We now introduce a parameter that combines all of the factors above and refer to it as the pole energy-to-noise ratio (E_p/N_o). For the n^{th} pair of complex conjugate poles, the E_p/N_o value is given by

$$\frac{E_{n,p}}{N_o} = \frac{\sum_{t=T_L}^{T_U} |A_n e^{s_n t} + A_n^* e^{s_n^* t}|^2}{\sigma_{noise}^2} \quad (7.2)$$

where $s_n = \sigma_n \pm j\omega_n$ is the n^{th} complex conjugate pole-pair. T_L and T_U are the beginning of the late time response and an arbitrary upper time limit, respectively. Thus, the energy content of the n^{th} pole, defined to be within the time window $T_L \leq t \leq T_U$, depends not only on the residue amplitude but also the damping coefficient $\sigma_n = \text{Re}\{s_n\}$. The noise is assumed to be additive white Gaussian with zero mean and variance σ_{noise}^2 because the measurement noise has Gaussian characteristics. Note that E_p/N_o is not dissimilar to E_b/N_o used in digital communications to observe the effect of noise on the detection of a single bit. The E_p/N_o values and the percentage energy content of the three dominant pair of poles are given in Table 7.1 for $SNR = 25$ dB of the entire transient signal.

Table 7-1 Energy Content of the Dominant Pairs of Complex Conjugate Poles of a Thin Wire Scatterer described in Table 6-1 and Section 7.1 for $SNR = 25$ dB.

<i>Pole Order / Dominant Pair</i>	<i>E_p/N_o</i>	<i>Percentage Energy</i>
1 st pair	24.4 dB	91.15 %
3 rd pair	14.6 dB	8.72 %
5 th pair	-4.5 dB	0.11 %

Figure 7.6 helps explain why the first dominant pole was not affected by noise. It is because the MPM accurately estimates pole positions up to 20 – 25 dB SNR . Below 20 dB there are perceptible errors in estimating the poles, as demonstrated in the estimation of the 3rd and the 5th order poles. Section 7.3 will present validation of the claim that E_p/N_o values are identical, then the estimated statistical parameters such as the standard deviation and degrees of freedom are also identical for any pole.

7.1.3 Cluster identification prior to statistical analysis

As mentioned earlier in this chapter, scatterer responses of a straight wire are numerically analyzed for different noise levels. The clustering algorithm discussed in Section 6.2 is applied here to identify distinct clusters of estimated poles about the actual poles. As seen in Fig. 7.6, the clusters about the dominant poles are clearly evident. The cluster of the estimated poles about any chosen dominant pole is selected and analyzed statistically, which is presented in the next section. A sample of the cluster of the 3rd order pair of dominant poles estimated from 91 realizations of transient response with *SNR* 25 dB is shown in Fig. 7.7. The cluster about the 3rd order pair of dominant poles is determined from all the estimated poles, shown in Fig. 7.6, using the modified optimal fuzzy clustering algorithm described in Section 6.3.

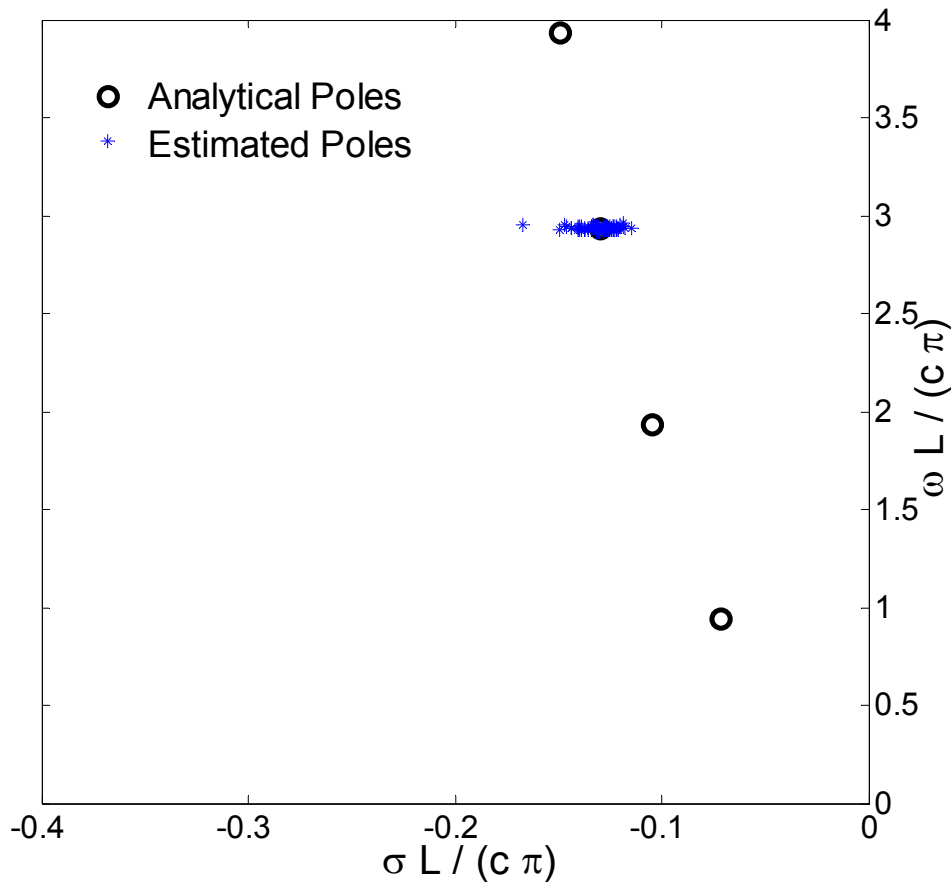


Figure 7.7 Estimated poles in the complex *s*-plane for the thin wire scatterer of Table 6-1 for 25 dB *SNR*. The cluster of estimated poles about the 3rd order pair of dominant poles is due to using MPM from 91 realizations of noisy transient response and applying the modified fuzzy clustering algorithm described in Section 6.3.

7.2 Statistical Analysis of the Estimated Poles within a cluster

In this section, the estimated poles within the cluster identified in the previous section are analyzed statistically to determine the mean, the standard deviation, and other parameters as applicable. First a brief introduction to the best-fit statistical distribution is presented in the following section followed by analysis to find the best curve fits to the histogram of the real and the imaginary parts of the estimated poles.

7.2.1 Student's t-distribution

Statistical parameters such as the population mean (actual mean) and variance (actual variance) are unknown in almost all measured data. These parameters are estimated from the available data of finite sample size using empirical curve fits to the histogram or the cumulative density function (*CDF*). The Student's t-distribution, proposed by W. S. Gosset in 1908, is a popular distribution used to match empirical data with heavy tails [15, 16]. The Student's t-distribution originates from the normal distribution with an additional parameter called the degrees of freedom, ν , that controls the shape of the curve. When ν approaches infinity, the Student's t-distribution approaches the smooth bell curve of normal distribution, as shown in Fig. 7.8. However, for small values of ν , the Student's t-distribution curve is very sharp with a long tail. Note that the comparison is presented for the mean values and the standard deviation values normalized to zero and unity, respectively.

Consider a continuous random variable z with unknown population mean and variance of μ and σ^2 , respectively. The distribution of z for a sample size of n is given by a Student's t-distribution with ν degrees of freedom. The probability density function (*pdf*) of the Student's t-distribution shifted to location μ and scaled by σ is given by [17]

$$f(z) = \frac{\Gamma\left(\frac{\nu+1}{2}\right)}{\sigma\sqrt{\nu\pi}\Gamma\left(\frac{\nu}{2}\right)} \left[\frac{\nu + \left(\frac{z-\mu}{\sigma}\right)^2}{\nu} \right]^{-\left(\frac{\nu+1}{2}\right)} \quad (7.3)$$

where $\Gamma(\cdot)$ is a gamma function. The Student's t-distribution shifted to μ and scaled by σ is also called the t location-scale distribution.

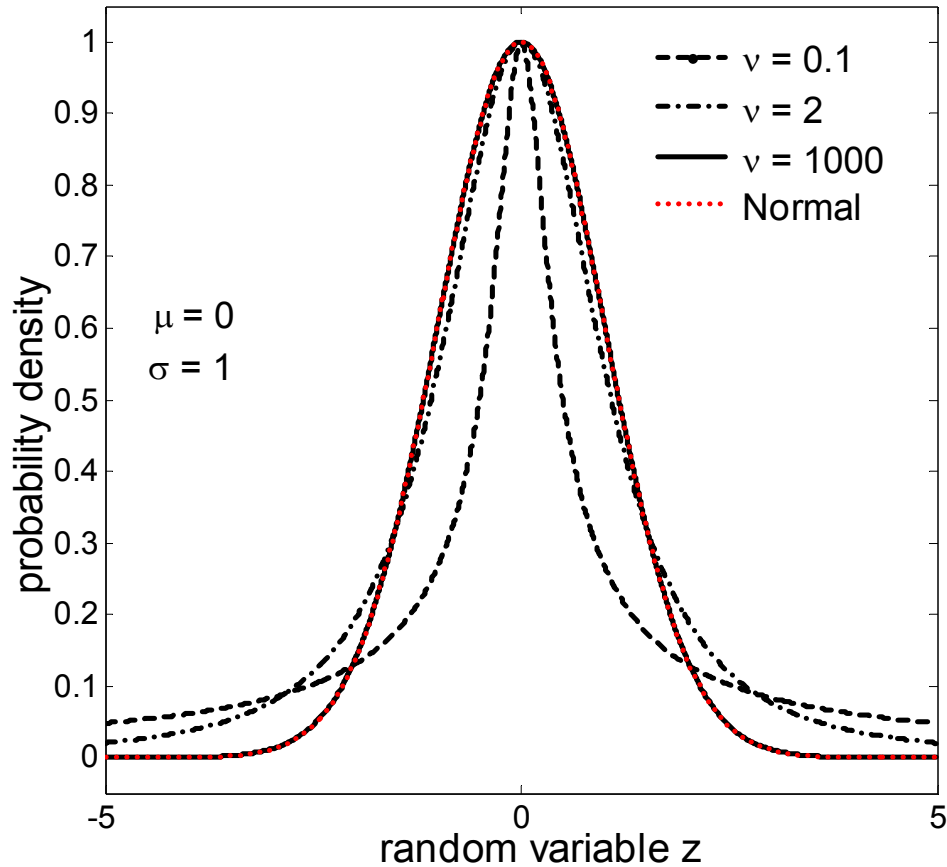


Figure 7.8 Student's t-distribution for various values of the degrees of freedom ν , compared to the normal distribution. (Curves are normalized to unity peak value with zero mean and unit variance).

7.2.2 Curve Fitting to the histogram of the estimated poles

In this section, histograms of the real and imaginary components of the estimated poles are plotted separately to find the best curve fit using the distribution fitting tool 'dfittool' in Matlab[®] 7.0.1. Figure 7.9 shows the best curve fits obtained using the Normal distribution and the Student's t-distribution for the histogram of the estimated pole real components of the 3rd order pair of dominant poles for an $SNR = 25$ dB (equivalently $E_{p3}/N_o = 14.4$ dB). The best fits are calculated by the 'dfittool' for a confidence of 95%, i.e. probability of estimating the parameters for this best fit is 95% accurate. Note that the solid curve given by the Student's t location-scale distribution shows a better curve fit than the dashed curve given by the Normal distribution. This distribution is the Student's t-distribution shifted in location to the mean (σ_{mean}) and scaled by

the empirically determined standard deviation. The estimated mean value ($\sigma_{mean} = -0.1297$) matches closely to the actual value ($\sigma = -0.1296$) of the real component of the 3rd dominant pole. The estimated standard deviation and the degrees of freedom values equal 0.0064 and 4, respectively.

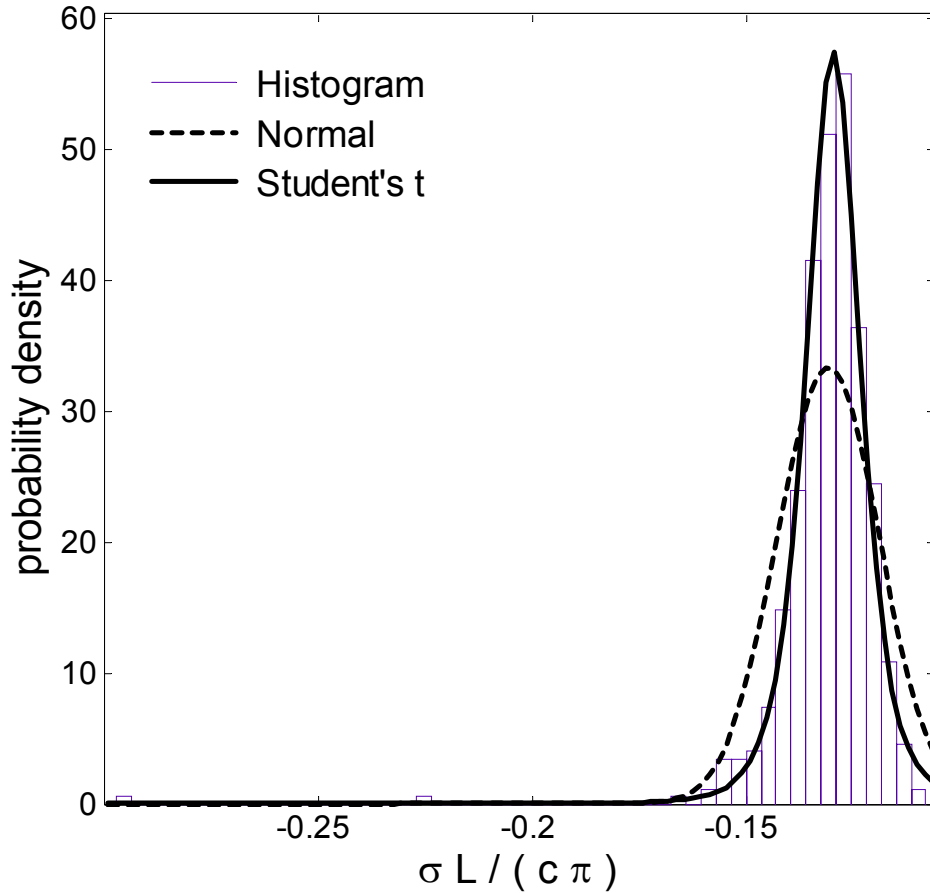


Figure 7.9 Best curve fit (95% confidence level) using Normal and Student's t-distribution to the histogram of the real component of the estimated poles in the cluster of the 3rd dominant pole identified in Fig. 7.7.

A similar curve fit to the histogram of the estimated pole imaginary components within the cluster formed about the 3rd order pair of dominant poles is shown in Fig. 7.10 for an E_p/N_o value of 14.4 dB obtained for $SNR = 25$ dB. Again, the Student's t location-scale distribution (solid curve) shows a better match than the Normal distribution (dashed curve). Moreover, the estimated mean $\omega_{mean} = 2.9336$ matches closely to the actual value $\omega = 2.9327$ of the imaginary component of the 3rd dominant pole. The estimated standard deviation and the degrees of freedom values equal 0.0062 and 3, respectively.

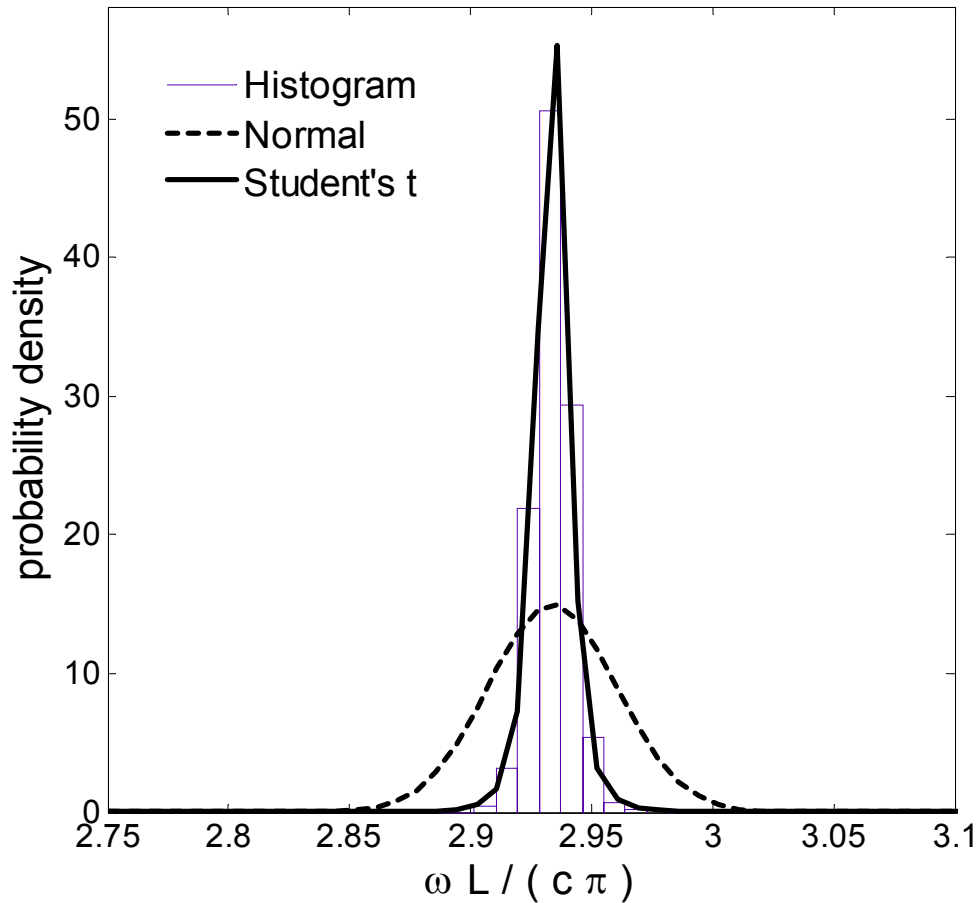


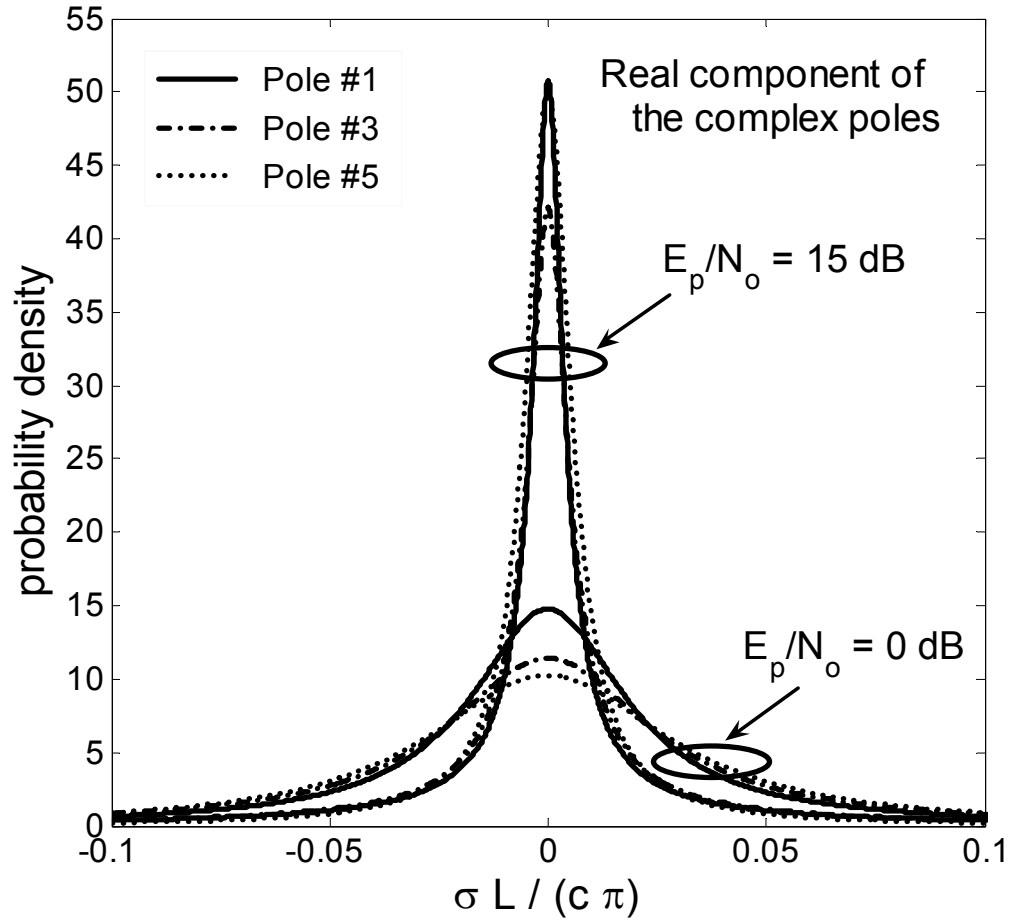
Figure 7.10 Best curve fit (95% confidence level) using Normal and Student's t-distribution to the histogram of the imaginary component of the estimated poles in the cluster of the 3rd dominant pole identified in Fig. 7.7.

7.2.3 Validity check of the E_p/N_o parameter

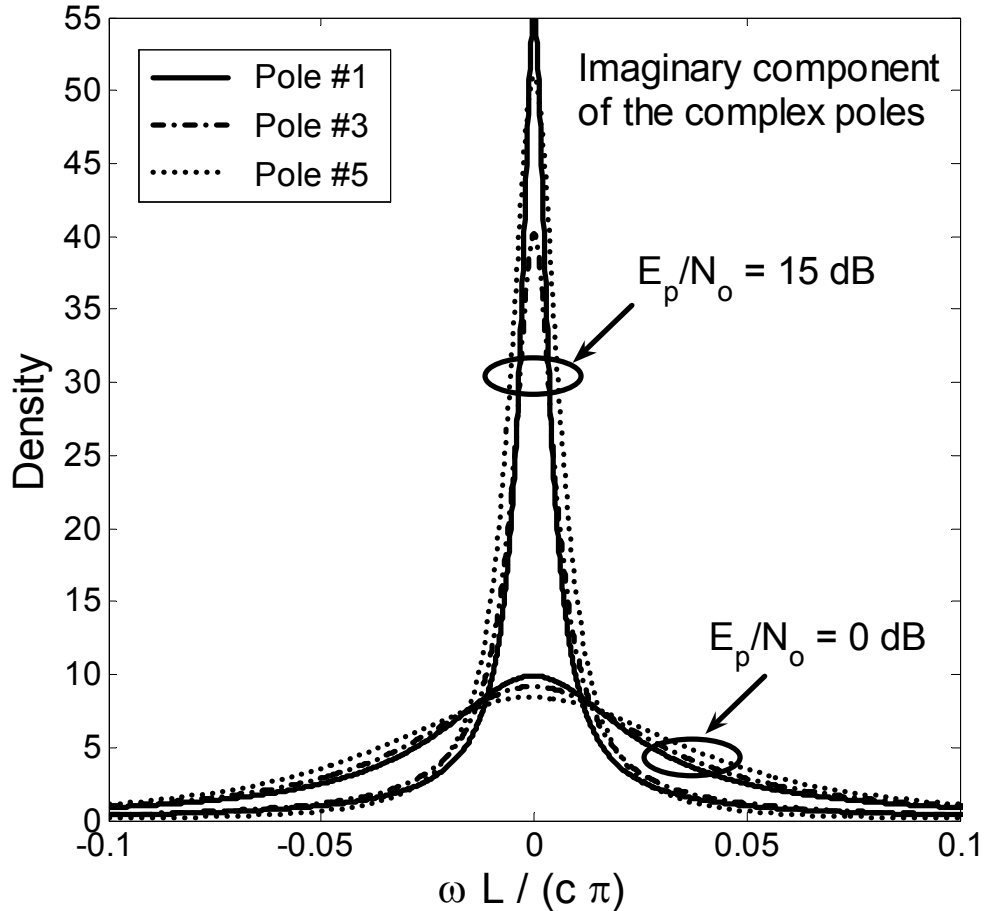
The parameter pole energy to noise ratio (E_p/N_o) was introduced in Section 7.1.3 with a note that it completely characterizes the distribution of the estimated poles and includes all the parameters that affect pole estimation for all the three dominant poles of the thin wire scatterer [17]. For the same value of E_p/N_o , the estimated statistical parameters such as the mean (μ), the standard deviation (σ) and the degrees of freedom (ν) of the real and the imaginary components of all the three dominant poles for were observed to be identical.

Fig. 7.11 (a) shows the Student's t-distribution of the real components of the three dominant poles for the thin wire scatterer with the parameter values identified using the best curve fit method outlined in Section 7.2.2. Similarly, Fig. 7.11 (b) shows the Student's t-

distribution for the imaginary components of the three dominant poles. In both the figures, the mean values are normalized to zero for comparison. The distribution plotted for the estimated standard deviation and the estimated degrees of freedom show a close match for each of the two examples of $E_p/N_o = 15$ dB and $E_p/N_o = 0$ dB. The next section presents the estimated statistical parameters corresponding to the best Student's t curve fit for different E_p/N_o and SNR values.



(a) Real component



(b) Imaginary component

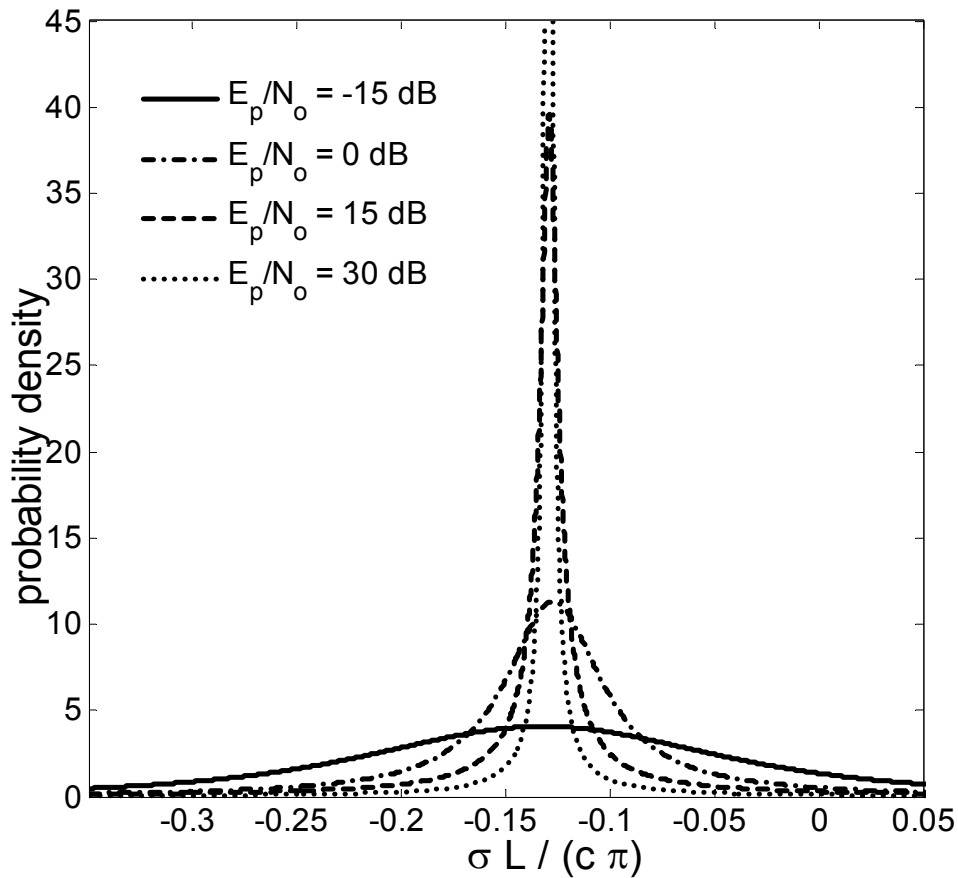
Figure 7.11 Comparison of the Student's t-distribution using the statistical parameters estimated from best curve fit to the corresponding histograms of the real and the imaginary components of the estimated poles in the clusters of the 1st, 3rd, and 5th dominant poles identified in Fig. 7.6.

7.3 Noise Effect on Statistical Distribution of the Estimated Poles

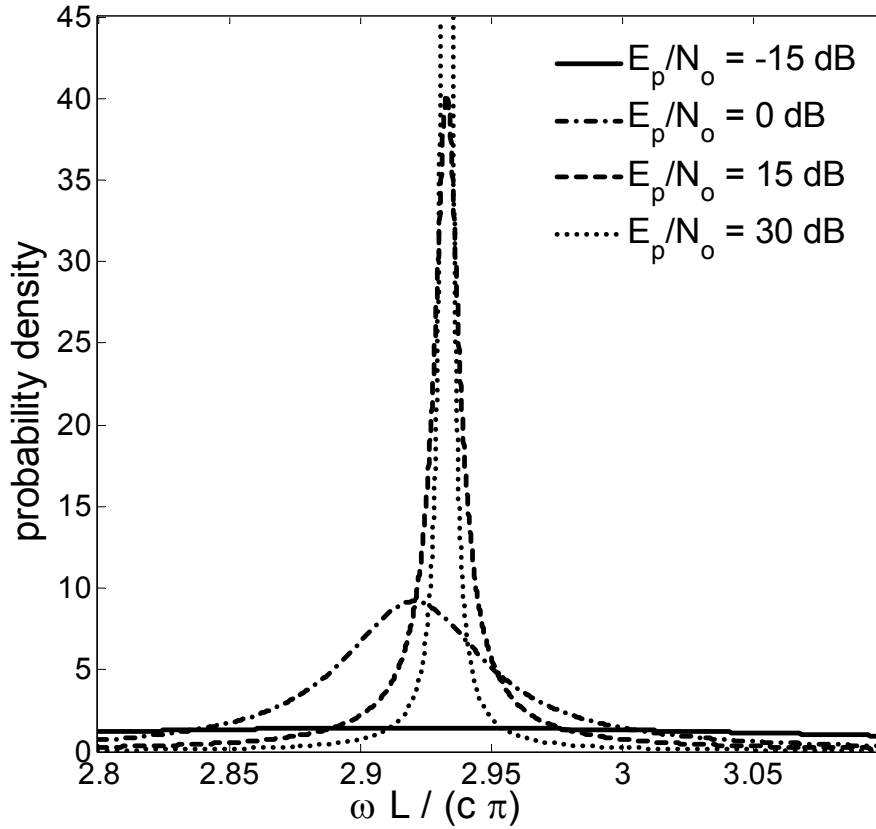
The best curve fits to the histogram of the real and imaginary component of the 3rd dominant pole were presented in the previous section,. Moreover, it was demonstrated that all the dominant poles of the thin wire scatterer described in Table 6-1 are affected equally for the same E_p/N_o values. In this section, the effect of the noise on the estimation of the real and the imaginary components is presented. Because the pole choice is not critical for a given E_p/N_o value, the mean value is normalized to zero to examine the effect of noise on the shape distribution. Thus, the effect of noise on the shape of the distribution, determined by the standard deviation and the degrees of freedom, is presented.

7.3.1 Effect of noise on the estimation of the real and the imaginary components

The Student's t-distribution parameters are recorded for the best fit to the histogram of the real and the imaginary component of the 3rd dominant pole for various E_p/N_o values. Fig. 7.12 (a) compares the statistical distributions of the real component of the 3rd dominant pole for different E_p/N_o values. Note that as the E_p/N_o value decreases, the standard deviation value increases due to the dominant effect of noise, causing the distribution to spread out. For the very low E_p/N_o value of -15 dB, the distribution exhibits a long tail that crosses the imaginary axis in the complex s-plane. This indicates that a significant number of estimated poles can have a positive real component resulting in an unstable estimated time domain response for very high noise levels. Moreover, the peak of the distribution curve, which corresponds to the estimated mean values, is very susceptible to noise and deviates about the true value for E_p/N_o values less than 0 dB.



(a) Real component



(b) Imaginary component

Figure 7.12 Comparison of the Student's t-distribution using the statistical parameters estimated from best curve fit to the corresponding histograms of the real and the imaginary components of the estimated poles in the cluster of the 3rd dominant pole identified in Fig. 7.7 for various E_p/N_o values.

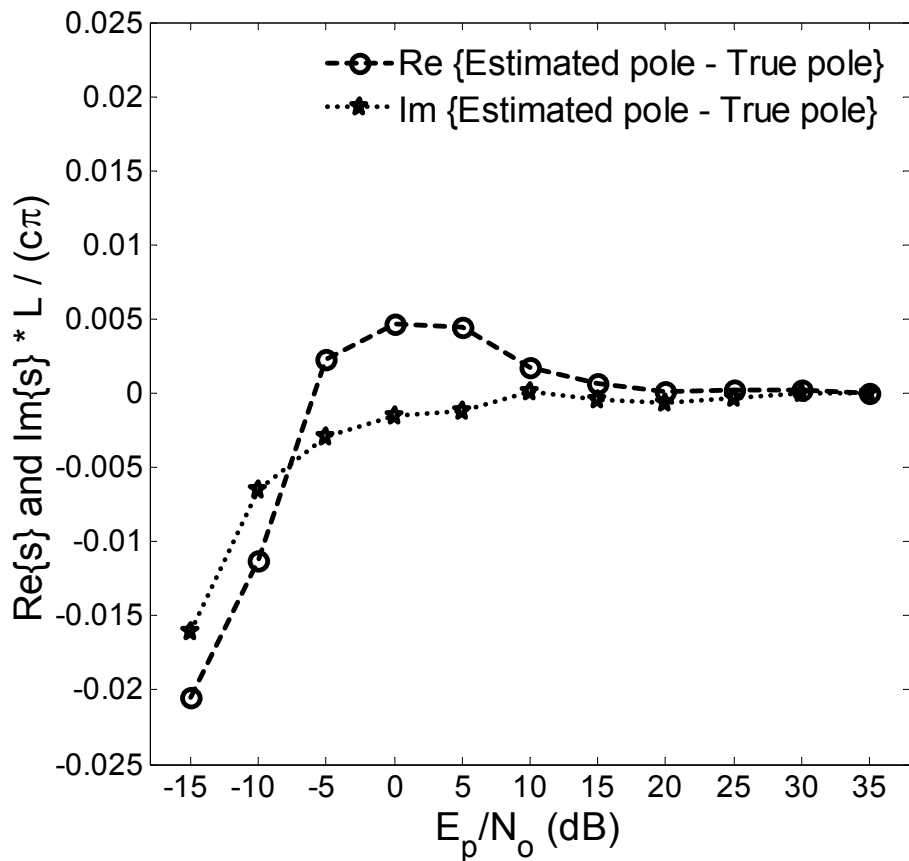
The imaginary component of the 3rd dominant pole pair behaves similar to the real component for the best-fit Student's t-distribution to different noise levels, which is defined by the E_p/N_o values. The following observations summarize the effect of noise on the imaginary component of the estimated complex poles as shown in Fig. 7.12 (b):

- As expected, the deviation in the expectation of the imaginary component increases with noise (i.e. the standard deviation value increases as the E_p/N_o value decreases).
- For very high noise levels ($E_p/N_o < 0$ dB), the distribution flattens out, indicating high uncertainty in estimating the imaginary component.
- The imaginary component is observed to be more susceptible to noise than the real component.

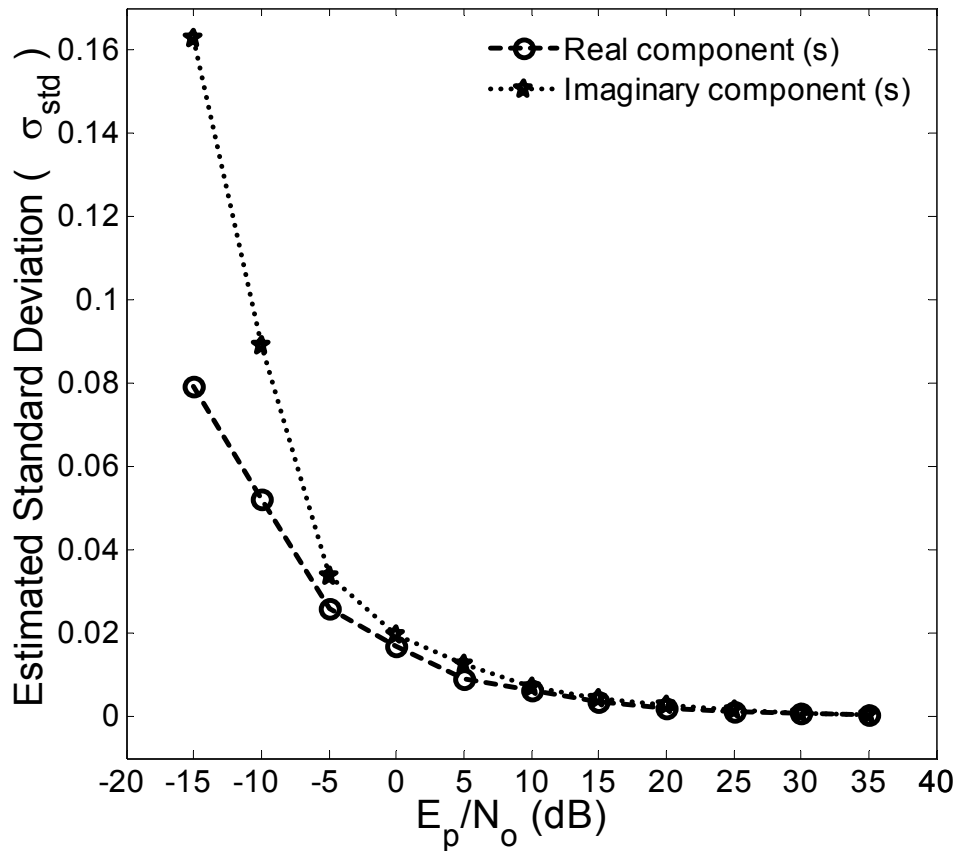
7.3.2 Effect of noise on the estimation of the statistical parameters

In the previous section, the effect of the noise on the estimation of the real and the imaginary components was presented separately in terms of the Student's t-distributions for the best fit to the histogram. This section presents the effect of noise on the statistical parameter estimation such as the mean, the standard deviation and the degrees of freedom. As previously illustrated, the choice of the pole is not critical for a given E_p/N_o value. Hence, although the results presented in this section are determined from the cluster formation about the 3rd order dominant pole, it is applicable to all dominant complex poles.

Figure 7.13 (a) compares the deviation in the estimated mean values of the real and the imaginary components from the actual value for different E_p/N_o values. Note that for $E_p/N_o > -5$ dB, the estimated mean value is within acceptable error region of ± 0.005 . And for $E_p/N_o > 20$ dB, the estimated mean values are accurate, which is also evident from the plot of the standard deviation versus the E_p/N_o values shown in Fig. 7. 13 (b).



(a) The estimated mean (μ)



(b) The estimated standard deviation (σ)

Figure 7.13 The estimated mean (μ), standard deviation (σ), and degrees of freedom (ν) recorded for the best fit Student's t-distribution to the corresponding histograms of the real and the imaginary components of the estimated poles in the cluster of the 3rd dominant pole identified in Fig. 7.7 for various E_p/N_o values.

The effect of noise on the estimation of statistical parameters for any chosen pole can be analyzed for E_p/N_o values. However, in practice the entire signal consisting of several dominant poles is affected by noise. Hence, it is important to determine the noise effect on all the dominant poles for different SNR values. Figure 7.14 compares the estimated standard deviation (σ) values for the real and the imaginary component estimation of the complex poles in the clusters of the 1st, 3rd and 5th dominant poles for different SNR values. The following observations summarize the effect of noise on the estimated standard deviation values, as seen in Fig. 7.14:

- Because the energy content of the pole decreases with increase in pole order, the standard deviation, for a given SNR , increases with the pole order.

- The real and imaginary components of each of the dominant pole pairs are equally affected by noise with the standard deviation values slightly greater for the imaginary components.
- For low SNR values, standard deviation values for the real component of the three dominant poles converges to a lower value than that of the imaginary component. Fig. 7.12 supports this observation that at high noise level, the estimation of the imaginary component is more susceptible to noise than the real component.
- For a given value of standard deviation, the difference in the curves along the abscissa in dB is equivalent to the difference in the energy of the dominant poles presented in Table 7.1, which is 9.8 dB between the 1st pole & the 3rd pole and 19.1 dB between the 3rd & the 5th pole.

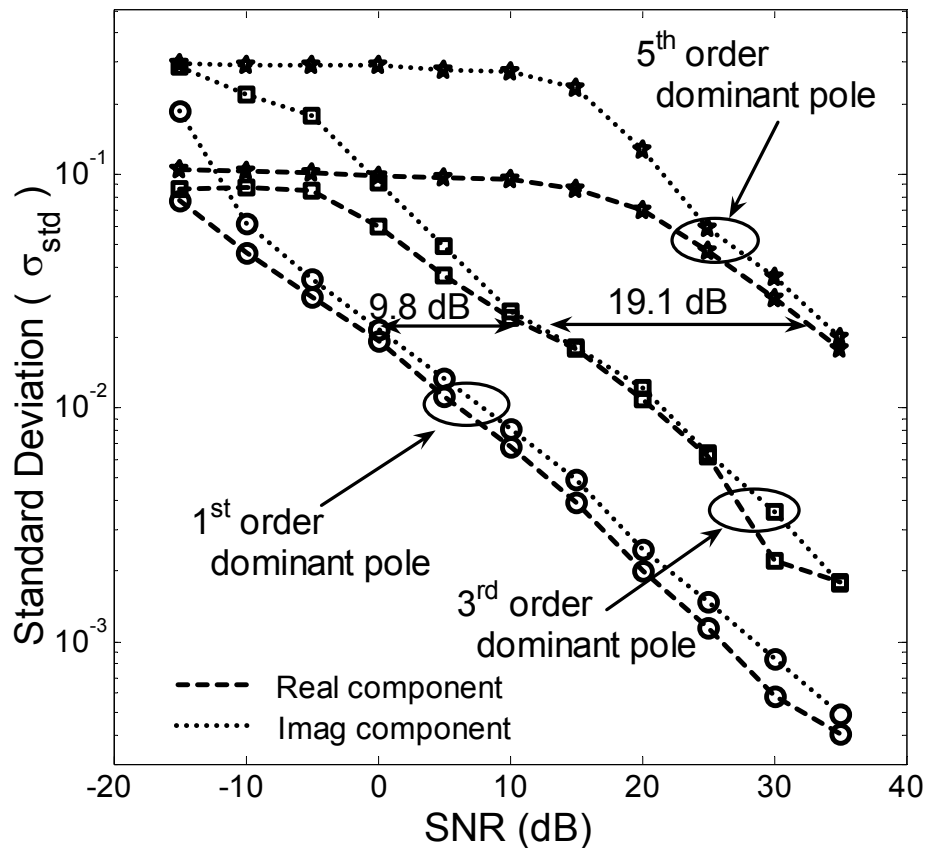


Figure 7.14 The estimated standard deviation (σ) values recorded for the best fit Student's t-distribution to the corresponding histograms of the real and the imaginary components of the estimated poles in the cluster of the 1st, 3rd and 5th dominant poles identified in Fig. 7.7 for different SNR values.

Similarly, Fig. 7.15 compares the estimated degrees of freedom (ν) values for the real and the imaginary components of the estimated poles in the 1st, 3rd and 5th dominant pole clusters for different SNR values.

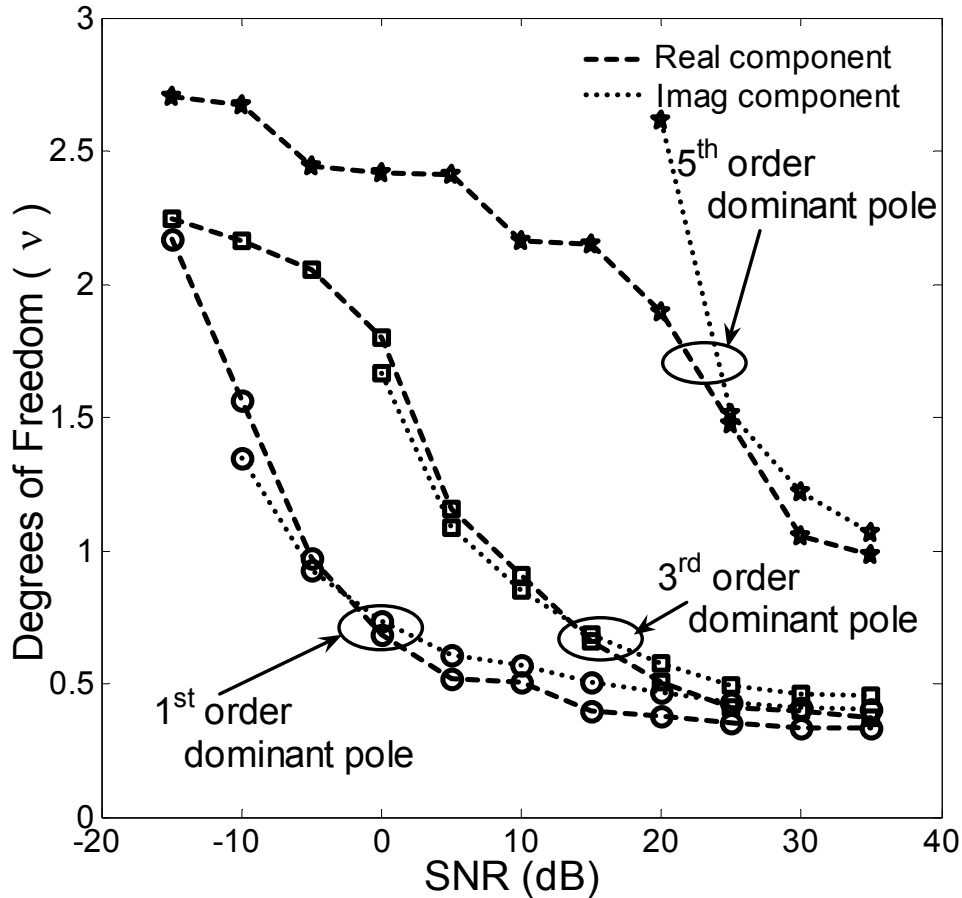


Figure 7.15 The estimated degrees of freedom (ν) values recorded for the best fit Student's t-distribution to the corresponding histograms of the real and the imaginary components of the estimated poles in the cluster of the 1st, 3rd and 5th dominant poles identified in Fig. 7.7 for different SNR values.

Note that a lower ν value indicates a sharp curve and a large ν value indicates a distribution with a shape close to a bell curve. The following observations summarize the effect of noise on the estimated degrees of freedom values, as seen in Fig. 7.15:

- For a given dominant order of poles, the sharpness of the shape of the distribution curve (given by the degrees of freedom ν) for the real and imaginary components are similar.

- Because the energy content of the pole is greater for lower pole order, the sharpness of the shape of the distribution curve (given by ν), for a given SNR , is also observed to be greater.
- For high SNR values, the sharpness of the distribution curve reaches a limit given by the convergence of the value for the estimated parameter ν .

7.4 Joint distribution over the complex s-plane

The effect of the noise on the estimation of the real and the imaginary components was presented in the previous section. This section presents the effect of noise on the joint estimation of the real and the imaginary components. The real component of the complex pole (damping coefficient) determines the energy content of the pole, which in turn determines the distribution of the imaginary component. This indicates that there should be a strong correlation in the estimation of the real and the imaginary component for a given dominant pole. The correlation between the real and the imaginary components is presented in Section 7.4.1.

A joint distribution of the real and imaginary components for a thin wire scatterer with three dominant poles is presented based on certain assumptions in Section 7.4.2. After identifying the optimal number of clusters in the complex s-plane, there are two options: estimate the fuzzy poles or estimate the statistical mean values within each cluster. Section 7.4.3 compares the fuzzy approach to the statistical approach (which uses fuzzy clustering) in terms of pole estimation accuracy.

7.4.1 Correlation between the real and the imaginary components

The cross-correlation coefficient of the real and the imaginary components of the estimated poles within the cluster of the 3rd order dominant pole is calculated as given by

$$C_{\sigma\omega} = \frac{E\left[(\sigma - \bar{\sigma})(\omega - \bar{\omega})\right]}{\sqrt{\text{var}(\sigma)\text{var}(\omega)}} \quad (7.4)$$

where $E[\cdot]$ is the expectation operator. The cross-correlation coefficient ($C_{\sigma\omega}$) offers insight into the influence of the estimated pole real component (σ) on the distribution of the imaginary component (ω). Fig. 7.16 plots the cross correlation coefficient ($C_{\sigma\omega}$) given by (7.4) for E_p/N_o

values. Note that for low E_p/N_o values corresponding to high noise level the real and the imaginary components of the estimated poles are nearly uncorrelated with $-0.05 \leq C_{\sigma\omega} \leq 0.05$. This is expected because for low E_p/N_o values the noise dominates over the damping coefficient effect. However, for $E_p/N_o > 8$ dB, the cross correlation coefficient ($C_{\sigma\omega}$) increases, indicating there is a strong effect of the damping coefficient on estimation of the imaginary component.

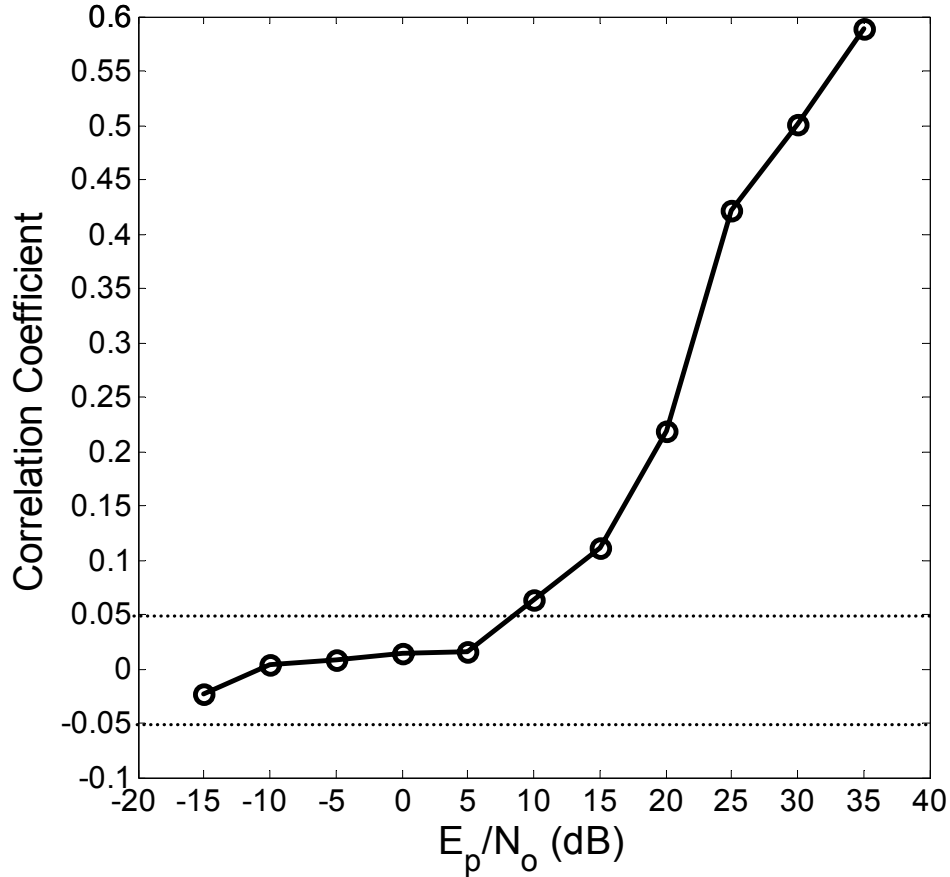


Figure 7.16 Cross-correlation coefficient ($C_{\sigma\omega}$) between the real and imaginary components of the estimated poles recorded for the cluster of the 3rd dominant pole identified in Fig. 7.7 for different E_p/N_o values.

7.4.2 Joint distribution of the real and the imaginary components

In the previous section, the real and the imaginary components of the estimated poles within the cluster of the 3rd order dominant pole of a thin wire scatterer were observed to be uncorrelated for high noise levels corresponding to the $E_p/N_o < 8$ dB. This observation permits us to make an assumption for the joint distribution for high noise levels. If the estimation of the real and the

imaginary components can be considered independent then their joint distribution is a product of their individual distributions [18]:

$$f_{\sigma\omega} = f(\sigma) f(\omega) \quad (7.5)$$

This joint distribution of the real and the imaginary components for the three dominant poles of a thin wire scatterer described in Table 6-1 is plotted in Fig. 7.17 for $SNR = 0$ dB. Note that the SNR is sufficiently low to invoke the above-mentioned assumption that the estimated real and the imaginary components are independent.

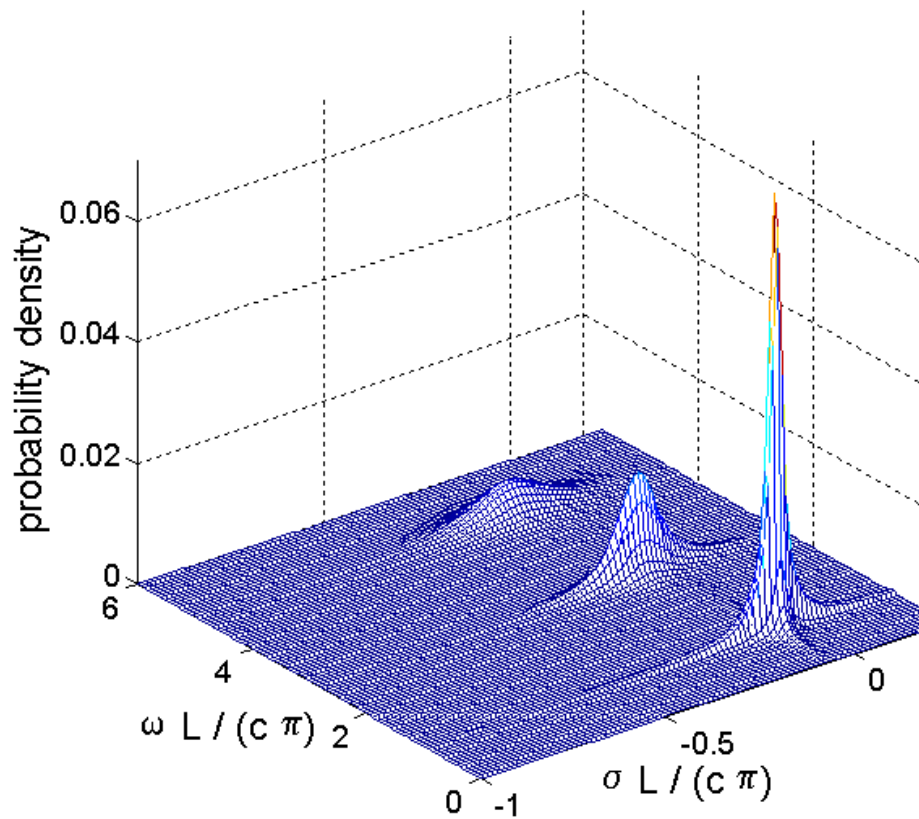


Figure 7.17 Joint distribution of the real and the imaginary components of the three dominant poles of the thin wire scatterer (described in Table 6-1) for $SNR = 0$ dB.

7.4.3 Enhanced Pole estimation with Fuzzy Clustering

In Chapter 6, fuzzy poles were presented and compared to the actual poles of the thin wire scatterer described in Table 6-1. In this chapter, the fuzzy clustering algorithm described in Chapter 6 was used to identify clusters about the dominant poles. The estimated fuzzy poles and

the statistical estimates of the dominant poles are compared to the analytically determined poles of the thin wire scatterer for $SNR = 0$ dB and 10 dB in Fig. 7.18. The fuzzy poles correspond to the optimal number of 9 clusters (shown in Fig. 6.11 for $SNR = 10$ dB). The statistical mean values of the dominant poles of the thin wire scatterer are estimated from the identified clusters about the dominant poles. Note that the estimated statistical mean values after fuzzy clustering offer a very close match to the dominant poles of the thin wires for both $SNR = 0$ dB and 10 dB.

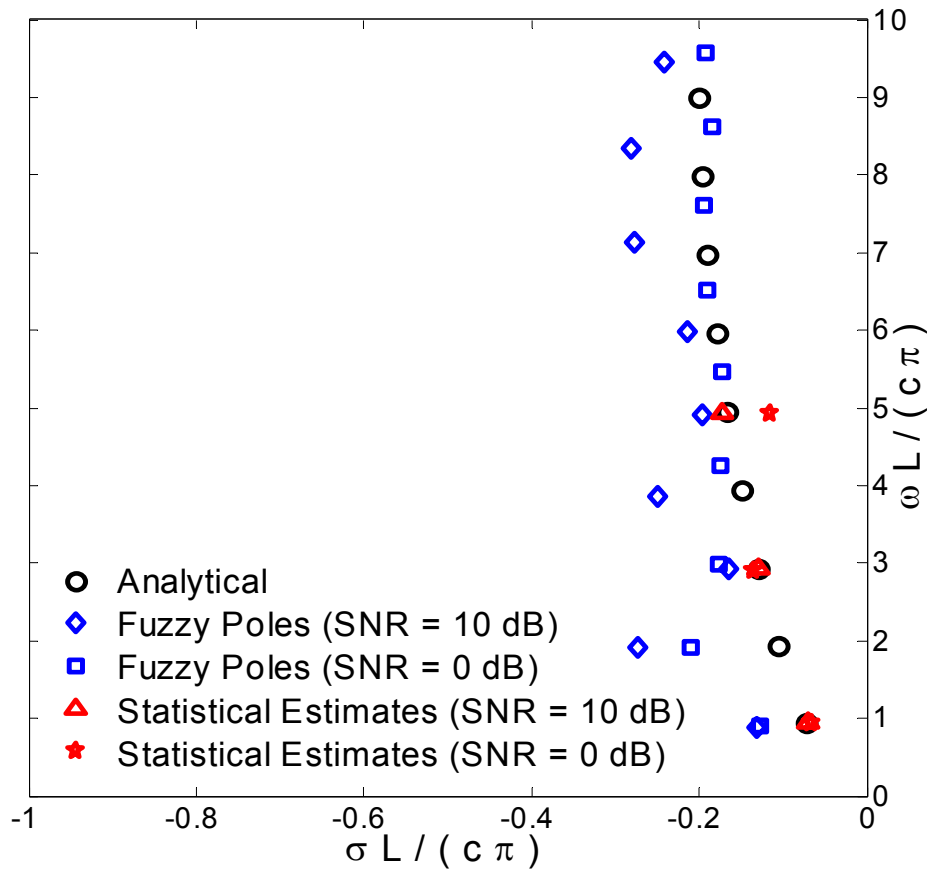


Figure 7.18 The estimated statistical mean values with fuzzy clustering and the fuzzy poles for $SNR = 0$ dB and 10 dB compared to the analytically determined complex poles of the thin wire scatterer described in Table 6-1.

The Unsupervised Optimal Fuzzy Clustering (UOFC) algorithm can be used to partition the estimated poles into clusters as well as determine the cluster centroids. After identifying the optimal number of clusters in the complex s-plane, there are two options: estimate the fuzzy poles or estimate the statistical mean values within each cluster. Figure 7.18 shows that after identifying the clusters, statistical approach offers better estimate of the actual pole.

7.5 Chapter Summary

This chapter presented a statistical investigation of the estimated complex poles of a noisy time-domain scatterer response. Thin straight wire scatterer responses were numerically analyzed for different noise levels. Complex poles cluster formations around the actual poles in the s-plane were exploited to determine the probability density distribution of the real and imaginary components, separately. A statistical curve fit using the 'dfittool' available in Matlab[®] 7.0.1 Statistical toolbox was applied to the histogram of real and imaginary components of the estimated complex poles within the cluster. The best curve fit was found to be a shifted and scaled form of the Student's t-distribution.

Based on the estimated statistical parameters such as the mean and the standard deviation, the probability density functions are plotted for various noise levels. In this chapter, we introduced a novel idea of pole energy to noise ratio (E_p/N_o) that completely captures the effect of noise on pole distribution. The proposed statement that E_p/N_o parameter completely defines the distribution is also validated. Another original contribution is determining a joint distribution of the real and imaginary components of the estimated poles in the complex s-plane.

Some important observations include:

1. For the same value of E_p/N_o the probability distribution of any pole is observed to be identical validating the proposed idea that E_p/N_o completely captures the effect of noise; see Fig. 7.11.
2. The standard deviation value increases as the E_p/N_o value decreases (i.e. as the noise level increases); see Fig. 7.12.
3. The imaginary component is observed to be more susceptible to noise than the real component; see Fig. 7.12.
4. The real and imaginary components of each of the dominant pole pairs are equally affected by noise with the standard deviation values slightly greater for the imaginary components; see Fig. 7.14.
5. At high noise level, the estimation of the imaginary component is more susceptible to noise than the real component; see Fig. 7.14 and Fig. 7.15.

6. For a given dominant pole order, the sharpness of the shape of the distribution curve (given by the degrees of freedom ν) for the real and imaginary components is similar; see Fig. 7.15.
7. Because the energy content of the pole is greater for lower pole order, the sharpness of the shape of the distribution curve (given by ν), for a given *SNR*, is also observed to be greater; see Fig. 7.17.

Advances in statistical characterization have promising applications in target identification and receiver design for wideband applications. After identification of the optimal number of clusters using the fuzzy clustering algorithms, the statistical approach offers better estimate of the actual pole compared to the estimated fuzzy poles (see Fig. 7.18).

References

- [1] K. S. Cho and J. T. Cordaro, "Calculation of the Singularity Expansion Method Parameters from the Transient Response of a Thin Wire," *Interaction Notes #379, AFRL Directed Energy Directorate*, Sept. 1979.
- [2] D. A. Ksienski, "Pole and Residue Extraction from Measured Data in the Frequency Domain Using Multiple Data Sets," *Mathematics Notes #80, AFRL Directed Energy Directorate*, Oct. 1984.
- [3] D. A. Ksienski and T. M. Willis, "Numerical Methods of Noise Reduction for Frequency Domain SEM," *Mathematics Notes #81, AFRL Directed Energy Directorate* Oct. 1984.
- [4] J. M. Pond, "Determination of SEM Poles from Frequency Responses," *Interaction Notes #408, AFRL Directed Energy Directorate*, July 1981.
- [5] A. Baev and Y. Kuznetsov, "Technique of ultra wideband radar target discrimination using natural frequencies," *Proceedings of the 15th International Conference on Microwaves, Radar and Wireless Communications, MIKON-2004*, vol. 3, pp. 905-908, May 2004.
- [6] A. Baev, Y. Kuznetsova, and A. Aleksandrov, "Ultra wideband radar target discrimination using the signatures algorithm," *Proceedings of the 33rd European Microwave Conference* vol. 3, pp. 987-990, Oct. 2003.
- [7] R. Carriere and R. L. Moses, "High resolution radar target modeling using a modified Prony estimator," *IEEE Transactions on Antennas and Propagation*, vol. 40 (1), pp. 13-18, Jan. 1992.
- [8] Y. Hua and T. K. Sarkar, "Matrix pencil method for estimating parameters of exponentially damped/undamped sinusoids in noise," *IEEE Transactions on Acoustics, Speech, and Signal Processing*, vol. 38 (5), pp. 814-824, May 1990.
- [9] M. VanBlaricum and R. Mittra, "Problems and solutions associated with Prony's method for processing transient data," *IEEE Transactions on Antennas and Propagation*, vol. 26 (1), pp. 174-182, Jan. 1978.
- [10] Y. Hua and T. K. Sarkar, "On SVD for estimating generalized eigenvalues of singular matrix pencil in noise," *IEEE Transactions on Signal Processing*, vol. 39 (4), pp. 892-900, Apr. 1991.
- [11] T. K. Sarkar and O. Pereira, "Using the matrix pencil method to estimate the parameters of a sum of complex exponentials," *IEEE Antennas and Propagation Magazine*, vol. 37 (1), pp. 48-55, Jan. 1995.
- [12] T. K. Sarkar, P. Sheeyun, K. Jinhwan, and S. M. Rao, "Application of the matrix pencil method for estimating the SEM (singularity expansion method) poles of source-free

- transient responses from multiple look directions," *IEEE Transactions on Antennas and Propagation*, vol. 48 (4), pp. 612-618, Apr. 2000.
- [13] A. Poggio, M. VanBlaricum, E. Miller, and R. Mittra, "Evaluation of a processing technique for transient data," *IEEE Transactions on Antennas and Propagation*, vol. 26 (1), pp. 165-173, Jan. 1978.
- [14] J. Cordaro and W. Davis, "Time-domain techniques in the singularity expansion method," *IEEE Transactions on Antennas and Propagation*, vol. 29 (3), pp. 534-538, Mar. 1981.
- [15] E. Kreyszig, *Advanced Engineering Mathematics*, 5th ed. New York: Wiley, 1983.
- [16] H. Stark and J. W. Woods, *Probability, Random Processes, and Estimation Theory for Engineers*, 2nd ed. Englewood Cliffs, N.J.: Prentice Hall, 1994.
- [17] W. H. Beyer, *CRC standard probability and statistics : tables and formulae*. Boca Raton, Fla.: CRC Press, 1991.
- [18] J. G. Proakis, *Digital Communications*, 4th ed. Boston: McGraw-Hill, 2001.

Chapter 8 – System level Performance Improvement using Pole–Dispersion Scatter Channel Model

Ultra-wideband (UWB) communication signal reception and channel capacity are limited by dispersion effects [1]. The antennas as well as the channel distort the transmitted pulse by dispersing (spreading) the signal energy over time, resulting in the performance degradation of correlation-based matched filter receivers [1-3]. This chapter presents experimental and simulated results demonstrating the advantage of using the pole-dispersion channel model proposed in Chapter 4 over conventional frequency-independent UWB channel dispersion models. Chapter 2 classified observable UWB channel dispersion into three categories: frequency (phase), resonant, and multipath dispersion. Chapter 3 demonstrated the limitations of various conventional UWB channel models in modeling all identified dispersion phenomena. Chapter 4 proposed a novel pole-dispersion UWB scatter channel model that includes frequency-dependent scatterer response based on the Singularity Expansion Method (SEM). The proposed channel dispersion model permits implementation of optimum matched filtering at the receiver in the presence of pulse distortion due to resonant dispersion.

Resonant dispersion of the incident pulse from scattering objects distorts the transmitted signal pulse-shape, reducing the signal-to-noise ratio at the output of the matched filter receiver (SNR_{out}) [4]. The proposed pole-dispersion UWB channel model can be used to provide a reference template for matched-filter receivers to compensate for the pulse distortion. Although channel dispersion cannot be mitigated, accurate modeling of the pulse distortion allows the receiver to capture the energy spreading of the distorted pulse. If the pulse distortion is expected

at the receiver, then matched filtering can be used to provide maximum achievable signal-to-noise ratio at the input to the receiver-detector.

The chapter begins in Section 8.1 with a brief tutorial on matched filtering at the receiver. Matched filtering in an ideal communication link with non-dispersive antennas and channel provides the maximum achievable signal-to-noise ratio (SNR) at the output of the filter. Section 8.1.1 develops an expression for the matched filter (MF) impulse response for a non-dispersive channel. Section 8.1.2 presents analytical expressions and prepares background for correlation based matched filtering in a dispersive channel with distorted received pulse. The matched-filter is easily implemented using a correlator, which is discussed in Section 8.1.3.

Section 8.2 presents matched filtering results for a non-dispersive UWB line-of-sight (LOS) channel. The transmit pulse-shape and the received signal pulse-shape for a LOS hallway environment are described in Section 8.2.1. The measured output of a correlation based matched filter receiver for this LOS UWB channel is presented in Section 8.2.2. In a communication link, the correlation peak of the matched-filter output is used as input to the detector. Section 8.2.3 presents the simulated performance of a measured non-dispersive LOS UWB communication link in terms of bit-error-rate (BER) at the output of the detector.

The received signal pulse-shape is distorted in dispersive channel conditions. Section 8.3 presents the performance of a correlation based MF receiver in the presence of resonant dispersion from finite dimensional scatterers. Section 8.3.1 describes the experimental setup for an indoor non-line-of-sight (NLOS) hallway environment that serves as a dispersive UWB channel. Section 8.3.2 presents correlation output results at the receiver using empirical data demonstrating superior performance of optimal matched filtering (OMF) versus conventional matched filtering (CMF). The performance improvement is shown in terms of the correlation-peak of the CMF and OMF matched-filter outputs. Section 8.3.3 presents performance improvement of the UWB communication link using a reference template based on the proposed pole-dispersion UWB channel model in terms of the bit-error-rate (BER) at the detector output.

Section 8.4 describes the susceptibility of the bit-error-rate (BER) performance of a UWB communication link using optimal matched filtering (OMF) to error in the channel estimation. Section 8.4.1 presents BER performance of OMF receiver using fewer numbers of dominant poles in modeling resonant dispersion response from scatterers. The effect of noisy channel impulse response (CIR) estimates on the BER performance of a communication link is

described in Section 8.4.2. Chapter 6 and Chapter 7 presented fuzzy and statistical approaches to model scatterer response in presence of noise with a few pairs of dominant poles. Section 8.4.3 presents BER performance using the estimated channel impulse response based on the combined fuzzy and statistical analysis for various noise levels. Performance improvement in terms of BER at the output of the detector is presented for simulated noisy time-domain responses of a thin wire scatterer. Finally, Section 8.5 summarizes important insights and observations presented in this chapter.

8.1 Matched Filtering Overview

Matched filtering prior to threshold detection at the receiver gives maximum achievable signal-to-noise ratio (SNR_{out}) at the input to the receiver detector [5, 6]. Matched filtering is used when the received signal pulse-shape is known at the receiver. And for a communication link using non-dispersive antennas and operating in a distortionless channel, the received pulse-shape is identical to the transmit pulse waveform.

The objective of the matched filtering approach is to determine the filter impulse response $h(t)$ or equivalently the filter transfer function $H(f)$ such that the SNR_{out} is maximized. Matched filtering approach maximizes the achievable SNR_{out} at the receiver by using a filter whose transfer function is given by [7]

$$H(f) = C_o \frac{S_R^*(f)}{N(f)} e^{-j\omega t_o} \quad (8.1)$$

where C_o denotes filter gain, $e^{j\omega t}$ is the phase shift introduced by the filter, $S_R(f)$ and $N(f)$ indicate the received signal spectrum and the noise power spectral density, respectively.

Section 8.1.1 presents an overview of matched filtering in a non-dispersive channel, i.e. a channel in which the received pulse waveform is not distorted and is identical to the transmit pulse waveform. The matched-filter impulse response, its output and achievable SNR_{out} are analytically described. Similarly, Section 8.1.2 discusses the conditions under which matched filtering can be achieved for a dispersive channel with pulse distortion. Performance degradation due to mismatch between the filter impulse response and the distorted received pulse is also described. Section 8.1.3 describes correlation implementation of matched filtering.

8.1.1 Matched Filtering in a Non-Dispersive Distortionless Channel

In an ideal communication link with a distortionless channel, the transmitted signal retains the pulse shape, and matched filtering provides the maximum achievable signal-to-noise ratio at the output of the filter (SNR_{out}) [5, 6]. For a distortionless channel with additive white noise having a power spectral density of $N(f) = N_o/2$, the matched-filter transfer function is given by

$$H(f) = \frac{2C_o}{N_o} S_R^*(f) e^{-j\omega\tau_o} \quad (8.2)$$

and the corresponding matched-filter impulse response is given by an inverse Fourier transform of the filter transfer function:

$$h(t) = F^{-1} \{ H(f) \} = K s(t_o - t) \quad (8.3)$$

where K is a constant (an amplitude scaling factor), t_o is the peak-signal time instant, and $s(t)$ is the known transmit signal waveform arriving at the receiver prior to signal reception. Note that the filter impulse response depends only on the known transmit pulse waveform. For simplicity, constant K is dropped without affecting the matched filter performance.

The output of the matched-filter with an impulse response of $h(t)$ matched to the transmit signal $s(t)$ for a received signal with white noise is given by [5]

$$\begin{aligned} y(t) &= \int_{x=0}^t r(x) h(t+x) dx = \int_{x=0}^t [s(x) + n(x)] h(t+x) dx \\ &= \int_{x=0}^t s(x) s(t_o - t + x) dx + \int_{x=0}^t n(x) s(t_o - t + x) dx \\ &= y_{ss}(t) + y_{ns}(t) \end{aligned} \quad (8.4)$$

where $r(t) = s(t) + n(t)$ is the received signal, $y_{ss}(t)$ is the time-autocorrelation function of the transmit signal pulse, $y_{ns}(t)$ is the time cross-correlation function of the transmit signal pulse and the receiver noise $n(t)$. The maximum autocorrelation value is achieved at the time instant t_o , which corresponds to the peak-signal time instant. If both the received signal and the reference signal are normalized to unit energy then the correlation peak $y_{ss}(t)$ at time-instant $t = t_o$ has maximum achievable value of unity. The sampled matched-filter output at the time instant t_o is used as input to the receiver detector [5]

$$y(t_o) = y_{ss}(t_o) + y_{ns}(t_o) \quad (8.5)$$

In presence of additive white Gaussian noise (AWGN) $n(t)$, a matched-filter with its impulse response matched to the transmit pulse waveform maximizes the signal-to-noise ratio at its output [5]. The signal-to-noise ratio at the output of the matched filter (SNR_{out}) is given by [8]

$$SNR_{out} = \frac{y_{ss}^2(t_o)}{E[y_{ns}^2(t_o)]} \quad (8.6)$$

which can be simplified to give [5]

$$SNR_{out,MF} = \frac{2E_s}{N_o}, \quad \text{where } E_s = \int_{-\infty}^{\infty} s^2(t)dt \quad (8.7)$$

where E_s is the energy content of the finite-duration received signal pulse. Expression (8.7) shows that the maximum achievable SNR_{out} depends on the energy of the signal and not the shape of the signal waveform. The performance of the matched filter receiver improves with the transmit signal energy, which can be increased either by increasing the transmit power or by increasing the signal duration [9].

8.1.2 Matched Filtering in a Dispersive Channel with Pulse Distortion

Frequency-dependent pulse scattering in a dispersive UWB channel distorts the transmitted pulse waveform. The resonant dispersion observed in the time-domain response of the scatterer (see Chapter 2) causes pulse distortion. If $s(t)$ were the transmitted pulse waveform, then the distorted received signal is given by

$$r(t) = h_c(t) \otimes s(t) + n(t) \quad (8.8)$$

where $h_c(t)$ is the frequency-dependent channel impulse response, and \otimes is the convolution operator. A conventional matched-filter (CMF) receiver uses the transmit pulse-shape as the reference template as given by (8.2) and (8.3). The CMF does not provide optimal results because the distorted received signal no longer matches the transmit pulse shape.

The output of the CMF with an impulse response of $h_{CMF}(t)$ matched to the transmit signal $s(t)$ for a distorted and noisy received signal is given by [5]

$$y(t) = \int_{x=0}^t r(x) h_{CMF}(t+x) dx \quad (8.9)$$

$$\begin{aligned}
&= \int_{x=0}^t [h_c(x) \otimes s(x) + n(x)] h_{CMF}(t+x) dx \\
&= \int_{x=0}^t s'(x) s(t_o - t + x) dx + \int_{x=0}^t n(x) s(t_o - t + x) dx \\
&= y_{s's}(t) + y_{ns}(t)
\end{aligned}$$

where $s'(t) = h_c(t) \otimes s(t)$ is the distorted received pulse-shape, $y_{s's}(t)$ is the time cross-correlation function of the received distorted pulse and the transmit signal pulse, and $y_{ns}(t)$ is the time cross-correlation function of the receiver noise $n(t)$ and the transmit signal pulse. The maximum value of the CMF output is sub-optimal, i.e. for both the received signal and the reference signal normalized to unit energy; the correlation peak is less than maximum achievable value of unity. This mismatch reduces SNR_{out} , and the CMF is no longer an optimal filter.

The signal-to-noise ratio at the output of the conventional matched filter (SNR_{CMF}) is given by [8]

$$SNR_{CMF} = \frac{y_{s's}^2(t_o)}{E[y_{ns}^2(t_o)]} = \xi^2 \frac{2 E_s}{N_o}, \quad \text{where } E_s = \int_{-\infty}^{\infty} s^2(t) dt \quad (8.10)$$

where ξ ($0 \leq \xi < 1$) is the mismatch factor that corresponds to the match in pulse-shape between the received distorted signal and the transmit signal. However, optimal implementation of the matched-filtering in a dispersive channel is possible if the frequency-dependent channel impulse function is known. The conventional channel models are frequency-independent and hence, use conventional matched-filter for distorted received signal. A frequency-dependent channel model that incorporates scatterer response can be convolved with the transmit pulse shape to provide the optimal matched filter impulse response.

An optimal matched-filter (OMF) uses an impulse response that is obtained by convolving the transmit signal pulse-shape with the estimated frequency-dependent channel impulse response (CIR). The OMF provides optimal results because the received signal distortion is incorporated in the filter impulse response. An accurate estimate of the frequency-dependent channel impulse response gives an exact match between the distorted received signal and the reference signal. The impulse response of the OMF is given by

$$h_{OMF}(t) = s''(t_o - t) \quad (8.11)$$

where $s'(t) = h_c'(t) \otimes s(t)$ is an estimate of the distorted received pulse-shape $s'(t)$, and $h_c'(t)$ is the estimated channel impulse response (CIR). The CIR estimate includes the frequency-dependent scatterer response that causes pulse distortion. The output of the OMF with an impulse response of $h_{OMF}(t)$ matched to the convolution of the transmit signal $s(t)$ and the estimated CIR for a distorted and noisy received signal is given by

$$\begin{aligned}
y(t) &= \int_{x=0}^t r(x) h_{OMF}(t+x) dx & (8.12) \\
&= \int_{x=0}^t [h_c(x) \otimes s(x) + n(x)] h_{OMF}(t+x) dx \\
&= \int_{x=0}^t s'(x) s''(t_o - t + x) dx + \int_{x=0}^t n(x) s''(t_o - t + x) dx \\
&= y_{s's''}(t) + y_{ns''}(t)
\end{aligned}$$

where $y_{s's''}(t)$ is the time cross-correlation function of the received distorted pulse-shape and its estimate, and $y_{ns''}(t)$ is the time cross-correlation function of the estimated received signal pulse and the receiver noise $n(t)$. The correlation peak of the OMF output is close to the optimum value of unity depending on the accuracy of the channel estimate. For both the received signal and the filter impulse response normalized to unit energy; the correlation peak is close to the maximum achievable value of unity.

The signal-to-noise ratio at the output of the optimal matched filter (SNR_{OMF}) is given by

$$SNR_{OMF} = \gamma^2 \frac{2E_{s'}}{N_o}, \quad \text{where } E_{s'} = \int_{-\infty}^{\infty} s'^2(t) dt \quad (8.13)$$

where $\gamma (\rightarrow 1)$ is the fraction of received signal energy captured using the reference template signal corresponding to the channel impulse response estimation error. The optimal implementation of the matched-filtering in a dispersive channel is possible only if the frequency-dependent channel impulse can be accurately estimated. Frequency-dependent pole-dispersion channel model based on the singularity expansion method (SEM) can be used to estimate the channel impulse response.

8.1.3 Matched-Filter Implementation using Correlation Detection

Matched filtering can be implemented using a variety of receivers, most popular being the correlation type receiver [5]. The previous sections described the matched-filter impulse response given by (8.3) and (8.11) as a time reversed version of the expected received pulse delayed by the pulse-duration for causality [10]. The matched filter being a time-invariant linear filter, its output is given by convolution of the input and the filter impulse response. The convolution process involves time-reversing either the input pulse or the filter impulse response. If the matched-filter impulse response is time reversed during the convolution process then the output of the filter is actually a cross-correlation of the received signal and its expected version at the receiver. Hence, a correlation-based receiver that correlates the received signal pulse-shape with the expected version of the received signal is a valid matched filter receiver [11]. Figure 8.1 illustrates correlation-based implementation of matched-filter receiver.

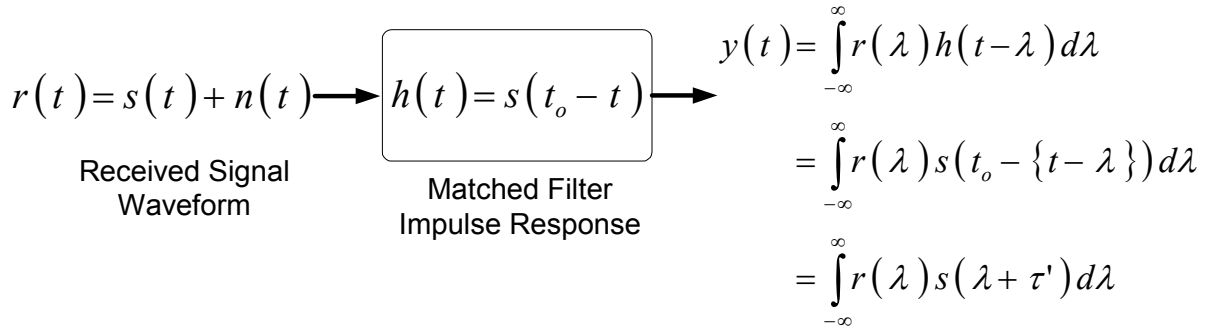
The correlation based matched-filter receiver uses a reference template to correlate with the received signal waveform. For a non-dispersive distortionless channel, a correlation based matched-filter receiver uses the transmit signal waveform as the reference template waveform. This is equivalent of having a filter with its impulse response matched to the transmit signal waveform as given by

$$h_{MF}(t) = s(t_o - t) \Leftrightarrow v_{ref}(t) = s(t) \quad (8.14)$$

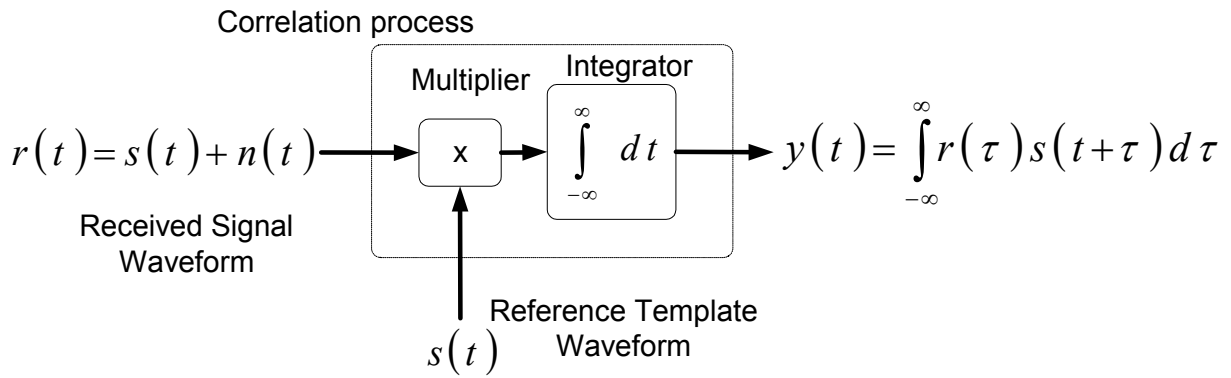
where $h_{MF}(t)$ is the matched-filter impulse response, $v_{ref}(t)$ is the reference template waveform for correlation based matched-filter, and $s(t)$ is the transmit pulse waveform. Similarly, for a dispersive channel with distorted received signal, a correlation-based optimal matched filter is realized by

$$h_{OMF}(t) = s''(t_o - t) \Leftrightarrow v_{ref,OMF}(t) = s''(t) = h_c'(t) \otimes s(t) \quad (8.15)$$

where $h_{OMF}(t)$ is the optimal matched-filter (OMF) impulse response, $v_{ref,OMF}(t)$ is the reference template waveform for correlation based OMF, $s''(t)$ is the estimated distorted received pulse waveform, and $h_c'(t)$ is the estimated channel impulse response.



(a) Matched-filter receiver



(b) Correlation-based receiver

Figure 8.1 Correlation-based implementation of matched-filter (MF) receiver.

8.2 Matched Filtering in a Non-Dispersive LOS UWB Channel

The previous section introduced matched filtering for both distortionless and dispersive channels. Matched filtering implementation using a correlation type receiver with a reference template that is correlated with the received signal waveform is briefly described. This section presents experimental results for matched filtering in a non-dispersive distortionless UWB channel. Section 8.2.1 describes an indoor line-of-sight (LOS) hallway environment over a short distance that is chosen to represent a distortionless UWB channel. The received signal waveform in a LOS condition inside a hallway environment is an attenuated and delayed version of the transmitted signal waveform retaining the transmit pulse shape.

Section 8.2.2 describes the output of the correlation type implementation of matched filter receiver. Section 8.2.3 describes the performance of the matched filter receiver in a distortionless UWB channel in terms of the achievable bit-error-rate (BER) at the output of the detector.

8.2.1 Experiments in an Indoor LOS Hallway Environment

An indoor hallway environment over a short distance can be considered to be a non-dispersive channel. Figure 8.2 shows an illustration of an indoor line-of-sight (LOS) hallway environment with a separation of 0.95 m. Two TEM horn antennas are used with a frequency range of 500 MHz to 12 GHz. The TEM horn antennas for transmission and reception are mounted on a pedestal at a height of 0.83 m.

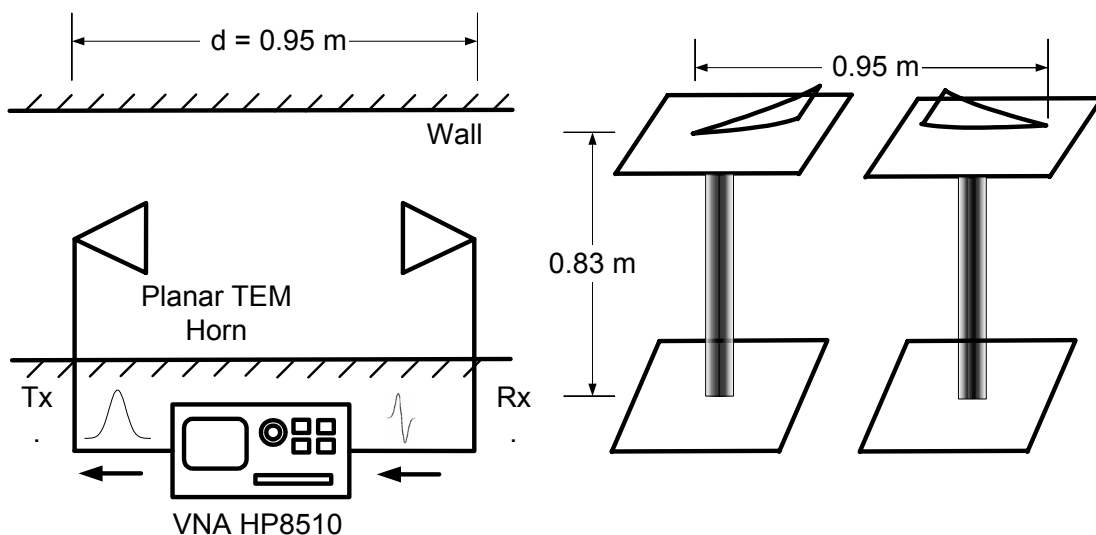


Figure 8.2 Measurement setup using two planar TEM horn antennas mounted on pedestals in a hallway environment oriented for direct line-of-sight (LOS).

Frequency-domain measurements are conducted using a vector network analyzer (HP-VNA #8510) over the frequency range of 50 MHz to 20.05 GHz. The inverse Fourier transform of the step frequency-domain measurements of the transmit signal is a Gaussian pulse with 50-psec duration and is shown in Fig. 8.3. The peak of the Gaussian transmit pulse is normalized to unity and shown over a 1 nsec time-window.

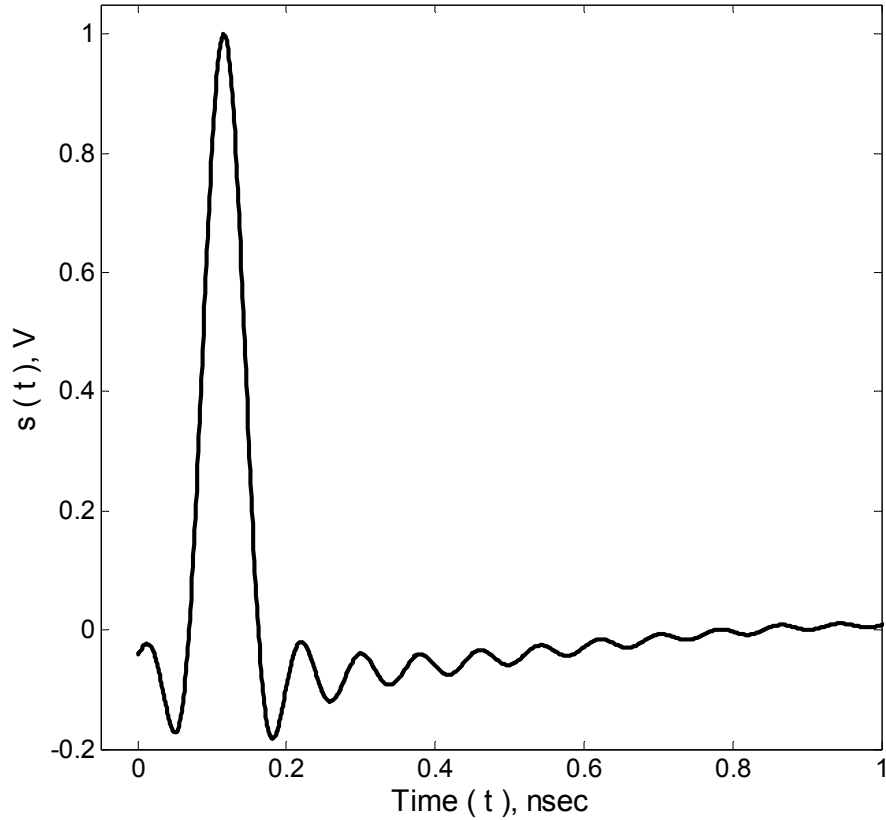


Figure 8.3 The Gaussian pulse of duration 50-psec at the input to the transmitting antenna obtained after IFFT of the measured frequency-domain response using an HP-8510 vector network analyzer (VNA).

The received signal waveform in a LOS condition inside a hallway environment is an attenuated and delayed version of the transmitted signal waveform. If $s(t)$ is the transmitted signal, then the received signal is given by

$$r(t) = A_o s\left(t - \frac{d}{c}\right) + n(t) \quad (8.16)$$

where A_o is the attenuation introduced by the channel, d is the separation and c is the speed of light. For the transmitted pulse waveform shown in Fig. 8.3, the received signal is an attenuated, noisy and delayed version of the transmit pulse and is shown in Fig. 8.4.

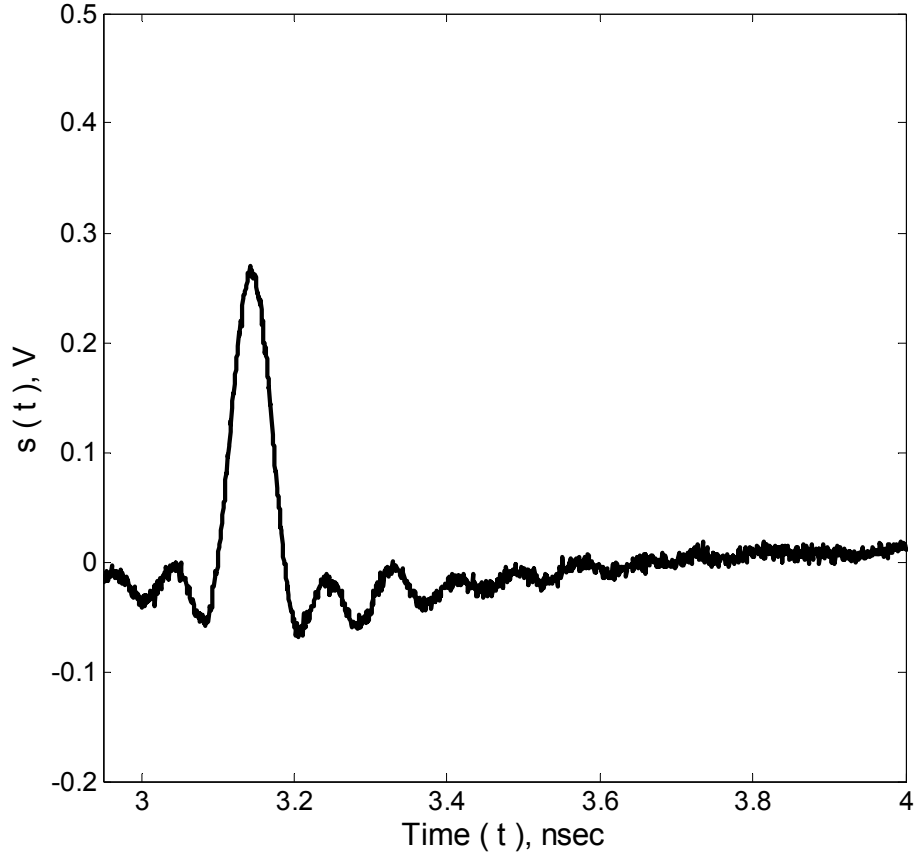


Figure 8.4 Received pulse in an indoor hallway environment at a distance of 0.95 m from the transmit antenna for the experiment setup shown in Fig. 8.2 and transmit pulse-shape shown in Fig. 8.3.

8.2.2 Correlation based Matched Filter Receiver

For a non-dispersive distortionless channel, a correlation based matched-filter (MF) receiver uses the transmit signal waveform as the reference pulse template as given by (8.14). The received signal shown in Fig. 8.4, and the reference signal based on the transmit pulse shown in Fig. 8.3 are normalized to unit energy to evaluate the performance of MF receiver. In this experiment in a LOS distortionless channel, the output of the matched filter receiver given by (8.4) is shown in Fig. 8.5, with the correlation peak equal to the maximum achievable value of unity. This maximum value of matched-filtering correlation output of unity is obtained only when the transmitted signal wave shape is maintained, i.e. the pulse is undistorted.

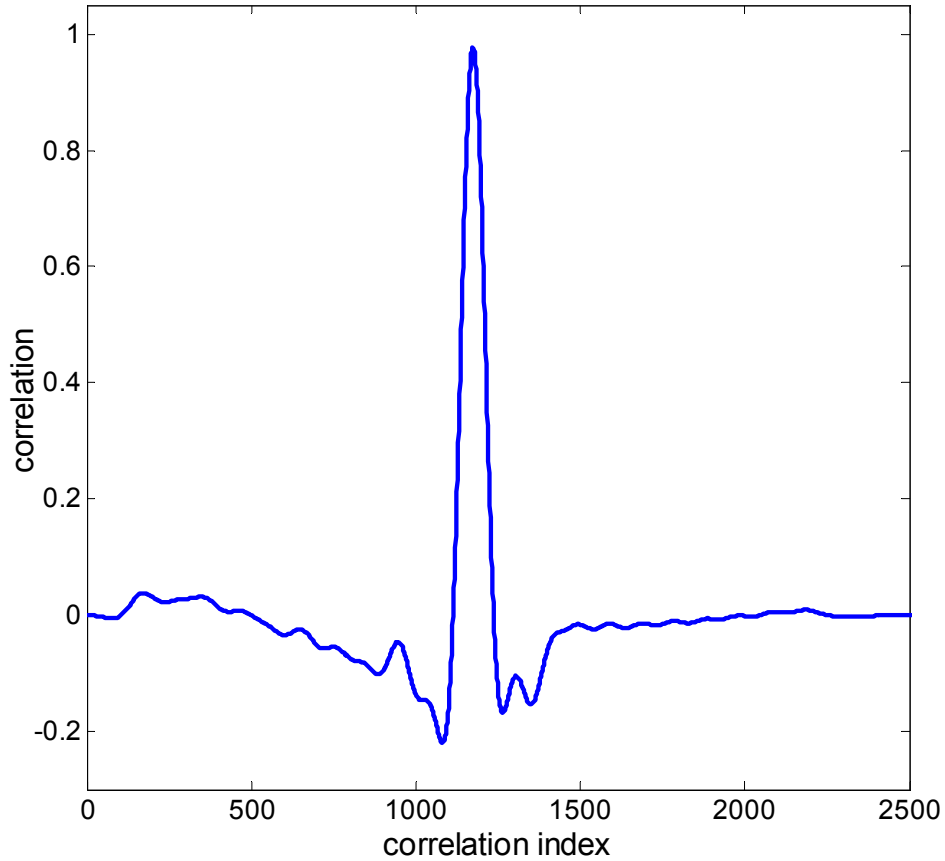


Figure 8.5 Correlation-based matched-filter output given by (8.4) for ideal distortionless channel conditions using the reference template waveform as the transmitted signal pulse-shape as given by (8.14). The received signal shown in Fig. 8.4 and the reference signal shown in Fig. 8.3 are energy normalized before matched-filtering.

8.2.3 Bit-Error-Rate Performance in a Distortionless UWB Channel

In a communication link, the correlation peak of the matched-filter output, given by (8.5), is used as input to the detector. The performance of a matched filter receiver is usually quantified using bit-error-rate (BER). Figure 8.6 illustrates the bit-error-rate (BER) simulation of a UWB communication link based on the measured transmit and received signals in an indoor LOS hallway environment. The measured received signal shown in Fig. 8.4 is phase modulated using random binary bits generated by the data source. This received signal is then corrupted with noise corresponding to various levels of E_b / N_o , i.e. the ratio of pulse energy to the noise power spectral density.

The correlation based matched-filter receiver cross-correlates the noisy corrupted received signal with the transmit pulse-shape as the reference signal as shown in Fig. 8.1(b). The sampled output of the matched filter at the time instant t_o , corresponding to the peak signal instant is used as input to the threshold detector. The detected data bits d_{est} are compared to the randomly generated data bits d to estimate the probability of error or the bit-error-rate (BER).

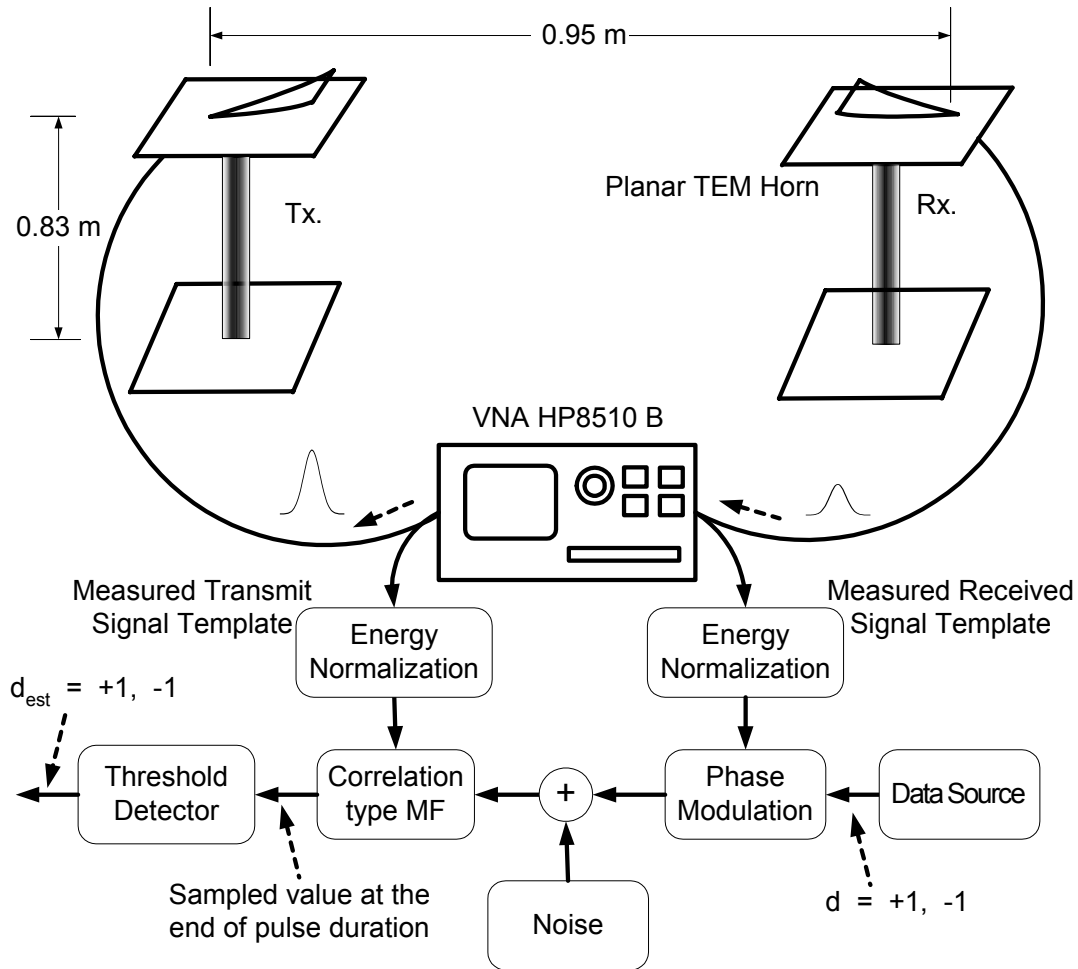


Figure 8.6 Block diagram of a UWB communication link simulated to determine bit-error-rate (BER) based on the *measured* transmit and received signals respectively shown in Fig. 8.3 and Fig. 8.4 in an indoor LOS hallway environment.

The BER performance of binary phase modulation in a distortionless AWGN channel is given by [7]

$$BER_{BPSK} = Q\left(\sqrt{\frac{2E_b}{N_o}}\right), \quad \text{where } E_b = \int_{-\infty}^{\infty} r^2(t)dt \quad (8.17)$$

where E_b is the energy content of the received signal waveform, and Q function is given by [7]

$$Q(x) = \frac{1}{\sqrt{2\pi}} \int_x^{\infty} e^{-\lambda^2/2} d\lambda \quad (8.18)$$

The bit-error-rate (BER) performance of correlation based matched filter receiver inside a LOS distortionless hallway environment for phase modulation is shown in Fig. 8.7. Note that performance is close to optimal with negligible deviation from the analytically determined performance due to measurement and numerical errors. This near-optimal performance as seen in Fig. 8.7 is because the maximum value of matched-filtering correlation output is close to unity as seen in Fig. 8.5.

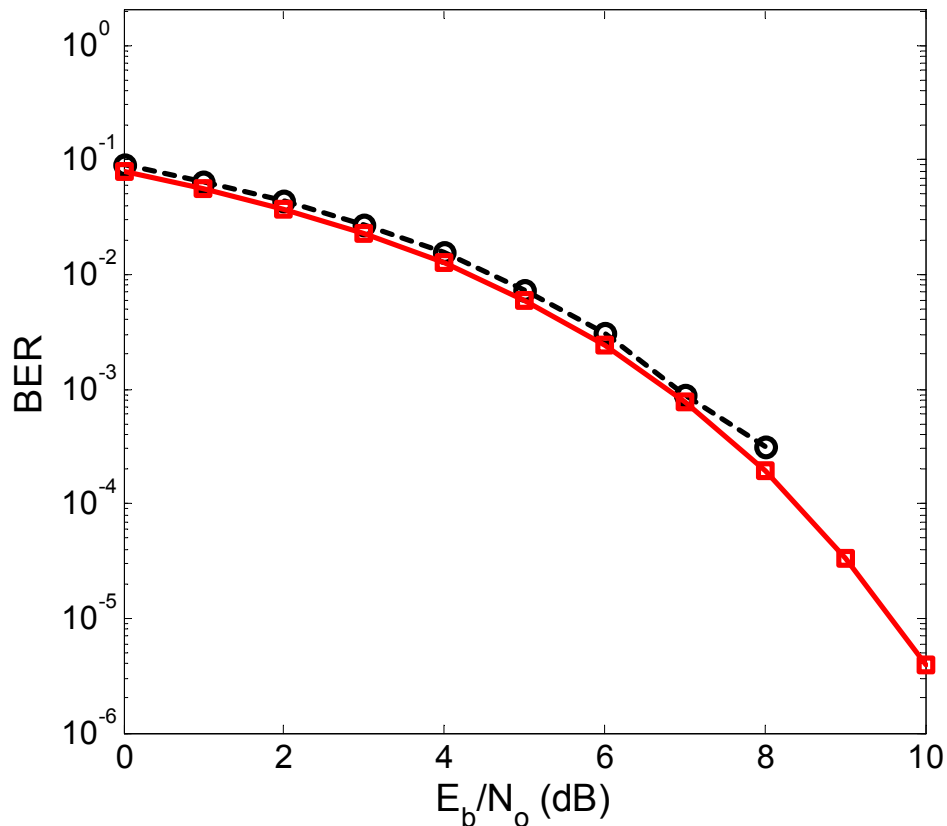


Figure 8.7 Bit-error-rate (BER) performance of a communication system simulated with binary phase modulation shown in Fig. 8.6 using *measured* transmit pulse (Fig. 8.3) and receive pulse (Fig. 8.4) waveforms in a distortionless UWB channel. The simulated BER performance from measured signals is shown by dashed line and the analytically determined BER given by (8.17) is shown by solid line.

8.3 Matched Filtering in a Dispersive NLOS UWB Channel

The previous section presented the performance of matched filtering in a distortionless line-of-sight UWB channel in terms of the matched filter output and bit-error-rate (BER). This section presents experimental results for matched filtering in a dispersive UWB channel where the received signal is significantly distorted. Section 8.3.1 describes an indoor obstructed non-line-of-sight (NLOS) path around a corner in a hallway to form a dispersive UWB channel. The experimental setup and observed pulse distortion due to resonant scattering from a fire extinguisher as a scatterer is also described.

Section 8.3.2 describes the output of the correlation type implementation of matched filter receiver for both a conventional matched filter (CMF) and an optimal matched filter (OMF). Section 8.3.3 describes the performance of the CMF and OMF receivers in terms of the achievable bit-error-rate (BER) at the output of the detector. Improvement in BER performance of the UWB communication link using reference template based on the proposed pole-dispersion UWB channel model is demonstrated.

8.3.1 Indoor NLOS Hallway Environment

The indoor hallway environment with obstructed conditions caused by a corner shown in Fig. 8.8 was used to form a dispersive channel. A fire extinguisher was present, creating a finite-dimensional scatterer. The TEM horn antennas for transmission and reception, mounted on a pedestal at a height of 0.83 m, are placed about 1.15 m from the scatterer. The scatterer presented here is a fire extinguisher of diameter 13 cm, and height 43.25 cm. Scatter response was measured in the frequency-domain using a vector network analyzer (HP-VNA8510) over the frequency range of 50 MHz to 20.05 GHz.

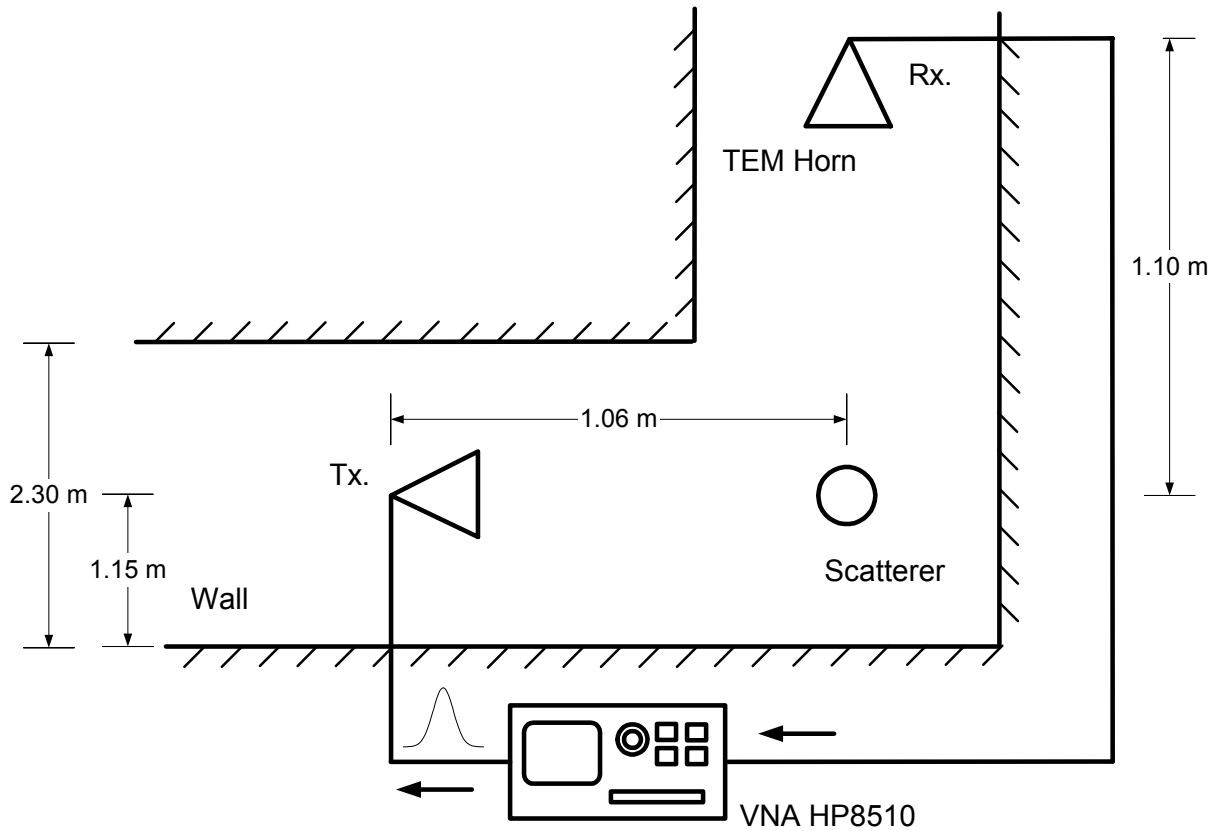


Figure 8.8 Measurement setup using two planar TEM horn antennas mounted on pedestals in a non-line-of-sight (NLOS) around a corner hallway environment.

For the transmitted signal waveform shown in Fig. 8.3, the received signal waveform in an obstructed (NLOS) condition inside a hallway environment with a fire extinguisher as a scatterer, is a significantly distorted version of the transmitted signal waveform. Figure 8.9 shows the received signal after subtracting for the unwanted responses from doorknobs and doorframes, and after deconvolving for the antenna response. The scatterer response was isolated using time gating of the received signal, which is described in Section 4.2. The received signal pulse-shape consists of a specular component (negative spike in Fig. 8.9) followed by the resonant dispersion component.

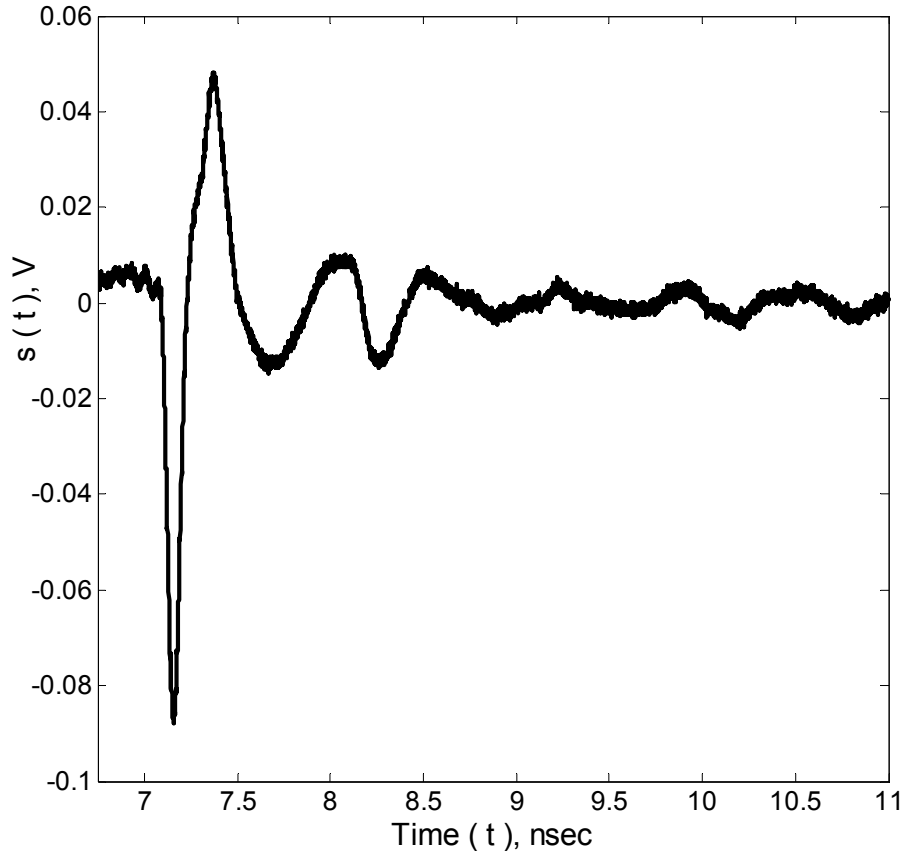


Figure 8.9 Received distorted pulse from a fire extinguisher of diameter 13 cm, and height 43.25 cm around a corner in an indoor hallway environment for the transmitted pulse shown in Fig. 8.3, with obstructed condition between antennas as shown in Fig. 8.4.

The resonant dispersion component observed after the specular reflection component is a frequency dependent phenomenon that cannot be modeled using conventional channel models. The received signal after subtracting for the unwanted scatter responses and after deconvolving for the antenna response is processed using the SEM approach to determine poles and residues associated with the scatterer response. The Matrix Pencil Method (MPM) of Section 4.1.3 is used to extract the poles and the corresponding residues from the transient response as described in Section 4.2.2 and Section 4.2.3. The dominant pair of complex conjugate poles based on the energy content as described in Section 5.3 and their corresponding residues are shown in Fig. 8.10.

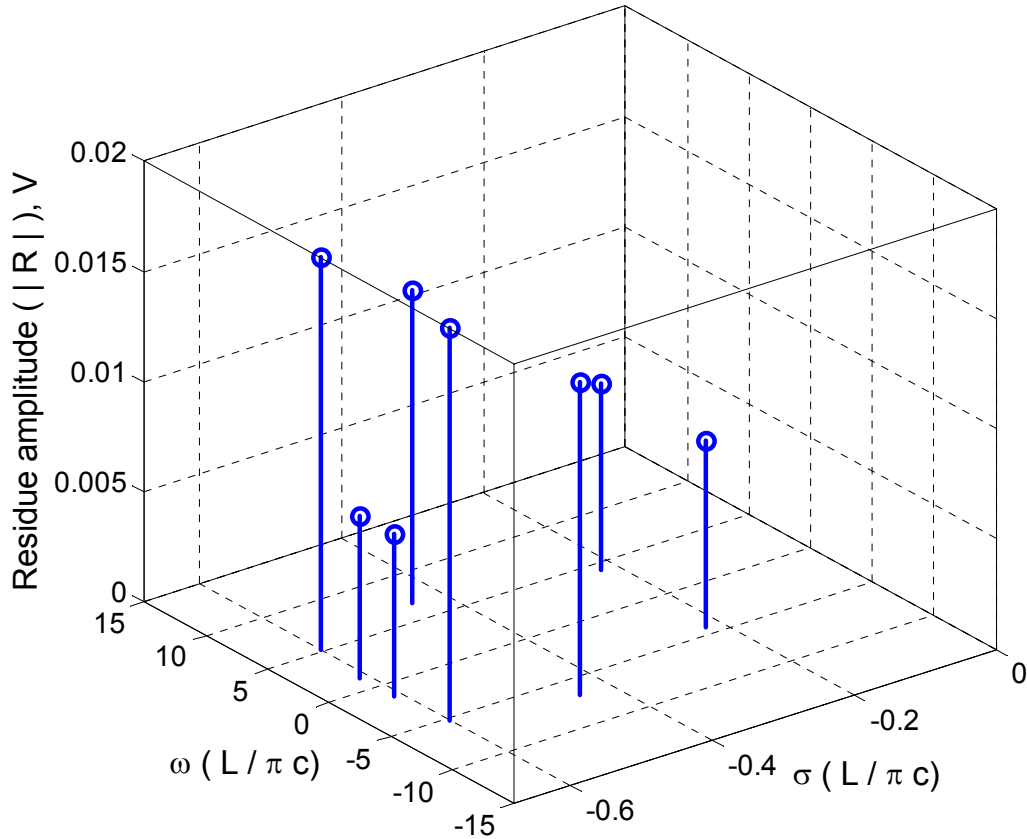


Figure 8.10 Dominant pairs of complex conjugate poles of a fire extinguisher of diameter 13 cm, and height 43.25 cm, and the corresponding residue amplitudes found by processing the received signal shown in Fig.8.9 using the Matrix Pencil Method (MPM) described in Section 4.2.

The received signal, after post-processing as described in Section 4.2, and the modeled response using the 4 dominant pairs of complex-conjugate poles is shown in Fig. 8.11. The specular component observed in Fig. 8.11 results from scatter-reflection off the fire extinguisher and retains the transmit pulse shape. The late-time response after the specular component is due to the resonant dispersion phenomena. This late-time response can be modeled using the singularity expansion method (SEM) described in Section 4.1.

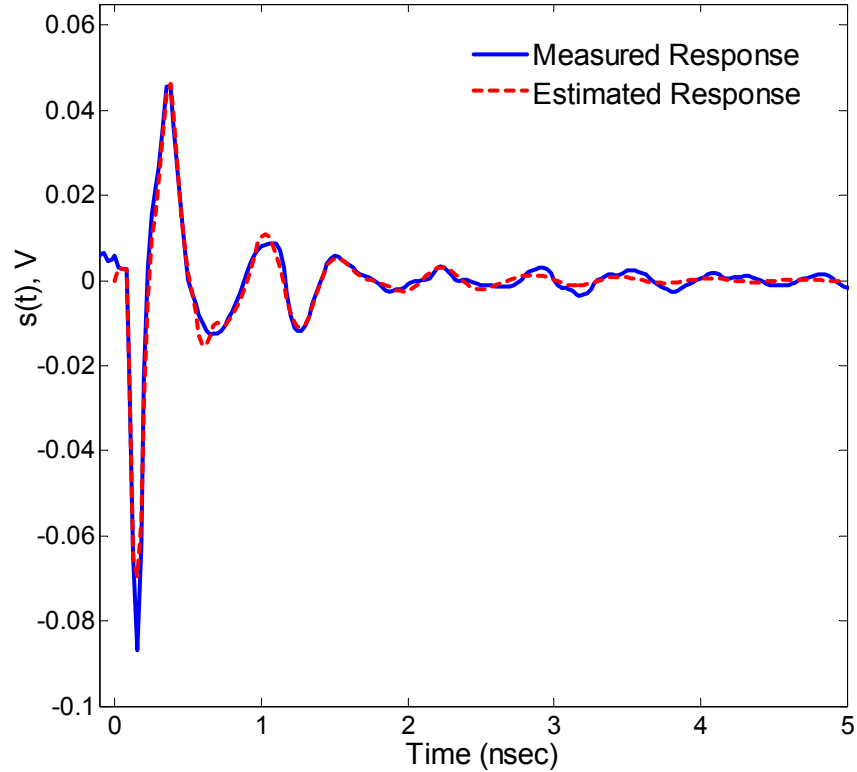


Figure 8.11 Received pulse from a fire extinguisher of diameter 13 cm, and height 43.25 cm after post-processing to remove unwanted scatterer and antenna responses. The modeled response uses 4 dominant pairs of complex-conjugate poles extracted using Matrix Pencil Method outlined in Section 4.2.

8.3.2 Conventional and Optimal Matched Filtering

This section demonstrates matched-filter receiver performance improvement by incorporating the resonant dispersion from finite-dimensional scatterers into the reference signal of the matched-filter using the pole-dispersion channel model. The output of the conventional matched filter (CMF) receiver given by (8.9) is shown in Fig. 8.12(a) for the transmit pulse shown in Fig. 8.3 and the distorted received pulse shown in Fig. 8.9. The peak correlation output of the CMF receiver given by the sampled value of (8.9) at time instant t_o using the transmit pulse-shape as the reference signal is 0.72. In comparison, the optimal matched-filter (OMF) uses a reference signal available from the pole-dispersion channel model given by (8.11) and shown in Fig. 8.11(b). The peak correlation output of the OMF receiver given by the sampled value of (8.12) at time instant t_o is 0.97.

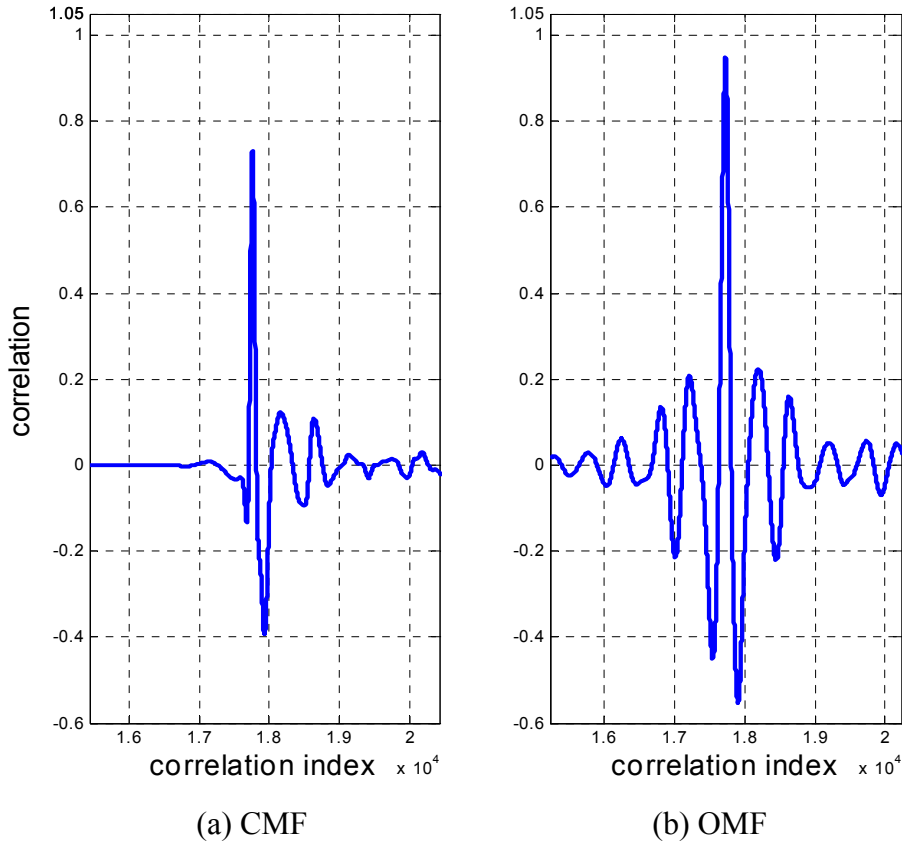


Figure 8.12 Correlation output of the matched filter given in Section 8.1.3 using (a) CMF receiver with the transmit pulse-shape (shown in Fig. 8.3) chosen as the reference signal, and (b) OMF receiver with the reference signal (shown in Fig. 8.11) and given by (8.15).

The peak signal-to-noise ratio at the output of the matched filter receiver (SNR_{out}) is larger for the optimal matched filter using a reference signal based on the pole-dispersion channel model than when using the conventional matched filter. The high correlation peak at the output of the matched filter receiver illustrates how closely the received signal is matched to the reference signal. This illustrates that the resonant channel model provides a closer match to the dispersive channel response. The reference signals and the received signals are energy normalized such that the ideal correlation peak output is unity. However, an ideal correlation peak of 1.00 was not achieved using the pole-dispersion resonant scatter channel model because the complex pole representation of the scatterer using $P = 4$ pairs of dominant poles offered a fairly accurate, but not an exact, match to the pulse distortion.

8.3.3 Bit-Error-Rate Performance in a Resonant Dispersive UWB Channel

The correlation peak of the matched-filter receiver as shown in Fig. 8.12 is indicative of the performance of a communication link in a dispersive channel. The performance of a matched filter receiver can also be described in terms of the bit-error-rate (BER) using the matched-filter output as input to the detector. Figure 8.13 describes a hybrid approach to simulate the bit-error-rate (BER) performance of a UWB communication link using the measured transmit and received signal waveforms, which is similar to the approach described in Fig. 8.6.

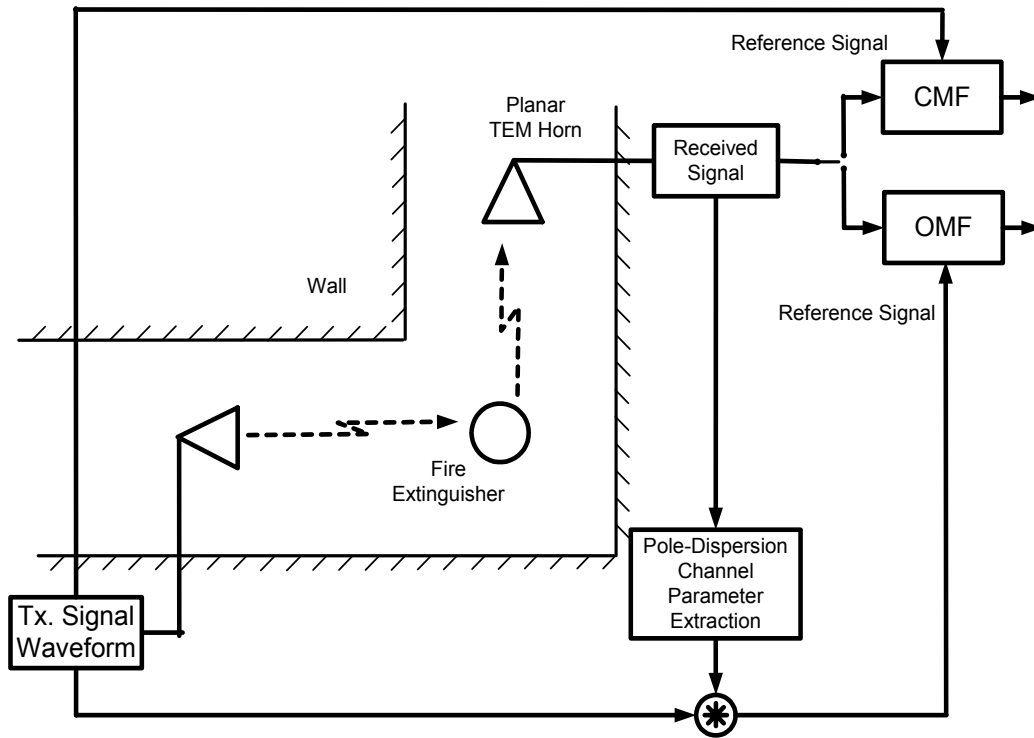


Figure 8.13 Block diagram of a UWB communication link simulated to determine bit-error-rate (BER) based on the *measured* transmit and distorted received signals respectively shown in Fig. 8.3 and Fig. 8.9 in an indoor NLOS hallway environment around a corner using a fire extinguisher as a scatterer.

The distorted received signal corrupted with additive white receiver noise is the input to the CMF and OMF receivers. The correlation based matched filter receivers (CMF and OMF) correlate the noisy corrupted received signal with the corresponding reference signals. The sampled output of the matched filter at the time instant t_0 , corresponding to the peak signal instant is used as input to the threshold detector. The detected bits are compared to the randomly

generated bits to estimate the probability of error. The bit-error-rate (BER) performance of a communication link using phase modulation and the correlation based CMF and OMF receivers for an obstructed NLOS dispersive UWB channel is shown in Fig. 8.14.

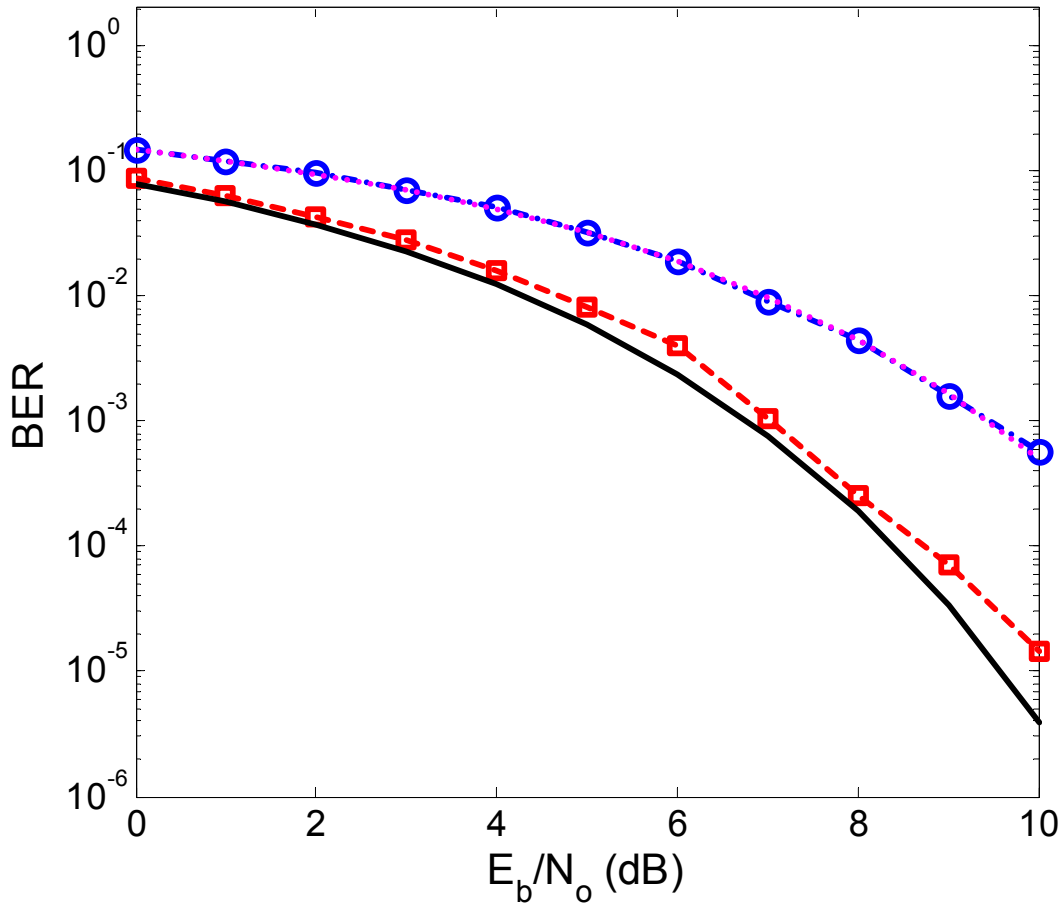


Figure 8.14 Bit-error-rate (BER) performance of a UWB communication system simulated with binary phase modulation in a NLOS dispersive channel shown in Fig. 8.13. The simulated BER performance curves for CMF and OMF receivers are respectively given by circular and square marks. The simulation uses the *measured* transmit pulse (Fig. 8.3) and receive pulse (Fig. 8.9) waveforms. The analytical performance of the conventional matched filter (CMF) receiver given by dotted line is from (8.19) using the measured value of $\xi^2 = 0.73$. The optimal performance is given by solid line and calculated from (8.17).

The BER performance of the CMF correlation receiver in Fig. 8.14 is significantly worse than the optimum achievable BER performance given by (8.17) and shown as the solid line. The poor performance of the CMF receiver is because of the signal energy loss due to mismatch in the pulse shape between the reference signal and the distorted received signal. The BER

performance of the CMF receiver follows from (8.10) with $\xi^2 = 0.73$, corresponding to the correlation peak shown in Fig. 8.12 (a), and is given by

$$BER_{CMF} = Q\left(\sqrt{\xi^2 \frac{2E_b}{N_o}}\right) = Q\left(\xi \sqrt{\frac{2E_b}{N_o}}\right) \quad (8.19)$$

where E_b is the energy content of the received signal waveform, and Q function is given by (8.18). In comparison, the BER performance of the OMF correlation receiver in Fig. 8.14 is close to optimal with little deviation from the analytically determined performance due to measurement and numerical errors and is given by

$$BER_{OMF} = Q\left(\sqrt{\gamma^2 \frac{2E_b}{N_o}}\right) = Q\left(\gamma \sqrt{\frac{2E_b}{N_o}}\right) \quad (8.20)$$

where γ approaches unity because the OMF reference signal given by (8.15) closely matches the distorted received signal.

8.4 Optimal Matched Filtering with Noisy Channel Estimate

This section describes the susceptibility of a UWB communication link using optimal matched filtering (OMF) to the errors in channel estimation. An error in channel estimation occurs if an insufficient number of poles and their corresponding residues are selected to model resonant dispersion. Section 8.4.1 presents BER performance of OMF receiver using fewer dominant poles in modeling resonant dispersion response from scatterers.

Another source of error in channel estimation is the presence of noise. The effect of noisy channel impulse response (CIR) estimates on the BER performance of a communication link is described in Section 8.4.2. A combined fuzzy-statistical approach described in Chapter 6 and Chapter 7 improves scatterer response modeling in presence of noise using only a few pairs of *fuzzy poles*. Section 8.4.3 presents BER performance results using the estimated channel impulse response based on the combined fuzzy and statistical analysis for various noise levels. Performance improvement in terms of BER at the output of the detector is also presented for simulated noisy time-domain responses of a thin wire scatterer.

8.4.1 Experimental Investigation of Resonant Dispersion Channel Modeling Error

Section 8.3.3 presented BER performance of the OMF receiver in presence of pulse distortion due to dispersive scatterer response. Near-optimal results of the optimal matched filter (OMF) are because the reference signal is given by the convolution of the transmit pulse-shape and the estimated channel impulse response; see (8.15). The correlation peak value at the output of the OMF depends on the accurate estimation of the frequency-dependent channel impulse response given by $h_c'(t)$.

Chapter 4 described singularity expansion method (SEM) based modeling of the frequency-dependent resonant dispersion response of finite dimensional scatterers. The channel impulse response with resonant dispersion can be modeled as a sum of damped exponentials as given by

$$h_c'(\tau) = a_n e^{j\theta_n} \delta(\tau - \tau_n) + \sum_{m=1}^{2P} R_{n,m}(\Omega_f, \Omega_r) e^{s_{n,m}(\tau - \tau_n - \Delta t_p)} u(\tau - \tau_n - \Delta t_p) \quad (8.21)$$

where P , s_{α} , and $R_{\alpha}(\phi, \theta)$ indicates the number of complex conjugate pole pairs, complex pole, and the corresponding aspect-dependent residue, respectively. The pole-dispersion channel parameters are extracted from the received signal $r(t)$ using the method outlined in Section 4.2. An error in channel estimation occurs if insufficient number of dominant pair of poles P is selected to model resonant dispersion. Figure 8.15 shows BER performance degradation of a communication link using OMF receiver with decreasing number of dominant pole-pairs used in modeling scatterer response.

The communication link used in experiment is the non-line-of-sight indoor hallway environment around a corner using a fire extinguisher of diameter 13 cm, and height 43.25 cm (see Fig. 8.8). As expected, performance degrades with fewer numbers of poles P used in modeling resonant dispersion because four dominant resonances are present in the response of the fire extinguisher. Using fewer poles lead to increasing error in resonant dispersion channel estimation, which creates mismatch between the distorted received signal $r(t)$ and the correlator reference signal $v_{ref,OMF}(t)$; see (8.15). This mismatch reduces the maximum correlation peak of the OMF receiver given by (8.12). Using more than $P = 4$ pairs of dominant poles does not offer significant improvement in BER performance as seen in Fig. 8.15 by using $P = 8$ pairs of dominant poles. The BER curves are obtained analytically using (8.20) with the values of the

mismatch factor γ obtained by the cross-correlation peak of the received signal $r(t)$ shown in Fig. 8.9 and the reference signal obtained from (8.15) using the estimated CIR given by (8.21).

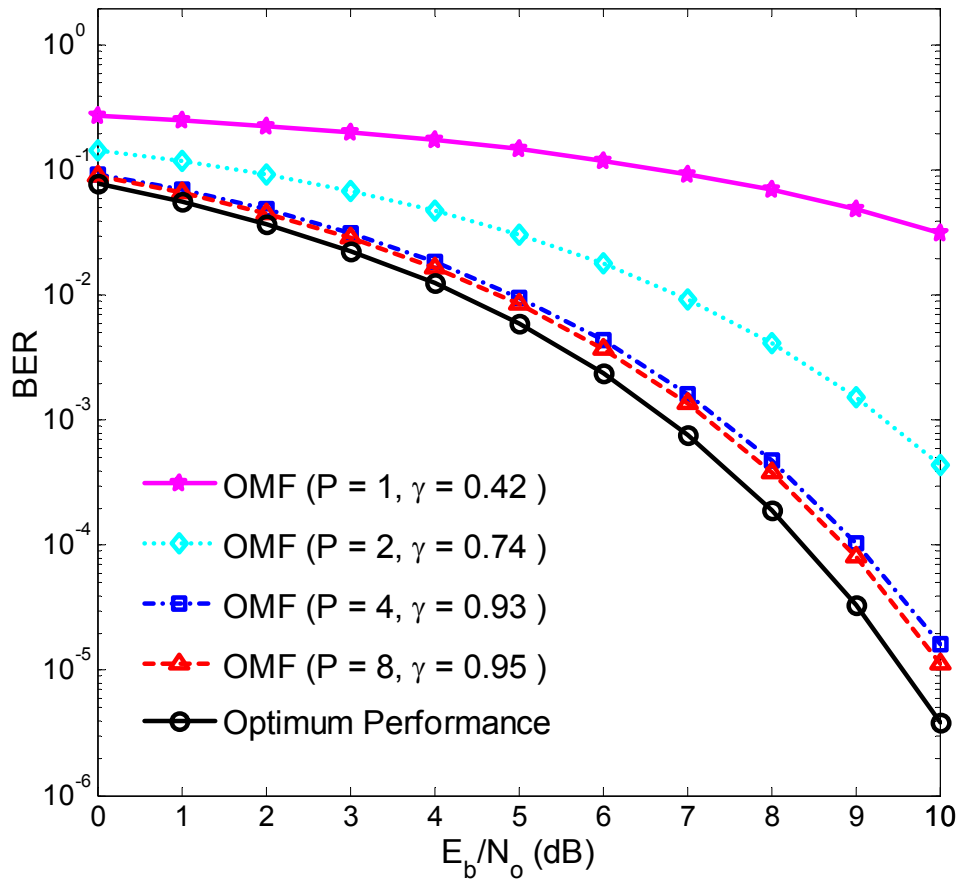


Figure 8.15 BER performance of a phase modulated dispersive UWB communication link shown in Fig. 8.13 using optimal matched filter (OMF) for various estimates of the channel impulse response (CIR) with the increasing number of dominant pole-pairs P . The mismatch factor γ is obtained by the measured correlation peak of the received signal $r(t)$ (shown in Fig. 8.9) and the reference signal obtained from (8.15) using the estimated CIR given by (8.21). The optimum performance is given by solid line and calculated from (8.17).

8.4.2 Investigation of BER Performance for Resonant Dispersion Channel Estimation Error due to Noisy Received Signal

The pole-residue parameters for the pole-dispersion channel model are estimated from a measured or simulated snapshot of the channel impulse response. Section 4.2 described in detail the process of estimating the pole-residue channel parameters. Pole positions in the complex frequency plane deviate due to noise [12, 13]. Section 6.1 describes the effect of noise on the

resonant dispersion channel impulse response estimation. The estimated residues corresponding to the spurious poles have incorrect values resulting in a poor match to the time-domain response. The bit-error-rate (BER) performance of a phase modulated communication link is investigated for resonant-dispersion channel-parameter estimation error due to noisy received signal.

An analytically determined response for a thin wire scatterer described in Table 6-1 is used instead of the fire extinguisher as scatterer to investigate the effect of noise [14]. Additive Gaussian noise is added to the thin wire scatterer response to investigate how does the noise affect channel impulse response (CIR) estimation, which in turn affects the overall performance of the communication link. The noise-corrupted response of the thin wire scatterer is processed using the Matrix Pencil extraction method (MPM) to extract the poles and residues for the pole-dispersion channel model as described in Section 4.2. Since the estimated poles are not accurate in the presence of noise there is a corresponding mismatch between the true CIR $h_c(t)$ and its estimate $h_c'(t)$, which is determined from the poles extracted using MPM in presence of noise.

The reference signal of the OMF receiver $v_{ref,OMF}(t)$ given by (8.15) no longer matches the distorted received signal due to the error in CIR estimation $h_c'(t)$ due to noise. This mismatch between the received signal and the reference signal reduces the correlation peak output γ^2 of the OMF receiver given by (8.12). This degrades the BER performance of a communication link using OMF receiver as given by (8.20) with the mismatch parameter γ measured at the output of the optimal matched filter (OMF). Figure 8.16 plots the BER performance degradation calculated using (8.20) due to decreasing SNR of the available received signal from which the channel dispersion parameters are estimated.

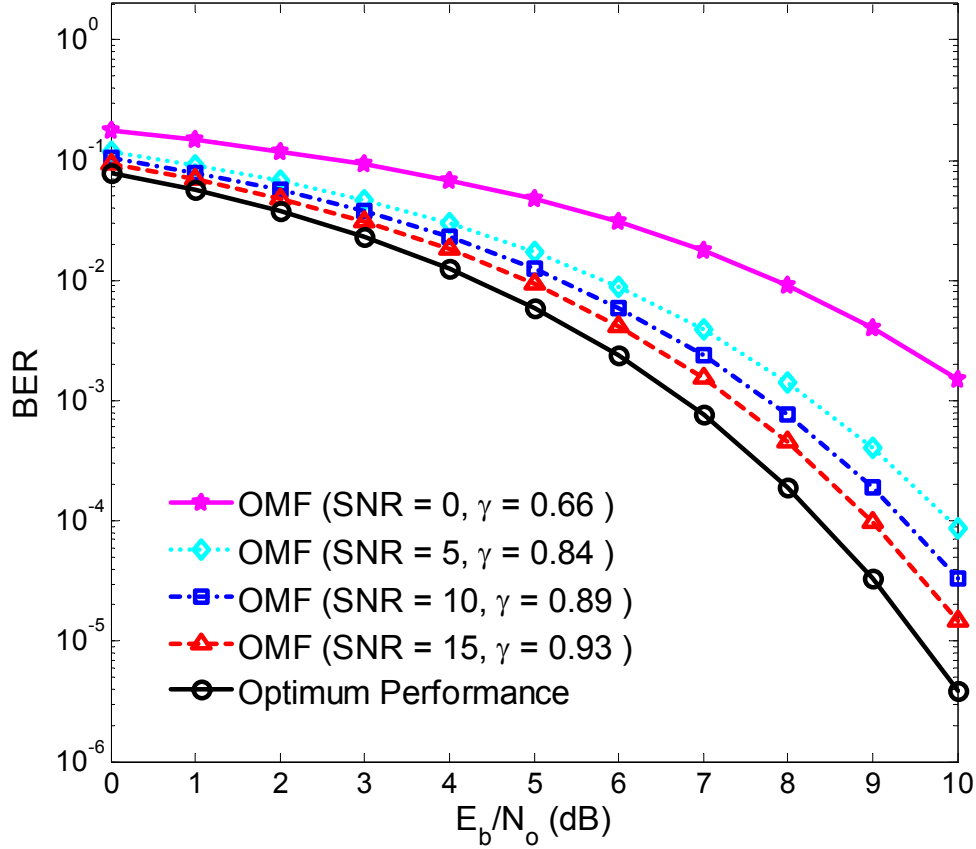


Figure 8.16 BER performance of a phase modulated UWB communication link calculated using (8.20) for decreasing SNR of the received signal. Noise causes error in resonant dispersive channel model estimation based on the received signal as described in Section 4.2. The resulting reference signal of the OMF receiver $v_{ref,OMF}(t)$ given by (8.15) and cross-correlated with the distorted received signal $r(t)$, gives the OMF receiver output γ^2 given by (8.12). The optimum performance is given by solid line and calculated from (8.17).

8.4.3 Investigation of BER Performance for Fuzzy-Statistical Estimation of Resonant Dispersion Channel

Noise severely limits accurate resonant dispersion channel estimation resulting in poor performance of matched-filtering in a communication link as demonstrated in the previous section. In Chapter 6, a fuzzy approach was proposed to circumvent the effect of noise. Cluster formation about the actual poles due to noise was exploited to represent the noisy transient response with a small number of fuzzy poles. Section 6.4 presented simulated as well as measured results demonstrating a close match of the estimated fuzzy poles to the actual poles of

thin wire and conducting sphere scatterers. This estimation was further improved in Chapter 7 by incorporating the statistical behavior of the estimated poles in presence of noise.

Figure 7.18 in Chapter 7 compares the fuzzy-statistical poles estimated from noisy channel impulse responses with theoretically determined poles of a thin wire scatterer described in Table 6-1. The estimated pole positions in the complex frequency-domain using the combined fuzzy-statistical approach offered a very close match to the dominant poles of the thin wires for $SNR = 0$ dB and 10 dB. Based on the estimated poles of the thin-wire using the combined fuzzy-statistical approach, the corresponding residues and the resonant dispersion channel impulse response were calculated.

In comparison to the channel estimation from a single snapshot of corresponding signal-to-noise ratios, channel estimation from the combined fuzzy-statistical approach offers a closer match to the distorted scattered signal received from the thin wire scatterer. This is evident at the output of the correlation-based matched-filter receiver given by (8.12) with the correlation peak value closer to unity. For energy normalized input and reference signals the correlation output peak corresponds to γ^2 .

The estimated CIR $h_c'(t)$ from the poles extracted using the combined fuzzy-statistical approach (described in Section 7.1) is more accurate than the estimated CIR from the poles extracted directly in presence of noise (described in Section 4.2). The reference signal of the OMF receiver $v_{ref,OMF}(t)$ given by (8.15) using $h_c'(t)$ from the combined fuzzy-statistical approach offers a better match to the distorted received signal compared to $h_c'(t)$ calculated directly from the noisy received signal. This increases the correlation peak output γ^2 of the OMF receiver given by (8.12), resulting in the BER performance improvement of a communication link given by (8.20) with the mismatch parameter γ measured at the output of the optimal matched filter (OMF). Figure 8.17 plots the BER performance improvement calculated using (8.20) due to improved dispersion channel estimation from the combined fuzzy-statistical approach for two noise levels corresponding to $SNR = 0$ dB and 10 dB.

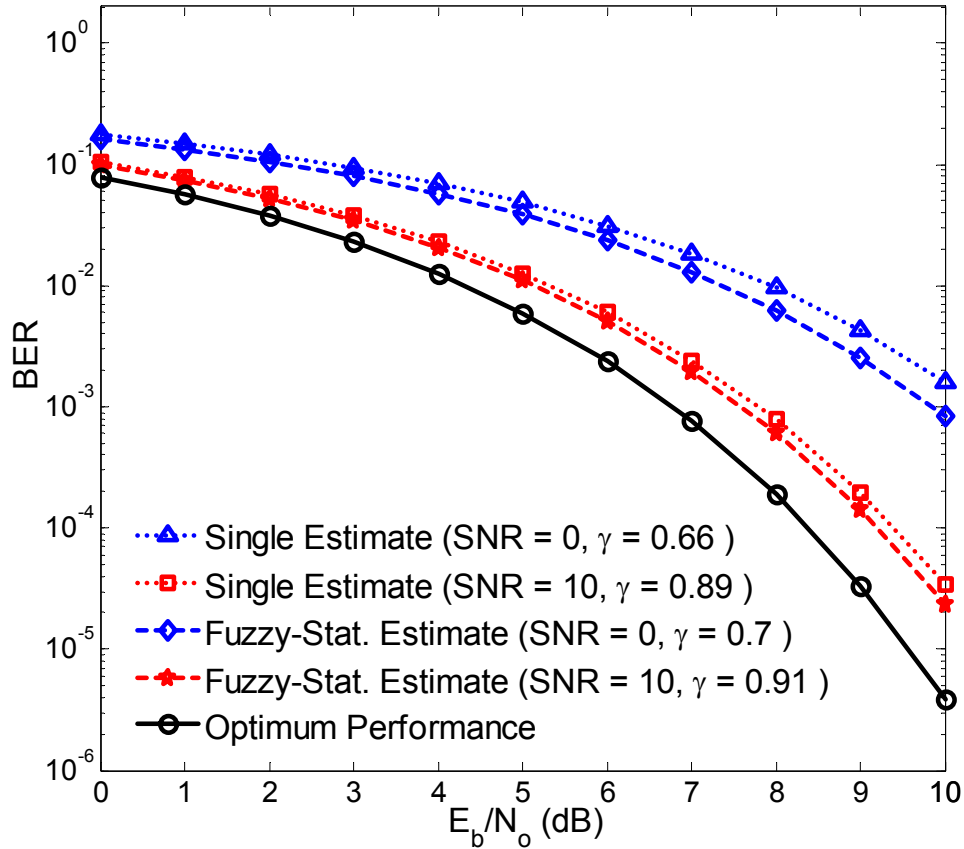


Figure 8.17 BER performance of a phase modulated UWB communication link calculated using (8.20) for improved dispersion channel estimation $h_c'(t)$ from the combined fuzzy-statistical approach for $SNR = 0$ dB and 10 dB. A thin wire described in Table 6-1 is used as a scatterer. The reference signal of the OMF receiver $v_{ref,OMF}(t)$ given by (8.15) is cross-correlated with the distorted received signal $r(t)$ to give the OMF receiver output (8.12). The optimal performance is given by solid line and calculated from (8.17).

8.5 Chapter Summary

This chapter presented simulated and measured results demonstrating the advantage of using the proposed pole-dispersion channel model (introduced in Chapter 4 and validated in Chapter 5) over the conventional frequency-independent channel models in modeling the UWB channel dispersion. The proposed pole-dispersion UWB scatter channel model includes frequency-dependent scatterer response and permits implementation of optimum matched filtering at the receiver in the presence of pulse distortion.

The chapter described correlation-based implementation of matched filtering using the expected received pulse-shape as the reference signal. Expressions for matched filter impulse

response or equivalently the reference template signal for correlation type implementation were developed in Section 8.1 for a non-dispersive as well as a dispersive UWB channel. Some important observations include:

1. The received signal waveform in a non-dispersive LOS indoor hallway environment is an attenuated and delayed version of the transmitted signal waveform; see Fig. 8.4.
2. For a non-dispersive channel, the correlation-peak of a correlation based matched-filter receiver equals maximum achievable value of unity; see Fig. 8.5. The received signal and the reference signal are normalized to unit energy.
3. The bit-error-rate (BER) performance of correlation based matched filter receiver inside a LOS distortionless hallway environment for phase modulation is close to optimal with negligible deviation from the analytically determined performance given by (8.17); see Fig. 8.7.
4. The received signal waveform in an obstructed (NLOS) condition inside a hallway environment with a fire extinguisher as a scatterer is significantly distorted version of the transmitted signal waveform; see Fig. 8.9.
5. The resonant dispersion channel model provides a closer match to the dispersion channel response with the reference signal available from the pole-dispersion channel model presents a correlation peak of 0.96. In comparison, the output of the conventional matched filter (CMF) receiver using transmit pulse-shape as the reference signal presents a correlation peak of 0.72; see Fig. 8.12.
6. The BER performance of the OMF correlation receiver is close to optimal compared to that of the CMF correlation receiver, which follows (8.10) with $\gamma^2 = 0.73$; see Fig. 8.13.
7. The BER performance of a communication link using OMF receiver degrades with decreasing number of dominant pole-pairs used in modeling resonant dispersion response from scatterer; see Fig. 8.15.
8. The pole-residue parameters for the pole-dispersion channel model are estimated from available channel impulse response through channel sounding. The BER performance of a communication link using OMF receiver degrades with increase in noise levels of the available channel snapshot; see Fig. 8.16.

9. The combined fuzzy-statistical approach improves channel estimation offering a close match to the distorted received signal and hence, improving the BER performance of a matched-filter receiver; see Fig. 8.17.

A significant contribution of this chapter is a demonstration that the pole-dispersion channel model proposed in Section 4.4 improves the BER performance of a communication link using matched-filter. Advances in accurate modeling of channel dispersion stands to benefit not only the UWB microwave communications but also in improving the performance of UWB based radar, and wideband acoustic signaling in dispersive ocean environment.

References

- [1] G. G. Joshi, W. A. Davis, and W. L. Stutzman, "Ultra-wideband (UWB) channel dispersion: classification and modeling," *Proceedings of IEEE Antennas and Propagation Society International Symposium, Washington D.C.*, vol. 1B, pp. 702-705, July 2005.
- [2] T. W. Hertel and G. S. Smith, "On the dispersive properties of the conical spiral antenna and its use for pulsed radiation," *IEEE Transactions on Antennas and Propagation*, vol. 51, pp. 1426-1433, July 2003.
- [3] R. C. Qiu, "A generalized time domain multipath channel and its application in ultra-wideband (UWB) wireless optimal receiver design-Part II: physics-based system analysis," *IEEE Transactions on Wireless Communications*, vol. 3, pp. 2312-2324, Nov. 2004.
- [4] J. P. Hermand and W. I. Roderick, "Acoustic model-based matched filter processing for fading time-dispersive ocean channels: theory and experiment," *IEEE Journal of Oceanic Engineering*, vol. 18, pp. 447-465, Oct. 1993.
- [5] J. G. Proakis, *Digital Communications*, 4th ed. Boston: McGraw-Hill, 2001.
- [6] J. G. Proakis and M. Salehi, *Communication Systems Engineering*, 2nd ed. Upper Saddle River, N.J.: Prentice Hall, 2002.
- [7] L. W. Couch, *Digital and Analog Communication Systems*, 6th ed. Upper Saddle River, N.J.: Prentice Hall, 2001.
- [8] B. Sklar, *Digital Communications : Fundamentals and Applications*, 2nd ed. Upper Saddle River, N.J.: Prentice-Hall PTR, 2001.
- [9] B. Friedlander and A. Zeira, "Detection of broadband signals in frequency and time dispersive channels," *IEEE Transactions on Signal Processing*, vol. 44 (7), pp. 1613-1622, July 1996.
- [10] G. Turin, "An introduction to matched filters," *IEEE Transactions on Information Theory*, vol. 6 (3), pp. 311-329, June 1960.
- [11] I. Glover and P. M. Grant, *Digital Communications*. London ; New York: Prentice Hall, 1998.
- [12] Y. Hua and T. K. Sarkar, "On SVD for estimating generalized eigenvalues of singular matrix pencil in noise," *IEEE Transactions on Signal Processing*, vol. 39 (4), pp. 892-900, Apr. 1991.
- [13] M. Van Blaricum and R. Mittra, "A technique for extracting the poles and residues of a system directly from its transient response," *IEEE Transactions on Antennas and Propagation*, vol. 23 (6), pp. 777-781, Nov. 1975.

- [14] J. Cordaro and W. Davis, "Time-domain techniques in the singularity expansion method," *IEEE Transactions on Antennas and Propagation*, vol. 29 (3), pp. 534-538, Mar. 1981.

Chapter 9 – Conclusions

Ultra-wideband (UWB) is expected to revolutionize high data-rate, short-distance wireless communications, but UWB data-rate capacity is severely limited by pulse distortion due to resonant channel dispersion. Resonant channel dispersion can be modeled with the singularity expansion method (SEM) with limited accuracy in presence of noise. A novel pole dispersion channel model was introduced in Chapter 4 based on the SEM to include resonant dispersion. This dissertation demonstrated improvement in the communication link under dispersive channel conditions.

An empirical investigation supports our claim that a correlation type matched-filter receiver using a template signal based on the pole dispersion channel model overcomes distortion related losses. The bit-error-rate (BER) performance improvement of a communication link in a resonant dispersive channel depends on the accurate channel modeling. A combined fuzzy-statistical analysis of simulated and empirically determined scatterer response allows near optimal performance of a correlation based matched-filter receiver. The advances in the characterization of resonant channel dispersion modeling will contribute to the development in ultra-wideband communications, surveillance, and radar systems.

9.1 Resonant Dispersion Modeling and Advantages

Ultra-wideband applications are performance limited by dispersion due to pulse distortion. For UWB communication systems, resonant dispersion follows multipath dispersion in limiting

achievable performance. This dissertation presented resonant channel dispersion modeling to improve the performance of a UWB communications system. The research approach consisted of four stages:

Channel Dispersion Classification

There is a lack of common understanding about *channel dispersion*. Chapter 2 identified three types of dispersion mechanisms such as multipath, frequency, and resonant channel dispersion. This initial study on dispersion was followed by a literature review of indoor and outdoor UWB channel in Chapter 3.

Resonant Channel Dispersion Modeling

A novel dispersion channel model was proposed in Chapter 4 as an extension to Turin's conventional channel model to include frequency-dependent dispersion effects. The frequency-dependent resonant scatterer response is modeled using the singularity expansion method (SEM) that is verified using canonically shaped scatterers such as a sphere and a thin wire scatterer in Chapter 5.

Robust Modeling in Presence of Noise

Chapters 6 and 7 covered the topics on accurate resonant channel modeling in presence of noise. The pole-residue resonant dispersion modeling based on SEM is very susceptible to noise. Multiple noisy time-domain snapshots of the scatterer response were processed using a blind fuzzy clustering approach to significantly improve resonant dispersion modeling in Chapter 6. A combined fuzzy-statistical approach was proposed in Chapter 7 to improve the robustness of resonant dispersion channel modeling in presence of noise. The modeling error is significantly reduced for the estimated pole-residue signatures of canonically shaped scatterers and analytically available pole-residue signatures.

System Level Improvement

Chapter 8 presents the final part of the research demonstrating that a matched-filter (MF) receiver achieves near-optimal performance. The applicability of the proposed dispersive channel model of Chapter 4 was evaluated using the optimal matched filtering (OMF). An optimal receiver is a matched-filter (MF) if the received signal pulse-shape is known at the receiver. Prior to transmitting pulses modulated by data bits, a communication channel must allow channel sounding to model dispersion using a correlation type MF receiver. Correlation

type MF receiver design should use a reference signal obtained from convolution of the transmit pulse and the estimated resonant channel dispersion model.

9.2 Summary of Contributions

In this dissertation a novel approach is proposed to model resonant dispersion from scatterers with application to indoor ultra-wideband communications. The proposed combined fuzzy clustering and statistical approach is shown as a solution to improved resonant dispersion channel estimation in presence of noise. The improved pole-residue based dispersion modeling improves the performance of a communication link using matched-filter receiver.

Scattering wave propagation mechanisms, especially the response of scattering objects to ultra-wideband pulse excitation, have not been comprehensively investigated. Chapter 2 described multipath and phase dispersive characteristics of outdoor and indoor ultra-wideband channels. An original contribution is an identification and classification of various types of observed dispersion mechanisms [1].

Most UWB channel models have been proposed by simply extending conventional wideband channel models. Chapter 3 presented a brief overview of various UWB channel models with special emphasis on frequency dependent UWB channel dispersion models. Limitations of all conventional UWB channel models in modeling all identified dispersion mechanisms were briefly discussed.

Chapter 4 described the Singularity Expansion Method (SEM) and the numerical techniques used for determining the pole-residue scatter signatures. The measurement setup and transient response analysis using the Prony's method, and the Matrix Pencil Method (MPM) is also described. A novel pole-dispersion channel model is introduced that includes resonant and multipath dispersion effects [1].

Chapter 5 validated the SEM based pole-residue dispersion modeling that is used in the proposed pole-dispersion channel model. The pole-residue dispersion characteristics of scatterer response are validated through comparison of the estimated complex-pole positions from measured data and the complex-pole positions available analytically for two types of canonical objects: a conducting sphere and a thin wire scatterer. In presence of noise, a dominant pole selection process based on the pole energy content is proposed to avoid selecting spurious poles.

Chapter 6 presented *fuzzy pole* representation of the estimated complex poles of a noisy time-domain scatterer response. Simulated results for two extreme cases of noise levels indicate that with increasing noise levels the optimal number of clusters needed to represent the noisy data increases. An original contribution is a modified fuzzy clustering approach to determine the optimal representation of the noisy data using fuzzy cluster centroids or fuzzy poles [2]. This permits an alternate approach to represent the dispersion of scatterer response in terms of a small number of equivalent fuzzy poles [3].

Chapter 7 presented a statistical investigation of the estimated complex poles of a noisy time-domain scatterer response. Complex poles cluster formations around the actual poles in the s-plane were exploited to determine the probability density distribution (*pdf*) of the real and imaginary components. In this chapter, a novel idea of pole energy to noise ratio (E_p/N_o) is proposed that completely captures the effect of noise on pole distribution in the complex frequency domain and is verified using simulated results. Another original contribution is determining a joint distribution of the real and imaginary components of the estimated poles in the complex s-plane [4].

The proposed pole-dispersion UWB scatter channel model includes frequency-dependent scatterer response and permits implementation of optimum matched filtering at the receiver in the presence of pulse distortion. Chapter 8 described correlation-based implementation of matched filtering using the expected received pulse-shape as the reference signal. The resonant dispersion channel model provides a closer match to the dispersion channel response with the reference signal available from the pole-dispersion channel model presents a correlation peak of 0.96. In comparison, the output of the conventional matched filter (CMF) receiver using transmit pulse-shape as the reference signal presents a correlation peak of 0.73. The BER performance degradation with decreasing number of dominant pole-pairs and with increasing noise levels in the channel estimation is also presented. A significant contribution of this chapter is a demonstration that the proposed pole-dispersion channel model improves the BER performance of a communication link using matched-filter.

Overall, this dissertation investigates improvement in UWB signal reception achieved by compensating for the distortion due to resonant channel dispersion.

9.3 Opportunities and Future Work

This doctoral research opens several research avenues by showing how the singularity expansion method (SEM) can be extended to severely noise-corrupted data. The SEM approach models the time-domain response of an unknown object (target) in terms of natural resonances. The natural resonances, also known as the poles, are indicative of the target size and can be used as target signature.

In this dissertation, a modified fuzzy clustering approach was proposed as a solution to overcome the effect of noise. Advances in identification of clusters using fuzzy algorithms have offered an alternative approach to study the distribution of the estimated poles about the actual complex poles within the cluster in presence of noise. The estimated fuzzy poles offer a close match to the actual poles determined from the simulated and measured responses of a thin wire scatterer. Advances in accurate target response modeling in terms of its unique signatures promise to offer significant improvement in buried landmine detection as well as early detection of breast tumors.

A combined fuzzy-statistical approach proposed in Chapter 7 offers near-accurate estimation of the target pole-residue characteristics. Because the approach is based on a blind partitioning algorithm that does not require any a-priori information of the scatterer dimensions, it simplifies target identification. If the target pole-residue signature is available for table look-up then it permits classification of UWB radar targets into friendly and hostile categories. Overall the results presented in Chapter 6 and Chapter 7 indicate that fuzzy-statistical characterization has promising application in target identification and discrimination, which uses noisy time-domain UWB radar responses. Hostile aircraft identification using noisy time-domain data from UWB short pulse radar stands to gain tremendously from this research on target signature estimation.

Inter-symbol interference (ISI) due to resonant pulse distortion was not investigated in this dissertation. Increasing symbol rates for high data-rate transmission capacity requires smaller time spacing between transmitted symbols. There is a strong possibility that resonant dispersion extends the pulse duration beyond the symbol time, i.e. the distorted pulse has not decayed before the next symbol arrives resulting in ISI. All communication links are designed to avoid ISI because it causes irreducible error floor in the bit-error-rate (BER) performance. There

is a potential for significant research in the investigation of inter-symbol interference from resonant dispersion due to various types of scatterers.

However, measurement noise limits the achievable benefits for these applications. Noise leads to estimation of false (or spurious) poles, which in turn leads to an inaccurate signature with high probability of false alarm. There are four potential research topics for future work:

- (a) Radar target identification,
- (b) Ground penetration radar for buried landmine detection, and
- (c) Breast tumor detection
- (d) Inter-symbol interference from resonant dispersion in communication systems.

References

- [1] G. G. Joshi, W. A. Davis, and W. L. Stutzman, "Ultra-wideband (UWB) channel dispersion: classification and modeling," *IEEE Antennas and Propagation Society International Symposium*, vol. 1B, pp. 702-705, July 2005.
- [2] G. G. Joshi, W. A. Davis, and W. L. Stutzman, "Statistical and fuzzy pole characterization of the complex poles of a conducting sphere and a wire," *presented at the URSI National Radio Science Meeting at Boulder, CO*, Jan. 2006.
- [3] G. G. Joshi, W. A. Davis, and W. L. Stutzman, "Fuzzy pole characterization of scatterer response for target identification," *IEEE Transactions on Antennas and Propagation*, under preparation and to be submitted.
- [4] G. G. Joshi, W. A. Davis, and W. L. Stutzman, "Fuzzy Pole Representation for SEM based Complex-Pole Scatterer Signature," *IEEE Antennas and Propagation Society, URSI/USNC, and AMEREM Joint International Symposium*, July 2006.

Author Vitae

Gaurav Joshi grew up in Gandhinagar and Ahmedabad in Gujarat state of India. He received his Bachelor in Engineering (B.E.) degree from the Electronics and Communications Engineering Department, L. D. College of Engineering, Gujarat University in 2000. Gaurav Joshi received his M.S. and Ph.D. degrees in Electrical Engineering from the Bradley Department of Electrical and Computer Engineering at Virginia Polytechnic Institute and State University (Virginia Tech) in 2002 and 2006, respectively. Since 2000, Gaurav has been a Graduate Research Assistant at the Virginia Tech Antenna Group (VTAG) where his research has concentrated on wireless communications and wideband signal propagation. His interests are in statistical signal processing, wireless communications, and electromagnetic propagation. He has also developed and investigated multi-antenna systems for diversity combining, adaptive beamforming and MIMO applications.